

https://dspace.org/

Cavitation due to Rarefaction Waves and the Reflection of Shock Waves from the Free Surface of a Liquid

Sam, Justin Shang

2006-11-14T08:58:07Z
http://hdl.handle.net/10539/1665

Downloaded from a DSpace repository. https://dspace.org/

Cavitation due to Rarefaction Waves and the Reflection of Shock Waves from the Free Surface of a Liquid

Justin Sam

A Dissertation submitted to the Faculty of Engineering and the Built Environment, University of the Witwatersrand, Johannesburg, in fulfilment of the requirements for the degree of Master of Science in Engineering.

Declaration

I declare that this dissertation is my own, unaided work, except where otherwise acknowledged. It is being submitted for the degree of Master of Science at the University of the Witwatersrand and has not been submitted before for any degree or examination in any other university.

……..	…….
Justin Sam	Date

Abstract

Cavitation was generated in tap water samples by the transmission of tension waves into the liquid, using a hydrodynamic shock tube. The liquid cavitated at absolute negative pressures of about -1 *bar*. Simulations of bubble responses showed qualitative agreement with experimental observations of oscillatory growth and collapse cycles. Pressure records showed secondary pressure pulsations, confirming the oscillatory nature of the collapse at each rise in pressure. More quantitative comparison of theory and photographic records would require a camera with a higher capture rate. Experiments using another experimental facility involved liquid compression waves with peak static pressures of up to about 1 *MPa*, which were transmitted from a conventional gas shock tube into a liquid section and were intended to be reflected at the free surface as expansion waves. These experiments were unsuccessful in producing absolute negative pressures or cavitation that was visible through an optical observation section. This was attributed to transition layer effects and pulse attenuation, which contributed to lowering of the peak negative pressure behind the expansion wave, as well as the depth of the transducer and observation section below the free surface, which may have been too low for the peak tension to be superimposed on the lower pressure behind the incident compression wave. Pressure records suggested that, for lower driver pressures, cavitation occurred below the observation section, although this could not be verified optically.

For long you live and high you fly
but only of you ride the tide
and balanced on the biggest wave
you race towards an early grave

- Roger Waters

Acknowledgements

The author is grateful for the valuable input of Professor B. W. Skews, whose guidance and assistance, throughout this project has been indispensable.

The author is also indebted to his mother, whose sacrifice, though not often spoken of, is always acknowledged.

Table of Contents

Title Page i

Declaration ii

Abstract iii

Acknowledgements v

Table of Contents vi

Table of Appendices x

List of Figures xi

List of Tables xv

Nomenclature xvi

1. Introduction 1

1.1. Definition of Cavitation 1

1.2. Types of Cavitation 2

1.3. Effects of Cavitation 3

1.4. Uses of Cavitation 5

1.5. The Study of Cavitation 8

1.5.1. Producing Controlled Cavitation 8

1.5.2. Definition of the Cavitation Threshold and Detectable Sizes 9

1.5.3. Detection and Visualisation 9

1.6. The Purpose of this Work 10

2. Shock Waves and Rarefaction Waves 11

2.1. Compressible Flow 11

2.2. The Conservation Laws for a Shock Wave 12

2.3. General Equations 14

2.4. Shock Waves and Rarefaction Waves in Gases 16

2.4.1. General Equations for Gases 16

2.4.2. Sound Waves in Gases 16

2.4.3. Finite, Isentropic Waves in Gases 17

2.4.4. Shock Waves in Gases 18

2.5. Shock Waves and Rarefaction Waves in Liquids 19

2.5.1. General Equations for Liquids 19
2.5.2. Sound Waves in Liquids 21
2.5.3. Shock Waves in Liquids 21
2.5.4. Finite Waves in Liquids 22
2.6. The Shock Tube 23
2.7. Methods of Analysis 24
2.7.1. The Wave Diagram 25
2.7.2. The Pressure-Velocity Diagram 27
2.8. Shock and Rarefaction Wave Interactions 27
2.8.1. Interactions of a wave with walls or contact surfaces 28
2.8.1.1. Reflection from a Rigid Wall 30
2.8.1.2. Shock or Rarefaction Wave Passing Through a Discontinuous Change in Cross-section 30
2.8.1.3. Free Surface Reflection 30
3. Cavitation 33
3.1. Liquids Under Negative Pressure 33
3.1.1. Cavity Dynamics of Bubbles Initiated in a Stretched Medium 35
3.2. Nucleation 36
3.2.1. Cavitation Nuclei 37
3.2.1.1. Miscible Liquids and Dissolved Solids 38
3.2.1.2. Non-miscible Liquids and Undissolved Solids 38
3.2.1.3. Dissolved Gas 39
3.2.1.4. Undissolved Gas and Vapour Bubbles 39
3.2.2. The Statistical Nature of Cavitation 41
3.3. Spherical Bubble Dynamics 42
3.3.1. The Rayleigh-Plesset Equation 43
3.3.2. The Response of Bubbles to Rarefaction Waves 45
3.4. Collapse of Cavitation Bubbles 47
4. Literature review 48
4.1. Pulse Reflection Experiments 48
4.1.1. Explosions 49
4.1.2. Bullet-Piston (B-P) Methods 50

4.1.3. Pulsed Electron Beam Generator 52
4.1.4. Illustrative Case 52
4.1.5. Intense Cavitation 54
4.2. Tube Arrest Methods 56
4.3. Hydrodynamic Shock Tube Methods 59
4.4. Ultrasonic and Wave-Focussing Methods 61
4.5. Gas Nuclei Studies 63
4.5.1. The Effect of Precompression 63
4.5.2. The Effect of Evacuation 65
4.5.3. Repeated Cavitation in a Single Sample 66
4.5.4. The Initial State of Samples of Liquid Water 67
4.6. Solid Nuclei Studies 67
4.7. Cavitation Thresholds 68
4.7.1. Liquid Purity 69
4.7.2. Rate of Stressing 70
4.7.3 Transition Layer 71
4.7.4. Measurement of Tensile Strengths 73
4.7.5. Overlapping of Tension Pulses 73
5. Experimental Facilities and Methods 75
5.1. The Mach 3 Shock Tube 75
5.1.1. Instrumentation 78
5.1.2. High-Pressure and Vacuum supplies 79
5.1.3. Flow Visualisation 79
5.2. The Mach 2 Shock Tube 79
5.2.1. Instrumentation 82
5.2.2. The High-Pressure Supply 82
5.2.3. The Liquid-Gas Interface 82
5.2.4. The Diaphragm Bursting Mechanism 82
5.3. Experimental Procedure 83
5.3.1. The Mach 3 Shock Tube 83
5.3.2. The Mach 2 Shock Tube 85

6. Experimental Observations and Results 87
6.1. The Mach 3 Shock Tube 87
6.1.1. Pressure Transducer Records 87
6.1.2. Photographic Records 89
6.2. The Mach 2 Shock Tube 92
7. Theoretical Analysis 97
7.1. The Mach 3 Shock Tube 97
7.1.1. Wave Diagram 97
7.1.2. Pressure-Velocity Diagrams 99
7.1.3. Bubble Dynamics Simulations 103
7.1.4. Computational Fluid Mechanics 111
7.2. The Mach 2 Shock Tube 111
7.2.1. Wave Diagram 112
7.2.2. The Area Change 114
7.2.3. The Motion of the Gas-Liquid Interface 118
7.2.4. The Effect of Pipe Wall Elasticity 120
7.2.4.1. Streeter's Method 120
7.2.4.2. Method of Characteristics 121
7.2.4.3. Elementary Calculation 122
8. Discussion 125
8.1. The Mach 3 Shock Tube 125
8.2. The Mach 2 Shock Tube 132
9. Conclusions 139
10. Recommendations 140
10.1. Improvements to the Mach 3 Shock Tube 140
10.2. Improvements to the Mach 2 Shock Tube 141
10.3. Further Studies 141
11. References 145

Table of Appendices

Appendix A: Entropic Relations for Arbitrary Gas States 162

Appendix B: Common Relations Across a Liquid Shock 163

Appendix C: Wave Diagram Considerations 166

Appendix D: One-Dimensional Interaction Problems 169

Appendix E: Collision and Reflection of Waves from a Rigid wall 171

Appendix F: Interaction of a Shock or Rarefaction wave with a Discontinuous Change in Cross-Section 173

Appendix G: Physical and Thermodynamic Properties of Various Substances 176

Appendix H: Summary of Experimental Cavitation Thresholds Values 180

Appendix I: The Initial States of Samples of Liquid Water 186

Appendix J: Assembly Drawings of the Mach 3 and Mach 2 Shock Tubes 188

Appendix K: Transducer Specifications and Gauge Factors 192

Appendix L: The Mach 3 Shock Tube: Additional Pressure Records 194

Appendix M: The Mach 3 Shock Tube: Photographic Records of the Lower Section of the Tube 196

Appendix N: The Mach 3 Shock Tube: Photographic Records of the Lower Section of the Tube 201

Appendix O: The Mach 3 Shock Tube: Photographic Records of the Free Surface of the Liquid Column 206

Appendix P: The Mach 2 Shock Tube: Additional Pressure Records 212

Appendix Q: Values of State Parameters in the Regions of the Wave Diagrams of the Mach 3 and Mach 2 shock tube 215

Appendix R: Results of Simulations of Bubble Response to Applied Pressure Variations 218

Appendix S: Overview of Cavitation Models Employed by Available CFD Codes 229

Appendix T: The Taylor Analysis of a Finite, Non-rigid Plate Subjected to a Square Pressure Wave 231

List of Figures

Figure 1.1.	The phase diagram of water.	3
Figure 2.1.	Moving and fixed shock reference frames.	12
Figure 2.2.	Required diaphragm pressure ratio for generating shock of strength γ in shock tube with air in the driver section and air, helium and hydrogen in the driver section.	24
Figure 2.3.	Required diaphragm pressure ratio for generating shock of Mach number M_{s1} in shock tube with nitrogen in the driver section and helium and nitrogen in the driver section.	24
Figure 2.4.	The wave diagram resulting from diaphragm rupture in a shock tube.	25
Figure 2.5.	Collision of a wave with a contact surface: initial and final conditions.	28
Figure 2.6.	Resultant absolute pressure vs. time at some depth below the free surface.	32
Figure 3.1.	Cavitation probability as a function of transducer driving voltage.	41
Figure 3.2.	A spherical bubble in an infinite liquid.	42
Figure 3.3.	Regions of the P-V_o plane.	46
Figure 4.1.	Cavitation zone development due to underwater explosion of a 1.2 g charge near the free surface of a liquid.	50
Figure 4.2	Photographs of cavity clusters that developed in distilled water samples tested immediately (upper frame) and one hour after (lower frame) being placed into a cuvette.	53
Figure 4.3.	Sequence of x-ray frames of cavitation zone dynamics resulting from shock wave reflection at a free surface.	54
Figure 4.4.	Process of intense cavitation in a liquid drop.	55
Figure 4.5.	Cavitation development in a tube due to downward acceleration of a cavitation tube.	59
Figure 4.6.	Side view of test section, showng the result of propagation of an evaporation wave through a superheated refrigerant sample.	61
Figure 5.1.	Photograph of the “Mach 3” shock tube.	76
Figure 5.2.	Photograph of the “Mach 3” shock tube test (driver) section.	77
Figure 5.3.	Photographs of the “Mach 2” shock tube.	81
Figure 5.4.	Photograph of the diaphragm bursting mechanism of the “Mach 3” shock tube.	83
Figure 6.1.	Pressure trace from test using the Mach 3 shock tube.	87
Figure 6.2.	Cavitation observed at the bottom of the Mach 3 shock tube.	89
Figure 6.3.	Cavitation observed at the middle section of the Mach 3 shock tube.	91

Figure 6.4.	Cavitation observed at the upper section of the Mach 3 shock tube.	92
Figure 6.5.	Pressure trace from test using the Mach 2 shock tube.	93
Figure 7.1.	Wave diagram of the Mach 3 shock tube.	98
Figure 7.2.	Pressure-velocity diagram for the collision of the expansion waves with the gas-liquid interface.	100
Figure 7.3.	Pressure-velocity diagram for the collision of the expansion waves with the base of the Mach 3 shock tube.	101
Figure 7.4.	Matlab Simulink model of the Rayleigh-Plesset equation	104
Figure 7.5.	Variation of bubble radius with time for growth of bubble (R_o 0.5 *mm*) subjected to step-function pressure drop from 7.93 to -1 *bar* at time zero.	105
Figure 7.6.	Variation of bubble wall velocity with time for growth of bubble (R_o 0.5 *mm*) subjected to step-function pressure drop from 7.93 to -1 *bar* at time zero.	105
Figure 7.7.	Variation of bubble wall acceleration with time for growth of bubble (R_o 0.5 *mm*) subjected to step-function pressure drop from 7.93 to -1 *bar* at time zero.	106
Figure 7.8.	Regions of the P-V_o plane (initial pressure 7.93 *bar*, surface tension 0.073 $J.m^{-2}$)	107
Figure 7.9.	Variation of bubble radius with time for collapse of bubble (R_o 0.5 *mm*) subjected to step-function pressure rise from -1 to 1 *bar* at time zero. $R(0)$=1*mm*, $\dot{R}(0)$=8.3 $m.s^{-1}$.	108
Figure 7.10.	Variation of bubble wall velocity with time for collapse of bubble (R_o 0.5 *mm*) subjected to step-function pressure rise from -1 to 1 *bar* at time zero. $R(0)$ = 1 *mm*, $\dot{R}(0)$ = 8.3 $m.s^{-1}$	109
Figure 7.11.	Variation of bubble wall acceleration with time for collapse of bubble (R_o 0.5 *mm*) subjected to step-function pressure rise from -1 to 1 *bar* at time zero. $R(0)$ = 1 *mm*, $\dot{R}(0)$ = 8.3 $m.s^{-1}$.	110
Figure 7.12.	Wave diagram of the Mach 2 shock tube (gas driver section: helium at 12 *bar*, gas driven section: air at 0.83 *bar*).	113
Figure 7.13.	Results from Chester-Chisnell-Whitham analysis and the quasi-steady analysis for the de-ampliification of a shock with initial Mach number M_{Si}.	116
Figure 7.14.	Results of simulations [46] of propagation of shock wave (M_S = 3) through a discontinuity with an area enlargement ratio of 1/10 at the instant 0.2 *ms*.	117
Figure 7.15.	Results of analysis of the liquid-air interface using Taylor's theory.	119
Figure 7.16.	Wave diagram of upper, liquid-filled section of the Mach 2 shock tube, including the effects of pipe stretch.	122
Figure 8.1.	Suggested pressure profile of the first compression wave transmitted into the liquid.	134
Figure D.1.	Collision of waves: initial and final conditions.	169

Figure D.2.	Overtaking of one wave by another: initial and final conditions.	170
Figure F.1.	Possible steady flow wave patterns for the passage of a shock wave through a small area enlargement.	173
Figure F.2.	Incident, reflected and transmitted waves in the interaction of a wave with an area enlargement discontinuity.	175
Figure I.1.	Histograms of nuclei number densities N_o in untreated, degassed and filtered tap water.	187
Figure J.1.	Assembly drawing of the Mach 3 hydrodynamic shock tube.	189
Figure J.2.	Assembly drawing of the liquid test section of the Mach 2 shock tube.	190
Figure J.3.	Assembly drawing of the modified gas driven-section of the Mach 2 shock tube.	191
Figure K.1.	Drawing of the PCB transducer, model 113A21	192
Figure L.1.	Pressure trace from test using Mach 3 shock tube; Sampling rate 1 *MHz*, 10000 data points.	195
Figure L.2.	Pressure trace from test using Mach 3 shock tube; Sampling rate 2 *MHz*, 10000 data points.	195
Figure P.1.	Pressure trace from test using Mach 2 shock tube; Driver section filled with helium at 12 *bar*; Sample rate 200 *kS/s*, Trigger level +0.1 *V*, source CH-1 (transducer 1), position –4 *V*, delay 0.	213
Figure P.2.	Pressure trace from test using Mach 2 shock tube; Driver section filled with helium at 8 *bar*; Sample rate 500 *kS/s*, Trigger level +0.1 *V*, source CH-1 (transducer 1), position 10%, delay 0.	213
Figure P.3.	Pressure trace from test using Mach 2 shock tube; Driver section filled with helium at 8 *bar*; Sample rate 200 *kS/s*, Trigger level +0.1 *V*, source CH-1 (transducer 1), position 10%, delay 0.	214
Figure P.4.	Pressure trace from test using Mach 2 shock tube; Driver section filled with helium at 8 *bar*; Sample rate 200 *kS/s*, Trigger level +0.1 *V*, source CH-1 (transducer 1), position 10%, delay 0.	214
Figure R.1.	Variation of bubble radius R with time for growth of bubble (R_o 0.2 *mm*) subjected to step-function pressure drop from 7.93 to –1 *bar* at time zero.	219
Figure R.2.	Variation of bubble wall velocity $\dot{R}$ with time for growth of bubble (R_o 0.2 *mm*) subjected to step-function pressure drop from 7.93 to –1 *bar* at time zero.	219
Figure R.3.	Variation of bubble wall acceleration $\ddot{R}$ with time for growth of bubble (R_o 0.2 *mm*) subjected to step-function pressure drop from 7.93 to –1 *bar* at time zero.	220
Figure R.4.	Variation of bubble radius R with time for growth of bubble (R_o 1 μm) subjected to step-function pressure drop from 7.93 to –1 *bar* at time zero.	220
Figure R.5.	Variation of bubble wall velocity $\dot{R}$ with time for growth of bubble (R_o 1 μm) subjected to step-function pressure drop from 7.93 to –1 *bar* at time zero.	221

Figure R.6. Variation of bubble wall acceleration $\ddot{R}$ with time for growth of bubble (R_o 1 μm) subjected to step-function pressure drop from 7.93 to –1 *bar* at time zero. 221

Figure R.7. Time taken t_v for bubbles of different initial radii R_o to expand to visible size R_V in adiabatic and isothermal growth cases (R_V was taken as 1 *mm*). 223

Figure R.8. Variation of bubble radius R with time for growth of bubble (R_o 10 μm) subjected to step-function pressure drop from 7.93 to 2339 *Pa* at time zero. 223

Figure R.9. Variation of bubble wall velocity $\dot{R}$ with time for growth of bubble (R_o 10 μm) subjected to step-function pressure drop from 7.93 to 2339 *Pa* at time zero. 224

Figure R.10. Variation of bubble wall acceleration $\ddot{R}$ with time for growth of bubble (R_o 10 μm) subjected to step-function pressure drop from 7.93 to 2339 *Pa* at time zero. 224

Figure R.11. Variation of bubble radius R with time for collapse of bubble (R_o 0.5 *mm*) subjected to step-function pressure rise from -1 to 1 *bar* at time zero. $R(0)$ = 2.5 *mm*, $\dot{R}(0)$ = 8.3 $m.s^{-1}$. 225

Figure R.12. Variation of bubble wall velocity $\dot{R}$ with time for collapse of bubble (R_o 0.5 *mm*) subjected to step-function pressure drop from -1 to 1 *bar* at time zero. $R(0)$ = 2.5 *mm*, $\dot{R}(0)$ = 8.3 $m.s^{-1}$. 225

Figure R.13. Variation of bubble wall acceleration $\ddot{R}$ with time for collapse of bubble (R_o 0.5 *mm*) subjected to step-function pressure drop from -1 to 1 *bar* at time zero. $R(0)$ = 2.5 *mm*, $\dot{R}(0)$ = 8.3 $m.s^{-1}$. 226

Figure R.14. Variation of bubble radius R with time for collapse of bubble (R_o 0.5 *mm*) subjected to step-function pressure rise from -1 to 6 *bar* at time zero. $R(0)$ = 2.5 *mm*, $\dot{R}(0)$ = 8.3 $m.s^{-1}$. 226

Figure R.15. Variation of bubble wall velocity $\dot{R}$ with time for collapse of bubble (R_o 0.5 *mm*) subjected to step-function pressure drop from -1 to 6 *bar* at time zero. $R(0)$ = 2.5 *mm*, $\dot{R}(0)$ = 8.3 $m.s^{-1}$. 227

Figure R.16. Variation of bubble wall acceleration $\ddot{R}$ with time for collapse of bubble (R_o 0.5 *mm*) subjected to step-function pressure drop from -1 to 6 *bar* at time zero. $R(0)$ = 2.5 *mm*, $\dot{R}(0)$ = 8.3 $m.s^{-1}$. 227

Figure R.17. Variation of bubble radius R with time for collapse of bubble (R_o 0.1 *mm*) subjected to step-function pressure rise from -1 to 1 *bar* at time zero. $R(0)$ = 1 *mm*, $\dot{R}(0)$ = 8.3 $m.s^{-1}$. 228

Figure R.18. Variation of bubble radius R with time for collapse of bubble (R_o 0.05 *mm*) subjected to step-function pressure rise from -1 to 1 *bar* at time zero. $R(0)$ = 2.5 *mm*, $\dot{R}(0)$ = 8.3 $m.s^{-1}$. 228

List of Tables

Table G.1.	Properties of liquid water.	176
Table G.2.	Properties of air (equivalent).	177
Table G.3.	Properties of helium gas.	178
Table G.4.	Properties of Polycarbonate (Grade: Makrolite 3103) .	179
Table G.5.	Properties of insertion rubber.	179
Table H.1.	Tensile strength values recorded from pulse reflection experiments.	180
Table H.2.	Tensile strength values recorded from tube-arrest experiments.	182
Table H.3.	Tensile strength values recorded from Berthelot tube experiments.	182
Table H.4.	Tensile strength values recorded from centrifugal stressing experiments.	183
Table H.5.	Tensile strength values recorded from superheating experiments.	183
Table H.6.	Tensile strength values recorded from inclusion experiments.	184
Table H.7.	Tensile strength values recorded from ultrasonic experiments.	185
Table H.8.	Tensile strength values recorded from other experiments.	185
Table H.9.	Values of the tensile strength of Mercury.	185
Table I.1.	Summary of experimentally obtained values of the bubble radius.	186
Table I.2.	Summary of experimentally obtained values of bubble concentration.	186
Table K.1.	PCB 113A21: pressure transducer performance.	192
Table Q.1.	Values of the parameters in the regions of the wave diagram of the Mach 3 shock tube.	217
Table Q.2.	Values of the parameters in the regions of the wave diagram of the Mach 2 shock tube.	217
Table R.1.	Results of simulations using Simulink – Adiabatic case (R_V taken as 1 mm).	222
Table R.2.	Results of simulations using Simulink – Isothermal case (R_V taken as 1 mm).	222

List of symbols

a	Speed of sound	$m.s^{-1}$
Â	Non-dimensional form of a	--
A ÂA	Cross-sectional area	m^2
A_W	Characteristic constant of a liquid medium	Pa
c	Specific heat of a liquid	$kJ/kg.K$
c_p	Specific heat at constant pressure	$kJ/kg.K$
c_v	Specific heat at constant volume	$kJ/kg.K$
e	Specific internal energy	kJ/kg
E	Total energy	kJ
E	Young's Modulus of Elasticity	Pa
E_f	Foundation Modulus	Pa
G	Fundamental derivative	--
h	Specific enthalpy	kJ/kg
H	Pressure head	m
k	Constant polytropic index	--
k_o	Initial volume concentration of gas/vapour in a liquid	--
K	Bulk modulus (The inverse of β)	Pa
K_S	Isentropic bulk modulus	Pa
K_T	Isothermal bulk modulus	Pa
m	Mass per unit area of a plate	kg/m^2
M	Mass of plate	kg
M	Mach number	--
M	Molecular mass or "weight" of the material	kg/mol
n	Adiabatic exponent of a liquid/constant polytropic index	--
N	Initial bubble number density in a liquid	--
p	Pressure	Pa
p_∞	Far-field pressure	Pa
P	Riemann variable or quantity	--
q	Heat transferred into a system per unit mass	J/kg
Q	Riemann variable or quantity	--
r	Reflection factor	--
R	Gas constant for a particular fluid	$J/kg.K$
R	Radius of a bubble	m
R_o	Universal gas constant	$J/kg.mol.K$

R_o	Radius of a bubble nucleus	m
R	Radius of a bubble	m
R_C	Critical radius	m
R_C	Minimum radius of visible bubble (within the framework of the detection method used)	m
s	Specific entropy	$J/kg.K$
S	Non-dimensional form of s	--
S	Surface tension	N/m
t	Time	s
t_V	Time taken for a bubble to expand to visible size	s
t^*	Rise/fall time of a pressure pulse	s
T	Temperature	K
u	Particle velocity	$m.s^{-1}$
$\hat{U}U$	Non-dimensional form of u	--
U_S	Shock velocity	$m.s^{-1}$
V_o	$(R/R_V)^3$	--
V	Volume	$m^3.kg^{-1}$
w	Finite wave speed	$m.s^{-1}$
w	Work done by the system on its surroundings	J
x	Displacement	m
Z	Acoustic impedance	$Pa.s.m^{-3}$
β	The compressibility or modulus of compressibility of a liquid	Pa^{-1}
ζ	Transverse displacement of a plate	m
γ	Adiabatic exponent (specific heat ratio) for a gas	--
γ	Shock strength	--
μ	Dynamic viscosity	$kg/m.s$
ν	Kinematic viscosity $\nu = \mu/\rho$	m^2/s
ρ	Density	kg/m^3
σ	Surface tension	N/m
τ	Non-dimensional form of t	--
Γ	Grüneisen coefficient	--

Other Subscripts and Qualifiers

For any variable X,

X_B	Within the bubble
X_G	Of the gas
X_L	Of the liquid
X_L	Conditions on the right side of an interface
X_R	Conditions on the left side of an interface
X_S	Shock conditions
X_S	Isentropic
X_T	Within the bubble
X_o	Initial conditions
X_{ij}	Ratio of quantity X at i over that at j
X_T	Isothermal
X_W	Water conditions
X_1	Initial conditions
X_2	Final conditions
$\dot{X}$	Rate of change of the variable X
$\ddot{X}$	Second derivative of X
δX	Small change in quantity X

1. Introduction

1.1. Definition of Cavitation

Cavitation is defined as the formation and activity of bubbles or cavities in a liquid i.e. the process of rupturing a liquid. In this context 'formation' refers, generally, both to the creation of a new cavity and to the expansion of a pre-existing one to a visible size [1]. Cavitation is a dynamic phenomenon, as it is concerned with the growth and collapse of vapour and gas filled cavities, which occurs only in liquids.

The expansion of bubbles, which are filled with gas or vapour or, usually, a mixture of both, in a liquid may be induced by reducing the ambient pressure or increasing the temperature by static or dynamic means. This bubble growth will occur at a nominal rate if it takes place by means of diffusion of dissolved gases into the cavity (mass transfer) or by expansion of the bubble contents with temperature increase or pressure reduction [2].

- Bubble growth by diffusion is called *degassing* or *gaseous cavitation* when induced by dynamic-pressure reduction [2].

Bubble growth will occur 'explosively' if it is primarily the result of vaporisation (mass transfer) into the cavity. This process is then called:

- *Boiling* if caused by temperature rise.
- *Cavitation* if caused by dynamic pressure reduction at constant temperature. This is also known as vaporous cavitation [2].

The previous description has distinguished boiling, vaporous cavitation and gaseous cavitation as related phenomena if not identical in all respects. Cavitation is sometimes more loosely described as being cause by static or dynamic means [2,3].

The conventional phase diagram [3] for water is shown in figure 1.1 (note that the scales are not linear). The curve labeled *l-v* represents points where the liquid and vapour are in equilibrium and is thus a curve of saturated temperature versus pressure. This liquid-vapour coexistence line is called the *binodal* [4]. From the arbitrary liquid state a, below the critical point, one may reach the vapour state by either increasing the temperature

above the saturation state at constant pressure (a to b, where b is a vapour state) or by decreasing the pressure at constant temperature (a to c, where c is a vapour state). These processes correspond to the processes of *boiling* and *cavitation* respectively [5]. Since cavitation results due to pressure variations, it may be controlled by controlling the minimum absolute pressure in a system [2].

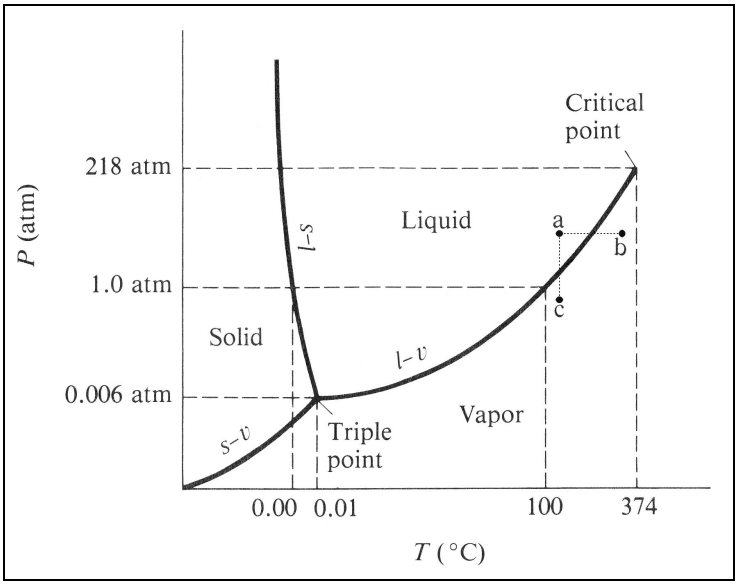


Figure 1.1. The phase diagram of water [3].

1.2. Types of Cavitation

Four types of cavitation may be distinguished according to the cause of inception [1]:

1. *Hydrodynamic Cavitation* is produced by pressure variations in a flowing liquid due to the geometry of the system or the rotation of a propeller. Each liquid element passes through the cavitation zone once.
2. *Acoustic Cavitation* is produced by sound waves in a liquid due to pressure variations or, as will be discussed later, *tensions*.
3. *Optic Cavitation and Particle Cavitation* is produced by photons of high intensity (laser) light and any other type of elementary particles (e.g. a proton) rupturing in a liquid. These types of cavitation are achieved by deposition of energy into a limited volume. Energy may also be introduced by very small heating elements.

Hydrodynamic cavitation includes *travelling* cavitation, where individual transient cavities form and move in a flowing liquid as they expand, shrink, and then collapse. The bubbles grow when passing through low-pressure regions and start to collapse shortly after they are swept into regions higher pressure. Alternately, hydrodynamic cavitation may occur on a body moving through a stationary liquid. Another type of hydrodynamic cavitation is *vortex* cavitation, where cavities develop in the cores of vortices as often occurs on the tips of ship propeller blades. The operation of valves and fittings involve changes in liquid flow velocity passing through them and may thus also be affected by cavitation [2,6].

In acoustic cavitation, sound waves of the high ultrasonic frequencies generated by a submerged piezoelectric sound transducer drive are used [2]. The waves produce a high-amplitude, high-frequency, alternating pressure field, thereby subjecting a sample of liquid to cycles of low and high pressure, which, if of a sufficiently large amplitude, may result in cycles of cavitation growth and collapse known as *vibratory* cavitation. This cavitation is often accompanied by low velocity liquid flow, of a time periods far greater than that of the cavitation cycles, which is in the order of milliseconds. Acoustic cavitation is, in general, a non-linear since changes in bubble radius is not proportional to the sound pressure [1]. Such acoustic techniques are frequently used to investigate the physics of the cavitation process since accurate variation of the sound field allows ample control of bubble size and distribution [7].

1.3. Effects of cavitation

Cavitation causes various hydrodynamic and other effects, which are often destructive. However, its destructive potential is beneficial in some applications.

In hydrodynamic cavitation, [2] cavitation alters the flow pattern and the dynamics of the interaction between the liquid and its boundaries, thereby restricting and reducing the force that may be applied to the liquid by a solid surface. Thus, the flow produced by a turning vane is reduced and the thrust produced by a ship's propellers is limited.

Noting that cavitation bubbles radiate acoustic pressure waves from their surfaces when they expand or contract, the cavitation, being inherently unsteady, may involve significant fluctuating forces and consequently resonant vibration (if one of the frequency components of the fluctuations equals the natural frequency of nearby equipment). Such instabilities resulting from cavitation may even affect liquid-propelled missiles [2].

Collapse of cavitation bubbles occurs 'implosively' for a vapour-filled bubble with insignificant gas content and less so if the gas content is high [2]. The asymmetry of cavity collapse, which leads to phenomena such as liquid jets [8,9], as well as central implosion and the emission of shock waves are potentially damaging and may result in material destruction [9,10].

Due to the low compressibility of the liquid and the high compressibility of the gas within the bubbles, a large amount of potential energy is stored when the bubbles expand. This energy is concentrated into a very small volume when the bubble collapses. Consequently, very high pressures and temperatures are produced, which may erode solids and initiate chemical reactions. The pressures and temperatures reached may be in the order of 50-1200 *MPa* and 5000-10000 *K* respectively [1,5,9]. The temperature of the material adjacent to a collapsing bubble may increase by 500-800 *K* [7].

Collapse may also, by a rebound effect, emit shock waves with pressures as high as 400 *MPa* [7] through liquid adjacent to bubble, which may erode adjacent walls. These shock waves result in significant noise, which may appear on pressure sensor readings as white noise covering a wide frequency band. Experiments have shown that cavitation noise and erosion are proportional [7].

The extreme temperatures in a collapsing bubble may also result in a phenomenon called sonoluminescence in which species in the gas phase are excited and relax by emitting photons [7,9]. The resulting flash of light that is discharged may be detectable for periods in the order of milliseconds, but are weak and only visible by magnification or in complete darkness [11].

Liquid films, usually between 0.1 and 10μm thick [8], are often rapidly deformed between separating sheets, thereby developing a tensile force within the film due to the relative motion of its bonding surfaces. The resulting cavitation of such films is an important aspect of processes such as lubrication and printing. Barrow et al. [8] explored the issue of cavitation damage due to cavity growth using an atomic force microscope and found evidence that when cavitation occurs in confined spaces, the growth of a cavity may be rapid enough for it to cause more damage to adjacent structures than its collapse.

Bubble generation [12] during the bubble-jet recording process occurs by nucleation of ink vapour at cavitation inception, followed by instantaneous boiling and ultimate bubble collapse. These events are initiated by short, rapid pulses of heat.

Transient cavitation has been observed near operating mechanical heart valves in vitro and inferred in vivo via the observation of pitting on explanted clinically used valves [13, 14]. When these valves open and close abruptly, pressure waves are induced in the fluid. If a rarefaction wave of sufficient strength is produced, cavitation may occur.

1.4. Uses of Cavitation

Though cavitation was first noticed for its disadvantageous effects, in a few applications, some effects may be beneficial and cavitation is employed to produce useful effect. Cavitation is used mostly in chemical processes and biological and medical applications.

In chemical processes, cavitation is usually used in one of two ways [7]:

1. The cavitation bubbles may act as a mixer, vigorous disturbance and increasing the contact area between two liquids or a liquid and a solid.
2. High temperatures and pressures during the collapse of cavitation bubbles promote and initiate chemical reactions, especially those occurring in “aqueous media”. In this phenomenon known as sonochemistry, cavitation is used to accelerate and selectively control chemical reactions.

The first method may promote emulsification (e.g. of immiscible liquids) in manufacturing processes and also aids cleaning processes. Emulsification is the means of removing oils by breaking them up into tiny droplets such that they may be rinsed away. The mixing effect of ultrasonic cavitation is proven to increase the rate of various processes such as: homogenisation, crystallisation, hydrogenation, filtration, high-shear extraction, defoaming, wax dispersion, de-agglomeration and particle disruption. Sonochemistry has a wide variety of applications, particularly in the chemical industry, as discussed in [9,15,16,17].

Acoustically induced cavitation is the foundation for many apparatus used to clean intricate parts [2]. In ultrasonic cleaning or ultrasonic chemical degreasing, the collapse of cavitation bubbles, formed in a cleaning solution, produces a scrubbing action. For example, ultrasonic cleaning is used in dentistry, machining, the chemical industry and in the power industry e.g. on the walls of heat exchangers [18]. Acoustic cavitation has many other industrial applications [19-21]. In metallurgical and machining processes, acoustic cavitation is also employed in the refining of molten metals, preparation of cast composite materials and in ultrasonic sharpening, cutting, metal welding, surface hardening and stress relief. Other applications of acoustic cavitation in the chemical industry include dispersion and coagulation, polymerisation and drug preparation.

Cavity collapse may lead to oxidation: According to the hot spot theory [9,22], the high temperatures and pressures at collapse cause dissolution of the liquid according to the chemical reactions shown in [23]. The free hydroxyl radicals formed, OH, are effective oxidising agents and thus readily cause decomposition of organic compounds. *Cavitating water jets* are well suited to the oxidation, and subsequent degradation of organic compounds [24]. These jets generate cavitation over a much larger volume than ultrasonic methods and are thus, generally, more efficient [23]. Cavitating jets are produced, using simple apparatuses, by maintaining a high pressure across a nozzle. The high-speed water jet is discharged, through the atmosphere or, when submerged, through a liquid. Vortex cavitation occurs in the low-pressure zone in the vortex core [24]. Cavitating jets are effective in removing chemical contaminants, such as pesticides and

biocides, from water as well as in oxidising arsenic to a form that may be more readily removable by precipitation and filtration [23]. Cavitating jets may also rapidly reduce large concentrations of bacteria (e.g. E. Coli) by more than five orders of magnitude. Algae concentrations may be reduced by a factor of 200 in just two hours [23]. Another application of cavitating jets is described in [25]. Impacts caused by the collapse of the cavitation bubbles have been used to introduce beneficial, compressive, residual stresses to materials, resulting in surface hardening and increased fatigue life of components. Other applications of cavitating jets [24] include cutting, cleaning, surface finishing and erosion testing.

Cavitation has been used in many biological and medical applications [7]. Localised cavitation is generated by the process of laser-induced optical breakdown, also known as photodisruption, allowing for surgery with micron precision beneath the surface of biological tissues (most of the energy in the optical pulses passes through the material) with virtually no collateral damage. Laser pulses used in this process are in the order of femtoseconds [26]. In this case, the mechanical effects rather than chemical reactions of cavitation are utilised. *Shock Wave Lithotripsy* (SWL) involves the destruction of stones by the use of focussed acoustic waves [27].

Acoustic cavitation may also destroy bacteria and yeast cells and has been used in the removal of cell contents such as enzymes and of viruses from infected tissue [7]. In addition to the oxidising reactions described above the effect may be attributed to the effect of cavities inside the bacteria and in part, due to the removal of dissolved gas.

Cavitation is employed in the delivery of drugs to localised areas [28]. Photomechanical drug delivery involves the use of a laser pulse to generate a cavitation bubble in a blood vessel due to the absorption of laser energy by blood clots or surrounding fluids such as blood. The hydrodynamic pressure arising from the expansion and collapse of the cavitation bubble may force drug into the clot or vessel wall.

The effects of cavitation bubble collapse may also be used beneficially in gene therapy and drug delivery by sonoporation or sonophoresis [29,30,31,32]. This is a therapeutic effect of high frequency ultrasound on living cells [29]. The ultrasound may be used to deliberately rupture microbubbles resulting in violent impacts on nearby cell walls and transient, reparable pores through which drug molecules, proteins or foreign genes may enter [29]. Such microbubbles, originally developed for use as contrast agents for diagnostic imaging [33], are commercially available and may be injected where required. This application might be particularly useful in (and indeed revolutionise) gene therapy and the delivery of toxic and non-toxic drugs [31].

A possible application of cavitation is that it may theoretically be used to drive micro-mechanical systems [12,34]. Rapid deposition of energy into a liquid causes it to vaporise explosively at high pressures and expand, thereby performing work on its surroundings. As sho??wn later, rapidly expanding bubbles may accelerate microscopic and nanoscopic particles. Zhao et al. [12] generated extremely rapid vapour explosions by heating liquids rapidly with “micro-heaters”.

Other applications of cavitation include its use as a flow-control mechanism in a Venturi tube or an orifice [2] in water treatment and purification of contaminated soil, in production, transportation and processing of petroleum and gas. In such cases, cavitation provides a choking phenomenon similar to that encountered in compressible flow. An obvious application of cavitation is its use for the removal of trapped gases in liquids [6].

1.5. The Study of Cavitation

1.5.1. Producing Controlled Cavitation

Experimental apparatus [2,7] such as Venturi tubes (and other conduits with geometrical flow restrictions) and variable-pressure water tunnels, with transparent-test-sections, have allowed researchers to observe the hydrodynamic cavitation and to investigate its effect on pumps and turbines.

When acoustic cavitation is induced by a piezoelectric transducer drive, cavitation eventually develops when the liquid is no longer able to follow the motion of the face of the transducer. Once cavitation occurs, a limit is reached and no more power may be transmitted to the liquid if the transducer power is increased [2]. This is because the cavitation zone then separates the transducer face from the body of liquid.

1.5.2. Definition of the Cavitation Threshold and Detectable Sizes

Cavitation in liquids is difficult to measure quantitatively. In order to enumerate the process of cavitation, the *cavitation threshold* is defined as the pressure at which a cavitation event, which is characterised by an explosive growth of bubbles, occurs [35], i.e. it is the "breaking tension" of a liquid. Various detection methods are used to register this threshold. The concept of a *visible* or *detectable bubble size* (one which may be detected within the framework of the technique used) is introduced [36].

1.5.3. Detection and Visualisation

There are several methods for detecting the presence of cavitation [2]. They include:

- Direct observation by visual and photographic means. This method necessitates the use of apparatus with transparent viewing, unless used in conjunction with x-ray techniques [36,37,38]. Microscopes may be used for increased spatial resolution.
- Light scattering methods: Indirect observation by allowing cavitation regions to scatter laser-beam light into a photocell. The occurrence of a cavitation at the interrupts the beam and the event is recorded [39,40].
- Light absorption methods: Indirect observation of effects of absorption of light exhibited by bubbles [41]. This method is generally less sensitive and simpler [36] than light scattering.
- Capacitance method [36]: Indirect observation of the free-surface dynamics, which may be quantitatively related to the cavity cluster dynamics. This method provides stable results but is less sensitive than light scattering methods.

- Acoustic method: an acoustic transducer may record the pulses emitted by the implosion of cavitation bubbles [39]. Acoustic detection may make use of the emitting transducer itself by the "echo phenomenon" [40].
- Indirect observation by sensing the noise caused by cavitation [2]. This method may detect mild cavitation that may be too slight to be observed visually.
- Indirect observation by measuring the size and number of pits in suitably placed, detectors made of, for example, aluminium foil [27].

For photographic methods, repetition rates below 5000 frames per second are, in general most practical for studying the overall nature of cavitation, whereas higher repetition rates are useful for studying the more obscure details [2].

1.6. The Purpose of This Work

This thesis is concerned with true cavitation brought about by pressure variations alone. The objectives were to demonstrate acoustic cavitation experimentally and confirm the results using relevant theoretical methods. A related objective was to determine the pressures at which cavitation occurred, i.e. the cavitation threshold, in water. As no acoustic cavitation experiments had been performed previously at the university, test facilities were to be designed and built.

2. Shock Waves and Rarefaction Waves

A violent pressure change caused by the sudden release of chemical, electrical, nuclear, or mechanical energy in a limited space [10] causes a zone of high pressure called a shock wave to propagate through a medium. [42]. Shock waves, which are *irreversible processes,* may occur in any elastic medium. A shock wave is a very sharp, thin front, across which flow properties, such as pressure, temperature, density, velocity and entropy change. Since, the thickness of a shock wave is typically in the order of a few angstroms [10], flow properties may be assumed to change discontinuously across a shock wave.

In general, the ratio of the higher pressure behind a shock wave to the lower pressure ahead of the shock is referred to as the shock strength. The ratio of higher density behind a shock to lower density ahead of it is called the shock compression. Similarly, here the density ratio across a rarefaction wave is referred to as the expansion. Shock waves at right angles to the upstream flow that occur in one-dimensional flow [43] are termed normal shock waves. The shock Mach number M_S is defined [44] as the Mach number of a supersonic flow in which the shock would be stationary and is thus always positive.

2.1. Compressible flow

The conservation equations of mass, momentum and energy respectively, for a perfect fluid in one-dimensional flow are (in partial differential equation form) [10]:

$$\frac{\partial \rho}{\partial t} + \frac{\partial}{\partial x}(\rho u) = 0 \qquad \text{(Mass or continuity)} \qquad (2.1a)$$

$$\frac{\partial}{\partial x}(p + \rho u^2) + \frac{\partial}{\partial t}(\rho u) = 0 \qquad \text{(Momentum)} \qquad (2.2a)$$

$$\frac{\partial E}{\partial x} + \frac{\partial}{\partial x}[E\rho u + pu] = 0 \qquad \text{(Energy)} \qquad (2.3a)$$

In differential form, the equations are [45]:

$$\frac{d\rho}{\rho} + \frac{dV}{V} + \frac{dA}{A} = 0 \qquad \text{(Mass)} \qquad (2.1b)$$

$$-dp = \rho V\, dV \qquad \text{(Momentum)} \qquad (2.2b)$$

$$\delta q - \delta w = dh + VdV + gdz \qquad \text{(Energy)} \qquad (2.3b)$$

Equations (2.1b), (2.2b) and (2.3b) are valid for diabatic and adiabatic (without heat addition) processes. The momentum equation (2.2b) is valid only for frictionless flows. In the conservation of energy equation, i.e. first law of thermodynamics, the term δw is the work done by the system on its surroundings ($\delta w = VdV$).

2.2. The Conservation Laws for a Shock Wave

Consider a piston, initially at rest, which impulsively acquires a finite velocity u_2. The fluid adjacent to the piston must move at the same velocity u_2, while the particle speed further downstream remains at its initial value u_1. These conditions are satisfied by a shock wave, moving at a speed U_S, which appears on the piston face and propagates into the fluid. ($U_S > u_2$). The velocities behind and ahead of the shock wave are u_2 and u_1 respectively. This discussion [46] is applicable to *laboratory frame* or *moving shock* coordinates where the relevant velocities on either side of the shock are u_2 and u_1. The laws that govern moving shock may be transformed into *shock-fixed* coordinates, where the relevant velocities on either side of the shock are v_2 and v_1, using the relations:

$$v_1 = -U_S + u_1 \text{ and} \qquad (2.4)$$

$$v_2 = u_2 - U_S \qquad (2.5)$$

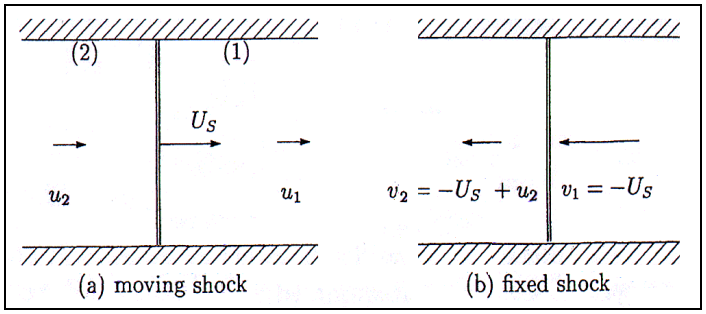


Figure 2.1. Moving and fixed shock reference frames [10].

If one considers a very small control volume enclosing a shock wave, heat transfer, friction and area changes become negligible. Then, the equations of continuity, momentum and energy for frictionless, adiabatic flow must be satisfied by both states upstream and downstream of a shock wave [45]. The basic conservation equations across a shock wave, derived from the conservation laws of mass, momentum and energy and known as the Rankine-Hugoniot equations, relate the flow properties across a shock wave discontinuity. The normal shock equations may be derived from the basic conservation equations in differential form [47] or other methods [10]. Being independent of state, the conservation equations may be applied to any material.

In moving-shock coordinates, the equation of continuity is stated generally, as [46]:

$$U_S(\rho_2 - \rho_1) = \rho_2 u_2 - \rho_2 u_1 \tag{2.6a}$$

In shock-fixed coordinates, using equations (2.1) and (2.2),

$$\rho_1 v_1 = \rho_2 v_2 \tag{2.6b}$$

In moving-shock coordinates, the equation of momentum conservation is, generally [46],

$$U_S(\rho_1 v_1 - \rho_2 v_2) = (p_2 + \rho_2 v_2^2) - (p_1 + \rho_1 v_1^2) \tag{2.7a}$$

In shock-fixed coordinates, using equations (2.1) and (2.2),

$$p_2 + \rho_2 v_2^2 = p_1 + \rho_1 v_1^2 \tag{2.7b}$$

In moving-shock coordinates, the equation of conservation of energy is, in the most general form [46],

$$U_S(\rho_1 E_1 - \rho_0 E_0) = (p_1 + \rho_1 E_1)u_1 - (p_0 + \rho_0 E_0)u_0 \tag{2.8a}$$

and in shock fixed coordinates, by defining the enthalpy as $h = pv + e$:

$$h_1 + \tfrac{1}{2} v_1^2 = h_2 + \tfrac{1}{2} v_2^2 \tag{2.8b}$$

Equations (2.3b), (2.4b) and (2.5b) may be combined [45] resulting in expressions for the property ratios across the shock. The property (pressure, density, sound speed) ratios across a shock wave may be expressed in terms of the upstream Mach number M_1 only [45] for an ideal gas. The strength of a shock may be specified in terms of the pressure,

density, temperature or particle velocity ratio across the shock or the shock Mach number since relationships between all of those quantities may be derived.

The following particularly useful relationship may be derived [47]:

$$\frac{p_2}{p_1} = \frac{2\gamma}{\gamma + 1} M_S^2 - \frac{\gamma - 1}{\gamma + 1} \tag{2.9}$$

or, after some manipulation [10],

$$\frac{p_2}{p_1} = \frac{2\gamma}{\gamma + 1} (M_S^2 - 1) + 1 \tag{2.10}$$

In addition, the pressure ratio may be expressed in terms of the density ratio as [48]:

$$\frac{\rho_2}{\rho_1} = \left(1 + \frac{\gamma + 1}{\gamma - 1} \frac{p_2}{p_1}\right) \Bigg/ \left(\frac{\gamma + 1}{\gamma - 1} + \frac{p_2}{p_1}\right) \tag{2.11}$$

which is known as the Rankine-Hugoniot relation [10].

2.3. General Equations

Using only the shock mass and momentum relations in shock fixed coordinates, the following equation expressing the speed of a finite wave may be derived [45, 48, 49]:

$$w = \sqrt{\frac{\rho_2}{\rho_1} \frac{p_2 - p_1}{\rho_2 - \rho_1}} \tag{2.12}$$

For infinitesimal changes in pressure and density ($p_2 - p_1 = \delta p$, $\rho_2 - \rho_1 = \delta\rho$) equation (2.12) reduces to the following equation from which the speed of sound may be calculated (assuming that the wave propagation velocity is dependent only on the thermodynamic state of the medium):

$$a = \sqrt{\left(\frac{\partial p}{\partial \rho}\right)_S} \tag{2.13}$$

The derivative in brackets is isentropic since $\delta\rho / \rho << 1$, implying an acoustic wave [49]. The adiabatic exponent is defined as [9]

$$\gamma = \frac{a^2}{pv} \tag{2.14}$$

A polytropic process is one, in any medium, which may be described by the relation:

$$\frac{p_2}{p_1} = \left(\frac{\rho_2}{\rho_1}\right)^k \qquad \text{or} \qquad pV^k = p\rho^{-k} = constant \tag{2.15}$$

where the exponent k, the constant polytropic index, may have any value from ∞ to $-\infty$, depending on the process. The values of k for isobaric, isothermal and adiabatic (or isentropic) processes in an ideal gas are 0, 1 and γ respectively. An isentropic process is defined as one, which is adiabatic and reversible [47].

Using Euler's equation of motion for the propagation of a one-dimensional disturbance and the continuity equation for unsteady and uniform one-dimensional flows, the wave equation, a partial differential equation that describes the propagation of waves with speed a, may be derived [10]. The one-dimensional form of the wave equation is [50]:

$$a^2 \frac{\partial^2 w}{\partial x^2} = \frac{\partial^2 w}{\partial t^2} \tag{2.16}$$

Since a wave, across which the pressure and density ratios are non-negligible, may still be approximately isentropic, as shown in [44], 3 types of waves may be distinguished:

- Sound waves (waves of negligible strength and compression or expansion)
- Weak waves (finite but isentropic)
- High amplitude waves (including strong shock waves)

In the acoustical approximation, it is assumed that the propagation and reflection of waves of relatively low but finite amplitude may be modelled by simple acoustic relations i.e. weak waves are approximated by sound waves. Since air is far more compressible than water, the acoustic approximation is valid over only a narrow range of wave pressures for air and over a relatively large range for liquids. For all fluids, non-linearities in the medium become more important [51] with increasing incident pressures. When the pressure and density ratios across a wave are non-negligible, the wave leads to particle flow that is non-negligible compared to the wave velocity, and that the compression across the wave is small and occurs adiabatically. Hence, the wave travels at a speed higher than the sound speed a. In the fast moving fluid, the wave travels at an increased

sound speed and its velocity of propagation is increased relative to a stationary observer. Indeed, in the first theoretical study of large amplitude sound waves [44], Poisson derived a relationship indicating that the velocity of propagation is the sum of the speed of sound and the disturbance (particle) velocity produced by the wave. Shock, weak finite-amplitude, and Mach waves are discussed in the following sections.

2.4. Shock Waves and Rarefaction Waves in Gases

2.4.1. General Equations for Gases

The perfect gas law is:

$$p = \rho RT \tag{2.17}$$

Since R_o is the universal gas constant,

$$R = \frac{R_0}{M} \tag{2.18}$$

The first law, equation (2.3b), and the second law ($ds = \delta q / T$) of thermodynamics and the definition of enthalpy combine to form the well-known "*Tds* equations" [47] from which the following equations relating two arbitrary states (even states on either side of a shock in a gas) are derived [52]:

$$s_2 - s_1 = c_v \ln\frac{T_2}{T_1} + R\ln\frac{v_2}{v_1} \quad \text{or} \quad s_2 - s_1 = c_p \ln\frac{T_2}{T_1} - R\ln\frac{p_2}{p_1} \tag{2.19}$$

The specific heat ratio γ of air varies by only about 5 % across the temperature range 250-1000 *K* and is considered constant. Similarly, c_p and c_v are considered constant [52]. For an ideal gas, the internal energy is a function of temperature only [46, 53]. The following equation is valid for a polytropic gas, such as air at moderate temperatures, and is assumed in most applications [46]:

$$e = c_v T = RT/(\gamma - 1) = p/[\rho(\gamma - 1)] \tag{2.20}$$

The internal and specific internal energies may be related by [46]:

$$E = e + \tfrac{1}{2}u^2 \tag{2.21}$$

2.4.2. Sound Waves in Gases

From the definitions of the specific heats c_p and c_v, and the adiabatic exponent γ, for gases obeying the ideal gas law, the adiabatic exponent reduces to the ratio of specific heats [10]. For an ideal gas, equation (2.14) and the ideal gas equation (2.17) give:

$$a = \sqrt{\frac{\gamma R_0 T}{M}}\sqrt{\gamma R T} = \sqrt{\gamma \frac{p}{\rho}} \tag{2.22}$$

For an adiabatic ($\delta q = 0$) process [47], from equation (2.15):

$$\frac{p_2}{p_1} = \left(\frac{\rho_2}{\rho_1}\right)^{\gamma} \tag{2.23}$$

Appendix A illustrates the derivation of following useful entropic relations,

$$\frac{p_2}{p_1} = \left(\frac{a_2}{a_1}\right)^{\frac{2\gamma}{\gamma-1}} e^{-\gamma(S_2 - S_1)} \tag{2.24}$$

$$\frac{\rho_2}{\rho_1} = \left(\frac{a_2}{a_1}\right)^{\frac{2}{\gamma-1}} e^{-\gamma(S_2 - S_1)} \tag{2.25}$$

The following isentropic relations are frequently derived from the adiabatic relation (2.23) and the sound speed equation (2.22) [9,44] or simply from (2.19) and (2.20), letting $S_2 = S_1$:

$$\frac{p_2}{p_1} = \left(\frac{a_2}{a_1}\right)^{\frac{2\gamma}{\gamma-1}} \tag{2.26}$$

$$\frac{\rho_2}{\rho_1} = \left(\frac{a_2}{a_1}\right)^{\frac{2}{\gamma-1}} \tag{2.27}$$

2.4.3. Finite, Isentropic Waves in Gases

The following equation, which is derived in [48], [46] and [42], relates the particle velocity u_2 behind an isentropic (compression or expansion) wave to the pressure ahead of the wave u_1 and the pressure ratio across the wave:

$$u_2 = u_1 \pm \frac{2a_1}{\gamma - 1}\left[\left(\frac{p_2}{p_1}\right)^{\frac{\gamma-1}{2\gamma}} - 1\right] \text{ for a gas} \tag{2.28}$$

Note that the positive sign applies for a wave moving in the positive direction (referred to as a *P*-wave) and the negative sign is valid for a wave moving in the negative direction (a *Q*-wave). Substituting the isentropic relation (2.26) into (2.28), one may obtain the velocity of propagation of a *P*-wave in a gas:

$$u + a = (u_2 - u_1) + a_1\left(\frac{p_2}{p_1}\right)^{\frac{\gamma-1}{2\gamma}} = +a_1\left[\frac{\gamma+1}{\gamma-1}\left(\frac{p_2}{p_1}\right)^{\frac{\gamma-1}{2\gamma}} - \frac{2}{\gamma-1}\right] \tag{2.29}$$

and the velocity of propagation of a *Q*-wave in a gas is:

$$u - a = (u_2 - u_1) - a_1\left(\frac{p_2}{p_1}\right)^{\frac{\gamma-1}{2\gamma}} = -a_1\left[\frac{\gamma+1}{\gamma-1}\left(\frac{p_2}{p_1}\right)^{\frac{\gamma-1}{2\gamma}} - \frac{2}{\gamma-1}\right] \tag{2.30}$$

Thus, when the wave is weak, its speed of propagation tends to the speed of sound a_1 and secondly that strong waves may propagate significantly faster than sound waves [42]. The speed of sound, pressure, density and temperature ratios across a wave separating the initial state 1 from the final state 2 are [46, 48]:

$$\frac{a_2}{a_1} = 1 - \frac{\gamma-1}{2}\frac{(u_1 - u_2)}{a_1} \tag{2.31}$$

$$\frac{\rho_2}{\rho_1} = \left[1 + \frac{\gamma-1}{2}\frac{(u_2 - u_1)}{a_1}\right]^{\frac{2}{\gamma-1}} \tag{2.32}$$

$$\frac{p_2}{p_1} = \left[1 + \frac{\gamma-1}{2}\frac{(u_2 - u_1)}{a_1}\right]^{\frac{2\gamma}{\gamma-1}} \tag{2.33}$$

$$\frac{T_2}{T_1} = \left[1 - \frac{\gamma-1}{2}\frac{(u_2 - u_1)}{a_1}\right]^{\frac{2}{\gamma-1}} \tag{2.34}$$

2.4.4. Shock Waves in Gases

Using the energy equation (2.3b) and equation (2.12), the Mach number of a shock wave in a gas may be expressed as [45]:

$$M_S = \sqrt{\frac{(\gamma+1)\,(p_2 / p_1) + (\gamma-1)}{2\gamma}} \tag{2.35}$$

2.5. Shock Waves and Rarefaction Waves in Liquids

While the generation, measurement and study of shock waves in air are relatively well advanced, liquid shock wave research has until recently been relatively unexplored due, in part, to the high sound speed of most liquids [51].

2.5.1. General Equations for Liquids

The bulk modulus K is the reciprocal of the compressibility β, which is defined by [10]:

$$-\frac{\Delta v}{v} = \beta.\Delta p \tag{2.36}$$

This equation expresses the change in specific volume, which occurs when a liquid with specific volume v and at a pressure p is subjected to a pressure rise of Δp. The values of K and β are, in general, different for isentropic and isothermal processes. The bulk modulus of compressibility may be considered constant [10] for the moderate pressures considered in the present discussion.

The modified liquid equation of state, known as Tait's equation, as derived in [54] is:

$$\frac{p'_2}{p'_1} = \left(\frac{\rho_2}{\rho_1}\right)^n \quad or \quad \frac{\rho_2}{\rho_1} = \left(\frac{p'_2}{p'_1}\right)^{\frac{1}{n}} \tag{2.37}$$

where p'_2 and p'_1 are known as the modified pressures:

$$p_1' = p_1 + A_W \quad \text{and} \quad p_2' = p_2 + A_W \tag{2.38}$$

Tait's equation may be written as the pressure-density relation for adiabatic compression:

$$p + A_W = \text{constant} \times \rho^n \tag{2.39}$$

The constants A_W and n are characteristic constants of the medium and are obtained empirically [42]. A_W is a weak function of entropy and n is a function of pressure and temperature but may be considered constant for weak to moderate shocks in water and in the range of pressure and temperature under consideration [54]. For the purposes of this report, it is assumed that $A_W = 296.3$ *MPa* and $n = 7.415$. These values are valid [10] for pressures below 2500 *MPa*.

The gas dynamics equations may be transformed to describe shock waves in liquids using the modified pressure instead of the pressure and the value n instead of the specific heat ratio γ e.g. equation (2.37) is analogous to the equation (2.23) for an isentropic flow in air. However, due to the large magnitude of A_W, the modified pressure ratio (or shock strength) is close to unity and thus, shock waves in water up to a few hundred bars may be regarded as weak and most waves in water behave like acoustic waves even for shock pressure changes of hundreds of megapascals [55]. This explains why the isentropic equation (2.37) is valid across shocks, for pressures up to 1000 *MPa* [43], although the analogous gas dynamics equation (2.23) is not, since shocks in gases can seldom be treated as isentropic. In addition, for practical cases, the particle velocities behind such weak shock waves in liquids are always subsonic [55].

For liquids and other relatively incompressible substances, it is unnecessary to distinguish between the specific heats [52] c_p and c_v and one may write $c = c_p = c_v$. Then, the entropy values on either side of a shock wave in water may be related by:

$$s_2 - s_1 = c \ln \frac{T_2}{T_1} \tag{2.40}$$

This equation is a simplification of equation (2.19) for air, with density taken as constant for the relatively incompressible substance. Though the equation (2.40) is a reasonable approximation, one should note that entropy changes in liquids are usually negligible. It follows that temperature changes across liquid shock waves are also usually negligible.

Itoh [10] has shown that the speed of sound behind an underwater shock wave is greater than the velocity of the shock at the same pressure. This implies that the strength of a shock wave that propagates in water is more easily attenuated than one in a gas. However, the calculated data of Kirkwood and Richardson as detailed in [55] contradicts these statements and demonstrated that the speed of sound behind an underwater shock is less than the velocity of the shock at the same pressure. This is also true in gas media. In any case, such wave-steepening or overtaking effects are only clearly observable at significantly higher shock pressures due to the high compressibility of liquids.

2.5.2. Sound Waves in Liquids

The speed of sound in a liquid may be expressed [42,43,51] as follows:

$$a = \sqrt{n \frac{p'}{\rho}} \tag{2.41}$$

This equation is identical to equation (2.22), with the specific heat ratio γ and the pressure of the air medium replaced with the adiabatic exponent n and the modified pressure of the liquid medium respectively. Using the one-dimensional wave equation, the sound speed in a liquid may be expressed in terms of the bulk modulus by [10]:

$$a = \sqrt{\frac{K}{\rho}} \tag{2.42}$$

where K is the isentropic bulk modulus K_S of the liquid, although the subscript has been dropped since it differs only slightly from the isothermal bulk modulus K_T for a fixed temperature and pressure (especially at low pressures) and can be used interchangeably.

The following equations (see derivation in appendix B) are the analogous to equations (2.26) and (2.27) with γ and p substituted with n and p' :

$$\frac{a_2}{a_1} = \left(\frac{p'_2}{p'_1} \right)^{\frac{n-1}{2n}} \tag{2.43}$$

$$\frac{a_2}{a_1} = \left(\frac{\rho_2}{\rho_1} \right)^{\frac{n-1}{2}} \tag{2.44}$$

2.5.3. Shock Waves in Liquids

Liquid shock waves may be generated using the following techniques, which are discussed in detail in [51]:

- *Underwater explosions* – the detonation of submerged explosive charges
- *Underwater spark gap discharge* – the rapid generation of a high voltage between two electrodes resulting in formation of high-pressure, high temperature plasma in a small volume and subsequently, a shock wave

- *High-power lasers or opto-electronic sources* –localised heating in a fluid, which causes expansion and spherical shocks
- *Electromagnetic emitters* – the acceleration of a plate in contact with the liquid by Lorentz forces
- *Liquid or hydrodynamic shock tubes* – the use of gas shocks to impinge upon and transmit shocks into liquid samples. This is discussed further in [56].

Using the Rankine-Hugoniot relation (2.11) and the Tait equation (2.37), the Mach number of a shock wave in a liquid may be expressed as [57]:

$$M_S = \sqrt{\frac{(n+1)\ (p_2' / p_1') + (n-1)}{2n}} \tag{2.45}$$

2.5.4. Finite Waves in Liquids

It may be proved, with a similar derivation to that in [48], [46] and [42] that:

$$u_2 = u_1 \pm \frac{2a_1}{n-1}\left[\left(\frac{p_2'}{p_1'}\right)^{\frac{n-1}{2n}} - 1\right] \text{ for a liquid} \tag{2.46}$$

where the positive and negative signs apply for waves moving in the positive direction (*P*-waves) and waves moving in the negative direction (*Q*-waves) respectively. As with gases, it may be shown, using the isentropic relation (2.43), that the velocity of propagation of a *P*-wave in a gas is:

$$u + a = (u_2 - u_1) + a_1\left(\frac{p_2'}{p_1'}\right)^{\frac{n-1}{2n}} = +a_1\left[\frac{n+1}{n-1}\left(\frac{p_2'}{p_1'}\right)^{\frac{n-1}{2n}} - \frac{2}{n-1}\right] \tag{2.47}$$

and the velocity of propagation of a *Q*-wave in a gas is:

$$u - a = (u_2 - u_1) - a_1\left(\frac{p_2'}{p_1'}\right)^{\frac{n-1}{2n}} = -a_1\left[\frac{n+1}{n-1}\left(\frac{p_2'}{p_1'}\right)^{\frac{n-1}{2n}} - \frac{2}{n-1}\right] \tag{2.48}$$

The following equations are analogous to equations (31), (32) and (33) respectively:

$$\frac{a_2}{a_1} = 1 \pm \frac{n-1}{2}\frac{(u_1 - u_2)}{a_1} \tag{2.49}$$

$$\frac{\rho_2}{\rho_1} = \left[1 \pm \frac{n-1}{2}\frac{(u_1 - u_2)}{a_1}\right]^{\frac{2}{n-1}} \tag{2.50}$$

$$\frac{p_2'}{p_1'} = \left[1 \pm \frac{n-1}{2}\frac{(u_1 - u_2)}{a_1}\right]^{\frac{2n}{n-1}} \tag{2.51}$$

where the positive signs are for *Q*-waves and the negative signs are for *P*-waves.

2.6. The Shock Tube

A shock tube is a device for generating flows in which shock waves appear in a laboratory environment. A typical shock tube consists of a closed duct separated into two compartments, a high-pressure driver section and a low pressure driven section, by a diaphragm. The diaphragm is ruptured (instantaneously in the idealised situation), either by pressure difference between the two sections or by pricking of the diaphragm with a needle [10], causing transient pressure disturbances: A shock forms in the driven section and a diverging expansion fan propagates into the driver section.

The pressure ratio required to generate a shock of strength γ depends on the initial gas temperatures and the properties of the gases and may be calculated by [48]:

$$p_{41} = p_{21}\left[1 - \frac{(n_1 - 1)}{(n_4 - 1)}\frac{a_1}{a_4}\frac{(p_{21} - 1)}{\sqrt{((n_1 + 1)(1 + n_1 p_{21})}}\right]^{-(n_4+1)} \tag{2.52}$$

where $p_{ij} = p_i/p_j$, $n_i = (\gamma_i + 1) / (\gamma_i - 1)$ and the states 1, 2 and 4 are those in the driven section, driver section and the region behind the shock wave respectively. This equation is presented in various forms in [48, 56, 44, 49]. The most important factors determining shock strength are the diaphragm pressure and sound speed ratios p_{41} and a_1/a_4. Equation (2.52) suggests the use of gases with low molecular weights and high sound speed, such as helium and hydrogen, in the driver section for producing strong shocks. Figures 2.2 and 2.3 show the variation of the shock strength of the first shock produced in a shock tube with diaphragm pressure ratio and illustrates the tendency of the shock strength to

tend to a value with increasing pressure ratio up to $p_4/p_1=\infty$. At room temperature, the maximum obtainable shock strengths P_{21MAX} (the shock pressure ratio) for each combination of gases in the shock tube are equal to: 574 for H_2 in the driver section and N_2 in the driven section, 132 for *He-air* and 44 for *air-air* combinations [56, 44, 48].

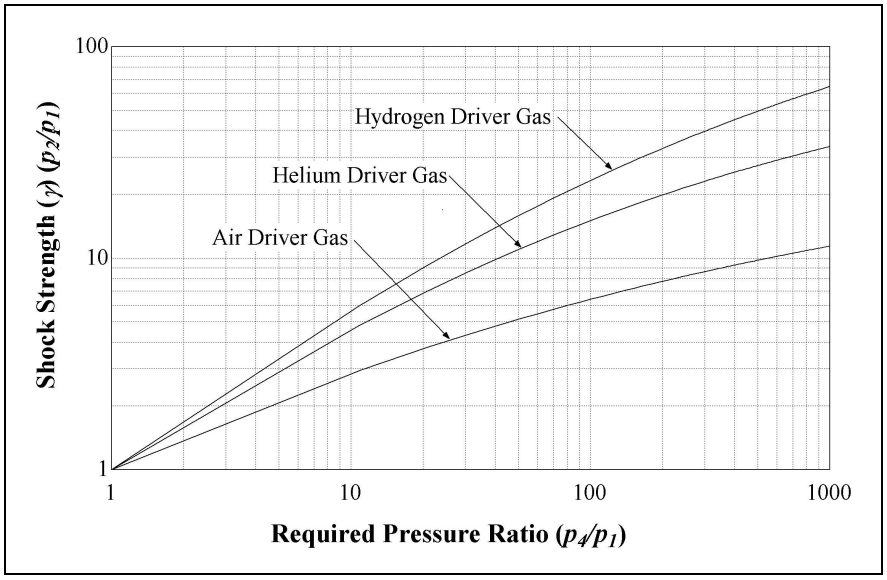


Figure 2.2. Required diaphragm pressure ratio for generating a shock of strength γ in a shock tube using air in the driven section and air, helium and hydrogen in the driver section.

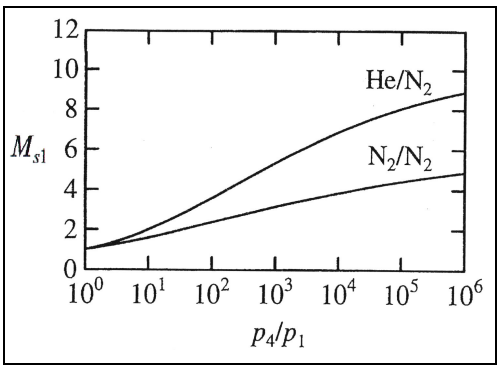


Figure 2.3. Required diaphragm pressure ratio for generating shock of Mach number M_{S1} in shock tube with nitrogen in the driven section and helium/nitrogen in the driver section.

2.7. Methods of Analysis

2.7.1. The Wave Diagram

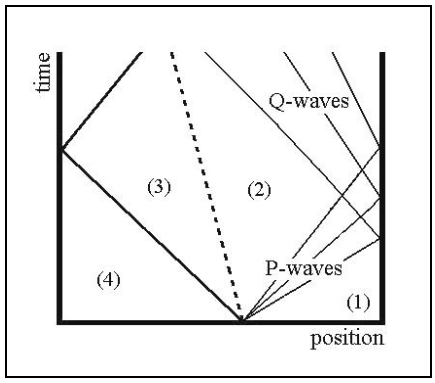


Figure 2.4. The wave diagram resulting from diaphragm rupture in a shock tube.

Shock tubes involve the propagation of pressure waves in ducts. If the cross-sectional dimensions of the duct relative to its length are negligible, the flow may be considered as one-dimensional. A graphical plot representing the propagation of pressure waves in such a duct is called a *wave diagram* and the method of computation is known as the *method of characteristics*. While the fundamental partial differential equations for compressible flow are too complicated to be dealt with directly, in such cases, the method of characteristics allows the state of the fluid, described by two state parameters, and the flow velocity at all times and points of the duct to be determined. A detailed discussion of wave diagram methods was given by Rudinger [44]. Here, only a few important, relevant facts are discussed.

Characteristic lines represent finite waves across which flow variables change discontinuously. They differ from shocks in that they are considered isentropic. A *P-wave* is the characteristic of a positive (right-going) wave and a *Q-wave* is the characteristic of a negative (left-going) wave. *P* and *Q* waves may be either expansion or compression waves. One *P*-wave, one *Q*-wave and a particle path [44] passes through every point of a wave diagram. It follows that in cases of adiabatic [43] flows in ducts of constant cross-section, the Riemann variables *P* and *Q* remain constant along its respective

characteristics [44]. P is constant along P-waves and Q is constant across Q-waves while P is constant across Q-waves and Q is constant across P-waves.

While any combination of a and u could serve as a flow variable, the following combinations are defined as the Riemann quantities in gases [44] and liquids [43]:

$$P = \frac{2}{\gamma - 1} a + u \text{ (in a gas)} \qquad P = \frac{2}{n-1} a + u \text{ (in a liquid)} \tag{2.53}$$

$$Q = \frac{2}{\gamma - 1} a - u \text{ (in a gas)} \qquad Q = \frac{2}{n-1} a - u \text{ (in a liquid)} \tag{2.54}$$

The slopes of the characteristics are then expressed as [44]:

$$\frac{dx}{dt} = u + a \qquad \text{(for } P\text{-waves)} \tag{2.55}$$

$$\frac{dx}{dt} = u - a \qquad \text{(for } Q\text{-waves)} \tag{2.56}$$

In water, the velocity $\hat{U}$ is very small compared with $\hat{A}$, and may usually be neglected in equations (2.55) and (2.56). The Riemann variables may be defined in more convenient, non-dimensional form, using the relations shown in appendix C:

$$P = \frac{2}{\gamma - 1} \hat{A} + \hat{U} \text{ (in a gas)} \qquad P = \frac{2}{n - 1} \hat{A} + U \text{ (in a liquid)} \tag{2.57}$$

$$Q = \frac{2}{\gamma - 1} \hat{A} - \hat{U} \text{ (in a gas)} \qquad Q = \frac{2}{n - 1} \hat{A} - U \text{ (in a liquid)} \tag{2.58}$$

An expansion fan is, in reality composed of an infinite number of Mach waves. However, for the purpose of analysis, an expansion fan is represented by a finite number of diverging characteristics, which separate finite regions of properties.

The Riemann quantities P and Q and the relations (2.26), (2.27), (2.28) and (2.44) are sufficient to solve for all wave diagram parameters across isentropic characteristic waves but not adequate when discontinuities such as shock waves and contact surfaces are encountered. However, simple matching relations (such as normal shock tables for shock

waves and the pressure and velocity compatibility relations for a contact surface) between adjacent regions may be used, rather than the general conservation equations.

Normal shock tables, derived from the Rankine-Hugoniot equations are convenient for solving for values across the shock and thus provide the matching conditions. Usually, only the pressure, density, sound speed and temperature ratios, the entropy change and the Mach numbers M_1 and M_2 are tabulated. These quantities may be calculated from the simple relations in appendix B. However, the quantities most useful for the solution of wave diagram problems, namely $\Delta P/\hat{A}$, $\Delta Q/\hat{A}$, $\Delta|U|/\hat{A}$ and ΔS are not usually tabulated but may be calculated as shown in appendix C, which describes shock relations for liquid water.

The paths of contact surfaces are easily plotted on a wave diagram as its velocity is the same as the equal velocities on either side of it (refer to section 2.8.1). For the purposes of wave diagram construction, contact surfaces are idealised as discontinuities. The widening of the contact surface by mass diffusion, which occurs when the gases are at rest or moving at constant velocity, as well as the instability and subsequent disintegration of the interface that occurs if the gases are accelerated toward the one of higher density, are neglected.

2.7.2. The Pressure-Velocity Diagram

Problems involving the one-dimensional interaction of shock and rarefaction waves may be solved graphically using a pressure-velocity diagram. This method is discussed at length in [46].

2.8. Shock and Rarefaction Wave Interactions

Shock and rarefaction wave interactions in a one-dimensional flow are the subject of the present discussion. The resulting flow field from all such interactions may, in principle, be obtained by solving the conservation equations of mass, momentum and energy in a one-dimensional flow, using the appropriate boundary conditions.

One-dimensional interactions can be one of three types:

- Collisions of two waves.
- Overtaking of one wave by another.
- Interactions of a wave with walls or contact surfaces.

General results of these types of interactions are summarised and noted, with reference to pressure-velocity diagrams, in appendix D. The third type is most relevant to discussion of free surface reflection and is discussed in detail in the following section.

2.8.1. Interactions of a wave with walls or contact surfaces

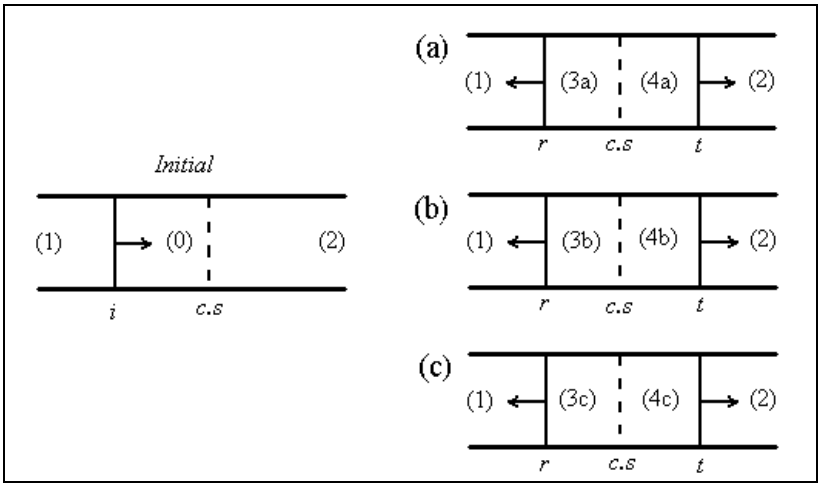


Figure 2.5. *Collision of a wave with a contact surface: initial and final conditions.*

Interactions of a wave with walls or contact surfaces occur frequently. A contact surface is defined as an interface between two or more sections of different fluids or of the same fluid at different states or entropy levels [44]. The boundary conditions across any contact surface are that the pressure and particle velocity left behind the transmitted wave must always equal the pressure and particle velocity left behind the reflected wave [44].

$$\hat{U}_L = \hat{U}_R \tag{2.59}$$

$$p_L = p_R \tag{2.60}$$

These continuity conditions are, generally, only true at the interface. The fluids on either side of the contact surface may have different densities and temperatures. The most general case of collision of a plane wave with a wall or contact surface, during which the above conditions must be satisfied, is illustrated in figure 2.6.

Thompson [49] has shown, by applying only the equations of conservation of mass and momentum to a control surface enclosing a wave, that the of speed of the wave relative to the fluid ahead of it (w) may be related to the states ahead (1) and behind (2) it by:

$$\rho_1 w(u_2 - u_1) = p_2 - p_1 \tag{2.61}$$

where the subscripts 1 and 2 denote the parameters ahead and behind the wave respectively. This can be rearranged giving, where Z is the impedance of the wave,

$$\frac{p_2 - p_1}{u_2 - u_1} = \frac{\delta p}{\delta u} = \rho_1 w = Z \tag{2.62}$$

Thus, for an acoustic wave, the acoustic impedance is:

$$Z = \rho_1 a \tag{2.63}$$

Extending the concept, the shock impedance is [10]:

$$Z = \rho_1 U_S \tag{2.64}$$

Since the characteristic impedance Z it is a proportionality constant between the impressed particle velocity δu and the pressure δp, it is a measure of the stiffness of a material. At the interface between two materials with equal acoustic impedance, an incident sound wave transmits with no reflected waves. For the collision of weak to moderate waves with a contact surface, the Riemann solution applies [46]. It states that for the collision of a shock with a contact surface, the reflected wave will be a shock for:

$$(\rho a)_T > (\rho a)_I \tag{2.65}$$

and a rarefaction wave for:

$$(\rho a)_T < (\rho a)_I \tag{2.66}$$

where the subscript T denotes a property of the undisturbed, receiving material into which a wave is transmitted and I denotes a property of the undisturbed material through which the incident wave travels. Wave impedances are discussed in detail in [46] and [58].

Reflection of a wave from a rigid wall, area change discontinuity or free surface may be considered as special cases of collision of a shock or rarefaction wave and are discussed in the following sections.

2.8.1.1. Reflection from a Rigid Wall

The collision of a shock wave with an infinitely rigid (no movement is possible) wall may be considered a special case of collision of a wave with a contact surface. In this case, the appropriate compatibility condition [55] is that the particle velocity behind the reflected wave must be equal to zero (as it is behind the wave that is transmitted through the wall), since the acoustic impedance of the wall is infinity. The reflection of acoustic waves in any fluid and that of finite waves in gas or liquid media from a wall are considered in appendix E.

2.8.1.2. Shock or Rarefaction Wave Passing Through a Discontinuous Change in Cross Section

An area change discontinuity may be described as a special type of contact surface. Disregarding any of unsteady disturbances described in appendix F the strength of a shock passing through a change in cross section is modified and a reflected wave created. When passing through an area enlargement, the transmitted shock will be weaker than the incident wave, since it must compress a greater volume of fluid. When passing through an area reduction, the transmitted shock will be stronger than the incident shock. Methods used to solve these problems, described by Rudinger [44] and, for acoustic waves, by Parmakian, are discussed in appendix F.

2.8.1.3. Free Surface Reflection

Consider the special case of normal incidence and collision of a shock wave with a contact surface, where the incident wave propagates in a liquid and the transmitted wave propagates in a gas. The surface of the water will initially be accelerated upwards. Since the compressibility of water is far greater than that of air (refer to the tables of properties in appendix G), there is virtually no opposition to motion of the boundary and hence no

restriction on the normal components of velocity [55]. At room temperature, the acoustic impedance of water is about 3500 times that of air (refer to appendix G). Since the acoustic impedance of the liquid is high, the velocity and displacement of the free surface (i.e. the velocity imparted to the medium) will be low, such that changes in gravitational potential energy are much smaller than the energy of compression [55]. The pressure of the air above the free surface cannot change significantly for all realistic movements of the surface [55] i.e. the accelerated liquid interface cannot transmit a significantly strong shock wave into the air above it, leaving the pressure of the air above the liquid at its initial value. Thus, free surface reflection of a shock requires that the pressure above the surface, and by the compatibility condition (2.60), below the surface as well, be unchanged [55].

A reflected rarefaction wave, and not a shock wave, is required to reduce the pressure to its initial value [55,59]. The profile of this rarefaction wave is the "negative" or a reflection [55,60] of the shock wave profile (essentially equal in magnitude or strength but opposite in sign to that of the incident wave). Thus, free surface reflection may be seen as an opposite case to that of rigid wall reflection where the reflected and incident wave are, in the acoustic approximation, of equal strength.

The resultant pressure variation at all depths below the free surface may then be determined by superposition (simply the algebraic sum) of the pressures in the incident compression and reflected rarefaction waves [36,55,60,61], taking into consideration the appropriate delay times (difference in time of arrival of the waves at the depth under consideration). This superposition principle is an acoustic approximation, which is valid since liquid shock waves are weak as discussed previously.

Consider the illustration of the absolute pressure at some depth below the surface shown in figure 2.6. As the head of the rarefaction progresses downwards, it encounters the pressure remaining behind the incident wave some depth below the surface, which has decayed. The negative rarefaction front (the pressure drop) is superimposed on the later, weaker part of the positive wave. Thus, the absolute pressure values depend on the rate of

decay of the incident wave, path differences and the depth under consideration. The net pressure behind the front may reach negative absolute pressures when the front encounters regions of lower excess pressure [55]. If the incident pressure wave is of sufficient strength, the reflected wave may decrease the pressure, at some depth below the free surface, below the threshold level, causing the liquid to cavitate. The dashed line on figure 2.6 represents the net pressure obtained by considering superposition of the incident and reflected waves but ignoring cavitation. It shows an unrealised state of tension that would occur if the liquid resisted cavitation, while the solid line in fig indicates the net pressure when cavitation occurs [55].

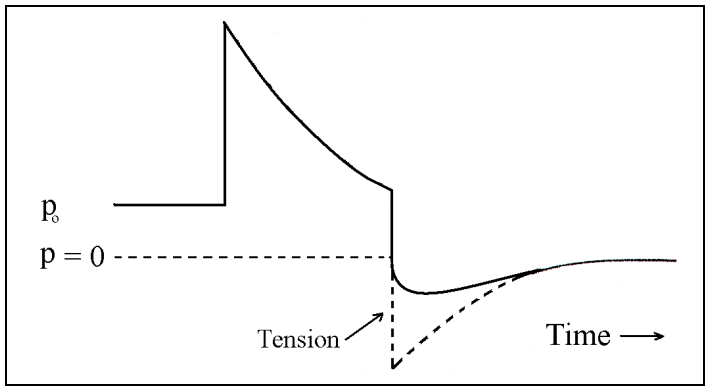


Figure 2.6. Resultant absolute pressure-time curve at some depth below the free surface (adapted from [55]).

3. Cavitation

The cavitation process is complicated by such factors as energy losses involved in the damped oscillations of a cavity, heat conduction, viscosity, compressibility, surface tension, temperature discontinuities at the phase interface [1] and transfer of heat and mass (by diffusion of permanent gas, evaporation of liquid and condensation of vapour) across the bubble wall. The problem involves, essentially, two phases coupled through a moving boundary (the bubble wall) [1].

3.1. Liquids Under Negative Pressure

A liquid may, depending on the ambient conditions, exist as:

- A subcooled liquid, also known as a compressed liquid or simply as a liquid [52], where the temperature of the liquid is below its saturation temperature and the liquid is under more pressure than it needs to be in order to stay liquid.
- A saturated liquid [52], that is, a liquid that is at its boiling point (or saturation temperature), which may coexist with its vapour phase.
- Liquid in a supercooled state, which is metastable with respect to freezing.
- Liquid in a superheated state, which is metastable with respect to boiling (liquid-vapour transition).
- Liquid in a stretched state, i.e. liquid under negative pressure, which is metastable with respect to cavitation (liquid-vapour transition).

Liquids may exist as *metastable* states (the last three mentioned above), which are states outside the stability region of the phase diagram of the substance, for a certain time. The present discussion will be limited to the last two (superheated and stretched) metastable states only. The condition of mechanical stability $(\partial P/\partial V)_T < 0$ must be fulfilled for both phases on the solid-liquid line, including the metastable section of this line [65]. At metastable states, the condition $(\partial P/\partial V)_T \to 0$ holds. Metastability means that a small can fluctuation or disturbance of the liquid of sufficient magnitude will cause [7,10,65] the

mechanical stability condition to be violated, which results in vapour, explosive or rapid boiling or cavitation in the liquid, which will revert to the positive vapour pressure.

Refer again to the conventional phase diagram for water, figure 1.1. It is known that the processes *a*-*b* and *b*-*c* correspond to those of boiling and cavitation. However, liquid may exist in the pressure-temperature region labelled 'vapour' as a 'metastable liquid'. From the arbitrary liquid state *a*, one may reach the metastable state by either increasing the temperature above its boiling point (*a* to *b*, where *b* is a metastable, superheated liquid state) at constant (ambient) pressure or by decreasing the pressure at constant temperature (*a* to *c*, where *c* is a metastable, stretched liquid state). Therefore, it is possible to reach liquid states usually associated with stable vapour states, which have lower chemical potential, without the vapour phase developing [66]. So arbitrary states in the vapour or metastable liquid region, such as *b* and *c* in figure 1.1, may exist as vapour, superheated liquids or liquids under negative pressure, depending on the way in which the state was reached. Cavitation results because stretched liquids tend to equilibrate to the vapour state [67]. The binodal is thus, in the case of superheated and stretched liquid, a boundary between stable and metastable liquid [1].

Interesting phenomena occur only in liquids under negative pressures. However, if one decreases the pressure below absolute zero pressure, which is not a particularly special point in fluids, the liquid properties do not change discontinuously at that point [68]. Martinás and Imre [69] have shown, using classical thermodynamics, that negative absolute pressure states, though forbidden in gases, are possible in liquids. For sufficiently large tensions, a liquid may be expected to be "pulled apart"; with 'holes' (i.e. a cavitation region) forming [55]. In very pure liquids with small nuclei, cavitation may occur at large negative pressures [70].

A liquid under negative pressure pulls inward on its container as opposed to exerting an outward pressure when under positive pressure. The intermolecular cohesive forces between the liquid molecules as well as the adhesive forces between the liquid and container allow liquids to withstand negative pressures [2,3]. Liquids under negative

pressures may be found quite widely in confined spaces in the human body [4] and in the xylem of trees [3,69].

From the elementary considerations of section 1.1 alone, one might expect that cavities form when the local, external, pressure drops to the saturated vapour pressure of the liquid at the current, ambient temperature i.e. the saturated vapour pressure within the bubble [2]. However, cavitation does not always begin near the vapour pressure: some experiments reveal deviations that are not reconcilable with this vapour-pressure concept [2] e.g. water has been subjected to a tension of -140 *MPa* before cavitating [66]. However, this required a very small liquid volume (an inclusion in a quartz crystal) to minimise the probability of impurities being present [66]. Thus, the cavitation threshold is also known as the *tensile strength* of the liquid, and is not, in general, equal to the vapour pressure [2,5], as will be shown, in terms of bubble dynamics, in section 3.3. In summary, if the pressure drops down to, or below, the vapour pressure any minute cavity will grow and if the pressure drops to absolute zero or negative pressures, the rate of bubble growth will increase [1].

3.1.1. Cavity Dynamics of Bubbles Initiated in a Stretched Medium

Hassanein et al. [71] postulated that a cavity that forms during a negative pressure phase initiates a relaxation shock wave when the stretched medium returns from low density and pressure to normal density and pressure. The shock is a result of the pressure difference across the bubble wall: the pressure in the cavities is equal to approximately zero while the liquid is at negative pressure.

Hassanein et al. concluded, from calculations [71,72], that any cavity that is initiated during a negative pressure phase will continue to grow and not collapse when the pressure increases. It will expand freely at a decreasing rate to a value determined by the amount of elastic energy stored in the system. This illustrates a difference between cavity dynamics in a stretched medium and cavitation initiated at positive pressures, where vapour bubbles collapse during an increased pressure phase. The conclusion that bubbles initiated in a stretched medium do not collapse, during the positive pressure phase, was

attributed to discharging or uploading of the liquid medium, away from the bubble, by the relaxation shock wave initiated at inception.

3.2. Nucleation

Knowledge of the local pressure variations alone does not determine when and how cavitation will occur [7]. Cavitation is a complex process where the liquid's physical state i.e. the nature and content of heterogeneities in the liquid and container walls play a major role in the nucleation of bubbles, are difficult to predict accurately. The influence of nuclei makes the prediction of when cavitation will occur, i.e. cavitation threshold, difficult [5,7,34].

From the theory of Fisher [40,73], the "homogeneous cavitation pressure", for pure water, has been estimated as –132 *MPa* in water. According to Young [1], the tensile strength of water at room temperature has been predicted as approximately –100 *MPa*. Other sources have estimated the ultimate tensile stress of water as 25-100 *MPa* [74,75] and "hundreds of atmospheres" [76]. Using classical nucleation theory [4], the tensile strength of water near the critical point has been estimated as –20 *MPa.* However, such values are unrealistic for most normal liquids [38].

Consider the first stage of cavitation, during which a bubble forms, which is referred to as the nucleation stage. There are two main types of nucleation [77]:

- Heterogeneous nucleation occurs when the bubble formation is influenced by external factors such as impurities or walls [5,66]. In this case, the major weaknesses, where rupture would be most likely to occur, are at sites in liquid-solid interfaces (walls or solid particles). Under practical circumstances, this is the most common type occurring. It is difficult to analyse quantitatively as the shapes and sizes of the nucleation sites vary greatly and are random.
- Homogeneous nucleation occurs only in the absence of impurities, walls, etc. This type of nucleation is thus an intrinsic property of the liquid system. As a result, homogeneous nucleation is simpler to describe quantitatively [66]. However, it requires special conditions and usually takes place very far from equilibrium

conditions [77]. In this method, thermal motions within the liquid form temporary, microscopic bubble nuclei that may expand to macroscopic sizes [5].

The above values are based on assumption of homogeneous liquid. Homogeneous cavitation, however, rarely occurs in nature and in practical applications [66]. Water, which has been elaborately filtered and pre-pressurised to several hundred atmospheres, may cavitate at tensions of -30 *MPa* [7]. When solid non-wetted nuclei of size 10^{-5} *mm* are present, it is likely that otherwise very pure water will rupture at tensions in the order of megapascals [7]. It is certain that cavitation may occur in untreated water at pressures between the positive vapour pressure and small negative pressures [7]. These empirical observations imply that nuclei or weak spots exist within liquids i.e. liquids are usually not homogeneous.

Now consider untreated water. Liquids that cannot withstand significant tensions may be expected to cavitate when tensile stresses in the order of one atmosphere are reached [78, 55, 61]. Studies of the liquid strengths [61] have showed that such liquids will sustain tensions with a limiting magnitude in the order of the vapour pressure (i.e. close to zero). Cole concluded, partly from an estimate that a negative pressure of -1 *bar* will support bubbles more than one or two microns in size and from observations of cavitation behind waves [55], that open water and water that has not been particularly well purified is unlikely to be able to sustain tensions greater than -1 *bar*. This is verified by the experimental results of Eldridge et al. [79], which indicated that open sea water can only sustain a negative pressure of only a few bars before cavitation occurs. Štuka et al. found that the magnitude of the tensile strength of non-degassed water is less than 5 *bar* [42].

3.2.1. Cavitation Nuclei

Detailed experimental studies have shown that even after several purifications, distillation and deionisation, real liquids settled contain microinhomogeneities, existing as microbubbles of free gas, solid particles or their combination, which act as cavitation nuclei [38,61,80]. The complex initial state of the liquid depends on the physical nature, size, distribution and concentration of these nuclei and determines the initial dynamics of

cavitation processes [35]. The intrusion of impurities or nuclei prevents liquids from sustaining tensions as readily as solids and reduces the tensile strength of a liquid from the high theoretical values listed to the low values encountered in experiments [2]. This explains why cavitation occurs at much lower tensile strengths than is estimated thermodynamically. In the absence of nuclei, a liquid may withstand large negative pressures in the order of the theoretical values [7,66]. However, this necessitates a small volume (to minimise the probability of impurities being present) of very pure liquid [81].

The many types of cavitation nuclei include permanent bubbles containing undissolved gas or uncondensed vapour and quantum vortices in Helium [1,82]. In seawater and other bodies of water exposed to the atmosphere, small vapor bubbles may originate from high-energy particles produced by cosmic rays or radioactivity. Other forms of nuclei include ionising particles and neutrons [70]. However, not all impurities in a liquid will affect the cavitation process or the tensile strength. The main types of impurities are distinguished between in the following sections.

3.2.1.1. Miscible Liquids and Dissolved Solids

The presence of a *miscible liquid or dissolved solids* does not change the physical properties of a liquid (such as viscosity, density and surface tension) significantly enough to affect the growth or collapse of cavities [2], unless present in large amounts and thus have little effect on the effective tensile strength of the solvent.

3.2.1.2. Non-miscible Liquids and Undissolved Solids

All liquids wet solids to some measurable extent but do so imperfectly [1,2]. For both *non-miscible* and *non-soluble substances,* when the bond at the interface between the liquid and the solid or between two dissimilar liquids (i.e. low wettability or hydrophobic) is low, weak spots are present and vapour bubbles form readily. This is expected as adhesion (wetting) is due to the same intermolecular forces that allow liquids to withstand tensions [2]. Wetting, surface tension, contact angles and the relation between them is given in [2]. High wettability between a liquid and a non-miscible liquid or undissolved solid impurity will not necessarily prevent that impurity from acting as a

nucleus and promoting cavitation. Experiments [2] suggest that the "rigidity" of a liquid is also an influential factor: Cavities may form, even at a hydrophilic surface, if it is too rigid to follow the motion of the liquid under consideration [83]. More detailed research in this area may be worthwhile.

3.2.1.3. Dissolved Gas

It is virtually impossible to eliminate dissolved gas from a macroscopic liquid volume, even after long periods of degassing [5]. Experiments (discussed in chapter 4) have shown that pressurised water samples may be more resistant to cavitation than unpressurised ones containing undissolved air [5], which may exhibit virtually no tensile strength. These experiments suggest that, in contrast with undissolved gas, gas that is entirely dissolved in the liquid does not promote cavitation or decrease the tensile strength of the liquid significantly.

3.2.1.4. Undissolved Gas and Vapour Bubbles

Even if no gas bubbles are visible, submicroscopic gas bubbles may act as nuclei [5,7]. Undissolved free bubbles filled with a mixture of the uncondensed liquid vapour and dissolved gases are the most obvious cavitation nuclei, typically present in liquids, to consider. Such bubbles of undissolved gas or uncondensed vapour are already cavities in the liquid and hence, must lower the tensile strength of a liquid. Many experiments [2] in hydrodynamic and acoustic cavitation show that the pressure at which cavitation occurred decreased as the vapour and gas content was reduced i.e. after degassing processes.

Free gas bubbles, particularly large, visible ones [7], will slowly (rise) float to the surface and escape. A bubble of radius $10\mu m$ in water will rise at a rate of about 0.3 $mm.s^{-1}$ [1]. In addition, diffusion of gas out of the bubble into the liquid will occur. Surface tension forces would increase the bubble gas pressure resulting in the gas and vapour content being completely dissolved and condensed [2]. Thus, diffusion and surface tension forces will cause a bubble to collapse completely [7]. It has been estimated [84] that an air

bubble, of radius $10\mu m$, in air-saturated water will take about 7 s to dissolve. Another calculation predicts a time of 2.5 s [5]. Similarly, vapour should condense completely [2]. In addition, free bubbles have been found to persist, even under pressurisation, although their sizes diminish [5]. Thus, some stabilising mechanism or "host" must be present for bubbles containing undissolved gas or uncondensed vapour to exist stably as nuclei in the liquid. Various stabilisation mechanisms have been proposed [1,2,5].

According to Harvey et al., [85] minute, undissolved gas nuclei pockets may exist in the microscopic and submicroscopic, hydrophobic cracks, crevices or interstices of hydrophobic solids, i.e. container walls or in imperfectly wetted, particles [2]. They are stabilised because, under such conditions, the surface tension acts to decrease rather than increase the pressure, thereby preventing the gas from dissolving [2]. Pressurisation may force such trapped nuclei to collapse by overcoming the surface tension and forcing liquid into the crevices, thereby dissolving the gas [2]. In other cases, the bubble will not collapse because its geometry is such that the gas-liquid interface has a convex curvature viewed from the liquid, such that the surface tension sustains the high pressure [5].

Fox and Herzfeld [2,86] proposed that small bubble nuclei are surrounded by monomolecular skins made up of organic impurities, which give the free surfaces of the bubbles sufficient elasticity to withstand high pressure [5], modify the effective surface tension, retard evaporation and act as diffusion barriers, thereby preventing the bubble from dissolving. The model of Harvey et al. is thought to be more satisfactory as it is able to explain all observed behaviours (e.g. scatter in the cavitation threshold as discussed later in section 4.4) without postulating improbable fluid properties [2]. Despite this, the organic skin mechanism is now more widely accepted because of studies confirming the existence of small amounts of surface contamination and their ability to generate significant surface effects [5]. Another stabilisation mechanism, involving the possible production of nuclei continuously by cosmic radiation has been suggested [5].

Consider the model of Harvey et al. It is known that cavitation often starts at or near boundaries. This is due to crevices, which are often present in container, pipe or channel

walls and are able to support gas nuclei of size in the order of 10^{-4} *mm* [2]. Experimentally [2,87], cavitation also occurs readily within the body of a sample of liquid. Within the body of the liquid, suspended, solid particles provide the crevices for nuclei stabilisation instead of the walls. Ordinary tap water may contain thousands of these solid particles per cubic centimeter [1]. The size, shape and number of solid particles affects the tensile strength of the liquid [1]. Suspended particles, such as atmospheric and industrial dust, with diameters in the order of 10 μm, may support gas nuclei of size in the order of 1 μm [2].

3.2.2. The Statistical Nature of Cavitation

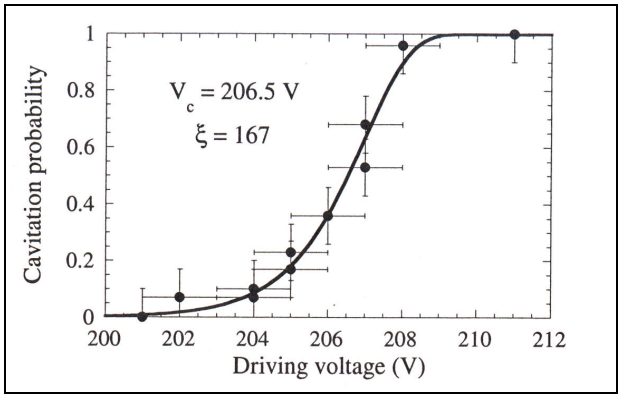


Figure 3.1. Cavitation probability as a function of Transducer Driving Voltage [40].

Cavitation is essentially a stochastic or intrinsically random phenomenon [40] i.e. repeated experiments under the same conditions do not always result in cavitation [35]. Caupin and Fourmond [40] induced cavitation in Freon ultrasonically, using a piezoelectric transducer, and detected inception using light scattering, optical imaging and acoustic detection methods. Their study illustrated the statistical nature of cavitation. The cavitation probability was defined as the fraction of nucleation events resulting from pulses of low pressure. Figure 3.1 is the result of their analysis of the probability of nucleation occurring. Its general trend is similar to that of results of Maris and Konstantinov [88] who used similar methods to produce cavitation in liquid Helium. The transducer driving voltage was approximately proportional to the maximum negative pressure produced at the focus i.e. the amplitude of the negative pressure swing at the

focus [88]. Thus, it is reasonable to assume that the variation of cavitation probability with the strength of a rarefaction wave in a liquid, rather than transducer driving voltage on the abscissa of the graph, will follow the same trend shown in figure 4.1. Isolated cavitation events may be caused by large, random nuclei [39].

3.3. Spherical Bubble Dynamics

The following theory, initially developed by Rayleigh [89] and later extended by Plesset et al. [90,91] allows analysis of the dynamic behaviour of a bubble in an infinite liquid.

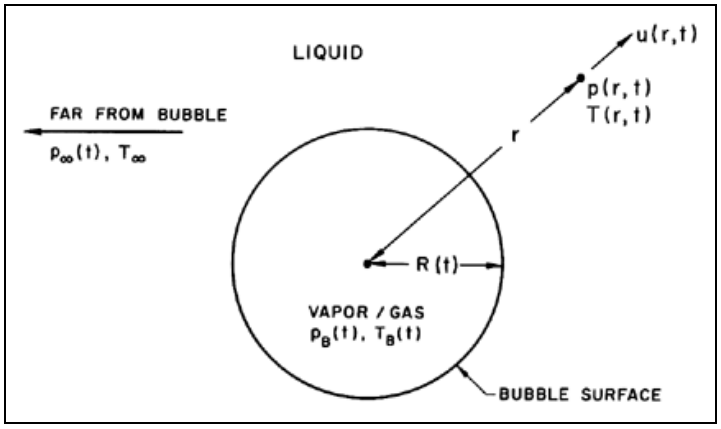


Figure 3.2. A spherical bubble in an infinite liquid [5].

A bubble is forced to collapse by external pressure and surface tension and forced to stay open by the pressure within it. Thus, a pressure balance across the interface of a perfect gas bubble of radius R yields [1,5]:

$$p_B - p_\infty = \frac{2\sigma}{R} \tag{3.1}$$

where p_B is the pressure within the bubble, p_∞ is the external pressure at infinity and σ is the surface tension, which is the manifestation of inter-molecular forces preventing hole formation [1,2,5]. If the bubble contains gas and vapour, then

$$p_B = p_G + p_v(T_\infty) \tag{3.2}$$

and from equations (3.1) and (3.2)

$$p_G + p_v(T_\infty) - p_\infty = \frac{2\sigma}{R} \tag{3.3}$$

where the bubble pressure is the sum of p_G, the partial pressure of the gas within the bubble [5] and p_v, the saturated vapour pressure, which is a function of external temperature only [52]. Consider a bubble in equilibrium in a liquid. In the following, parameters at this initial equilibrium state are represented using the subscript *i*. If the temperature in the bubble is uniform and the bubble is assumed to contain only vapour, then $p_{Bi} = p_{vi}$ and from equation (3.1), the stability condition is [1,2,5,77]:

$$p_\infty = p_{vi} - \frac{2\sigma}{R_i} \tag{3.4}$$

Thus, the external liquid pressure p_∞ must be lower than the vapour pressure p_{vi} for the bubble to remain in equilibrium. If p_∞ is maintained at any value below $p_v - 2\sigma / R_i$, then the excess pressure causing growth will increase and the bubble will no longer be in equilibrium and will expand [1,2,5,77]. If, the radius of the largest bubble nucleus present is referred to as the critical radius and denoted by R_{Ci}, then the liquid tensile strength is

$$p_{vi} - p_\infty = \Delta p_c = \frac{2\sigma}{R_{Ci}} \tag{3.5}$$

Thus if one assumes $p_{vi} = 0$, then the cavitation threshold will be negative $p_c < 0$ i.e. the liquid will sustain a negative pressure before cavitating. If one assumes that $p_{vi} = 2339\ Pa$ then $p_c < 2339\ Pa$. This illustrates that, cavitation occurs, in general, at a pressure below the saturated vapour pressure. Winterton [77] modified the stability equation (3.5) to include the contact angle of a crevice for heterogeneous cavitation. However, his equations are not readily applicable due to the need for specification of nucleation site parameters, which vary widely and are difficult to quantify.

3.3.1. The Rayleigh-Plesset Equation

The general form of the Rayleigh-Plesset equation is [5,89,90,91]:

$$\frac{p_B(t) - p_\infty(t)}{\rho_L} = R\frac{d^2R}{dt^2} + \frac{3}{2}\left(\frac{dR}{dt}\right)^2 + \frac{4\nu_L}{R}\frac{dR}{dt} + \frac{2S}{\rho_L R} \tag{3.6}$$

In the above equation, it is assumed that the bubble contains both vapour and contaminant gas. It is also usually assumed that no appreciable mass transfer occurs between the gas and liquid except by vaporisation and condensation i.e. no diffusion takes place. Defining

a reference state, denoted by the subscript *o*, at which the bubble radius, external temperature and the partial pressure of the gas within the bubble are R_o, T_∞ and p_{Go} respectively, and assuming that the ideal gas equation are valid during the compression and expansion of the gas, the partial pressure at any time is:

$$p_G = p_{Go}\left(\frac{T_B}{T_\infty}\right)\left(\frac{R_o}{R}\right)^3 \tag{3.7}$$

Combining equations (3.2), (3.6) and (3.7) yields the following equation, equation (3.8)

$$\frac{p_V(T_\infty) - p_\infty(t)}{\rho_L} + \frac{p_V(T_B) - p_V(T_\infty)}{\rho_L} + \frac{p_{Go}}{\rho_L}\left(\frac{T_B}{T_\infty}\right)\left(\frac{R_o}{R}\right)^3 = R\frac{d^2R}{dt^2} + \frac{3}{2}\left(\frac{dR}{dt}\right)^2 + \frac{4\nu_L}{R}\frac{dR}{dt} + \frac{2S}{\rho_L R}$$

It is now assumed that the expansion and compression of the gas in the bubble are polytropic processes. Thus, in terms of the polytropic constant *k*,

$$p_G = p_{Go}\left(\frac{R_o}{R}\right)^{3k} \tag{3.9}$$

and the third term in equation (3.8) becomes:

$$\frac{p_{Go}}{\rho_L}\left(\frac{T_B}{T_\infty}\right)\left(\frac{R_o}{R}\right)^{3k} \tag{3.10}$$

The first term in equation (3.8) is referred to as the *tension or driving term* as it is associated with the external, driving pressure field, while the second term is called the *thermal term* as it is associated with thermal effects and the first and second terms on the right-hand side of the equation are the *inertial terms*. Brennen [5] defined the *first critical time* as the time during a bubble's growth when the order of magnitude of the thermal term increases and approaches the order of magnitude of the inertial terms. Once this time has elapsed, the comparative significance of the terms in the equation (3.8) changes, with the thermal term becoming dominant. This first critical time depends on the first term (the tension) and a thermodynamic quantity that in turn depends on the liquid temperature only. The value for water, at temperatures of about 20°*C*, is in the order of *10 s*, as estimated by Brennen [5]. This is much longer than the duration of the growth phase of a cavitation bubble. Thus, bubble growth occurring in water at room temperature is said to be "inertially controlled", which simply means that the growth is unhindered by thermal

effects i.e. the growth does not take long enough for the thermal term to become dominant. Consequently, T_B=T_∞ and the thermal term in equation 3.8 is neglected, giving

$$\frac{p_V(T_\infty) - p_\infty(t)}{\rho_L} + \frac{p_{Go}}{\rho_L}\left(\frac{R_o}{R}\right)^{3k} = R\frac{d^2R}{dt^2} + \frac{3}{2}\left(\frac{dR}{dt}\right)^2 + \frac{4\nu_L}{R}\frac{dR}{dt} + \frac{2S}{\rho_L R} \qquad (3.10)$$

In summary, this equation was developed on the basis of the following assumptions [5]:

- The bubble is isolated in an infinite liquid (i.e. unaffected by solid particles, walls and other bubbles).
- The bubble contains both vapour and contaminant gas.
- The liquid is a Newtonian fluid.
- The bubble remains spherical throughout the growth or collapse process.
- The liquid density, ρ_L and viscosity μ_L, as well as the temperature of the liquid T_∞ (and hence T_B) are constant and uniform.
- The bubble contents are homogeneous and the temperature, $T_B(t)$, and pressure, $p_B(t)$, within the bubble are uniform. The polytropic assumption, equation 3.9, and ideal gas equation apply for the bubble contents.
- It is assumed that the growth and collapse events occur too rapidly for significant mass transfer of contaminant gas to occur between the bubble and the liquid i.e. the mass of contaminant gas in the bubble is constant and no diffusion takes place.

The form of Rayleigh's equation above only applies if the speed of the collapsing bubble wall, $\dot{R}$, is small compared to the speed of sound in the gas a_g. i.e. $\dot{R} / a_g$<<1 [11].

3.3.2. The Response of Bubbles to Rarefaction Waves

Qualitative analysis using the first integral of the Rayleigh equation has shown [92] that, assuming an instantaneous pressure drop three types of solutions are possible for different values of the pressure at infinity p_∞ and the nucleus radius R_o:

- Unbounded bubble growth.
- Asymptotic attainment of a finite size during an infinite time.
- Periodic oscillations of the nuclei.

With the only other possibility being of invisible bubble pulsations.

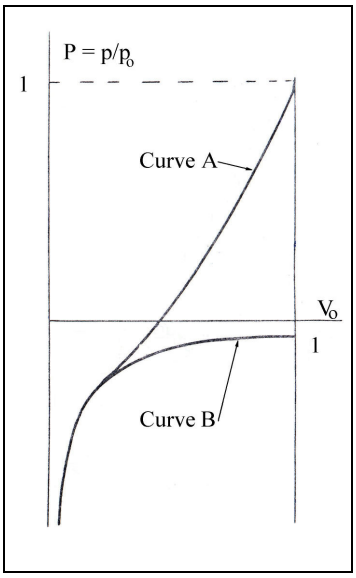


Figure 3.3. Regions of the P-V_o plane (adapted from [92]).

Which region occurs depends on the rarefaction wave strength (p/p_o) and the initial radius R_o and visible radius R_v as illustrated in figure 3.4, where R_o and R_v are expressed in terms of the non-dimensional parameter $V_o=(R_o/R_v)^3$. From this qualitative numerical analysis, Kendrinskii also found that cluster formation may develop in two ways [92]:

1. In weak rarefaction waves (e.g. waves across which the pressure drops from a value p_o to a value of about $p_\infty \approx -0.1p_o$) or acoustic fields, the time to attain visible size depends largely on the initial radii R_o in the spectrum. The zone is gradually saturated with bubbles, which attain visible size after different time intervals according to their initial size [2,92].
2. In intense rarefaction phases, where the negative pressure may be large, the cavitation zone is instantaneously saturated by bubbles of the same size. All of the bubbles of the whole initial spectrum of nuclei attain detectable size simultaneously. Thus, the bubble density and concentration peaks immediately in the cavitation zone, which is characterised by a uniformity of bubble sizes.

These theoretical results have been verified empirically and are acknowledged as experimental facts [92].

The oscillation of a regular cavitation bubble is similar to that of a gas sphere containing detonation products, which results from an underwater explosion. Such a gas sphere may be considered as a large cavitation bubble [10]. In all cases, the inertia of the liquid and the elasticity of the liquid and gas provide the necessary conditions for an oscillatory system [55]. The oscillation of a gas bubble proceeds as follows: Firstly, during bubble growth, the expansion is sustained by the inertia of the out-flowing liquid [55]. This process slows down as mass is transferred from the liquid to the cavity, which becomes increasingly occupied. The dense fluid within must rearrange to accommodate more molecules [4]. Then as the gas pressure within the bubble drops, the external pressure constrains the bubble and causes it to contract. The bubble contracts until the gas compressibility becomes significant, arrests the motion and then reverses it [55]. The oscillations continue with diminishing amplitude until a uniform state is reached [4].

3.4. Collapse of Cavitation Bubbles

If an expanding bubble is subjected to a rise in pressure, its growth will be arrested and it will collapse violently and possibly disappear by solution of gases and condensation of vapour [2]. Xiao et al. [4] simulated the collapse of a cavitation bubble, using a *Molecular Dynamics* approach, which has been shown to be a better suited to the final stage of collapse and to provide a more realistic description than traditional fluid mechanics or classical nucleation theory, which provides no details of the collapse process. Simulations showed that bubble collapse to an undetectable size is followed by the previously discussed damped oscillatory behaviour, which may or may not be detectable. It was found that the larger the initial bubble size, the more pronounced the oscillatory nature of the collapse and the higher the final temperature will be. According to the simulations, the final temperature was at least (for the smallest bubble) 9 times the critical temperature (about 5800 K for water). Bubbles may either collapse while retaining spherical form and then emitting shocks at the instant of rebound or, in the presence of other cavities, walls or free surfaces, in asymmetric form resulting in liquid jets and violent impacts at solid boundaries [93].

4. Literature Review

The present discussion is a review of studies that have shown methods of studying the effects and behaviour of cavitation processes. Tensions and cavitation may be induced in a liquid by static or quasi-static methods (by the Berthelot or centrifugal methods) or by dynamic methods (pulse reflection techniques, tube arrest or shock tube methods). Overton and Trevena [95] and Williams and Williams [96] provided a good overview of dynamic stressing, while both static and dynamic methods are surveyed in [59] and [76]. Appendix H lists cavitation thresholds determined by static and dynamic experiments.

Berthelot Tubes are a widely used method for subjecting liquids to negative pressures and producing cavitation. They are discussed, at length, in [2,59,75,97-103]. In these experiments, cavitation is most likely to occur at the walls i.e. by loss of adhesion [73,99,103]. The centrifugal method is discussed, in detail in [2,59,104]. It essentially involves a horizontally spinning tube filled with liquid in which tension is generated by centrifugal force [2]. Dynamic methods are the main focus of this chapter.

4.1. Pulse Reflection Techniques

Pulse reflection techniques make use of the phenomenon described in section 2.8.1.3. Such experiments usually differ in the methods used to produce the incident compression pulses and in the nature of the “free surface.

These experiments may also differ in the method of reflection. The concept of *free surface reflection* and its associated consequences, as described earlier, need not involve a gas-liquid interface. A similar phenomenon will occur when a compression wave propagating in a high impedance medium is reflected at any relatively low impedance boundary [96]. Davies et al. [2,105] performed “free surface” reflection using a tube with pistons at both ends. One was struck by a lead bullet to generate a compression pulse within the tube. The other piston, which was light, acted in as a free surface, reflecting a rarefaction wave when impinged upon by the pulse. The liquid-gas interface in free

surface reflection experiments may also be replaced by a low inertia or free plate as illustrated by the experiments of Eldridge et al. [55,79] who used a 0.5 *mm* thick sheet of cellulose acetate, about 150 *mm* in diameter and backed by air. A common material used as a flexible membrane in such experiments is Mylar. The technique of pulse reflection in which the liquid is confined between a solid surface and a flexible membrane, is referred to as the cell method [59].

4.1.1. Explosions

The earliest experiments using pulse reflection techniques were performed in studies of underwater explosions in large bodies of water [59,60,61,106,107]. In general, the resulting pulses have shorter rise times than those generated in "bullet-piston" experiments (described in section 4.1.2) and similar decay time constants in the order of 10^{-3}-10^{-4} *s* while tensile strength values are in the order of megapascals [107].

On a smaller scale, Wilson et al. [59,80,95,108] detonated small (0.1*g*) explosive charges, resulting in spherical compression waves in water that were reflected at a free surface above the charge. The maximum tension that can be sustained by ordinary settled tap water was estimated as –0.85 *MPa* while the value for deionised and degassed (by evacuation) water was –1.5 *MPa* [59,80,108]. These tensions were determined by taking high-speed photographs of the surface effects and relating the liquid particle velocity to the maximum tension using the Rankine-Hugoniot equations [59].

Richards et al. [109] ignited an oxyacetylene mixture in gas above a liquid column. The detonation wave was transmitted into the liquid as a compression wave, which was subsequently reflected as a tension pulse at a thin sheet, made of Mylar, which supported the column at the lower end. The maximum pressure behind the transmitted compression waves was about 72 *MPa*. The duration of the maximum tension was 300-400 μs. The tensile strength recorded, for deionised water, was –1.2 *MPa*.

Kedrinskii studied the effects of the underwater explosion of a 1.2 *g* charge of high explosive, fixed 5 *cm* below a free surface as detailed in [36,37,38,80,106]. Free surface

reflection of the shock waves resulted in intense rarefaction waves [80]. The photographs taken at high speed, figure 4.1, showed that the violent cavitation caused spalls or layers to became detached from the main cavitation zone. This effect is similar to the well-known effects of brittle solid fragmentation when a strong shock propagates through the solid and encounters a solid-air interface [38]. Thus, a cavitating liquid exhibits both plastic (foam) and brittle (spalls/droplets) behaviour [37,80]. The phenomenon of free surface reflection is essentially the same as that of spalling of metals [80].

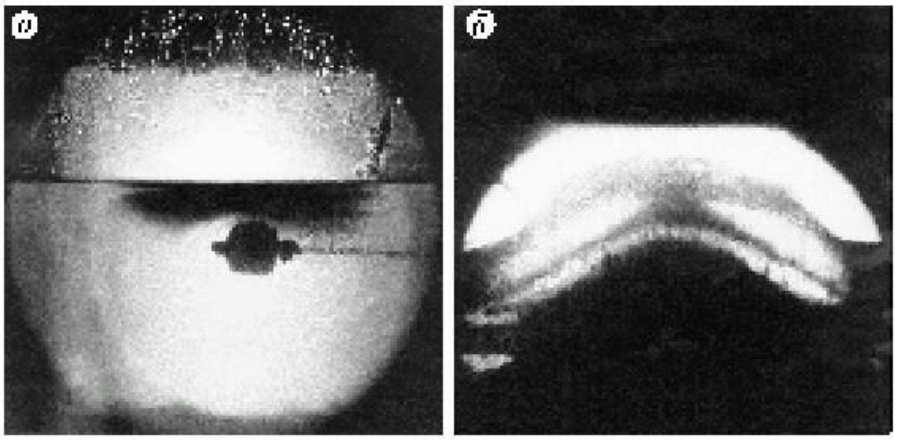


Figure 4.1. Cavitation zone development due to underwater explosion of a 1.2g charge near the free surface of a liquid.

A mass of bubbles formed by intense cavitation (due to a free surface reflection), may, in effect, became a new free surface for the remaining body of liquid such that the wave reverberating within a layer with two free surfaces [110].

4.1.2. Bullet-Piston (B-P) Methods

The bullet-piston (B-P) method is the most widely employed method of achieving pulse reflection [96]. In such experiments, the initial compression wave is produced by impact of a bullet on a piston in contact with the test liquid as explained in [111]. Typically, the rise time and total duration of the incident wave are in the order of 50 and 500 microseconds respectively [59]. Incident shocks with peak pressures of up to 30 *MPa* may be generated in water using this method [59].

Couzens and Trevena [112] performed conventional B-P experiments using a vertically mounted stainless steel tube 1.4 *m* in length with an internal diameter of 25.4 *mm*. The bullet was fired, by a 0.22-*in*. calibre rifle, at a piston below the water column. The resulting liquid pulse had a rise time of approximately 50 μs and a decay, after the peak pressure, lasting 300-500 μs. Empirical relations between the viscosities of different liquids and their tensile strength were derived. The relations indicated that liquids with high viscosity are able to withstand greater tensions than those with lower viscosity, as the investigators had expected intuitively. Bull [113], Carlson and Levine [114] and Williams and Williams [96] performed similar experiments using various liquids (water, olive oil, syrup, etc), glycerol and silicon oils respectively and derived similar empirical relations for these liquids. Bull used a B-P method, similar to that of Couzens and Trevena [112], while Williams and Williams [96] used a cylindrical tube (1.4 *m* long, inner diameter of 24 *mm*). In their B-P method, the lower piston was impacted upon by the bolt of a cattle stun gun instead of a bullet. Carlson and Levine employed the cell method and generated incident compression pulses by using a pulsed electron beam generator as described in section 4.1.3 [59,114]. Sedgewick and Trevena [98] found that polyacrylamide solutions with high viscosity had lower tensile strengths that those with lower viscosities. It was thought that this discrepancy might have been due to interactions between polymer molecules.

Sedgewick and Trevena [115] performed B-P experiments using very similar equipment to that of Couzens and Trevena described above. The study illustrated that boiling and deionisation of a water sample increases its tensile strength. Sedgewick and Trevena [98] later extended these B-P experiments with the same equipment and found that the dissolution of polymer additives in deionised water did not affect the cavitation threshold of the solvent noticeably. Overton and Trevena [95] performed B-P experiments using very similar equipment and water as the test liquid. Pressure traces indicated maximum tensions of about –0.45 *MPa*. All of these tubes used were vertically mounted and made of stainless steel tube 1 *m* in length with an internal diameter of 25.4 *mm*. The bullet was fired, by a 0.22-*in*. calibre rifle, at a piston below the liquid column.

When using B-P and similar methods, additional factors, such as the length of the piston, have been found to affect the observed cavitation threshold [116]. Overton and Trevena considered a pulse, initiated by impact of a bullet on a piston, that travels through the piston and reaches the piston face where it is partly transmitted into the liquid and partly reflected back into the piston. The reflected wave is reflected again when it reaches the opposite face of the piston. As a series of such "internal reflections" occur, a succession of compression waves are transmitted into the liquid. It follows that, if the piston is short, then the compression waves will be close together resulting in a higher peak pressure than if the piston is long [95,116].

4.1.3. Pulsed Electron Beam Generator

Carlson and Henry [59,95,117] produced stress waves, by deposition of energy, using a pulsed electron beam generator, into a solid, 2 *mm* thick plate made of composite organic material, adjacent to a liquid sample. These waves were transmitted into the 3 *mm* thick sample of glycerol, and were almost unaffected at the interface due to the similar acoustic impedances of the plate and liquid. The compression waves, which had short durations of about 0.1 μs, were reflected at a 6 μm thick sheet of Mylar film, which acted as a free surface. The cavitation threshold of glycerol was measured as 60.8 *MPa*. Carlson and Levine [114] and later, Carlson [118] extended the experiments using glycerol and mercury as test liquids respectively.

4.1.4. Illustrative Case

Special consideration is now given to a recent study that yielded important information about cavitation: Kedrinskii et al. [35] produced cavitation and investigated the effects of certain factors on the process using the free surface reflection method. Water resulting from a single distillation without any additional purification was tested. The compression waves (typically with rise times of about 1.7 μs and of duration in the order of 3-5 μs) were generated by an electromagnetic acoustic emitter as described in [51].

High speed filming showed that there were significant differences between the dynamics and intensity of cavitation near the free surface and at greater depths. When experiments

were performed immediately after the liquid samples were placed, the cavitation bubbles were uniformly distributed over the cavitation zone. However, when a sample was left to settle for one hour before being tested, a dense, localised layer of bubbles formed approximately 3 *mm* below the free surface. These differences in cavity formation are depicted in figure 4.2. This effect of the time of contact of liquid with the atmosphere was attributed to the layer of liquid near the free surface becoming saturated with air. This probably increased the concentration and initial, equilibrium radii of the cavitation nuclei. Thus, while leaving water to settle allows free bubble nuclei to escape or dissolve as discussed in section 3.2.1.4, the amount of cavitation nuclei may actually increase.

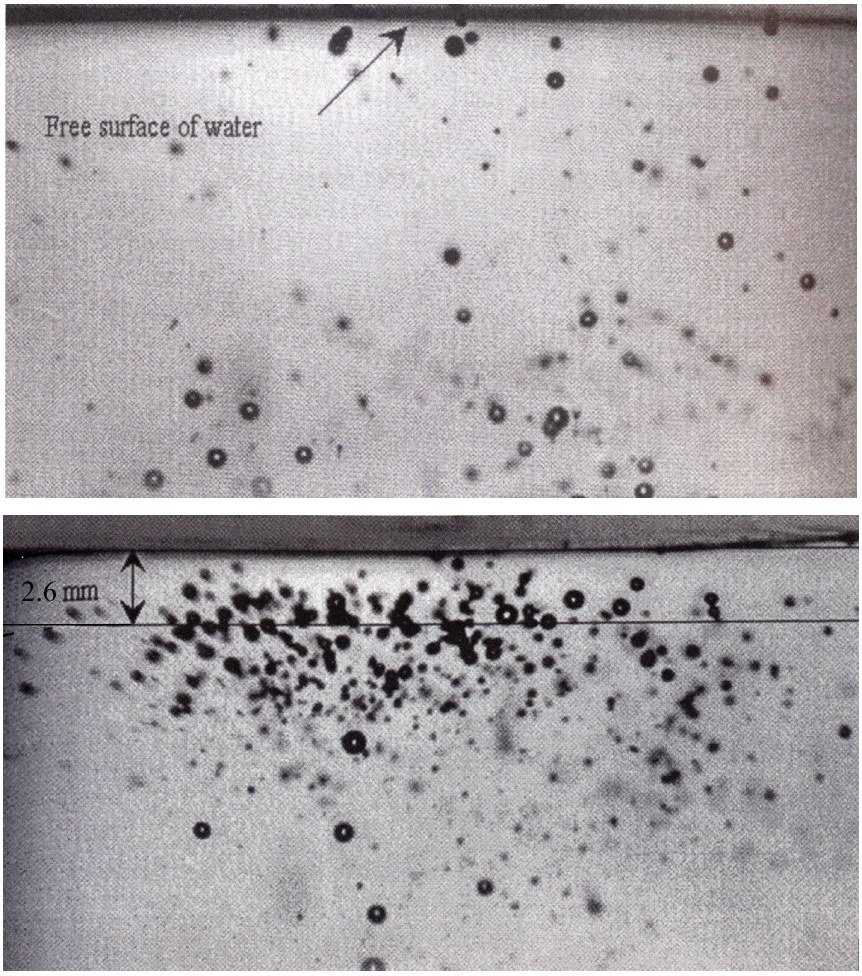


Figure 4.2. Photographs of cavity clusters that developed in distilled water samples tested immediately (upper frame) and one hour after (lower frame) being placed into a cuvette [35].

The light scattering method showed that the cavitation zone reached a state where approximately 50 bubbles per cubic centimeter were present with bubble diameters ranging from 70 to 170 μm (average ~130). Using light absorption and capacitance methods simultaneously, the threshold of cavitation inception of distilled water was determined as between –2.7 and -2.9 *MPa*. Compression pulses with pressures of about 2.9 *MPa* had to be generated in order to produce cavitation.

4.1.5. Intense Cavitation

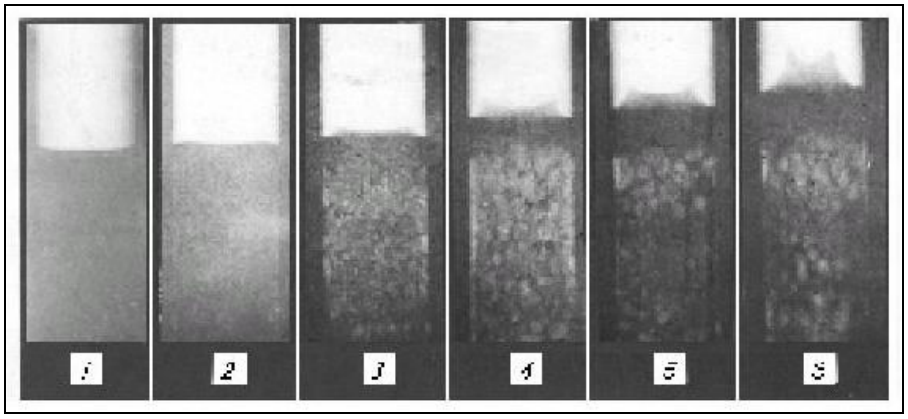


Figure 4.3. Sequence of x-ray frames (time between frames is 200 μs) of cavitation zone dynamics resulting from shock wave reflection at a free surface.

Under intense tensile stresses, cavitation is characterised by practically unbounded, inertial growth of bubbles [38]. On a larger scale, intense cavitation, or "cavitation destruction", involves large scale change of state by unlimited development of clusters of bubbles, until the liquid is transformed into a foam type structure [36], followed by (disintegration) fracture into cavitating fragments [80] and then transition into a gas droplet phase state [36]. A complete inversion of the two phase state of liquids occurs [7,106]: The initial liquid medium, containing a dispersed gas phase (gas bubble nuclei) is converted, ultimately, into a gas medium containing the dispersed liquid phase (droplets). A suitable mathematical model (the "frozen" field model), for describing the late stages of intense cavitation resulting from unbounded growth of bubbles, has only

recently been developed [119,120]. Kedrinskii performed pulse-reflection experiments using shock tubes to illustrate intense cavitation.

In one case, a shock wave was generated in the liquid by the impact of a piston [38]. The use of three x-ray apparatus, triggered by pressure gauge signals, with different time delays, allowed ultra-high-speed x-ray pictures to be obtained. Computer processing allowed the internal structure of the opaque cavitation zone to be determined as shown in figure 4.3.

Kedrinskii et al. [37,38,121] performed novel experiments to investigate the inversion of two-phase liquid to states (transition from a bubbly liquid to a gas droplet structure). A drop of distilled water, only about 1 *cm* wide [37,38], or a drop of viscous liquid, such as a gum-resin-acetone solution [121] was placed on the diaphragm of an electromagnetic shock tube. The shock tube generated a 5-6 *MPa* short (3-4 μs long) shock wave, which impacted the diaphragm. The shock waves were transmitted into and reflected from the free surface of the drop, resulting in negative pressure and cavitation (mainly in the central region of the drop). The liquid underwent a process of transformation from liquid to a foam or mesh type structure as shown in figure 4.4.

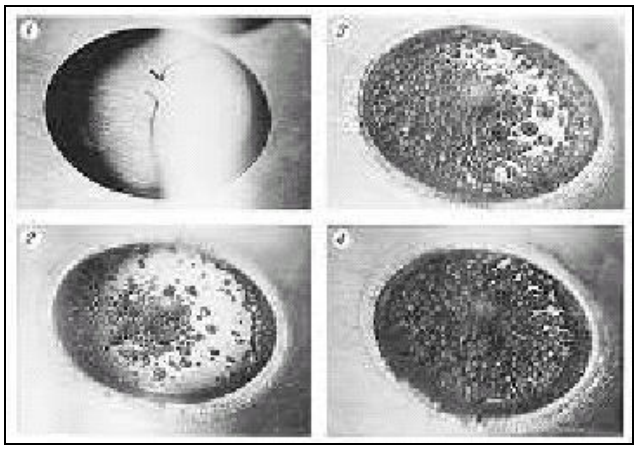


Figure 4.4. Process of Intense Cavitation in a Liquid Drop for times 0, 50,60,70 μs [121].

4.2. Tube Arrest Methods

Tube arrest or "cavitation tube" methods involve impact resulting in downward acceleration of the solid boundary at the bottom of the column. The inertia of the liquid caused it to continue its upward motion, resulting in a tension wave. The wave was first thought to originate at the bottom of the column and travel upwards [87,95,122,123,124] because cavitation usually occurs near the base [125]. However, studies [125,126] have shown that, in fact, the tension pulse originates from the top of the liquid column and travels downwards as assumed in [127]. Cavitation tends to appear at the base because the tension at the base increases momentarily after the pulse is reflected, resulting in cavitation in the vicinity as confirmed by photographs [125]. The tension wave arises from continuing upward motion of the free surface [125].

Chesterton [87,95] performed experiments using a "tube arrest method". His apparatus consisted of a vertically mounted glass tube, half-filled with water. The tube was pulled down against tensioned supports and then released. This caused it to accelerate upwards, over about 50 *mm*, before being stopped by a rubber buffer. At this buffer, the tube accelerated downwards at a rapid rate. High-speed photographs showed cycles of cavitation growth and collapse. Overton and Trevena [95], and, more recently, Williams et al. [126,127] performed similar experiments. Chesterman [87], Overton and Trevena [95] and [127] used glass, Perspex and polycarbonate tubes, with similar internal diameters of 25.4, 11.5 and 21 *mm*, respectively. All of the tubes were 1 *m* long. In some experiments, Chesterman used a square (15×15 *mm*) Perspex tube [87].

Chesterton [87] could vary the tube velocity at impact between 2 and 6 $m.s^{-1}$. He tested distilled water and acetone solutions. He found that repeated stressing caused a decrease in tensile strength: In his tube arrest experiments, initial repeated tests (referred to as "priming") were required before cavitation occurred in acetone solutions and carbon tetrachloride, while the number of cavities that formed apparently increased with the number of tests performed. Chesterman showed that a single, isolated bubble could be produced and analysed. This was achieved, firstly, by suitable control of the number and type of "priming" tests run and, secondly, by close-up photography and special negative

processing. This illustrates the value of the tube arrest method in that a single cavity can be studied.

Overton et al. [95,122] also used water as the test liquid. By varying the height through which the tube traveled before being arrested, they varied the magnitude of the tension pulse generated. Overton and Trevena measured tension pulses in the order of -0.15 *MPa* [95]. High-speed photography showed that a small cluster of bubbles formed 1-2 *cm* above the base of the tube. Overton et al. later extended this method [122] and investigated other liquids.

Williams et al. [124-127] used water that had been subjected to filtration and "nuclear grade" deionisation processes. The full experimental details regarding the experimental equipment and methods of Williams et al. are given in [124-127] (reference [128] details older equipment). The impact velocity of the tube was about 5 $m.s^{-1}$ in [126]. Earlier work [123,124] on the problem was focused on explaining effects of secondary pressures waves, which limited the usefulness of the method [123], as discussed later. More recent work [125,126] was more focused on the study of the effect of cavitation bubble collapse and may contribute significantly to the assessment of the safety and effectiveness of low-frequency ultrasound. One conclusion of this recent work was that shocks resulting from cavitation bubble collapse and rebound may be reflected at a free surface, resulting in a tension wave that may cause further cavitation [126] as supported by photographic records. The characteristic times of these waves are similar to those arising in biomedical applications. Williams et al. [124] built a separate rig and confirmed that tensions pulses could propagate further cavitation, the extent of which was also investigated.

In other experiments [125,126], an air bubble was introduced through a metered syringe, such that it rested below the free surface. The tube arrest method was subsequently employed, thereby generating cavitation at the lower end of the tube. When those bubbles collapsed, a shock wave was initiated, which then traveled upwards and impinged upon the bubble near the surface. Collapse of this bubble produced a liquid jet in the direction of the free surface. Such experiments have been performed in water [126], and motor

lubricants [125]. The results were confirmed by video images and pressure records [125,126]. In water, a liquid jet produced in this way extended about 1 *cm* above the free surface. In the lubricants, the liquid jet pierced a latex membrane stretched across the top of the tube. This collapse behaviour near a free surface is similar to the that of bubbles near flexible membranes or solid surfaces coated with an elastomer (see references in [125]) and thus warrants further consideration.

Williams et al. also used the tube arrest method to find the tensile strength of water [126, 127]. Tension pulses with stressing rates of about 10 $bar.\mu s^{-1}$ were produced. Sometimes, one or more isolated cavities were visible at the base of the tube. On other occasions, bubbles formed both within the body of the liquid and at the tube walls and base. The experimenters used pressure transducers indirectly, by determining the speed of the initial tension pulse, from which the associated pressure changes were calculated. The calculation method is detailed in [125,126,127]. The mean value yielded a value of 62.5 *MPa* for the tensile strength of water.

Lackmé [59,95,129] created an upward-travelling expansion pulse by fixing a metal plate to the bottom of a vertical bar, which supported a column of liquid above it, and dropping a weight to fall on the plate. This method is similar to the tube-arrest method. The column of liquid was contained in a tube with an internal diameter of 2 *cm* and a length of 40 *mm*. The duration of the tension pulses were about 100 μs and could be varied by changing the height of the fall of the weight. The water column could be subjected to tension waves of up to -0.5 *MPa*. This method is relatively unexplored.

Another experiment involving downward acceleration of a tube was performed by Hansson et al. [130]. They used a rectangular (12×18 *mm*) tube, supported by a spring. Impact of a mass on the upper end of the tube resulted in downward acceleration for a few hundred microseconds. For large accelerations, cavitation occurs, as illustrated in figure 4.5. This case is analysed theoretically in [36,37,38,80,92,106,130].

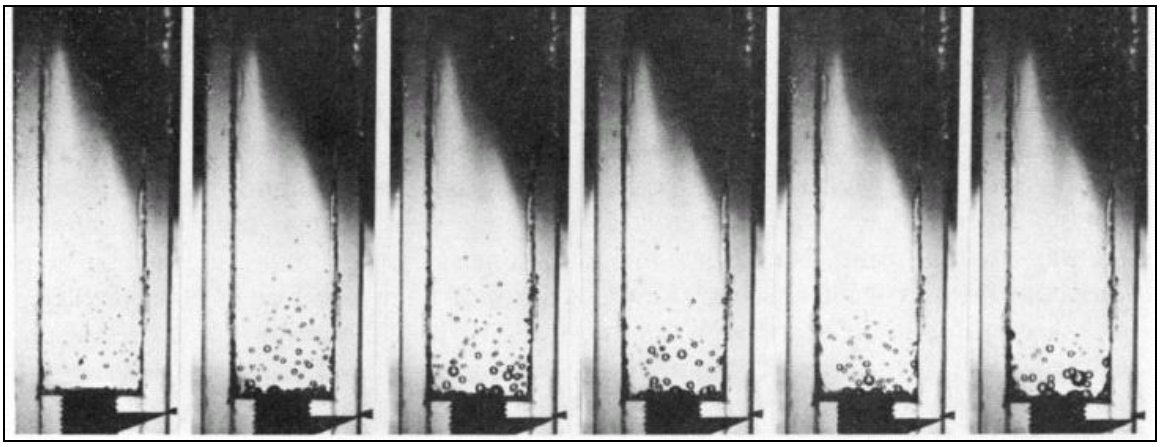


Figure 4.5. Cavitation development in a tube due to downward acceleration of $1.59\times10^4\ m.s^{-2}$. Time between each picture is effectively 50 μs [130].

4.3. Hydrodynamic Shock Tube Methods

Fujikawa and Akamatsu [93,94] employed a more simple method to study cavitation. Their equipment consisted of a hydrodynamic shock tube made up of a 1.8 *m* long, gas-filled driven section above a 2.2 *m* long driver section, filled with water to a height of 2*m*. Their aim was to observe bubble growth and collapse (due to shocks) and dependencies on the initial gas pressure p_{Go} within the bubbles and the distance from the from tube walls to the bubbles and to investigate the mechanism of violent impact leading to damage to walls.

The expansion fan impinged on the free surface of the liquid and was transmitted into it, thereby initiating bubble growth. The rarefaction wave transmitted into the water was also reflected at the bottom, increasing the magnitude of the tension further. The expansion waves were subsequently reflected from the free surface as downward-travelling shocks, which initiated bubble collapse.

The driver section was filled with a helium-air (ratio of 60 to 40) mixture pressurised to 2.64 *atm* while the driven section was left at atmospheric pressure (air at 1 *atm*). This allowed a small negative absolute pressure of –0.46 *atm* to be generated in the liquid behind the expansion wave reflected from the bottom of the tube. Hydrogen-filled

bubbles, with radii R_o equal to 0.14 *mm*, were generated by electrolysis, using platinum electrodes, to make collapse phenomena more readily visible (refer to [93] for details). The initiation of the bubbles was synchronised with the electro-magnetically actuated diaphragm burst mechanism such that the expansion waves and bubbles reached the test section at the same time.

The bubbles expanded and reached a size of $R = 1$ *mm*. Pressure traces showed that the jet impingement was undetectable while the violent impacts due to shock waves from rebound were detectable regardless of whether the collapsing bubble was spherical or asymmetric. The compression pulses from collapsing cavities had durations of about $1\mu s$.

During explosive eruption of a volcano through a vent, magma, which has high gas content, propagates towards the earth's surface while dissolved gases contained therein come out of solution. Once the magma reaches the earth's surface, the degassing may become explosive, with the final result being total fragmentation into discrete particles. Explosive volcanic eruptions (of liquid magma, ash, etc.) are often driven largely due to rapid fragmentation [131], which is often a major factor in determining the intensity of the eruption [132]. The process is essentially a wave process where an expansion fan, centred at the vent, propagates through the magma, accelerating it towards the surface.

Sturtevant et al. [133] performed experiments using a shock tube technique in which the magma was simulated by superheated, volatile refrigerant R12 and R114 liquids. The liquid was placed in the high-pressure section driver section. The refrigerant R12 was pressurised to 5.69 *bar*, which is slightly above the saturation pressure at 20°C. The driven section was evacuated. When the diaphragm was ruptured, rapid decompression occurred as tensile stresses were applied. Figure 4.6 is a photograph of the refrigerant R12 liquid in the test section during an experiment. The liquid level was initially at the 8*cm* mark. The photograph shows that the combination of superheat and low pressure had caused the liquid to cavitate or boil intensely forming a two-phase bubble mass above the liquid (appears dark due to backlighting). Such an expansion wave, which results in explosive vaporisation, is referred to as an evaporation wave.

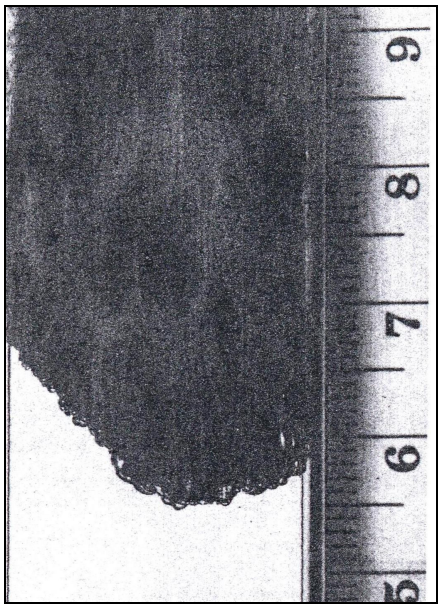


Figure 4.6. Side view of test section, showing the result of propagation of a evaporation wave through a superheated refrigerant sample [133].

Alidibirov and Dingwell [132] used the same explosive degassing technique, but performed the experiments on actual magma samples at high temperatures.

4.4. Ultrasonic **and Wave-Focussing Methods**

Ultrasonic methods usually involve a transducer that passes a high-frequency wave through a liquid, thereby subjecting it to a compression and tension during the positive and negative half-periods of each pressure cycle respectively. For sufficiently high wave amplitudes, a bubble will grow during negative half-cycles and collapse during the compressional half-cycles [59]. These methods are not discussed in detail. It has been suggested that these methods are not strictly relevant in measuring cavitation thresholds due to the effects of rectified diffusion, which makes comparison with other methods difficult [76]. Rectified diffusion implies that periodic pressure variations will, in the long term, encourage gas to diffuse into the bubble and should decrease the observed tensile strength [134]. Ultrasonic methods generally yield low cavitation threshold values ranging from about -1 *bar* (gassy water) to -20 *bar* (degassed water) [107].

Negative pressures and/or cavitation may be achieved in liquids by focusing sound waves generated by a *hemispherical ultrasonic transducer*. Tensions occur during the negative part of the pressure swing at the acoustic focus. Importantly, such experiments usually produce homogeneous cavitation as the acoustic focus is far from walls. Experiments of this nature are discussed in [34,40,88,135,136]. For example, Arora et al. [34] used a piezoelectric shock wave generator (a modified version of a commercial extracorporeal lithotripter) to focus strong shock waves at the liquid sample at its acoustic focus. The pressure record at the focus showed a shock with a peak pressure of about 24 *MPa*, followed by a large negative pressure phase, where absolute negative pressures as low as -7 *MPa* were produced in filtered, deionised and degassed (the concentration of oxygen impurities was 3.3 *mg* per litre of liquid) water.

Müller [54] generated weak spherical shock waves in water by underwater spark discharge. The shock waves were focussed when reflected at ellipsoidal reflectors resulting in pressure rises of up to 130 *MPa* at the focal "spot". In every experiment, shadowgraph images showed a diffracted wave, generated at the reflector edge and small cavitation bubbles that appeared in the focus region. On collapsing a few microseconds later small, intensive, spherical shocks were generated and micro liquid jets formed in the direction of boundaries. In the focal region a complete chain of bubbles collapsed almost simultaneously, forming a new pressure distribution and an envelope of shock fronts, which were visible on the shadowgraph image, as a dark ring. Such focussed shocks, produced by half-ellipsoid reflectors, are applied in the medical field, in fracturing kidney stones. Using the same experimental method and soft reflectors (made of polyurethane foam), which act like a water-air free surface due to their very low acoustic impedance, Müller generated converging expansion waves, thereby producing negative pressures up to –9 *MPa* in deionised, degassed water before cavitation occurred.

A study by Bailey et al. [27] also shows the effect of such soft reflectors. They used a Dornier HM-3 type lithotripter with rigid and *pressure-release* (i.e. soft) reflectors. The intensity and destructive potential of cavitation produced was measured by the sizes of

pits in aluminium foil detectors and by the amplitude of shocks emitted at collapse. Cavitation was detected by passive acoustic and high-speed photography methods. The pressure release reflectors practically eliminated tissue damage in pig kidneys, which were evident in experiments using the rigid reflectors. However, the pulses produced by the pressure-release reflectors were ineffective in stone comminution. These effects were attributed to cavitation of relatively low intensity occurring due to stifling of bubble growth by the positive pressure peak following the negative pressure. In contrast, the rigid reflector waveforms caused cavitation of duration 50 times that resulting from the pressure release reflectors. The cavitation intensity was at least 3 times larger.

4.5. Gas Nuclei Studies

Studies have shown the effects of pressurisation, evacuation and repeated stressing on the tensile strength of liquid samples.

4.5.1. The Effect of Precompression

As mentioned earlier, studies have been made to compare the characteristics of pressurised and unpressurised samples of water. Harvey et al. [85,137-139], Knapp [140] and Briggs [141] subjected samples of water to high hydrostatic pressure and then determined their tensile strengths using various methods. Firstly, they measured the saturation temperature of the liquid at atmospheric pressure and the corresponding saturation pressure. The effective tensile strength was calculated as the difference between the saturation pressure corresponding to the previously measured saturation temperature (from saturated steam tables) and the saturation pressure corresponding to the local atmospheric temperature. Harvey neglected the latter pressure as it is close to zero. This process was not true cavitation, but rather boiling, as it was caused by temperature increase and not pressure decrease. Kenrick et al. [142] and Winterton [77] have performed similar superheating experiments.

In all of the experiments of Harvey et al. [137-9], unpressurised water samples, containing undissolved air, boiled within a few degrees of the saturation temperature at

the relevant atmospheric pressure. This corresponds to cavitation occurring at or near the vapour pressure and implies that the samples were found to be unable to sustain significant tensions. However, after being pressurised, all samples boiled at considerably higher temperatures when tested at the same pressures (corresponding to higher effective negative pressures). Calculations showed that pre-pressurised liquid samples exhibited substantial, effective tensile strengths. Since pressurisation could not have affected the total gas content of the system, the high-pressure treatment must have forced the initial gas bubbles into solution [2]. This effect increased with the level of pressurisation but appeared to reach an upper limit of about 13-20 *MPa*, above which the tensile strength could not be increased. Briggs achieved similar results. Trevena [143] and Winterton [77] discussed the effect of precompression in detail.

Harvey et al., Briggs and, more recently, Knapp and Winterton found that even when samples were treated and handled in the same way throughout, the observed boiling point showed wide scatter. In Knapp's experiments on pressurised samples, the boiling point values varied from 127-227ºC, corresponding to maximum tensions of about -2.5 *bar* and -2.6 *MPa* and respectively. Harvey measured a maximum temperature corresponding to a tensile strength of 1.6 *MPa* while Briggs (264-267ºC) calculated values of between -4.9 and -5.2 *MPa* using water, contained in tubes with bore diameters in the range 0.2 - 0.5 *mm*, which had previously been boiled. Such scatter in fact, validates the stabilisation model of Harvey et al. [85], which implies that the physical characteristics of the hosts (interstices) are uncontrolled, vary widely and respond differently to pressurisation [2] such that pressurisation reduces the size of nuclei but may not remove all of them. Thus, the model implies that observed boiling points and tensile strengths are expected to show scatter since they are determined by the nuclei remaining after pressurisation, which is a random function of the heterogeneities in the liquid e.g. If one particle has, by chance, a satisfactorily shaped crack, it may act as a nucleus that will resist dissolution of free gas, even after pressurisation [2]. Variations, in the contact angles of interstices, of even a few degrees can significantly affect the pressure at which nucleation occurs [77]. The scatter of the experimental results provides further verification of the model of Harvey et al. over the organic skin model, which predicts more regular characteristics [2].

Harvey [139] also produced true cavitation dynamically, by rapid withdrawal of a square ended rod from a liquid. The rod was inserted into a liquid sample and pressurised to remove free gas from its surface before being withdrawn at speeds of up to about 37 $m.s^{-1}$ by means of a spring bow. The unpressurised samples showed cavitation at the end of the rod during withdrawal while the treated samples did not. Knapp [2] made the same conclusion from experiments involving hydrodynamic cavitation in a Venturi tube.

Iyengar and Richardson [144] and Hayward [145,146] have also shown the effect of precompression. The former used a transducer to initiate cavitation in degassed water, tap water and seawater. The voltage across the transducer required to induce cavitation was found to increase (i.e. the tensile strength increased) when pressures of 7 and 20 *bar* were applied to the liquid samples [144] until an upper limit of maximum tensile strength was reached after about 25 and 60 *s* respectively. Winterton [77] built three rigs for boiling point and cavitation threshold measurements in distilled water. In one rig, the lower end of a vertical tube was exposed to a reservoir and a vacuum pump, allowing tensions of up to –0.74 *bar* to be obtained at the top of the tube, 7.5 *m* above the water level in the reservoir. In one series of tests, deactivation pressures of up to 5 *bar* for 30 minutes yielded no effect, while other tests showed increased boiling points or cavitation thresholds with greater precompression until upper limits approached asymptotically. In one set of experiments, the boiling point appeared to decrease with increasing "dissolved air content". This is at variance with the earlier statements that dissolved gas content does not affect cavitation thresholds. Thus, either dissolved gas does actually have an effect on tensile strength, or the manner in which the dissolved gas content was increased (by exposing the liquid to gas in a reservoir) may have introduced undissolved gas content.

4.5.2. The Effect of Evacuation

Rather than converting undissolved gas bubbles into a form (dissolved) less likely to act as cavitation nuclei, undissolved gas may be removed completely from a liquid. Overton et al. [122] studied the effect of reducing the amount of entrained gas, trapped in crevices at solid boundaries, by evacuating the liquid using a vacuum pump before transferring it

to the test chamber of the aforementioned tube arrest apparatus. This degassing was found to raise the cavitation threshold, measured under dynamic conditions, by a factor of about 2 (refer to appendix H, table H.2). A better alternative would have been to evacuate the tube with the liquid *in situ* as some air is entrained during filling [122]. Jones et al. [147] and Overton et al. [148] studied the effects of degassing, using Berthelot tube methods. Jones et al. showed that the tensile strength of distilled water (recorded as 3.5 *MPa*) could be increased to 4.7 *MPa* by evacuating samples prior to testing. Overton et al. used deionised water as the test liquid. Samples were degassed, by repeated evacuation, in a separate, sealed vessel before being transferred to a Berthelot tube. Between degassing and sealing of the Berthelot tube, the liquid was exposed to the atmosphere for less than 2 minutes to minimise air content. The breaking tensions of the samples varied greatly between -3.0 and -6.9 *MPa* although most of samples cavitated in the upper range of -4.6 to –6.9 *MPa*.

4.5.3. Repeated Cavitation in a Single Sample

Ohde and Tanzawa [149] studied the effects of repeated cavitation in water-filled Berthelot tubes. The cavitation strength of degassed water, though widely scattered, was found to increase gradually with the number times it was stressed. It was also found that degassing of the metal container was needed to achieve negative pressures below –10 *MPa* (-17 *MPa* was achieved in water, but only after several thousands stressings showing widely scattered negative pressures). Again, the wide scatter was attributed, largely, to uncontrollable randomness of gaseous nuclei on the tube wall. The effect of repeated cavitation has also been studied by Sedgewick and Trevena [98,115]. They found, using Berthelot tube methods, that polymer solutions had to be recycled a few times before being able to sustain any tension [98]. In addition, as tests, using the B-P method, were repeated, the tensile strengths of water and polymer solutions rose by 20 [115] to 30% [98] respectively before levelling off at final values. In [115], tests were repeated every 3 minutes, the minimum for their apparatus [143]. After about 12 repeated tests, the tensile strength of a sample of ordinary tap water increased from 9.0 to 11.0 *bar*. When this sample was left to settle for 24 hours and tested again, its tensile strength was approximately 9.8 *bar* [115]. The progressively higher tensile strength recorded as the

liquid is repeatedly tested is attributed to the exhaustion of cavitation nuclei on the tube wall [149] i.e. some of the bubble nuclei in the water are removed (rise and disappear into the atmosphere) in each successive test [115]. The influence of cavitation history has also been studied in [122,128] and is discussed further in [143]. Overton et al. [122] performed tube arrest experiments on many liquids, including seawater, deionised water, tap water and Jet A-1 fuel. Many series of tests were performed, with intervals between each test varied between 15 seconds and 5 minutes. Since the cavitation threshold is dependant on the time interval, it is also dependant on the frequency of testing: a higher frequency of stressing (i.e. shorter time interval between each shot) leads to a lower tensile strength because it gives less time for the nuclei to escape completely [122]. Alternatively, as the frequency increases, the recovery between shots decreases [143].

4.5.4. The Initial State of Samples of Liquid Water

Various studies of the initial state of liquid samples have been performed. These include the investigations of [150-154] and [38]. Experimentally determined and typical values of the radii of free gas bubbles, the initial number of bubbles per unit volume and the volume concentration of the gas phase in treated and untreated water samples is shown in appendix I.

4.6. Solid Nuclei Studies

Parametric studies of relations between tensile strength and the characteristics of nucleation sites in solid particles and walls are difficult because natural particles are of irregular, random shape [39]. To investigate the role of the surface structure and particle size of solid nuclei on cavitation inception, while eliminating doubts concerning the size, shape and texture of solid nuclei, Arora et al. [34] and Marschall et al. [39] deliberately seeded samples of water with spherical particles with known characteristics. Marschall used a circulating water system, with a ‘vortex-flow’ nozzle, to study the cavitation process, while Arora et al. used a shock wave generator (as mentioned in section 4.4).

Marschall et al. [39] seeded filtered, degassed (to about 0.2 *bar*) tap water, which had initial particle sizes of less than 1 μm (larger particles were filtered out), with solid balls

with radii between 1.5 and 38 μm. They detected cavitation by using an acoustic and a light scattering method. Seeding of the liquid with the smallest spheres of radius 1.5 μm did not result in a measurable decrease in the tensile strength even though they were hydrophobic and distinctly larger than the natural nuclei remaining after filtration. It was concluded that a liquid containing near spherical solid nuclei has a greater tensile strength than one containing natural particles of the same size i.e. the irregular shape of natural particles contributes significantly to their role as nuclei. The addition of spheres much larger than the natural nuclei (10-40 μm in size) reduced the tensile strength by only between one and two thirds of that measured for the unseeded water. The fact that the cavities that developed on these larger balls were much smaller than the balls themselves validates the hypothesis that the suitability of particles as cavitation nuclei depends on their fine scale surface. Since Marshall et al. [39] found that even very smooth particles can reduce the tensile strength of a liquid, the experiments confirmed the effect of the size of solid nuclei [34].

Arora et al. used filtered, deionised and degassed water (initial maximum bubble radius was thought to be in the order of 50 *nm*) as their test fluid. The liquid was placed in a flask and seeded with hydrophilic, polystyrol particles, with radii between 30 and 150 μm, and density of 1.07 $kg.m^{-3}$. Initials test using globally spherical particles were found to yield no noticeable effect on the tensile stress and, in fact, no cavity formed on them, even for the highest device settings. This is in conflict with the findings of Marschall et al. [39]. Pictures of explosive bubble growth on particle surfaces, which was found to occur at tensions of about –2.8 *MPa*, were captured using a sensitive camera, equipped with a long distance microscope. They showed that the growing bubbles accelerated the solid particles, on which they formed, into translatory motion. This effect might be applied in the acceleration of microscopic and nanoscopic particles as noted in section 1.4.

Free bubbles may also be deliberately introduced into the liquid by electric sparks, electrolysis or by energy deposition using a laser [93]. Electrons, which may act as

cavitation nuclei, may be deliberately introduced into a liquid by a radioactive source and discharged through a metal tip. This is useful for studying heterogeneous cavitation [88].

4.7. Cavitation Thresholds

Appendix H provides a summary of many cavitation threshold values determined by different methods. It is evident that, in general, the experimental values and the theoretical values in section 3.2 differ greatly. Threshold values close to the homogeneous nucleation pressure have only been obtained in inclusions in minerals such as quartz, calcite, fluorite due to the small volumes involved, which minimises the probability of nuclei being present. For example, water was superheated up to more than 300°C in inclusions, but only up to about 270°C in laboratory tubes (refer to table H.5).

Discrepancies between values from dynamic and static experiments are evident e.g. Sedgewick and Trevena demonstrated tensile strengths of deionised water samples of 1.0 *MPa* and 2.23 *MPa* (mean value) using dynamic (B-P) and static (Berthelot tubes) methods respectively [98,115]. The tables in appendix H show that the cavitation thresholds determined using static methods are, in general, greater than those determined using dynamic methods, for liquids of comparable purity.

The differences in threshold values may be attributed, largely, to variations in the purity of test liquids and their containers, differences in the rate of stressing and, in the case of, pulse reflection experiments, the nature of free surfaces. The first factor has been discussed in this chapter and accounts for the wide scatter, as explained earlier (sections 3.2.2 and 4.5.1). The threshold data is essentially different and depends on both the state of the liquid and the dynamic of tensile loading.

4.7.1. Liquid Purity

Firstly, it should be noted that it is highly unlikely that different investigators will utilise liquid samples purified (distilled, filtered and/or deionised) to the same degree [35]. The effect of liquid purity is illustrated in the summary of threshold values obtained by centrifugal stressing methods, table H.4: Threshold values obtained for degassed/distilled

water are an order of magnitude greater than those obtained for tap water. The difference appears less marked in other cases. The significantly higher threshold values (relative to values from similar experiments) obtained by Williams et al. [125-7] were obtained using heavily purified water. Samples were processed by a two-stage, reverse osmosis, ion-exchange purification system with a activated carbon filter for organics, a 'nuclear grade' deionisation stage that reduced trace metal contamination to under part per billion levels and a final 0.2 μm membrane filter [96, 124-127]. Photographic evidence and tension wave velocity measurements indicated that cavitation occurred within the body of the liquid in these experiments. This accounts, partly, for the relatively high cavitation threshold determined in these experiments [127].

4.7.2. Rate of Stressing

Firstly, it should be noted that all stages of cavitation are characterised by the relaxation of tensile stresses [38]: The appearance of clusters of bubbles interrupts the continuity of the liquid phase [2] i.e. the homogeneity of the liquid is altered. Thus, in acoustic cavitation the rarefaction waves are quickly absorbed [80] or extinguished [55] by the gas-filled bubbles (note again that the pressure of a gas may never be below absolute zero) while further pressure decrease is prevented [55]. This explains why the tension due to rarefaction waves from free surface shock wave reflection, as illustrated in figure 2.6, is not reached: the negative pressure phase is immediately distorted [35] and the tension is relieved [7]. Thus, cavitation alters the applied pressure field that caused it [106].

The profile of a rarefaction wave is continuous and peaks after a finite time denoted by t^*. The stress rate affects the observed tensile strength as during the rise time (the period $t \leq t^*$) of the front, the volume concentration of free gas increases by several orders of magnitude i.e. the state of the medium is changed significantly [36,60]. As explained above, the applied stress field itself is changed by the developing cavitation, resulting in a lower observed tensile strength. If the rise time is instantaneous i.e. the negative pressure is applied instantaneously or for a time during which the cavitation nuclei have not expanded appreciably ($t \approx 0$), then the cavitation threshold is unaffected during the rise time and may reach its maximum value. Once it has reached that maximum value,

cavitation occurs and the tension is relieved. Thus, threshold discrepancies may be due to the rate of stressing of a liquid, which has been found to be an important factor in determining cavitation threshold: For a given liquid, the cavitation threshold increases with increasing stressing rate (i.e. steeper pressure change) [35,96,116,127] e.g. Kedrinskii et al. [35] found that increasing the length of the pressure pulse by a factor of 2 led to a decrease of the observed cavitation threshold by a factor of about 4.

Experiments may be classified as either static or quasi-static (Berthelot tube, superheating and centrifugal methods) or dynamic (pulse reflection, tube-arrest and ultrasonic methods). In B-P experiments, the incident compression and reflected expansion waves typically have durations in the order of a millisecond and have stress rates of up to 1 $atm.\mu s^{-1}$ [76]. The high rate of stressing (10 $bar.\mu s^{-1}$) accounts, partly, for the relatively high tensile strength value (shown in table H.2 determined in the tube-arrest experiments of Williams et al. [127]. Turning attention to the threshold values for Mercury shown in table H.9, the tensile strength value determined by Carlson [118] is higher than that of Williams et al. [125] due to the much higher stressing rate (106 $bar.\mu s^{-1}$) involved in his experiments (achieved using the pulsed electron beam generator method). Williams et al. used the tube arrest method, which resulted in stressing rates of about 1 $bar.\mu s^{-1}$ and led to an observed threshold value of 300 *MPa*, while Carlson achieved a much higher value of 1900 *MPa*, which is comparable to the homogeneous value 2230 *MPa* [72].

In B-P experiments, in order to achieve higher peak pressure in the liquid, bullets of greater mass or greater velocity at impact should be used. It has been shown that the use of bullets with greater momentum results in higher rates of stressing of the compression wave in the liquid (and hence that of the expansion wave that results from free surface reflection), which in turn affect the observed cavitation threshold [116].

The conclusion, based on the arguments above, is that there are no established critical values of the critical tensile stresses causing cavitation in a real liquid, even if the gas content of the liquid is fixed [60].

4.7.3. Transition Layer

Some threshold values for water, determined by Berthelot tube, superheating, centrifugal and tube-arrest methods, are in reasonable agreement with theoretical estimates in the order of tens of megapascals [107,155]. However, in the case of free surface reflection of compression pulses with rise times in the order of a millisecond (i.e. B-P experiments except that of Williams [96]), the highest tensions recorded were less than -4 with no other values exceeding -1.5 *MPa* [59,112]. In Berthelot tube experiments, the tension develops over a period of several minutes, while in dynamic experiments: stress develops over typically, 10^{-6} to 10^{-3} *s* [96,156]. Thus, the rate of stressing cannot account for the low values recorded in pulse reflection studies since the stressing rate is lower in the Berthelot tube case. The apparent discrepancies have been resolved, partly, by considering the nature of free surface reflection [107].

In reality, a free surface or liquid-vapour interface is not of zero thickness. A transition layer, of finite thickness, exists, at a free surface, between the liquid and vapour as discussed in [127,157]. The density decreases with height within the transition layer [107,127,134], as confirmed by x-ray studies [127]. The characteristic thickness of the layer is in the order of 3 intermolecular distances of water surfaces [157]. A pulse can be reflected up and down many times, within the layer, but with decreasing amplitude [134]. This transition layer is thought to be both a source of nucleation for vapour bubbles and is, importantly, a major factor in making the free surface an imperfect reflector [134]. Attenuation and dispersion of pulses within the transition layer results in anomalously low measurements of their amplitude (and hence the cavitation threshold), after reflection and below the layer [126-7]. Thus, pressure transducers cannot measure the tensile strength in such pulse reflection experiments [107,134,155] directly. The effect of the transition layer on incident pulses was illustrated in experiments by Sedgewick and Trevena [74,107,115,134] and Couzens and Trevena [111-112,107]. They found that a pressure pulse is not reflected as a mirror image tension pulse even if the peak pressure is so low that cavitation does not occur and distort the pressure profile. The peak tension is significantly less than the peak positive pressure and is accompanied by distortion of the reflected pulse profile, which was ‘spread’ or ‘drawn out’ [107,134].

Sedgewick and Trevena investigated if the effect of the layer was influenced by the presence of ions or gas and found that the ratio of peak tension to peak positive pressure for tap water was 0.34 while the ratio was 0.36 for deionised water and 0.50 for both boiled tap water and boiled deionised water [74,107]. Thus, the presence of ions may affect the ratio slightly while the presence of dissolved gas definitely and substantially affects the ratio. Couzens and Trevena [107, 111-2] found that the ratio of the magnitude of the peak tension to the peak positive pressure was about 0.5 for boiled, deionised water over a fairly wide range of incident wave peak pressures.

The existence of similar transition layers at solid-liquid interfaces may partly account for cavitation at solid walls as well as the relatively low tensile strength values recorded in pulse reflection experiments using flexible membranes [127]. However, the high tensile strength value obtained by Marston and Unger [158], who used a Mylar membrane for pulse reflection, suggests that solid membranes behave as perfect reflectors of compressive pulses [156]. Thus, the low values obtained by Richards et al. [109] in similar pulse reflection experiments involving Mylar membranes cannot be attributed to transition layers but are, instead, due to the low acquisition rates and rise times of transducers used in their experiments [156].

4.7.4. Measurement of Tensile Strengths

Other differences between threshold data may be attributed to different pressure and force measuring equipment used [2,60,96]. Another important factor has recently been considered. Tensile strength measurements may be underestimated in some cases, due to inadequacies of pressure transducers as shown in [96,124,156]. The transduction equipment used by various researchers [95,109,112,115,122] had an equivalent sampling rate of less than 10 *kHz* and included a transducer with a rise-time of approximately 6 μs. The pressure records resulting from such equipment were deemed inadequate and may underestimate the tensile strength of liquids by as much a factor of 3 [124]. Williams et al. showed that by overcoming the adequacies, low values of tensile strength could be reconciled with higher values of up to about 60 *bar* [96,124].

4.7.5. Overlapping of Tension Pulses

The last factor suggested as a possible cause of discrepancies in the tensile strength is the effect of overlapping of the tension pulse resulting from free surface reflection with the tension pulse reflected from the base of the liquid column, which results in cavitation. It is known that cavitation regions may affect the speeds of waves passing through them such that they may appear to propagate at low speeds tending to the sound speed in water vapour (approximately 494 $m.s^{-1}$) as opposed to the high speeds associated with water [96,124-7,156]. This accounts for some low measured values of the tensile strengths.

5. Experimental Facilities and Methods

Two shock tubes were designed and built for the purpose of achieving low and possibly negative absolute pressures and consequently producing visible cavitation in a liquid. The experimental equipment, and their design, are described in the present sections 5.1 and 5.2, while the procedures of operation are detailed in section 5.3.

The first shock tube was designed to generate flows in which strong expansion waves propagate directly towards and impinge onto a column of water. This shock tube was designed such that the Mach number of a shock wave resulting from diaphragm burst was to be about 3. In the following, it will be referred to as the *Mach 3 shock tube*. The second shock tube was designed to generate shock waves, with conventional gas driver and driven sections, which would impinge on and transmit into a column of water. The transmitted shocks were intended to reflect as expansion waves at the free surface of the liquid, thereby lowering pressures below the ambient, initial value and possibly causing cavitation. In the design case, a shock waves produced in the gas driven section resulting from diaphragm burst were intended to have Mach numbers of about 2 and thus, in the following, it will be referred to as the *Mach 2 shock tube*.

5.1. The Mach 3 Shock Tube

The first shock tube is vertically mounted and clamped, at one place, to a wall, as illustrated in figure 5.1 and the assembly drawing (appendix J), of the tube. As shown, the driver section is situated below the driven section.

Circular steel tubes were used for the driven section and part of the driver section of the tube since they are relatively easy to obtain and rigid and do not introduce stress concentration areas as encountered in square tubes. However, circular tubes are not ideal for accommodating windows (essential in most cavitation studies) and a transition section from circular to square cross-section, which leads to attenuation or modification of waves passing through it [93], is usually required. Instead, a transparent tube was chosen to

facilitate optical observation of the test section. *Polycarbonate* was chosen for its high strength, low water absorption (0.12 % after 24 hours and 0.35 % after equilibrium is reached). Polycarbonate tubes are not as easily obtainable in small quantities as sheets. Polycarbonate is also known by the trade name Makrolon and the tube obtained was a general purpose grade Makrolon 3103. This material has yield and ultimate tensile strengths of 65 and 70 *MPa* respectively [160].

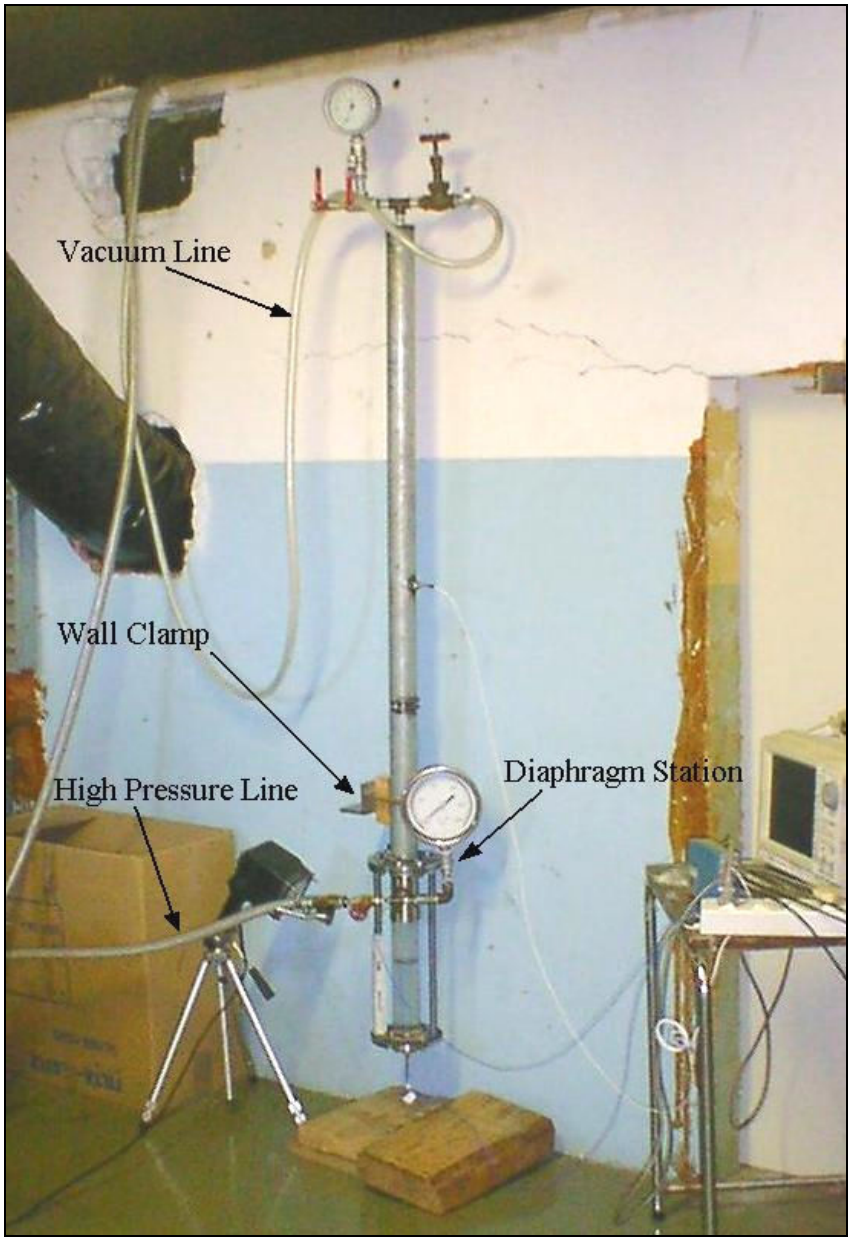


Figure 5.1. Photograph of the "Mach 3" shock tube.

The lower, driver section consists of a flange welded to a pipe with a collar on its other end. The polycarbonate tube, supplied by *Seal Cool Industries cc.*, is tightly clamped between the collar and the base of the shock tube bottom by the flange arrangement at the bottom. Rings, cut from rubber sheets, were clamped at the ends of the polycarbonate tube to prevent leakage.



Figure 5.2. Photograph of the "Mach 3" shock tube test (driver) section.

The upper, driven section consists of a 1.35 *m* long stainless steel tube welded onto a flange. The chamber was designed to allow sufficient time for the expansion waves to travel through the water column and be reflected back upwards through the column before the shock interfered with the low pressures. A single polyurethane diaphragm of thickness 125 microns was used in each test. A diaphragm and a gasket were clamped between the two flanges of the driver and driven sections.

The driver section was designed for adequate static strength, corresponding to the maximum design pressure, while assuming a large safety factor to withstand transient loads, [48] and to withstand the high pressure behind the reflected shock. The polycarbonate tube, the most likely source of failure, could be considered as a thin-walled vessel making the well-known hoop stress relation $\sigma = pr/t$ valid [161]. The tube was designed to withstand a pressure of 1 *MPa* with a safety factor of approximately 6 on the yield strength. In small shock tubes, such as this one, the tube and its supports are not subjected to significant axial, impulsive loads following the diaphragm burst [48]. Thus, the clamping mechanism was only designed, using standard procedure for offset bolt wall mountings [161], to support the static loads of the structure.

5.1.1. Instrumentation

Three PCB (model number 113A21) pressure transducers were installed: two in the shock tube walls of the driver and driven sections and one mounted axially into the bottom of the tube. The piezoelectric pressure transducers used were supplied by *PCB Piezotronics, Inc.* and are designed specifically for use in applications requiring high frequency, near non-resonant response such as shock tubes [162,163]. The transducers consist of quartz slides, an insulator and a metal housing. When the pressure is applied to the quartz crystal sensing elements, they produce an electric charge. By converting the charge to a voltage, the pressure applied to the transducer is known. The sensors were installed into convenient M10×1 thread adaptor housings, which diminished the need for precision machining. A transducer mounting port is illustrated in appendix J. Dimensions and instructions for preparing ports are given in installation drawings in [163]. When considerable leaking occurred through the gap between the housing and transducer, they were effectively sealed using commercially available silicon sealant.

The transducer specifications are given in appendix K. The transducers were connected to the signal conditioners by general purpose, white, coaxial Teflon cable assemblies (series 002) and low-noise, blue, coaxial, Teflon cable assemblies (series 003) of various lengths with 10-32 plugs on either end. The signal output from the signal conditioners was fed

into a high-speed digital oscilloscope. Throughout testing, two oscilloscopes, a Yokogawa DL708E and a Yokogawa DL1200A, were used.

During testing, a pressure gauge calibrated from 0 to 1000 *kPa*, provided by *Kerr Valve and Industrial Supplies (Pty) Ltd*, and a gauge calibrated from –100 to 2400 *kPa*, supplied by *Wika Instruments (Pty) Ltd*, were used. The low pressures at the vacuum pump outlet and in the driven section were measured using two barometrically compensated, Speedivac (type C.G.3) vacuum gauges with dials calibrated 0-40 *Torr* and 0-100 *Torr*, respectively, which read absolute vacuum pressures.

5.1.2. High–pressure and Vacuum Supplies

The driver section high pressure supply was provided by the laboratory compressor (0-80 *psi* gauge), which was charged to about 10 *MPa* before each series of tests. A *Speedivac High Vacuum Pump* manufactured by *Edwards High Vacuum Ltd*. was used to reduce the pressure in the driven section. The pump was a single-stage model (Model number ISC4508, Serial number 3688). Pressures as low as 5 *mm Hg* could be obtained at the vacuum pump outlet.

5.1.3. Flow Visualisation

A Reflecta Flectalux GLX1006 lamp, mounted on a tripod, was used to illuminate the test section. Pictures were recorded using a high-speed camera that was manually triggered. An EG&G Reticon camera, fitted with a 2.8/135 Meyer-Optik Görlitz Orester lens (Serial no. 4095303), was used. The camera's maximum capture rate was 1000 *frames / second*.

5.2. The Mach 2 Shock Tube

The second shock tube is also vertically mounted. It was constructed by modifying the shock tube designed and built by Karnovsky [42] for shock focusing experiments. It consists of a gas driver section at the bottom, a gas driven section in the middle and a

water filled test section at the top. The tube extends across two floors as illustrated in figure 5.3.

The gas driver and driven sections are made of mild steel and has been tested at a pressure of 17200 *kPa*. The driven section used by Karnovsky [42] was modified by adding a diaphragm bursting mechanism (refer to the the drawing of the modified gas driven section in appendix J). In addition, a portion of pipe was cut off the top and a new flange added to accommodate the water-filled test section. A hole had been drilled into the wall, which served as a vent, allowing the high pressure in the shock tube to normalise to atmospheric levels after tests [42]. The driven section was held in place by a clamp bolted onto the adjacent wall and a large steel disc resting on the floor above it. A gasket was clamped in place, below the diaphragms, between the driver and driven section flanges.

The water-filled test section is made of stainless steel and was designed to accommodate polycarbonate (supplied by *Plastic World (Pty) Ltd.*) windows, for optical observation of cavitation, near the top. This section was clamped to the floor to prevent longitudinal and lateral movement of the upper portion of the tube above the bellows units. In order to allow the liquid shock wave to become fully formed before reaching the free surface, the upper section was designed to be as long as possible. The length of the pipe used, limited by space constraints, was 2.1 *m* while the wall thickness was approximately 4 *mm* (the inner and outer diameters were equal to 52.5 and 60.32 *mm* respectively, as specified by the manufacturers). As the initial pressure in the tube was small and equal only to the hydrostatic pressure, it was not designed for static strength. It was designed to withstand a maximum shock wave pressure of 2.5 *MPa* assuming a safety factor of about 10 on the yield stress.

The windows were incorporated by cutting through the top portion and fitting two Polycarbonate sheets in place of the tube walls. Each sheet was fixed in place by 22 M4 bolts, which were intended to ensure adequate pressure along the window edges to ffffffffffffffffffffffffffffffffffff

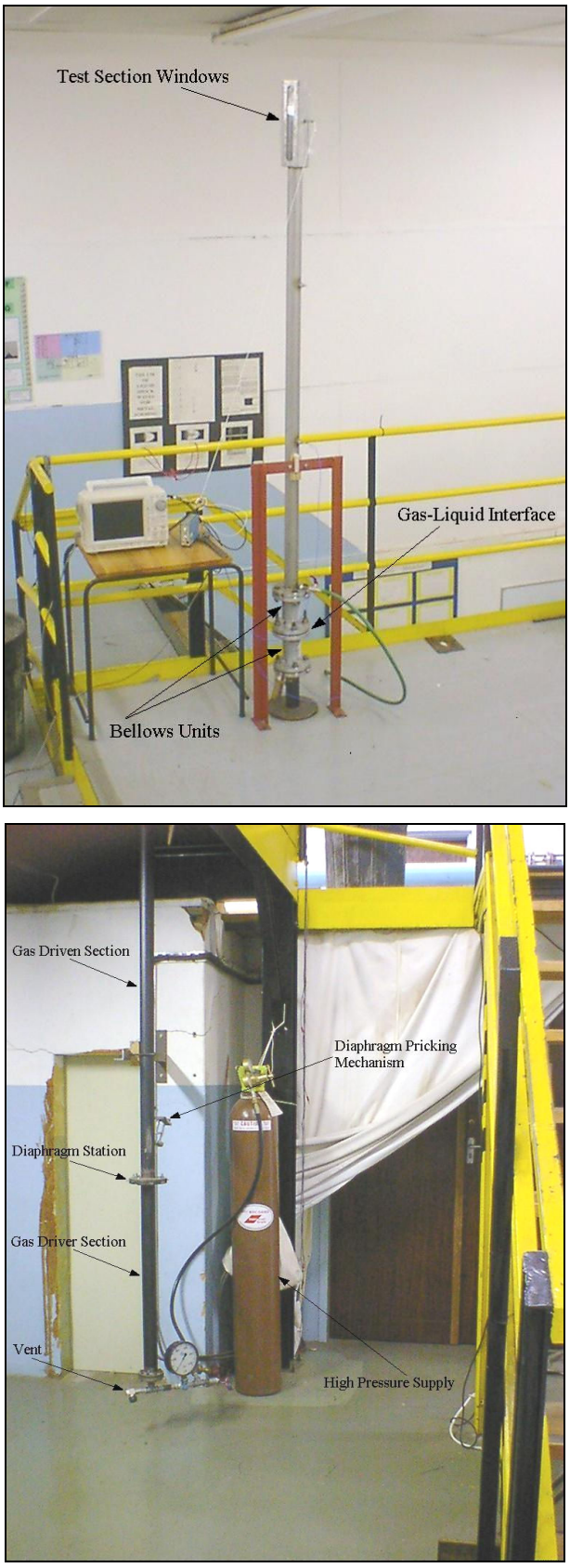


Figure 5.3. Photographs of the "Mach 2" shock tube.

prevent leakage. Assuming a safety factor greater than 5, the windows and associated bolts were designed to withstand shock pressures of up to 2.5 *MPa*.

5.2.1. Instrumentation

Four PCB113A21 pressure transducers were mounted along the tube wall. All transducers and associated power supplies and oscilloscopes used were the same as those used for experiments using the Mach 3 shock tube. Again, their specifications are given in appendix K. The same 0-1000 *kPa* pressure gauge mentioned above was used throughout testing.

5.2.2. The High–Pressure Supply

A Helium cylinder, supplied by *African Oxygen Limited* (AFROX), was used as the high-pressure supply for the driver section. The cylinder contained instrument grade helium with total impurities less than 7 *vpm* (parts per million by volume) pressurised to 20 *MPa*. It was connected to the driver section by a regulator.

5.2.3. The Liquid–Gas Interface

A sheet of water resistant material was used as an interface between the gas driven air section and the column of water in the test section above it. Different materials, namely, stainless steel, polycarbonate (supplied by *Plastic World Pty. Ltd.*), silicon rubber and insertion rubber (supplied by *TRUCO* or *Transvaal Rubber Company Pty. Ltd.*), were used as the interface. It was clamped in place between two single axial bellows units supplied by *Spirax Sarco (Pty) Ltd.*. The bellows (Product code SAF 50-25-40) have a nominal diameter of 50 *mm* and were welded to standard BS4505 stainless steel flanges. Such a bellows unit is usually used as an expansion joint i.e. to absorb dimensional changes for preventing pipe strains from becoming too large. In this case, the bellows were intended to allow the interface to move when struck by the gas shock wave and so transmit shock waves into the liquid.

5.2.4. Diaphragm Bursting Mechanism

The diaphragm bursting mechanism is illustrated in figure 5.4. The needle is pulled away from the diaphragm and held in place by a catch. It is released when the driver section is fully pressurised and diaphragm is to be burst. It was found that the bursting mechanism performed adequately over the entire range of testing pressures.



Figure 5.4. Photograph of the diaphragm bursting mechanism on "Mach 2" shock tube.

5.3. Experimental Procedure

5.3.1. The Mach 3 Shock Tube

The following preparation procedure was done before each series of tests:

1. Switch the PCB line power supplies on at least an hour before commencing a test to allow them to stabilise.
2. Switch on the oscilloscope and check the connections between the transducers, power supplies and the oscilloscope.
3. Check that the vacuum pump has sufficient oil and replenish if necessary.

4. Cut diaphragms such that they will comfortably separate the driver and driven section but allow sufficient space for the bolts.
5. Place the camera approximately 5 to 6 *m* away from the tube, with the lens focussed horizontally, at a portion of the test section.
6. Note the atmospheric pressure

Before each test:

7. Fill the test (driver) section, from the top of the assembled driver section, with approximately 500 *ml* of water.
8. Insert a single 125 micron diaphragm between the compression and expansion chambers above the gasket and tighten the bolts.
9. Ensure that a valve between the compressor supply and driver section and the "vent" valve, are closed. Open the valve between the vacuum pump and driven section.
10. Switch the vacuum pump on and allow it to run (letting the gases achieve thermal equilibrium before burst) until the required driven section pressure obtained. Close the valve between the vacuum pump and driven section.
11. Set the required parameters on the oscilloscope.
12. Start the camera capture program and choose the "acquire" option (the program then waits for the user to press a key to trigger the capturing process).

Then, the following steps were completed during the experiment

13. The compression chamber was charged to a pressure of about 7.5 *bar* by opening the valves from the high pressure supply. This is done slowly enough to allow observation of the burst pressure and to allow the gases to achieve thermal equilibrium.
14. When the pressure gauge of the driver section reaches a value of approximately between 6 and 7 *bar*, press the trigger key on the keyboard, while the pressure rises. This has usually proved to be sufficient for capturing the events within the test section when a frame rate of 1000 frames per second is used.
15. Observe the driver pressure at diaphragm burst

After each test, complete the following steps:

16. Open the vent above the driven section to relieve the high pressure within the tube.
17. Follow the prompts on the computer monitor to view and save the captured frames.
18. Save the oscilloscope traces to floppy disc, the hard drive or print the results directly from the oscilloscope.
19. Process the data, using a suitable program such as Micrsoft Excel.

The quartz crystals of a piezoelectric pressure sensor generate a charge when pressure is applied. The charge eventually leaks to zero, even though the electrical insulation resistance is fairly large, and thus the sensors may only measure dynamic pressure changes. Consequently, oscilloscope readings had to be adjusted to the known pressures in the driver and driven sections (read off the gauges) after being converted to pressures using the calibration gauge factors shown in appendix K, section K.2.

In order to eliminate extraneous effects and thereby increase reproducibility, care must be taken, throughout the experiment, to keep all transducer wires still.

The pressure transducer in the top (driven) chamber was connected to channel 1 of the oscilloscope. The volts per division was set to 500 *mV/div*. Nominally, the trigger level was set to about -150 *mV* based on the middle transducer i.e. data acquisition commenced once the pressure at the transducer, exposed to air above the water column, dropped slightly. The upper and lower pressure transducers mounted in the bottom chamber walls were connected to channels 2 and 3 and set to 1 *V/div* and 2 *V/div* respectively. The time per division (for all channels) was set to 2 *ms/div*.

5.3.2. The Mach 2 Shock Tube

The experimental procedure to be completed before, during and after tests using the Mach 2 shock tube is similar to that of the Mach 3 facility above. It differs in that no vacuum pump is used and that the following additional steps apply:

Before each series of tests,

1. Clamp a plate or sheet of appropriate size, to serve as an interface between the liquid above and the air below, between the bellows units.

Before each test, the upper part of the tube is prepared as follows:

2. After ensuring that the drainage valve is closed, fill the upper test section of the tube, from the top, such that the free surface of the water is visible through the windows and the uppermost transducer is submerged.

The gas driver and driven sections are prepared as follows:

3. Unbolt the driver section.
4. Retract the diaphragm bursting mechanism needle and fix it in place, using the catch.
5. Insert two 125 *micron* thick diaphragms between the compression and expansion chambers, above the gasket, and bolt the sections together.
6. Ensure that the vent valve is closed and that the valve between the driver section and the gauge of that section is open.

During the experiment,

7. Pressurise the driver section slowly, allowing the gas to achieve thermal equilibrium before burst, until the required pressure is reached. Close the high-pressure supply valves.
8. Close the valve between the driver section and the gauge of that section, simply to protect it from transient pressures and moisture.
9. Release the diaphragm bursting needle.

Four pressure transducers were connected to the oscilloscope. The volts per division was set to 1 or 2 *V/div*. The trigger level was set to about +100 *mV* (for a slight pressure rise) based on the transducer in the air driven section. The time per division (for all channels) was usually set to 1 or 2 *ms/div*.

6. Experimental Observations and Results

In this section, the results of tests, in the form of pressure and photographic records is noted. More detailed discussion of these observations is reserved for the next chapters.

6.1. The Mach 3 Shock Tube

6.1.1. Pressure Transducer Records

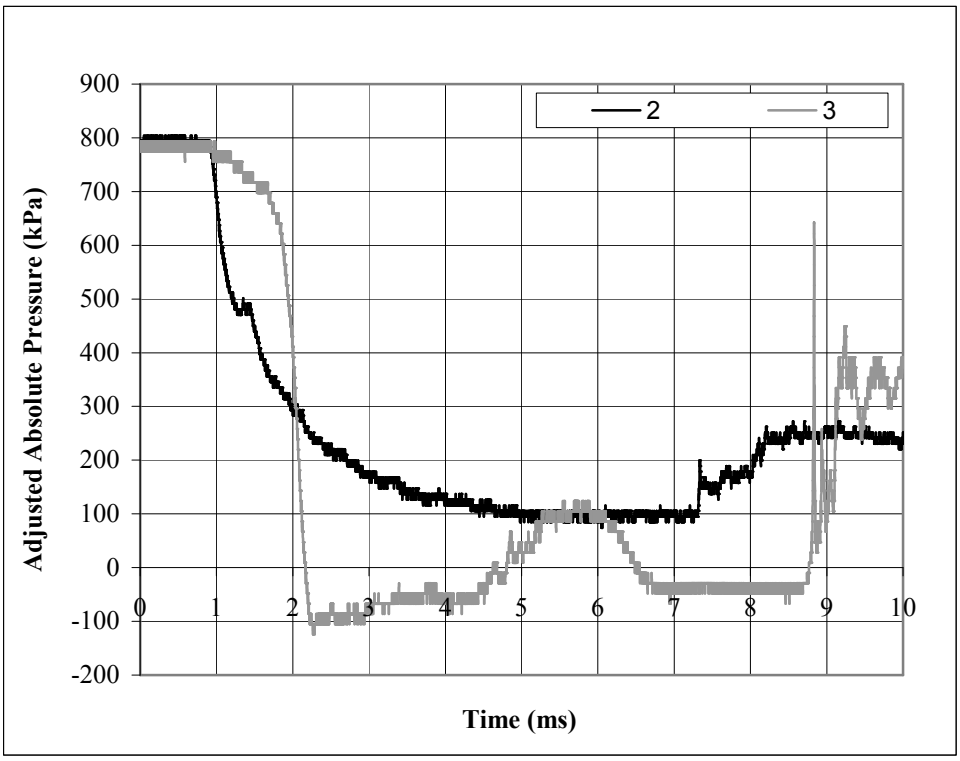


Figure 6.1. Pressure trace from test using the Mach 3 shock tube.
Sampling rate 1 *MHz*, 10000 data points.
(43C)

Figure 6.1 is a typical pressure trace recorded during a test. It shows the absolute pressures at the two transducers in the driver section, adjusted to the pressure before diaphragm burst. The atmospheric pressure during this test was 82.5 *bar*. A negative value of the absolute pressure of –100 *kPa* is recorded at the transducer mounted axially in the bottom of the tube, referred to in the following as *transducer 3*. The middle transducer, in the following referred to as *transducer 2*, recorded a minimum pressure of

1 *bar*. A very noticeable feature of the graph is the stationary point on the pressure record of transducer 2, which occurs when the local pressure has dropped to about 470 *kPa*. This is the point where the expansion wave, reflected from the top of the water surface arrives back at transducer 2. The pressure variations from the transducer in the driven section were of no interest and no pressure records are shown here.

Transducer 3 shows that the liquid at the base of the tube sustained an absolute negative pressure for approximately 3 *ms*. Then the pressure at the base of the liquid column rises to the same value as the air above it before dropping again, to a value of about –30 *kPa*. This pressure rise is attributed to the reflection of the expansion waves at the free surface, which results in downward-travelling compression waves. A shock wave, with a strength γ of approximately 2, is recorded at transducer 2 after approximately 7.3 *ms*. In addition, at approximately 8.7 *ms*, the pressure at transducer 3 rises abruptly, reaching a peak pressure of about 6.5 *bar*. This is followed by oscillating pressure variations above and below a pressure of about 3.5 *bar*.

Similar pressure records are shown in appendix L. These results were recorded from tests under the same conditions but show the pressure variations with different time scales to illustrate the overall trend of the pressure variations. In all experiments, the pressure records appeared fairly similar to figure 6.1. The maximum negative pressure in the liquid varied within the range –90 to –150 *kPa*. The most significant differences occurred between records of the pressure at transducer 3 when the pressure increased abruptly (e.g. the first pressure rise between 4 and 7 milliseconds and the second pressure rise at 9.7 *ms* on figure 6.1). Figures L.1 shows the first pressure rise followed by distinct pressure pulsations that proceed with decreasing amplitude. Figure L.2 shows a less regular pressure variation. The pressure oscillations are also visible from closer inspection of figure 6.1. Note that, in all experiments conducted, the pressure at transducer 3 immediately after the first pressure rise was approximately equal to the pressure, at the same time, at transducer 2. In all tests, the second, more abrupt, pressure rise appeared similar to the corresponding event shown in figure 6.1, although the peak pressures varied between about 350 and 700 *kPa*.

6.1.2. Photographic Records

Appendices M, N and O show sequences of photographs captured during experiments at a rate of 1000 frames per second. The pictures presented in appendix M correspond to the same test corresponding to figure 6.1 and the discussion above.

No pressure waves were visible in the photographs. Large pressure gradients (e.g. shock waves) may be visible when simple direct photography, with no optical arrangements, is used if the subject is suitably illuminated [55]. In this case, however, the pressure gradient involved here may be too low to cause visible effects. In addition, due to the high sound speed in water, any wave will travel the distance from the free surface to the tube base and back in less than half a millisecond. Thus, the photographs, separated by millisecond intervals, cannot be expected to consistently capture the waves if they are visible. A wave could not be visible in consecutive frames and may not be captured at all.

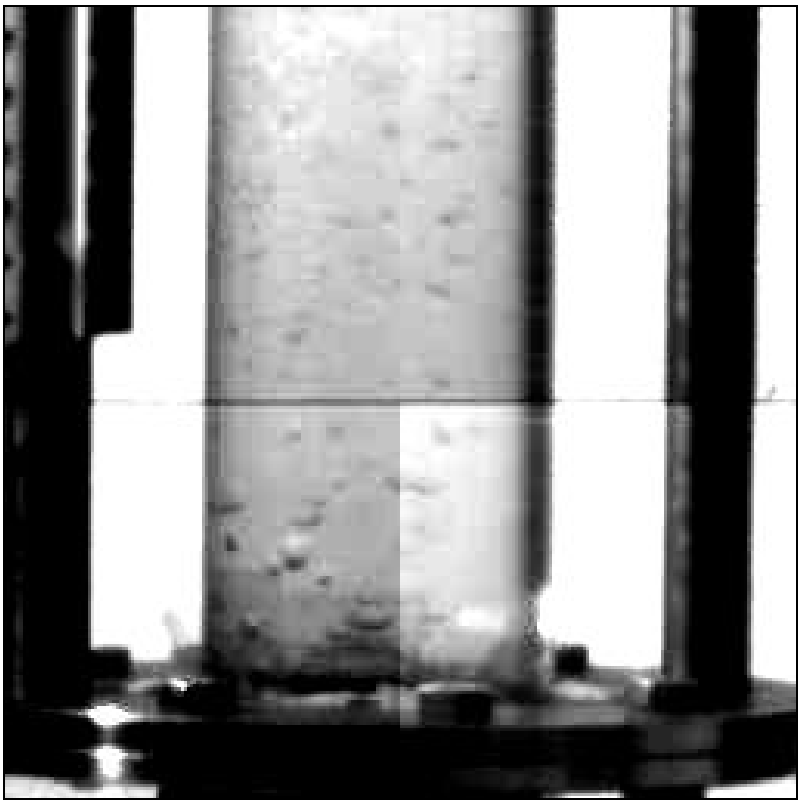


Figure 6.2. Cavitation observed at the bottom of the Mach 3 shock tube (appendix M, frame 4).

In the first three frames, no bubbles are clearly visible. The absolute pressure in the test section at the corresponding times approaches 7.93 *bar*. It appears as if cavitation occurs both within the body of the liquid and on the walls of the tube: The next frames illustrate saturation of the test section with bubbles of varying sizes. In frame 4, reproduced in figure 6.2, a large bubble with a diameter of approximately 5 *mm* is observed. The relatively large sizes an number of the bubbles suggest that the favourable nucleation sites are abundant.

Evidence is present of the oscillatory nature of the cavitating bubbles: In the three frames following frame 4, the number and sizes of visible bubbles decreases progressively. The largest bubble in frame 4 disappears from view in frames 5-7. In frames 8 and 9, bubble growth has occurred throughout the region of the tube under consideration. The intensity of the cavitation appears to have increaseed from the previous frames. A particularly large bubble, with a diameter of about 4.8 *mm* (estimated from enlarged pictures of these frames), is present in the bottom left hand corner of the frames. In frames 10 and 11, very few of the bubbles are clearly visible. Then, from frame 12, it is evident that another growth period occurs. The intensity of cavitation appears to decrease from frame 13 to 15. In frame 16, some bubbles appear to have expanded again. Over the next frames, the bubbles disappear again. Enlarged images of the frames showed that growth occurred at frame 22, although this is not clearly visible here.

It is evident that the intensity of cavitation decreased as the oscillations progressed. This implies damping of the bubble growth and collapse cylces. The frames that show markedly greater cavitation intensity than the adjacent frames before and after them are judged to be frames 4, 8, 12, 16 and 22. This seems to suggest that the period of oscillation of the bubbles is about 4 *ms*. However, this statement is based on rather inaccurate data: The period of oscillation may be smaller than the time interval between each camera frame (1 *ms*). In addition, from the trend shown and bearing in mind the camera's relatively slow frame rate, it is reasonable to assume that the cavitation intensity decreases throughout the sequence of frames, even though the number of visible bubbles appears greater in frames 8 than in frame 4.

Cavitational activity was not limited to the lower section of the tube. Appendices N and O show sequences of photographs from other tests, performed using the same method, but with the camera focussed on the middle and upper segments of the test section respectively.

Referring to appendix N, it it observed that no cavitation is clearly visible in the first 3 or 4 frames. Then, cavition, beginning at the lower section, is visible. The cavitation appears to intensify in frame 5, with a large bubble (diameter approximately 5.4 *mm*) forming in the lower region. Cavitation intensity appears to decrease markedly in frames 6-8. Frame 9, reproduced in figure 6.3 illustrates that cavitation then develops intensely. Many bubbles, of varying sizes and reasonably close together, form over the entire middle section. The rest of this record shows successive bubble growth and collapse phases. The intensity of cavitation appears to reach progressively decreasing maximums. Frames 13 and 17 show maximums of the cavitation intensities, which again suggests a period of oscillation of 4 *ms*.

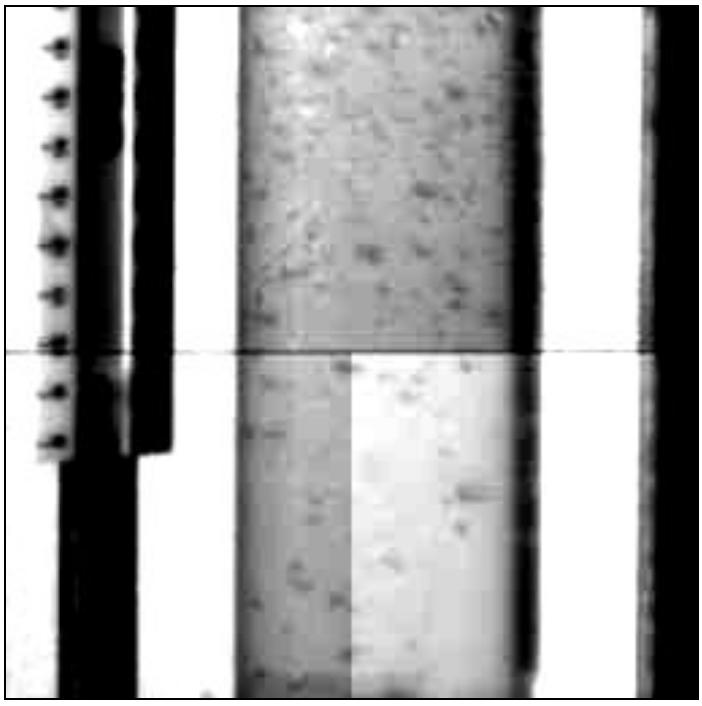


Figure 6.3. Cavitation observed at the middle section of the Mach 3 shock tube (appendix N, frame 9).

Appendix O appears to illustrate different behaviour. In the first frame, two bubbles are barely visible near the free surface. In the next four frames, a few isolated bubbles form beneath the free surface. The next frames show slight, initial disturbance of the free surface, which corresponds to the passage of the rarefaction wave through the the liquid column. The free surface appears relatively undisturbed from its initial position. In frames 6 and 7, the free surface begins to assume a "corrugated" shape as a result of many bubbles forming and coalescing in the region. Figure 6.4 is an enlargement of frame 18 and illustrates the nature of the free surface region after the passage of the wave. The initial level of the liquid column is lowered as the vapour mass forms above it. The rest of the pictures show vaporisation of the top layer of the liquid while the isolated bubbles below the free surface persist.

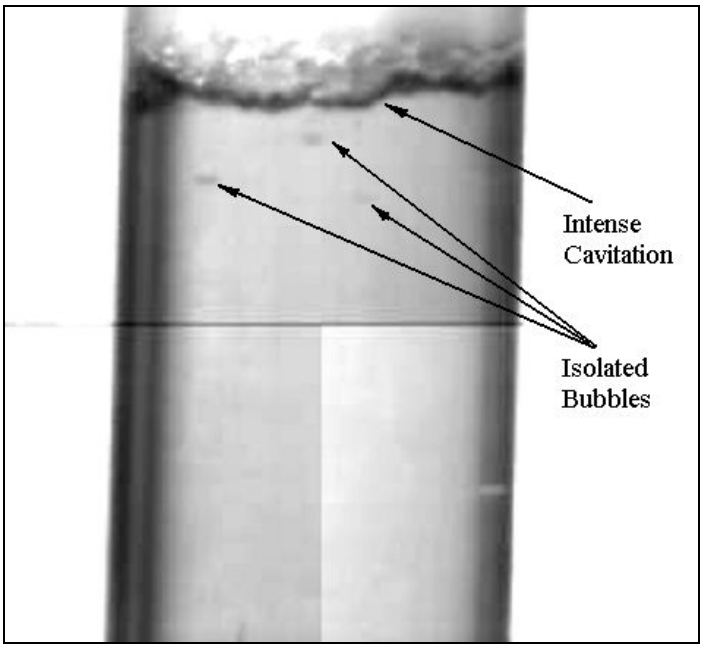


Figure 6.4. Cavitation observed at the upper section of the Mach 3 shock tube (appendix O, frame 18).

6.2. The Mach 2 Shock Tube

Initially, difficulties in producing a liquid shock were encountered: As mentioned earlier (section 5.2.3), a number of different interfaces between the air and water sections of the tube were tried. In early attempts, a single sheet of polycarbonate (6 and 8 *mm* thick) or

stainless steel was clamped between the bellows. However, the bellows did not provide enough movement for the interface to transmit a shock into the water. Later, a 1 *mm* silicon rubber sheet proved too weak and broke after just one completed test. Finally, insertion rubber sheet was used. Since 2 *mm* thick sheet was found to break after only 3 or 4 tests, a 4*mm* thick was used instead. Use of the thick insertion rubber resulted in compression waves in the water of similar magnitude to those obtained using silicon rubber and thin insertion rubber. Consequently, the thick insertion rubber was chosen, as it did not break, even after more than 30 tests.

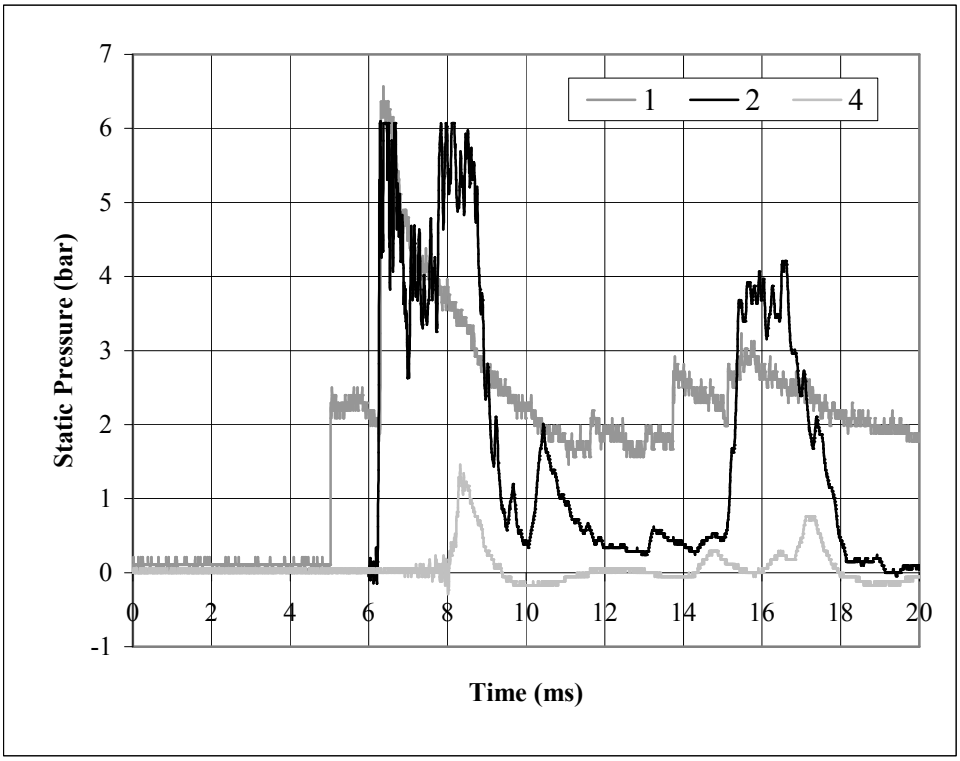


Figure 6.5. Pressure trace from test using the Mach 3 shock tube. Sampling rate 1 *MHz*, 10000 data points. Driver section filled with helium at 12 *bar*. Trigger level +0.1V, source CH-1, position –4V, delay 0.

Figure 6.5 shows a typical set of pressure traces recorded. The absolute pressure during this test was 0.831 *bar*. In the following, the transducer mounted in the wall of the air-filled driven section will be referred to as transducer 1, while the first, second and third

transducers encountered by an upward-travelling pulse in the liquid section are referred to as transducer 2, 3 and 4 respectively.

The pressure behind the air shock wave, recorded at the first transducer, transducer 1, at 5.0 *ms*, is approximately 2.5 *bar*. This is followed by another shock at 6.2 *ms*. These two shocks correspond to the upward-travelling incident wave and downward-travelling reflected waves. The strengths of the incident and reflected waves are as 4.0 and 2.1 respectively. The reflected shock is re-reflected at the bottom of the shock tube and then travels up the tube. It crosses transducer 1 again and is reflected from the interface again: the second incident and reflected waves occur at 13.8 and 15.1 *ms*.

The pressure trace for transducer 2 shows that a shock wave of pressure 6.1 *bar* was transmitted into the water column. This corresponds to a shock strength of about 7.3. From closer inspection (shortening the time scale), it was evident that this shock wave had a measurable rise time of approximately 60 μs. The pulse is not a strictly discontinuous shock wave. The initial pressure rise at this transducer is followed by a drop and subsequent rise in pressure. Then the pressure drops rapidly, reaching a minimum value of 33.5 *bar* (static pressure) at 10 *ms*. It appears that weaker compression waves are experienced at transducer 2 during the time interval between 9.5 and 15 *ms*. Then, the pattern appears to repeat, with lower amplitude waves, from 15.1 *ms*. As stated earlier, this repeating pressure variation is due to the re-reflection of the gas shock wave at the lower end of the tube, which results in another compression pulse that is transmitted into the liquid.

The pressure record of transducer 4, 60 *mm* below the free surface, shows unexpected results: the main compression wave appears to have decayed to a much weaker wave behind which the pressure was only 1.5 *bar* (an almost three-fold decrease in shock strength to a value of 2.8). In addition, the compression wave seems to have been preceded by a low amplitude transient pressure disturbance between 7 and 8 *ms*. After the main compression wave, a negative static pressure occurs for about 2 *ms*. However, this pressure is not a tension since it is equivalent to an absolute pressure of about 0.7 *kPa*.

Since this value is well above the vapour pressure, no cavitation is expected. Between 14 and 18 *ms*, slight pressure increases occur. Again, these were due to the waves resulting from transmission of a second shock from the gas section into the liquid.

Pressure records from transducer 3 were not included in figure 6.5 but follow the same trends as the records from transducer 4 except that the pressures involved are higher. The magnitudes of the pressures at transducer 3 are approximately halfway between those of transducer 2 and 4. This indicates that the attenuation of the compression wave is cumulative and approximately proportional to the distance travelled.

Appendix P shows additional pressure records from other tests. Figure P.1 shows pressure records from a test under the same conditions as figure 6.5. Figure P.1 differs from figure 6.5 in some respects. Firstly, the strength of the first incident gas shock wave is weaker. It follows that the reflected gas shock and the transmitted liquid shock are weaker. In addition, the unexplained compression waves, between the first and second main waves transmitted from the gas section, result in much greater pressure increases. In other similar tests, these unexplained increases in pressure were less than those shown in figure P.1. In figure P.1, most of the compression pulses after the main wave seem to be of similar strength. Otherwise, pressure records of figure P.1 resembled those shown in figure 6.5. For all tests using a 12 *bar* driver section, no negative pressures, or even pressures near the vapour pressure, were recorded at either of the transducers.

Figures P.2, P.3 and P.4 show pressure records from tests in which the driver section was filled with helium and pressurised to 8 *bar* before bursting the diaphragm. These records show inconsistencies and significant deviations from figures 6.5 and P.1. Consider the records from transducer 1 in figures P.2, P.3 and P.4. Firstly, the upward-travelling gas shock waves, incident on the interface, appear to not be fully formed i.e. The pressure rises twice before a larger pressure rise, corresponding to the reflected wave from the interface, is registered. Secondly, the gas shock strength varies. The strengths of the incident wave vary between 3.3 and 4.1 while the reflected wave strength is close about 2.0 in all three cases. The static pressure behind the reflected shock is similar in figures

P.3 and P.4 (6.0 and 5.8 *bar* respectively); the value in figure P.2 is only 4.7 *bar*. Again, these pressure waves are repeated, when the gas shock travels the length of the gas section of the tube, is reflected and reaches the interface again.

The pressure records for transducer 2 in figures P.2, P.3 and P.4 show that for an 8 *bar* driver pressure, the transmitted shock is actually greater than the pressure behind the reflected gas shock. The pressure records for transducers 2 and 3 show that after the passage of initial compression waves, the static pressure drops rapidly to a negative value of between -1 and -2 *bar*. This corresponds to negative absolute pressures with magnitudes slightly below –1 *bar*. During these low-pressure phases, high pressure 'spikes', up to pressures of about 1 *MPa* are recorded at these transducers. It should be noted that these abrupt changes in pressure occur before the second compression pulse is transmitted into the liquid section. The peak pressures vary with a maximum value of about 10 *bar*.

Consider lastly, the pressure records of transducer 4 situated 60 *mm* below the free surface in figures P.1, P.2 and P.3. The initial compression wave is attenuated markedly. In all cases, the pressure rise is followed by a low-pressure phase lasting about 2 *ms*, as recorded in the experiments using driver pressures of 12 *bar*. In all tests using the 8 bar driver pressure, the lowest static pressure, recorded during this phase (see figure P.3), was approximately –0.5 *bar*. This corresponds to an absolute pressure of about 0.325 *bar* (the atmospheric pressure was 0.825 *bar*), which is an order of magnitude greater than the vapour pressure of water at 20°C.

7. Theoretical Analysis

7.1. The Mach 3 Shock Tube

The experiments using the Mach 3 shock tube showed that cavitation was induced in the liquid. In this section, an attempt is made to explain the results theoretically.

7.1.1. Wave Diagram

KASIMIR (Copyright 1993 by Stoßwellenlabor, RWTH Aachen University) is a program used to simulate the physical phenomena inside one-dimensional shock tubes. It calculates the wave diagram, including information about the state variables at all points and the shock, compression and expansion waves and, displaying it on the screen. Inputs to the program include wall types (rigid for the current application), driver and driven section pressures and the expansion fan pressure ratio, which is, nominally, the pressure ratio across each characteristic in the expansion fan. For some combinations of inputs, the program would fail and generate an error message. In such cases, it was necessary to calculate the wave diagram using established methods. In the following, the built in real gas model for air (an air model consisting of nine components) was used. The results were found to be almost identical to results obtained using the ideal air model.

Figure 7.1 is the wave diagram for the first shock tube with the driver section pressurised to 7.93 *bar* and the driven section evacuated to a pressure of 0.027 *bar* (both pressures are absolute). The lower, test section containing the liquid column is represented by the positive positions from 0 to 0.419 *m* while the position values from 0 to –1.350 *m* correspond to the driven section. Thus, note that upward velocities are indicated as negative and downward velocities as positive.

The initial temperature of the gases (states A and B) and water (state W_1) before diaphragm rupture is usually room temperature [48] and taken as $20^{o}C$. Thus, the reference value of the speed of sound a_0 was 343.7 $m.s^{-1}$ for all gas regions of the wave

diagram and 1482 $m.s^{-1}$ for all water regions. Entropy changes in the liquid were neglected. The analysis neglects losses caused by the rupture of the diaphragm as well as the influence of the boundary layer. All pressures are absolute values. Bold lines represent shock waves.

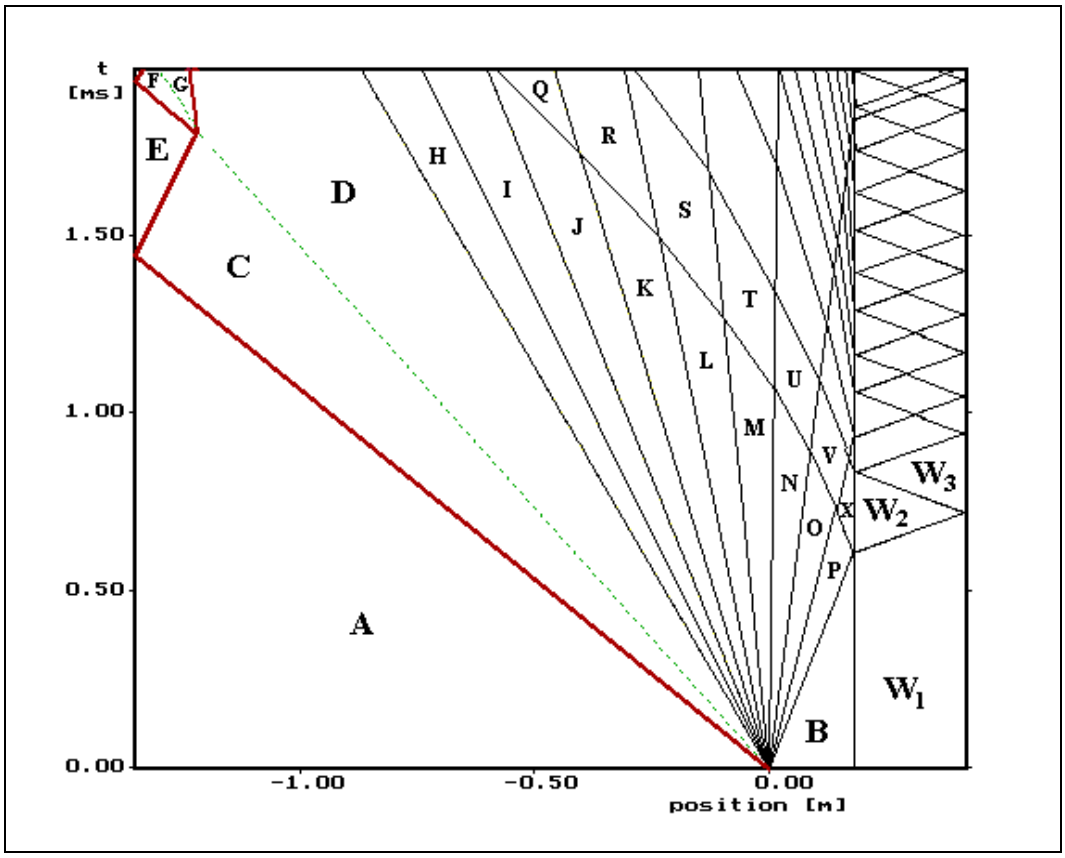


Figure 7.1. Wave Diagram of the Mach 3 Shock Tube
(driver section: air at 7.93 *bar*, driven section: air at 0.027 *bar*).

Note that the waves resulting from upward-travelling expansion waves that collide with the free surface (i.e. waves transmitted from the liquid to the gas) may be neglected for the same reasons that the gas above the free surface reflection of a shock remains unchanged (refer to chapter 2). The wave diagram predicts pressure variations, at the transducers, which are in satisfactory agreement with the experimentally recorded values.

The values of the fluid properties at the above regions are summarised in appendix Q, table Q.1. It may be seen that the pressure in region W_3 (behind the expansion wave

reflected off the bottom of the shock tube) is slightly negative (-0.645 *bar*). Since a gas cannot sustain any negative pressure [69], the compatibility condition used to construct the wave diagram, namely that the pressures on either side of the interface are equal, cannot be satisfied. Consequently, the method of characteristics becomes ineffective for solving the regions that follow the collision of the expansion wave with the free surface. The unlabelled regions in figure 7.1 are the unsolved regions.

7.1.2. Pressure-Velocity Diagrams

Since the wave diagram procedure was of no use once a negative absolute pressure value was reached and could thus not yield values for the lowest pressure reached in the liquid (an important parameter affecting cavitation), a different approach was required. The collision of the expansion fan with the liquid surface is illustrated graphically in the pressure velocity or *p*-*v* diagram, figure 7.2. Again, the convention, in this case, is that negative and positive signs correspond to upward and downwards velocities respectively. The curves labelled *i*, *r* and *t* represent the loci of states, which may be reached by a point on them an incident, reflected or transmitted expansion wave propagating in the relevant medium. Note that the transmitted wave has a positive slope but appears vertical because it propagates in water, which has a relatively high acoustic impedance. Curves for reflected waves starting from any pressure on the incident wave curve may be plotted. However, only selected loci, starting from pressures of 5.569, 3.911, 2.746, 1.929, 1.355 and 0.951 *bar*, are plotted here. These are the pressures in the regions *P*, *O*, *N*, *M*, *L* and *K* behind the six characteristics on the wave diagram closest to the liquid column.

Using the same naming conventions as in chapter 2, the initial state of the air and water are denoted by (1) and (5) respectively. These states are coincident on the *p*-*v* diagram because of the compatibility conditions on the pressures and velocities across the contact surface. The incident expansion wave causes the air of state (1), above the liquid sample, at rest and a pressure of 7.93 *bar*, to be expanded to the state (4) and to acquire an upward velocity. The reflected wave causes the pressure to drop further and the magnitude of the velocity to decrease until a state (2) is reached. The water at state (5) is expanded and

accelerated upwards by the transmitted wave to a state (3), which by compatibility has the same pressure and velocity as (2). Thus, these states are coincident.

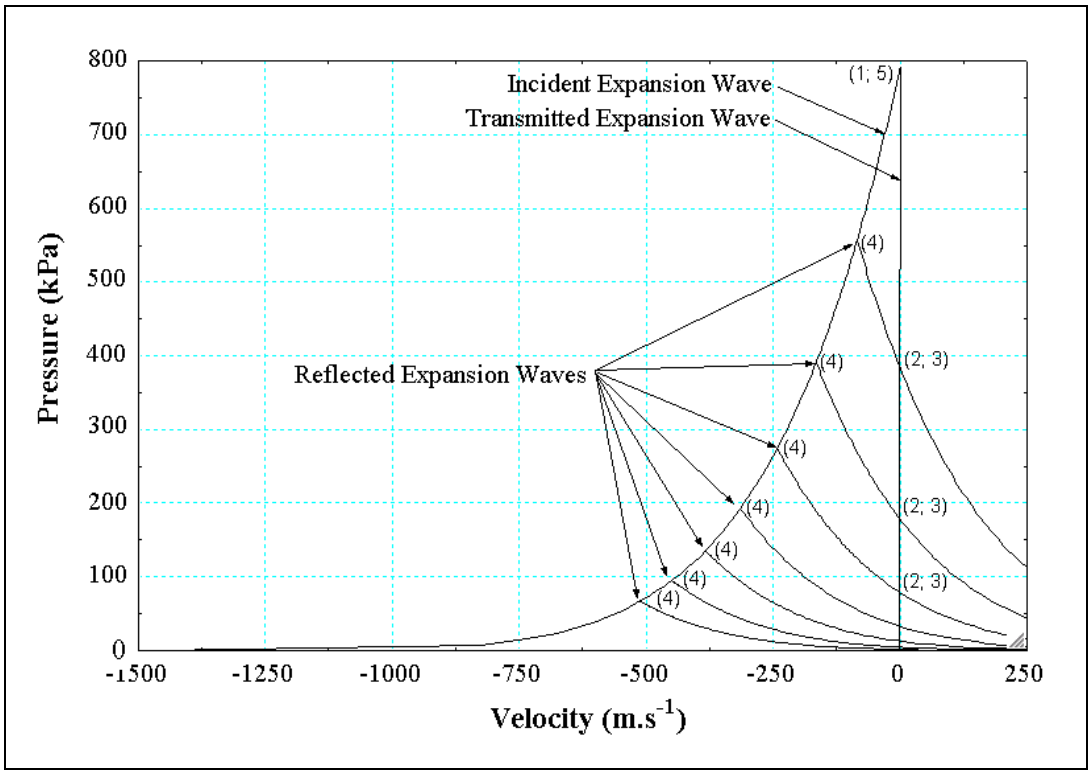


Figure 7.2. Pressure-velocity diagram for the collision of the expansion waves with the gas-liquid interface (initial driver pressure 7.93 *bar*).

As the lowest negative pressure obtained in the water is required, the lowest pressure behind the downward-travelling, incident waves, 1.929 *bar* (the state *M* on the wave diagram), was chosen as the starting point for the reflected wave curve. Thus, the pressure at the state (2,3) is, from closer inspection of the diagram, approximately 0.33 *bar*, while the velocity of the air and water is approximately 0.5 $m.s^{-1}$ upwards. In summary, the analysis predicts that the pressure of the air, initially at 7.93 *bar*, is reduced (by 6.00 *bar*) to 1.929 *bar* and then (by 1.60 *bar*) to 0.33 *bar* by the incident and reflected waves respectively. The pressure of the water is reduced, by the transmitted wave, to 0.33 *bar* (a pressure drop of 7.6 *bar*).

The pressure in the liquid is reduced further when the transmitted wave collides with the bottom of the tube, which is assumed to be a rigid wall. For this second interaction, another pressure-velocity diagram was constructed. The diagram, presented in figure 7.3, simply shows the "acoustic doubling" effect discussed in appendix E i.e. the incident and reflected rarefaction waves are of equal strength. Thus, since the pressure drop caused by the incident wave was about 7.6 *bar*, the resulting, minimum absolute pressure in the liquid is approximately –7.27 *bar*. Graphically, this pressure could be obtained by extrapolating the curve, on figure 7.3, which corresponds to the reflected expansion wave starting at 33 *kPa* until it intersects the curve of the transmitted expansion wave.

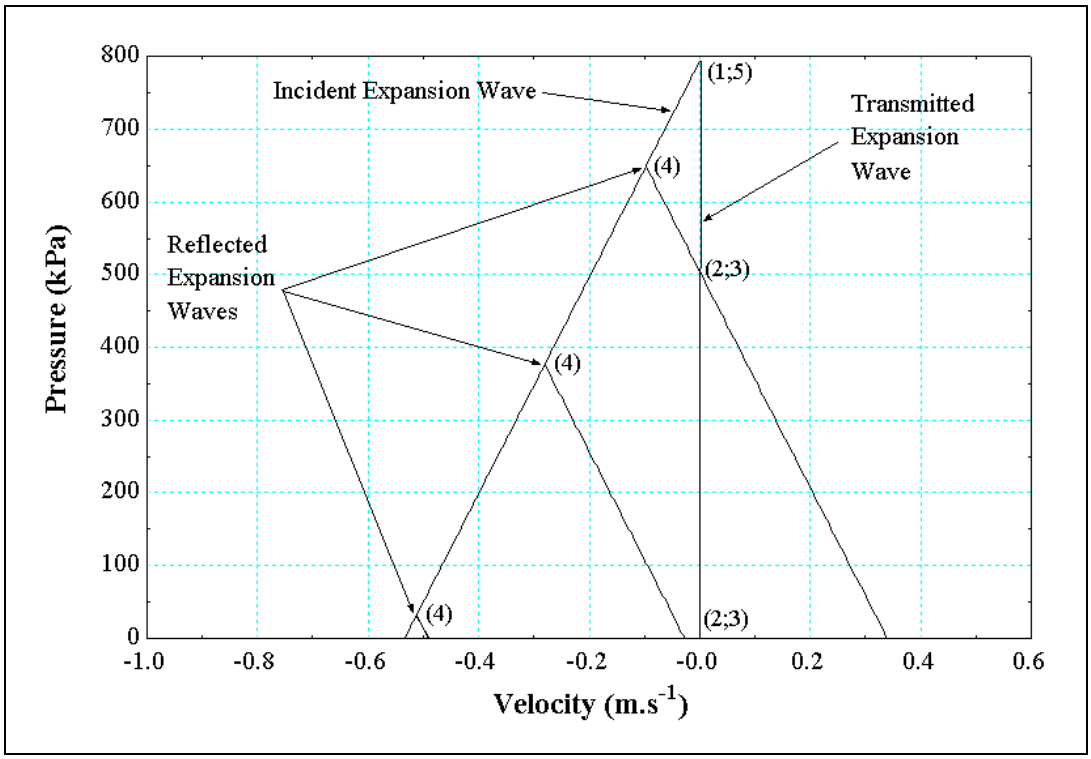


Figure 7.3. Pressure-velocity diagram for the collision of the expansion waves with the base of the Mach 3 shock tube (initial driver pressure 7.93 *bar*).

Although the analysis up to this point provides a plausible and representative maximum negative pressure value, it neglects three important factors:

1. The reflection of the expansion waves, at the free surface, results in downward-travelling compression waves, which raise the pressure. In similar work [93],

these waves were purposely used to initiate bubble collapse. These compression waves result in the rise in pressure that follows the initial tension in the liquid, as shown on pressure records from transducer 3: figures 6.1, L.1 and L.2.

2. Secondly, consider the strong, downward-propagating shock wave that results from the reflection of the initial shock, formed at diaphragm burst, at the upper wall. This incident gas shock impinges on the free surface and increases the liquid pressure before all of the downward-propagating waves in the expansion fan have entered the liquid. The rise in pressure caused by this shock, and the shock resulting from its reflection at the base of the tube, would certainly increase the pressure well above the atmospheric pressure, as well as cavitation bubble collapse. This was confirmed by the pressure records (refer to figure 6.1): The abrupt pressure increase at transducer 3 occurred follows a shock experienced at transducer 2. The pressure records showed adequate agreement with the wave diagram, figure 7.1. However, the shock strength, from figure 6.1, is only between 2 and 2.5 while the strength of the shock, which is weakened by the expansion wave system it travels through, was estimated as between 6 and 10. This value was determined by treating the free surface of the liquid as a rigid wall.
3. Thirdly, some of the upward-travelling expansion waves would be curved on the wave diagram (towards the liquid column), due to the their interaction with expansion waves reflected from the liquid surface, and impinge upon the liquid before the strong shock, thereby reducing the pressure further. The parameters of these waves could not be calculated accurately using the wave diagram method because, again, the negative pressure in the liquid limited its effectiveness. Thus, the magnitude of the maximum negative pressure may be lower (due to the strong shock) or greater (due to curved waves entering the liquid) than 7.27 *bar*, as found by combining the wave diagram and *p*-*v* diagram methods.

A further analysis of the “strong” shock was carried out. The limiting value of negative pressure in the liquid must be that resulting from transmission of the characteristic waves that impact the free surface at the same time as the strong shock wave. Only the waves in the expansion fan that arrive at the free surface before or at the same time as the strong

shock, were considered. They were treated as a single wave. The low pressure behind the single incident wave was then easily calculated as 2.72 *bar* using an extended wave diagram, including times up to 10 *ms* and a very long driver section to neglect the effect of the expansion waves reflected from the free surface. The characteristic between regions *M* and *N* on figure 7.1 has a very slight gradient and would thus not reach the liquid surface before the strong shock wave, while the characteristic between *N* and *O* reaches the liquid well before the shock. Thus, the value of pressure obtained seems reasonable as it is close to the value at *N*, 2.746 *bar*. Then, the interaction of this single wave with the free surface (transmission and reflection) was solved on close inspection of the same *p*-*v* diagram, figure 7.2. This yielded a value of 0.77 *bar* for the pressure of the liquid behind the transmitted expansion fan. Again, when the expansion fan is reflected at the base of the tube, the drop in pressure (-7.16 *bar*) caused by the expansion wave is doubled. Thus, the maximum tension to which the liquid may be subjected, in this method is –6.39 *bar*. This minimum pressure is the absolute limiting value that is approached. It is not sustained for an appreciable length of time before the pressure increases. This correction, from the value of –7.27 *bar*, accounts for the effect of the strong shock, but the magnitude of the actual tension imposed on the liquid may be greater or lower due to curved expansion waves waves that may enter the liquid and the compression waves from the free surface, respectively.

It should be obvious that the magnitude of this negative pressure exceeds the value encountered in the experiments, where maximum tensions of about –1 *bar* were measured. It is, thus concluded that cavitation occurred before this value was reached, and prevented further pressure decrease. The high number of large bubbles observed (e.g. figure 6.2 and 6.3) and intense cavitation (figure 6.4) appear to account for this.

7.1.3. Bubble Dynamics Simulations

The Rayleigh-Plesset differential equation, equation (3.10), including viscosity effects, was modelled using Simulink ® (Copyright by the *The Mathworks, Inc. 1990-2004)*, which is integrated into MATLAB ®. The model is shown in figure 7.4. The inputs

required for the model were the initial bubble nucleus radius R_o, the initial rate of growth $\dot{R}_o$ and the pressure field *p(t)*. The main difficulty encountered in these simulations was associated with the latter: It was shown, in sections 7.1.1 and 7.1.2, that determination of the pressure variation imposed on the liquid involves consideration of many factors.

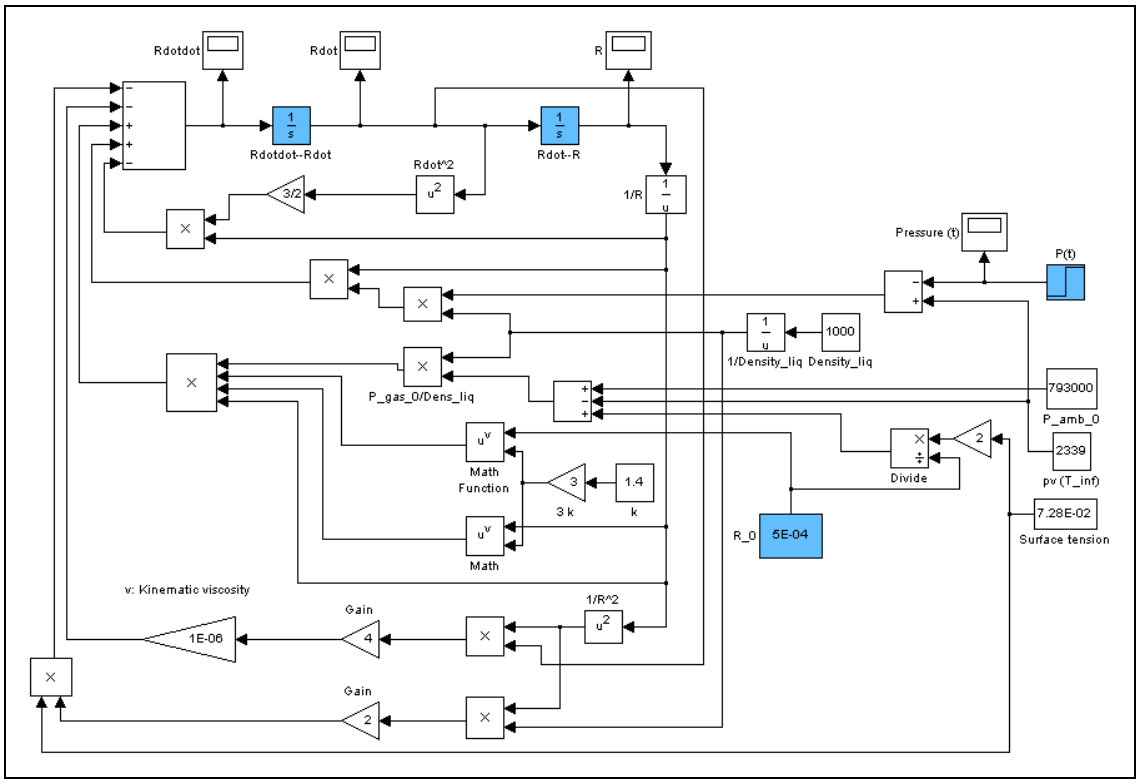


Figure 7.4. Matlab Simulink model of the Raleigh-Plesset differential equation.

The shaded block in the far-right section of the figure 7.4 is the pressure variation input. The ambient pressure variation with time could be represented by various blocks such as a step-function and ramp-function. The lowest shaded block is the nucleus radius R_o. The first and second shaded blocks from the left are integrator blocks, which require, as inputs, the initial rate of change of bubble radius and initial bubble radius, respectively. Figures 7.5, 7.6 and 7.7 show results of a simulation of bubble growth using the Simulink model. The pressure drop due to the expansion waves is represented by simply a step-function input, occurring at the time equal to zero, with the initial and final pressures equal to 7.93 and –1 *bar* respectively. This approximates the pressure variations recorded by transducer 3 mounted at the base of the Mach 3 shock tube.

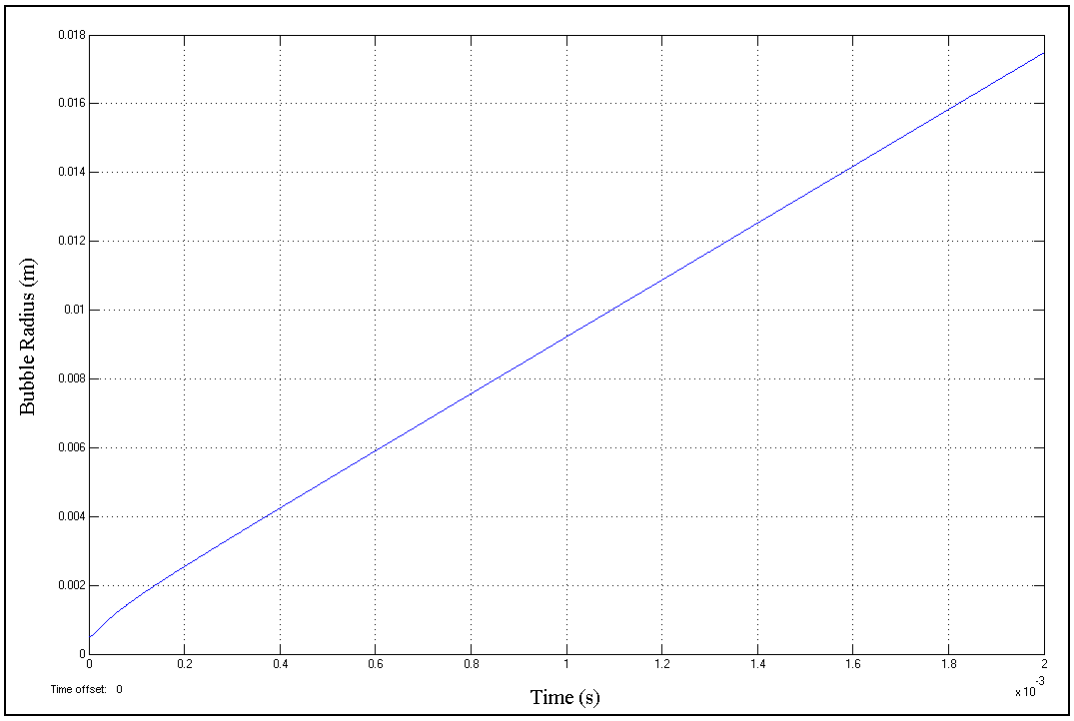


Figure 7.5. Variation of radius with time for growth of bubble (R_o 0.5 *mm*) subjected to step-function pressure drop from 7.93 to –1 *bar* at time zero.

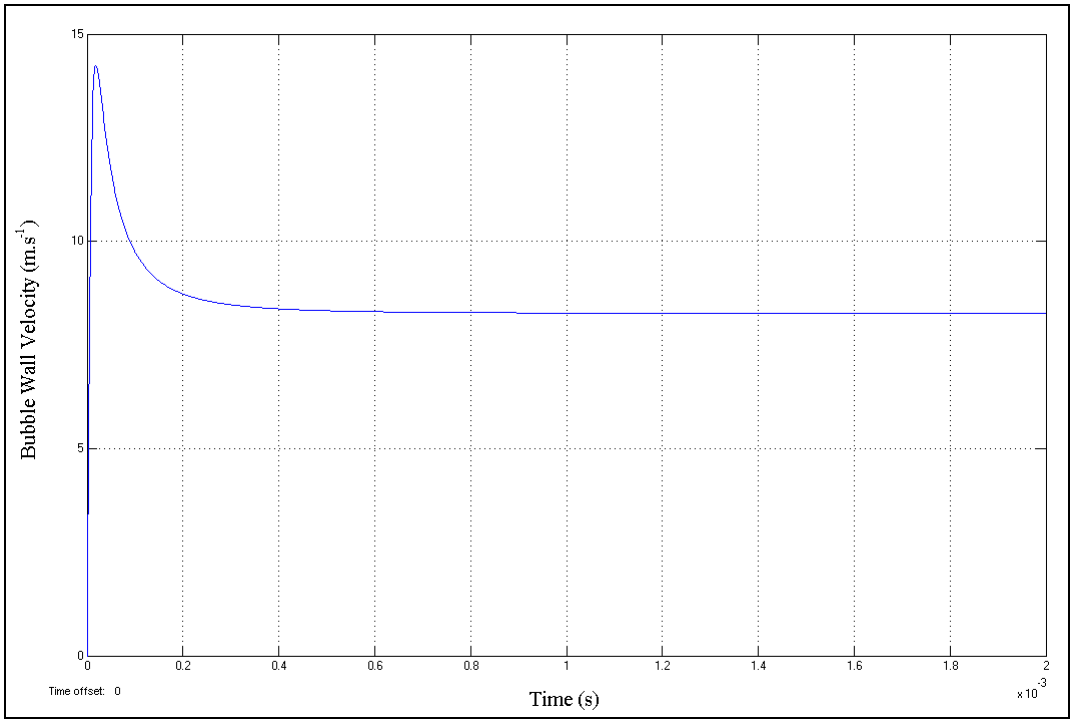


Figure 7.6. Variation of bubble wall velocity with time for growth of bubble (R_o 0.5 *mm*) subjected to step-function pressure drop from 7.93 to –1 *bar* at time zero.

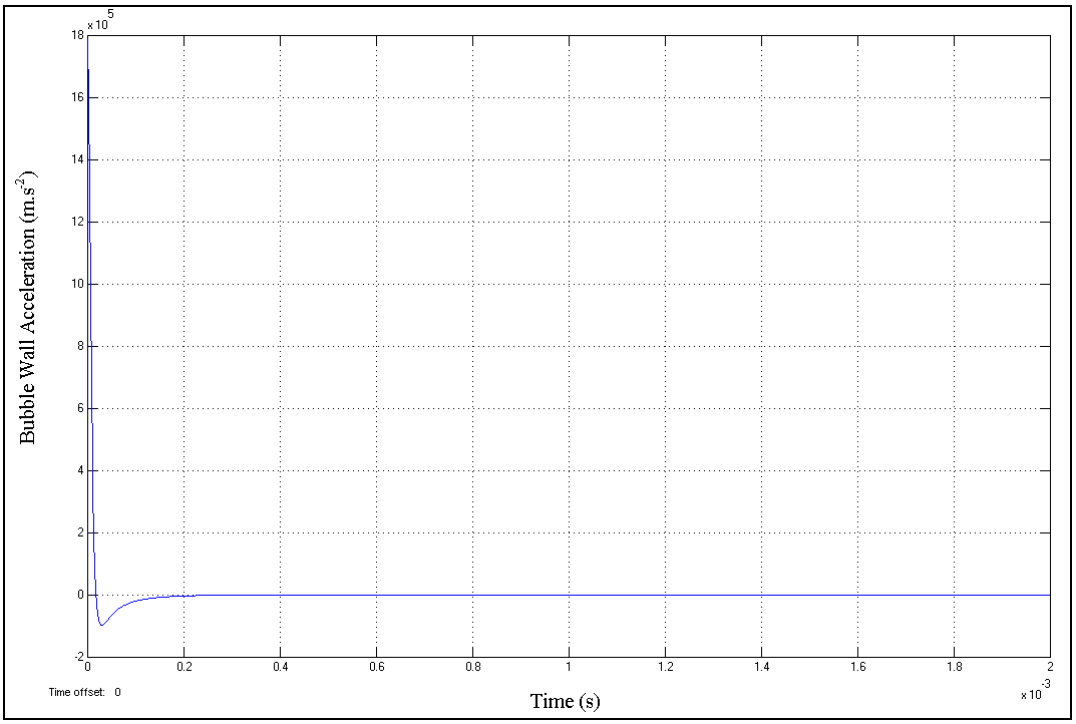


Figure 7.7. Variation of bubble wall acceleration with time for growth of bubble (R_o 0.5 *mm*) subjected to step-function pressure drop from 7.93 to –1 *bar* at time zero.

The initial values R_o and $\dot{R}_o$ in the above simulation were equal to 0.5 *mm* and 0 respectively. The figures show that the bubble wall accelerates to a maximum velocity of 13.98 $m.s^{-1}$ before stabilising at a speed of about 8.26 $m.s^{-1}$. Figure 7.5 shows that the bubble wall expands without bound. The radius reaches a rather unrealistic value of 17.3 *mm* after 2 *ms*. Appendix R shows additional simulations for the same input pressure but widely different nucleus sizes, in adiabatic and isothermal growth.

The general trend of the results here and in appendix R (figures R.1-R.7 and tables R.1 and R.2) is the same. The bubble wall velocity rises rapidly and reaches a peak value denoted by $\dot{R}_{MAX}$ after a time t_V. The velocity then approaches a constant velocity, $\dot{R}_{FINAL}$, asymptotically. Table R.1 and R.2 show that this final rate of expansion is relatively constant. The velocity can be estimated quite accurately using the equation $\dot{R}_{FINAL} = [\frac{2}{3}(p_V - p^*_\infty)/\rho_L]^{\frac{1}{2}}$, where p_V, p^*_∞ and ρ_L are the vapour pressure, the final pressure after the pressure drop and the liquid density respectively. $\dot{R}_{MAX}$ increases

slightly with increasing initial bubble radius R_o, while the time taken to expand to this maximum growth rate increases significantly: the growth of the bubble of radius 1 μm up to a peak rate of about 13 $m.s^{-1}$ is indiscernible from figure R.5, even though the time scale has been shortened. In addition, the time taken in attaining visible size t_V decreases markedly with increasing R_o, while the radii at fixed times increase. Thus, the model predicts that, in the experiments, the bubble nuclei do not appear simultaneously. The sizes of the bubbles when they become visible will vary according to their initial sizes. This is in agreement with the experimental evidence of figures 6.2 and 6.3 and appendices M and N.

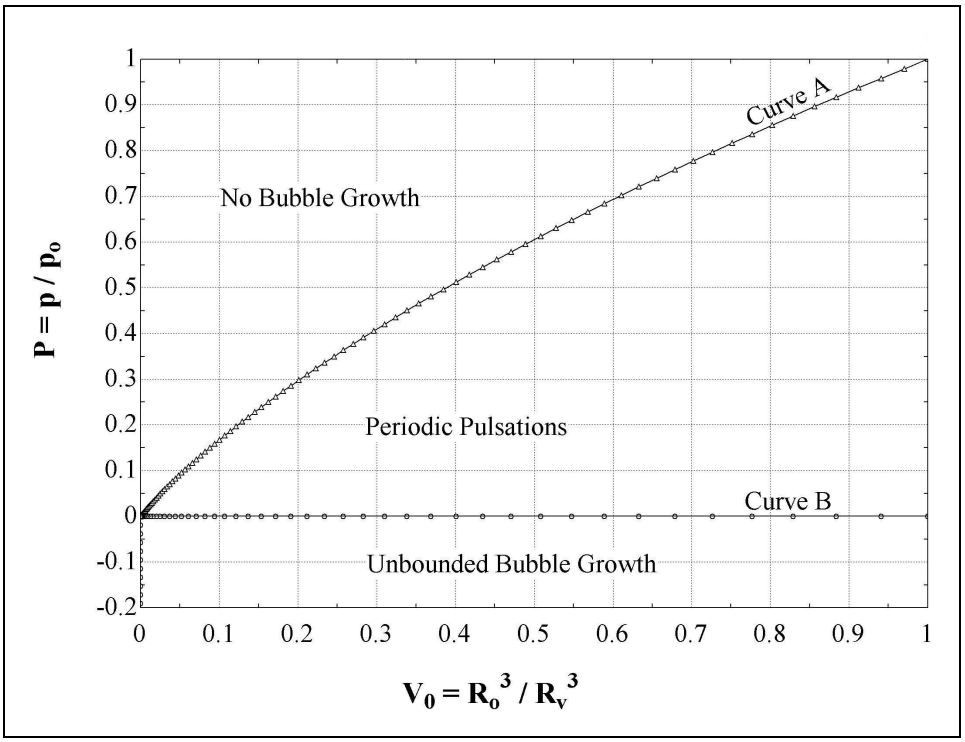


Figure 7.8. Regions of the P-V_o plane (initial pressure 7.93 *bar*, surface tension 0.073 $J.m^{-2}$).

It is also evident that for the pressure variation described above, the model predicts unbounded growth, with no periodic oscillations, for all nuclei sizes continued. Figure 7.8 depicts the response of a bubble to a rarefaction wave, in the P-V_o plane. The curves were plotted using the theory explained in section 3.3.2 and [92]. Interestingly, the plot shows that almost any negative pressure will lead to unbounded growth. Figures R.8, R.9 and

R.10 illustrate a typical case of periodic, oscillating growth of a bubble (R_o = 10 μm) subjected to a pressure drop, from 7.93 *bar* to the vapour pressure 2339 *Pa*, at time zero. The bubble oscillates with diminishing amplitude and period.

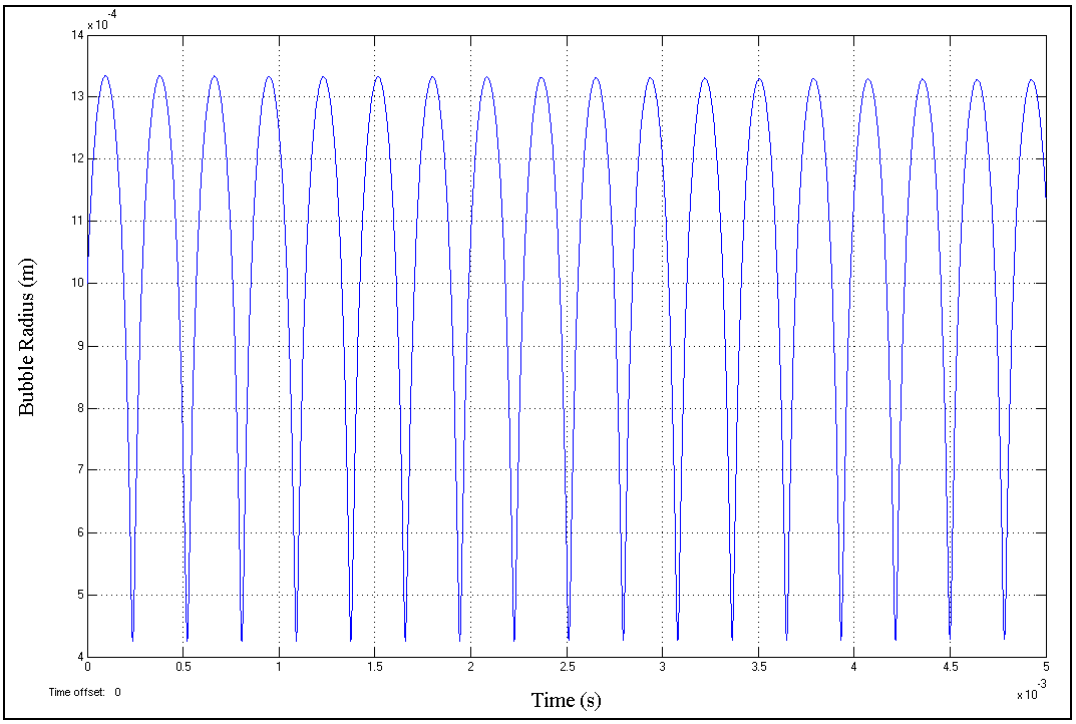


Figure 7.9. Variation of radius with time for collapse of a bubble (R_o 0.5 *mm*) subjected to step-function pressure rise from -1 to 1 *bar* at time zero. $R(0)$=1 *mm*, $\dot{R}(0)$=8.3 $m.s^{-1}$.

The analysis of bubble growth has shown, unequivocally, that no bubble oscillations will occur, in the test liquid of the Mach 3 shock tube. However, photographic evidence (appendices M and N) proves the contrary. It has been found that such oscillations may have been caused, at bubble collapse, by pressure increases due to compression waves. As discussed in section 6.1.1 and 7.1.2, two pressure increases are experienced at the bottom transducer. Firstly, the pressure rises from –1 to 1 *bar*. This was attributed to reflection of the expansion waves from the free surface. Later, the pressure increases to up to more than 6 *bar*. Figures 7.9, 7.10 and 7.11 are results of simulations of the response of a bubble, with an initial radius R_o of 1 *mm*, subjected to a pressure rise from –1 *bar* to some value p_∞^*, at a time zero. At this instant, the bubble radius $R(0)$ is 5 *mm*, while the bubble wall velocity $\dot{R}(0)$ is 8.3 $m.s^{-1}$. The plots show oscillations with

approximately constant period and slightly diminishing amplitude. Thus, the bubble collapse is followed by cycles of rebound and collapse.

Figure 7.11 shows that the maximum bubble wall acceleration, at the instants of minimum bubble radius, is almost than 3.5×10^{6} $m.s^{-2}$. These corresponds to the instants of bubble rebound. The acceleration of the liquid surrounding the bubble has the same high velocity. This illustrates the potential for significant shock waves to be radiated from the bubbles at collapse.

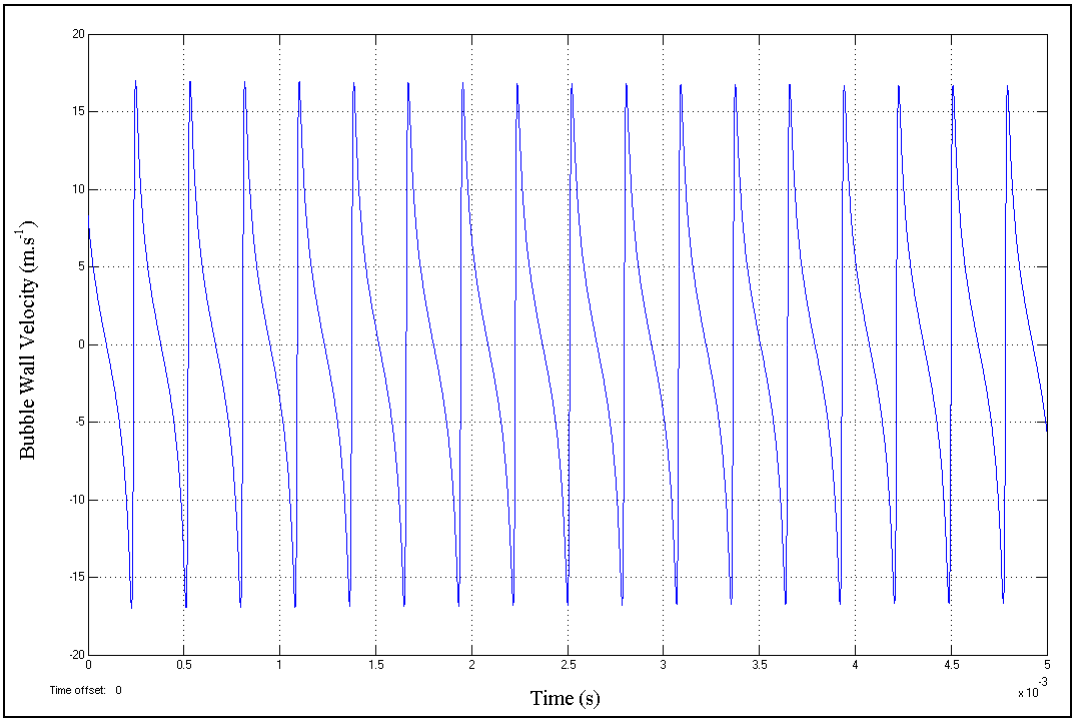


Figure 7.10. Variation of bubble wall velocity with time for collapse of bubble (R_o 0.5 *mm*) subjected to pressure rise from -1 to 1 *bar* at t = 0. $R(0)$=1 *mm*, $\dot{R}(0)$=8.3 $m.s^{-1}$.

Appendix R (figures R.11-18) shows similar results for different values of the parameters. Comparison of figures 7.9 and R.11 shows that the frequency of oscillation decreases with decreasing radius *R(0)*. Both figures show oscillations with near constant periods over 5 *ms*. However, figures M.17 and M.18 show oscillations with progressively increasing periods. Such oscillations proceeded until a singularity occurred at the instant of rebound of the bubble after collapse from a large size.

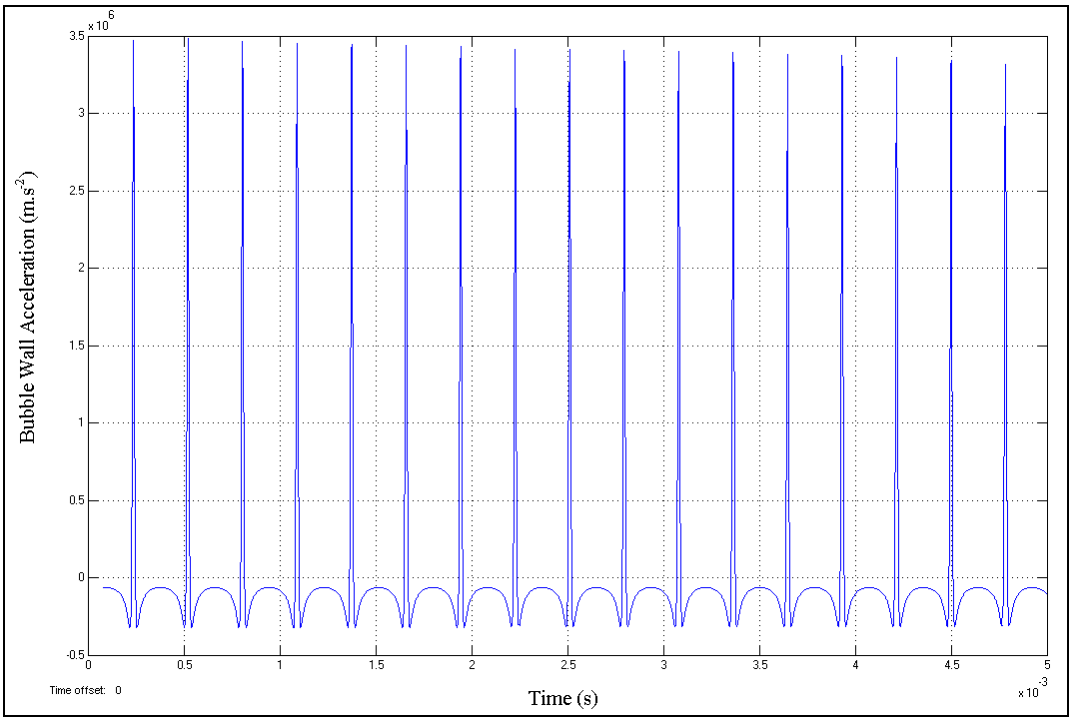


Figure 7.11. Variation of bubble wall acceleration with time for growth of bubble (R_o 0.5 *mm*) subjected to pressure rise from -1 to 1 *bar* at t = 0. $R(0)$=1 *mm*, $\dot{R}(0)$=8.3 $m.s^{-1}$.

Now consider figures 7.9, R.11 and R.14. In figures R.11 and R.14, the amplitude increases progressively as oscillations increase, while the amplitude decreases slightly. This implies that an increase in the radius of the bubble $R(0)$ before collapse or an increase in the pressure p_∞^* (i.e. a stronger compression wave) results in progressively increasing amplitude and hence, in effect, more intense rebounds from minimum size. The effect of $R(0)$ on the intensity of the rebound is in agreement with the molecular dynamics simulations [4] (refer to section 3.4). The effect of p_∞^* is physically realisable: An increased pressure on the bubble causes greater compression of its contents, resulting in more intense collapse and rebound. Comparison of figure 7.9 with figure R.17 and of figure R.11 with figure R.18 illustrates that a smaller nucleus radius, R_o, also results in more intense rebound. This is understandable since if equation (3.3) is applied for the initial nucleus in equilibrium, then the initial gas pressure p_{Gi} will be larger for smaller values of R_o (assuming the same values for p_∞, p_v and σ). From equation (3.9), this results in higher gas pressure at the instant of rebound.

In figure 7.9, the period of oscillation is approximately 0.29 *ms*. In the case of figure R.11, the period is below 1 *ms* for the first 30 *ms*, while for the case of figure R.14, the period increases from 0.2 *ms* to about 2 *ms* over the first 10 *ms*. In figures R.17 and R.18, the period reaches values between 4 and 8 *ms*.

From this analysis of bubble collapse, it is concluded that bubbles of different sizes may show very different collapse behaviour, even under the same pressure field e.g. compare figures 7.9 and R.11. The analysis suggests bubble oscillations with periods in the order of tenths of milliseconds initially and possibly in the order of milliseconds for later times. Thus, the bubble behaviour at collapse caused by the compression waves in the Mach 3 shock tube may account for the observed oscillations detailed in section 6.1.2.

7.1.4. Computational Fluid Mechanics

Modelling of cavitation using CFD is a complex task. Density ratios between the phases in such multi-fluid problems involving air and water are high (in the order of 1000). The codes adopted by most commercial CFD packages have only recently been developed and little information on their applications is available [164]. The relevant methods are discussed briefly in appendix S. It was found that none of the available CFD packages could simulate cavitation while considering the liquid, vapour and non-condensed gas to be compressible at the same time.

7.2. The Mach 2 Shock Tube

Since experiments showed unexpected results, namely apparent decay of shock waves to low values, various factors were analysed to determine the cause of the discrepancies. First, the wave diagram of the tube was constructed to ascertain if the unexplained pressure variation or the low shock strengths measured below the free surface may have been caused by any extraneous waves or if any unforeseen interactions took place. Other factors are discussed in sections 7.2.2, 7.2.3 and 7.2.4.

7.2.1. Wave Diagram

Figure 7.12 is the wave diagram for the second shock tube with the driver section pressurised to 12 *bar* and the driven section at atmospheric pressure 0.83 *bar*. The liquid section is filled with water to a level of 60 *mm* above the transducer 4. In KASIMIR, the built-in ideal gas models for air and helium were used. The characteristics and related state variables in the upper, water-filled section of the tube were calculated manually. The bold lines represent shock waves. The values of the fluid properties corresponding to the labeled regions of the wave diagram are summarised in appendix Q, table Q.2. For clarity, a portion of the gas section, from about 5 *ms* onwards and the resultant, transmitted liquid waves, are omitted. In addition, the waves in the liquid, reflected from the gas-liquid interface were not plotted. The compression and expansion waves are expected to be reflected as expansion and compression waves respectively.

Firstly, one can see that the depth of the uppermost transducer below the free surface is large enough to ensure that the incident and reflected waves should be distinguishable in pressure traces recorded there: The incident and reflected waves travel the distance from the transducer to the free surface and back again in approximately 80 μs. Since this value is much larger than the rise time of the transducer, the pressure waves should be resolved on pressure records.

The motion of the free surface was also analysed to determine any effects the acceleration of the free surface might have on the readings of the upper transducer, which was close to the free surface. The initial velocity of the liquid at the free surface was found to be less than 0.5 $m.s^{-1}$. Thus, over the time interval between the the arrival of the incident wave at transducer 4 and that of the reflected expansion wave, the free surface moves upwards less than 20 μm. It is concluded, from this insignificant value, that the motion of the free surface does not affect the transducer readings.

7.1

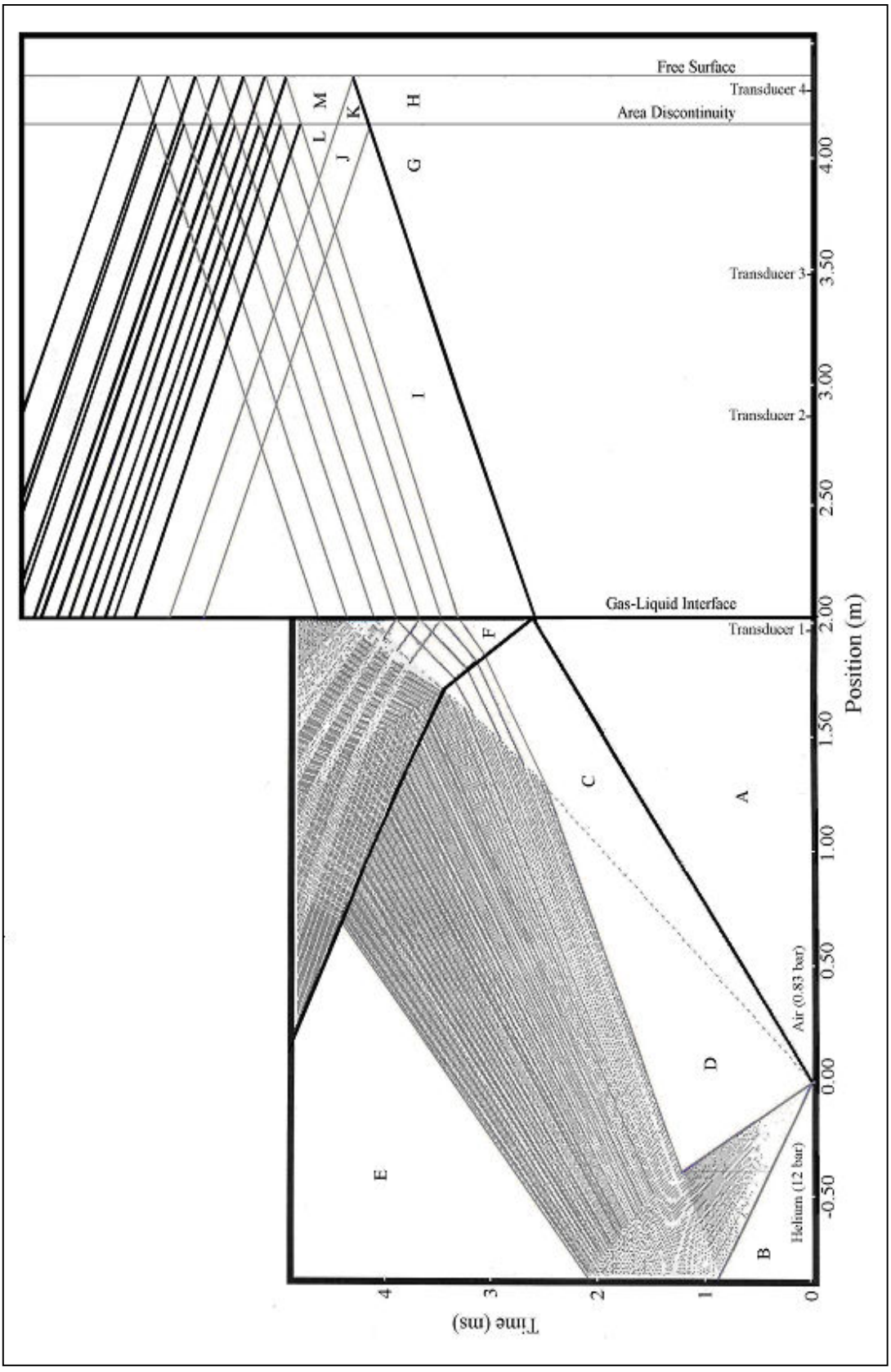


Figure 7.12. Wave diagram of the Mach 2 shock tube.

Other wave diagrams were constructed for different driver-section pressures (the driven-section pressure was 0.83 *bar* in all cases). In the case of the driver-section filled with helium at 8 *bar*, the wave diagram was similar to figure 7.12 although the time interval between the arrival of the shock and that of the head of the expansion fan was less. This is expected as the lower diaphragm pressure ratio should reduce the shock speed markedly but not affect the head of the expansion fan much.

Figure 7.12 and its associated parameters shown in table Q.2 involve certain assumptions that differ from the experiments. Firstly, table Q.2 indicates that the pressure behind the gas shock reflected from the gas-liquid interface is over 17 *bar*. This value is much higher than the experimental values because the interface was assumed to behave like a rigid wall and that reflection that occurred at it was perfect or 'hard' reflection, which corresponds to a reflection factor equal to 1. The relatively low density of the rubber means that the reflection factor is lower than one [43]. Kosing assumed a value of 0.35 for plastic [43]. In the present case, such a value of the reflection factor would result in more reasonable estimates below 10 *bar*, for the pressure behind the reflected gas shock. Secondly, when the gas waves impinged upon the interface, transmitted waves were assumed to form instantaneously. This approximation is justified as the low inertia of the interface should not delay the transmission of waves significantly and appeared to be in agreement with the pressure records. The following sections improve on the predictions of the wave diagram by analysing the effects of other factors.

7.2.2. The Area Change

A discontinuous area change exists between the pipe section and the optical observation section. This was incorporated to facilitate the windows. Figure 7.12 shows reflected expansion waves where waves pass through the area change. For clarity these reflections are not shown for the downward travelling waves, though it should be understood that those waves are also strengthened as they pass through an area reduction.

The quasi-steady analysis, described by the comprehensive procedure of Rudinger [44] was applied to determine the loss of normal shock strength across the area change

between the pipe section and the optical observation section. The steady flow pattern was expected to be reached quickly since the change in cross-section is rather small [46]. Referring again to appendix F, figure F.1, the standing shocks in cases (*B*) and (*C*) and the shocks that are swept downstream in cases (*C*) and (*E*) are caused by the local particle or flow speeds being greater than the wave speeds [46]. This condition is unlikely for waves in water due to the high acoustic impedance of the medium and the low flow speeds. Thus, the condition that would result in the present case is case (*A*). In any case, the waves swept downstream in a liquid medium would be practically coincident on the wave diagram due to their similar speeds.

The cross-sectional areas below and above the area discontinuity are (A_1) 2206 mm^2 and (A_2) 2709 mm^2 and respectively. Thus, the upward-travelling waves pass through a discontinuity where the area increases by 22.8 %. The quasi-steady analysis predicted that for an incident shock wave of $p_2/p_1=6$ in the pipe-section, the pressure ratio across the shock wave that is transmitted into the optical observation section will 5.54. Due to the near acoustic behaviour of shock waves in liquids, simpler methods than that of Rudinger may be employed. The waterhammer analysis of Parmakian [6] was used for the present case. The author found that the maximum error between these methods, for the current case was approximately 3%.

In another approximate method, the *Chester-Chisnell-Whitham Channel Formula*, the transmitted shock strength is determined analytically by considering the primary effects of the area change on the wave but neglecting secondary effects of overtaking disturbances [165]. This method show good agreement with the quasi-steady analysis for weak shocks and small area ratios, as shown in figure 7.13. In [165], the one-dimensional equations of unsteady motion were solved numerically for gases over a wide range of incident shock strengths and area ratios. The results also showed good agreement with the methods described above for weak shocks and small area ratios.

The methods of Rudinger, Parmakian and the Chester-Chisnell-Whitham formula are suited to cases where area changes are gradual or “small” [46,165,166]. It is thus

necessary to discern whether the area change involved in the present discussion are small. Rudinger [44] stated that for the quasi-steady analysis to accurately describe the interaction of a shock with an area change, the condition $\ln(A_2/A_1) \leq 0.1$ must hold. The area ratio under consideration, 1.228 results in $\ln(A_2/A_1) \leq 0.2$ and thus, the accuracy of the results of the analysis here is uncertain.

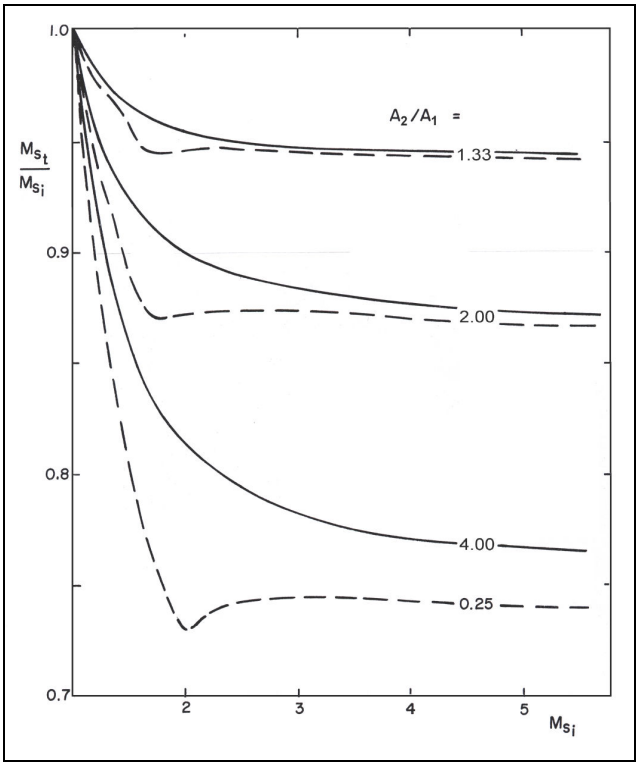


Figure 7.13. Results from Chester-Chisnell-Whitham analysis (solid lines) and the quasi-steady analysis (dashed lines) for the de-amplification of a shock with initial Mach number M_{Si} (adjusted from [165]).

The results of the quasi-steady analysis, though conceivable, do not, generally, represent accurate, 2-D flow. Parts of the flow field may never approach a 1-D flow. While some two-dimensional flow results approach the respective 1-D results after sufficiently long times, some are genuinely 2-D and cannot be reduced to a one-dimensional equivalent [166]. The real flow pattern at such an interaction is more complex with two-dimensional effects as illustrated in figure 7.14 from simulations using 2-D numerical code [46]. The figure shows a strong, step-profile shock after passing through a discontinuity with a

large area ratio of 10. The working fluid is air. The absolute pressure behind the transmitted shock may be expected to be about 40% that behind the incident shock. The simulation, though very different from the present discussion of the shock in the Mach 2 shock tube, illustrates the two-dimensional effects that may be present in it. Since the incident shocks in the Mach 3 shock tube case are effectively much weaker and pass through a discontinuity with a much smaller area ratio, the ratio of the transmitted wave strength to that of the incident wave may be expected to be much greater than 40 %. Since pressure traces show that this is not true, it is doubtful that the area discontinuity alone is the cause of the decayed shock.

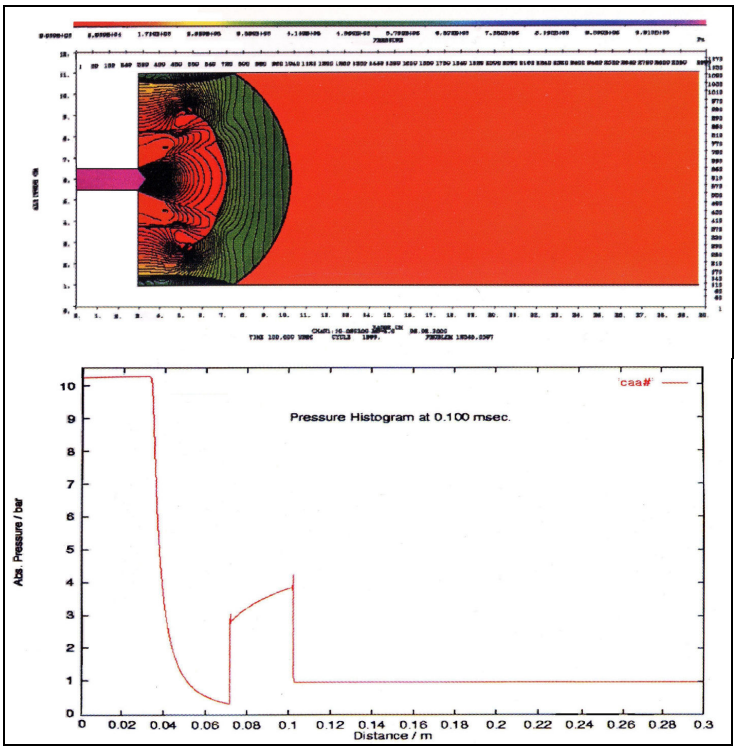


Figure 7.14. Results of simulation of propagation of shock wave (M_s = 3) through a discontinuity having an area enlargement ratio of 1/10 at the instant 0.1 *ms* [46].

The pressure records show that the first transmitted liquid shock becomes progressively weaker, even before reaching the area discontinuity. Thus, other factors must have contributed to the decrease in shock strength.

7.2.3. The Motion of the Interface

The wave diagram, figure 7.12, implies that the initial shock wave has a step-profile although the pressure records showed that the pressure decreases after the peak value is reached. In addition, pressure records showed that the ratio of the transmitted shock strength to that of the incident shock varied for different incident shock strengths. Thus, it is not certain how the strength of the transmitted shock and expansion waves were related to that of the incident waves in the gas and further analysis was performed to describe the nature of the transmission of the shock.

It was thought that the pressure recorded at the transducer just below the surface was smaller than predicted by theory due to extraneous waves originating from the motion of the rubber interface. If the plate were to accelerate downwards (or if its motion decelerates while moving upwards), expansion waves would be emitted upwards into the water column. These waves might be expected to overtake and weaken the shock wave, causing the apparent decay noted section 6.2.

The insertion rubber sheet, which acted as the air-water interface, was treated as an isotropic plate and as such, resists bending and has complex internal stresses, as opposed to a membrane, which has little stiffness (rubber properties are listed in appendix G). The actual occurrence of transmission and internal reflection of elastic waves within the plate will be neglected (this implies infinite velocities of waves in the plate). The plate was assumed to not move appreciably, such that the vertical displacement of the plate, over its whole area, could be assumed equal.

The analysis is based on the theory of Taylor [167], who explored the behaviour of a non-rigid plate of finite size and derived, with simplifying assumptions, an equation that describes the motion of the plate in terms of the incident pulse parameters. The vertical displacement of the plate may be expressed by the equations derived in appendix T.

As described in appendix T, the author found that, including the effect of the column of liquid above the plate, which served to stiffen the plate against vibration; the effective

natural frequency of vibration of the interface ω_n in the first mode was found to be 19745 $rad.s^{-1}$. Using the values given in appendix T, the motion of the interface was calculated and the results are shown in figure 7.15. It was found that the plate accelerated for approximately one millisecond before reaching a constant velocity, which was maintained until the plate started decelerating approximately 4 *ms* after impact of the wave. This means that upward-travelling expansion waves could only be generated from the interface surface 4 *ms* after the shock wave was generated. Such waves would be too late to catch up and attenuate the shock wave or interfere with the shock and reflected expansion registered at the uppermost pressure transducer, near the free surface. In any case, it is unlikely that any waves from the interface could catch up with the shock due to the acoustic nature of all waves in water i.e. the shock and expansion waves travel at a speed very close to the sound speed. Thus, it was concluded that extraneous effects from the interface did not attenuate the shock wave or interfere with the pressure readings at the uppermost transducer.

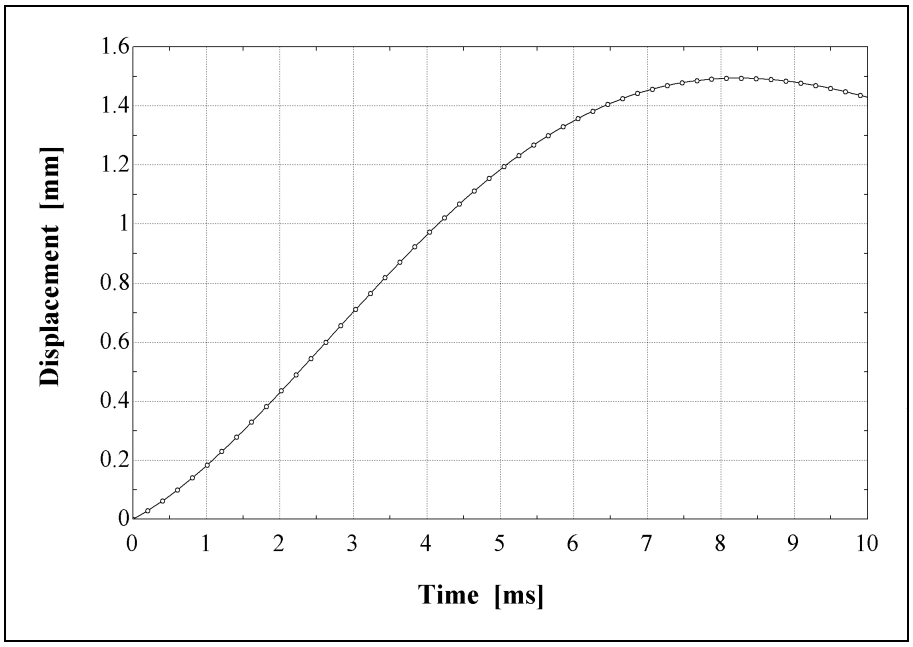


Figure 7.15. Results of analysis of the liquid-air interface using Taylor's theory [167].

7.2.4. The Effect of Pipe Elasticity

For a shock wave propagating in a tube, elasticity of that pipe may attenuate the shock strength in the same way as an area increase does. The reduction of shock strength due to pipe stretch is a relatively unexplored effect.

7.2.4.1. Streeter's Method

The only known analysis of the effect of pipe elasticity on compressible flows is that of Streeter [168] who expressed the rate of area increase as a function of the modulus of elasticity, diameter and thickness of the pipe:

$$\frac{dA}{dt} = \frac{D^3 \pi}{4t'E} \frac{dp}{dt} \tag{7.1}$$

For small time increments ($dt \approx \Delta t$),

$$\Delta A = \frac{D^3 \pi}{4t'E} \Delta p \tag{7.2}$$

So, the change in area from its initial area, at any point, is a function of the excess pressure at that point. For discontinuous waves, the area is assumed, as is usually done in waterhammer problems [6], to change instantaneously as implied by equation (7.2).

The effect of pipe wall elasticity on sound speed may be computed from the following equation [168,169]:

$$a = \sqrt{\frac{K/\rho}{1 + (K/E)(D/t')Y}} \tag{7.3}$$

It is evident that if the modulus of elasticity were approximated to infinity, the sound speed would reduce to equation (2.42). Taking the density as 1000 $kg.m^{-3}$, and the bulk modulus as 21.96×10^8 $N.m^{-1}$, the speed of sound predicted by equation (7.3) is 1375 $m.s^{-1}$ compared to the value of 1482 $m.s^{-1}$ obtained from equation (2.42).

Streeter [168] divided the pipe into a number of portions of equal length, and since the magnitudes of the gradients of the characteristics were all equal, the wave diagram was divided into a grid. Interior points were solved for using the two characteristic equations in finite difference form. At the ends, the two unknowns were solved by two relations,

one provided by the characteristic relation of the characteristic, which passed through it, and the other from the external boundary condition, which must be specified.

Attempts to calculate the effects of pipe stretch using this analysis and variations thereof did not yield any plausible results. It was concluded that this procedure could not be applied in the present case as the shock wave travelling up the pipe, with decreasing strength, presented a moving boundary condition.

7.2.4.2. Method of Characteristics

Consider figure 7.16, the wave diagram of the liquid-filled tube section. The region of the wave diagram of the water column behind the shock was divided into regions (labelled *O*,*R*,*S*,*T*,*U*,*V*,*W*,*X*,*Y*,*Z*) separated by a family of characteristics. Each expansion wave in the family implies a weakening of the upwards-travelling shock wave due to pipe stretch. In reality, there would be an infinite number of reflected expansion waves between the waves, but since the wave diagram method can only be applied for a finite number of waves, the infinite number of expansion waves was represented by nine characteristics. For the purposes of ascertaining the effect of pipe stretch, only the portion of the tube from the region *U* upwards was considered. This allowed a known value of *Q* to be established since the pressure in region *U* corresponds to that recorded by transducer 2, behind the shock. Then, the value of *Q* in region *U* was calculated from the known shock strength and shock tables. Firstly, *Q* was made to vary uniformly from the value at *U* to the value behind the last characteristic. The latter was taken as the atmospheric conditions as the compatibility condition requires that the pressures on either side of the free surface remain unchanged. However, this proved to be incorrect since it caused the pressure to vary almost uniformly from the first wave (i.e. the pressure at *U*) to the last (atmospheric pressure). The correct method would have been to choose the values of *Q* at the characteristics such that they varied from the value at *U* to the value at *Z*, since the characteristics between *Z* and *J* and between *K* and *M* are not caused by pipe stretch, but rather by the area discontinuity and free surface respectively. However, the value of *Q* at *Z* could not be determined since the strength of the last rarefaction wave resulting from

the free surface reflection could not be established. Thus, no results could be obtained from this method.

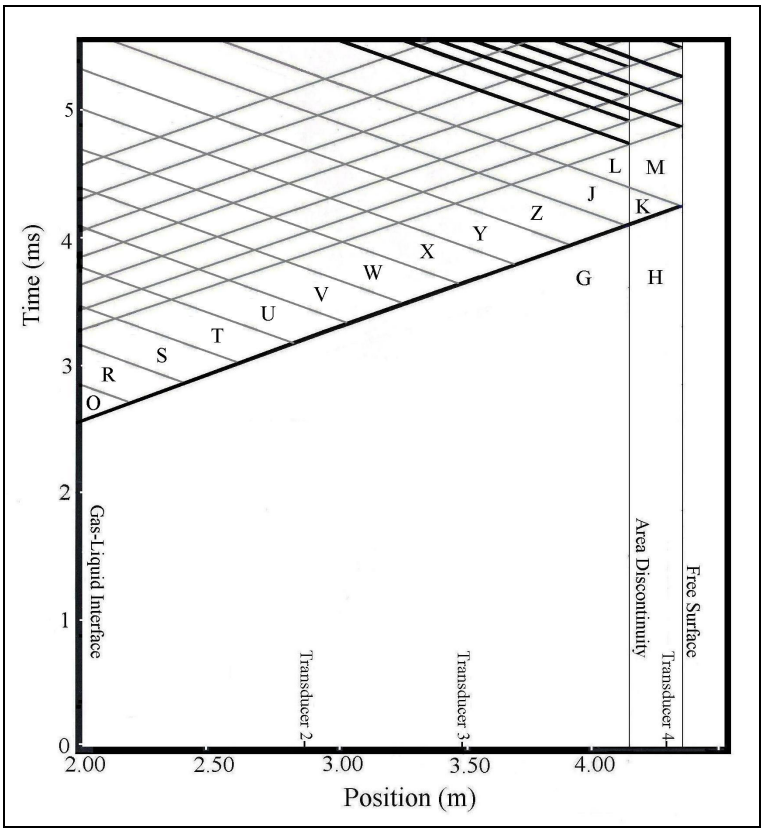


Figure 7.16. Wave diagram of the upper, liquid section of the Mach 2 shock tube, including the effects of pipe stretch.

7.2.4.3. Elementary Calculation

A more simple method, based on equation (7.2) and the definition of the bulk modulus (2.36) was used after Streeter's method and the adaptation of the method of characteristics proved ineffective. The method is, essentially, a calculation of the drop in pressure of the liquid behind the shock wave due to pipe stretch. The reduction in pressure is attributed directly to the change in the total volume occupied by the mass of compressed liquid behind the shock.

The transducers are located 0.831, 1.481 and 2.286 *m* above the interface. When the shock is at each of the transducers, the area change is calculated using equation (7.2), where the initial area A_i and initial pressure p_i are the same reference area and pressure for each calculation. Since the area change is proportional to the overpressure,

$$\frac{\Delta V_1}{V_1} = \frac{\Delta V_2}{V_2} = \frac{\Delta V_3}{V_3} \tag{7.4}$$

In the most general way, the constant in the sound speed equation (7.3), *Y*, may be calculated by $Y = K_1(1+\nu) + K_2(\frac{5}{4} - \nu)$ for a pipe anchored at the upstream end only, $Y = K_1(1+\nu) + K_2(1-\nu^2)$ for a pipe anchored against longitudinal movement and $Y = K_1(1+\nu) + K_2$, or alternatively $Y = 1 - \frac{\mu}{2}$, for a pipe with expansion joints throughout its length where $K_1 = 2t/D$ and $K_2 = D/(D+t)$. The expressions for a pipe with expansion joints throughout its length reduce to approximately 1. The pipe of the Mach 2 shock tube, with an expansion joint on one end and a free end, is assumed to have a value of *Y* of approximately 1.

From the definition of the bulk modulus of compressibility, the change in pressure can be expressed in terms of finite, non-specific volumes:

$$\Delta p = -\frac{\Delta v}{v_i}\frac{1}{\beta} = -\left(\frac{(1/\rho_f) - (1/\rho_i)}{1/\rho_i}\right)K = -\left(\frac{\rho_i}{\rho_f} - 1\right)K$$

$$= -\left(\frac{(M/V_i)}{(M/V_f)} - 1\right)K \tag{7.5}$$

Since the present case involves a constant mass of water at each transducer,

$$\Delta p = -\left(\frac{V_f}{V_i} - 1\right)K = -[C]K \qquad \text{where } C = \frac{\Delta V}{V_i} \tag{7.6}$$

However, since both ΔV and V_i are a function of the length of tube considered, C is constant for all sections considered. Thus,

$$C_{T1} = C_{T2} = C_{T3} = \Delta V / V_i = \Delta A / A_i = 4.2 \times 10^{-5}$$

Since the pipe inner diameter is 52.5 *mm*, the initial area is

$$A_i = 2164.8\ mm^2$$

For a shock pressure of 6 *bar*, the change in area is

$$\Delta A = \frac{(52.5\times 10^{-3})^3 \pi (6\times 10^5)}{4(3.75\times 10^{-3})\,(200\times 10^9)} = 0.091\ mm^2$$

Thus, the change in pressure (from the nominal value of 6 *bar*) felt the transducers is

$$\Delta p_{T1} = \Delta p_{T2} = \Delta p_{T3} = -92246\ Pa$$

In conclusion, this method predicts that the effect of pipe stretch is to lower the shock pressure from 6 to 5.08 *bar* (a 15% decrease in pressure). However, this elementary method does not imply a cumulative effect i.e. the strength of the shock wave does not decrease progressively as the wave propagates up the tube, rather, its strength is smaller than its original value (at the bottom end), but constant along the pipe length. The magnitude of the estimated pressure drop is too small to completely account for the decay of the shock evident from the pressure traces.

8. Discussion

8.1. The Mach 3 Shock Tube

The direct method of creating tensions in liquids, using a hydrodynamic shock tube, is a relatively unexplored approach, making comparison difficult. The only known, similar study using water is that of Fujikawa and Akamatsu [93]. Their studies differ from the experiments using the Mach 3 shock tube in that their driven section was left at atmospheric pressure and not evacuated. In addition, their driver section was pressurised to only about 2.64 *bar* as opposed to the corresponding value of 7.93 *bar* in the Mach 3 shock tube. The effect of the far greater diaphragm pressure ratio in the Mach 3 shock tube was that the expansion fan was substantially more 'spread out' i.e. some of the characteristics (refer to the wave diagram, figure 7.1) in the expansion fan reached the driven-section of the tube. This did not occur in the tube of Fujikawa and Akamatsu. The theoretical analysis of chapter 8 also showed that greater negative pressures, of up to –6.39 *bar*, could be achieved in the Mach 3 shock tube than in the tube of Fujikawa and Akamatsu who obtained tension of less than –0.5 *bar*). The longitudinal dimensions of their tube was also significantly larger e.g. Their liquid column is 2 *m* in height compared to the height of the column, about 300 *mm*, used in the Mach 3 shock tube. This allowed Fujikawa and Akamatsu to observe greater temporal resolution in pressure traces and high-speed camera pictures. It should be noted that the magnitude of the maximum negative pressure that the test liquid, in the Mach 3 shock tube, is subjected to could be increased, from the estimate 6.39 *bar*, to greater values by lengthening the driven section, thereby delaying the increase in the liquid pressure caused by the shock that is reflected from the upper end of the tube.

The main conclusion made from experiments using the Mach 3 shock tube, as evidenced by pressure transducer and photographic records, was that cavitation, induced by rarefaction waves, was successfully demonstrated in tap water. According to the pressure records from transducer 3, at the bottom of the tube, and the photographic records, cavitation occurred at a pressure of –1 *bar*. This inability to withstand more substantial

negative pressures is consistent with the values of Cole [55] and Eldridge [79] for untreated water (refer to section 3.2). The likelihood of higher tensions occurring at the tube walls and at the liquid-gas interfaces was reduced further by the presence of free gas and other impurities [55]. Experimentally, it is difficult to distinguish homogeneous nucleation from heterogeneous nucleation that occurs on small, invisible solid particles within the body of the liquid [5]. However, the low tensions achieved indicate that heterogeneous nucleation occurred. It is difficult to ascertain, from the photographs, if the nucleation occurs at solid boundaries or within the body of the liquid. Cavitation occurred throughout the height of the liquid column. However, the formation of cavities at the top of the column appeared different to that elsewhere. The more intense cavitation at the top is attributed to the saturation of the top layer of the liquid with suitably large gas nuclei as experienced by Besov et al. [35]. The 'corrugated' surface of the modified free surface showed that bubbles had formed and coalesced such that the top layer of liquid was totally evaporated.

The high-speed camera available was, presumably, not fast enough to accurately capture the oscillating bubble or other effects, such as sonoluminescence as discussed in the following. Nevertheless, the period of oscillation of the pulsating bubbles, suggested by the experimental photographic records, appeared to be approximately 4 *ms*. In addition, the oscillations of a bubble do not, in general, have a constant period [2,112,95,124,156,170,171]. Thus, in the present case, the "point-by-point" (i.e. constant frame rate) photographic method used may not accurately demonstrate the irregular bubble oscillations [2]. The bubble simulations (section 7.1.3) using the Raleigh-Plesset equation showed that no oscillations occurred during the growth phase of all nuclei sizes considered. The oscillations were, instead, thought to have occurred at collapse. In all experiments, the collapse may have been initiated by pressure increases. The pressure increased to positive pressures less than 3 *ms* after the initial negative pressure was reached. The simulations predicted oscillations at bubble collapse of varying amplitude and frequency with periods of oscillations varying in the order of tenths of milliseconds or milliseconds. The period depended significantly on parameters such as the size when

the pressure increases. The photographic records suggested more regular characteristics, with all bubbles reaching maximum size and disappearing almost simultaneously.

Pressure records also appear to indicate bubble oscillations. At each increase in pressure from negative to positive values, oscillations were recorded at the submerged transducer at the bottom of the tube. These pulsations were evident in all pressure records although the peak pressures and trends of the pulsations varied to some extent. These variations suggest cavitational effects. *Secondary pressure pulses* have been recorded and observed in tube-arrest experiments [87,95,122,124-126] and B-P experiments [112,170] and analysed, in detail, in [95,123]. In such experiments, the pressure pulsations have been found to correspond to the oscillations of the bubbles. In all pressure records from the lowest transducer in the Mach 3 shock tube, the pressure pulsations appeared to have periods of less than half a millisecond. Thus, like the simulations, the pressure records suggest oscillation periods smaller than that showed by the experimental, photographic records.

Furthermore, these simulations predicted that bubbles of various sizes grew to sizes of up to about 20 *mm* ($R \approx 10$ *mm*), 1 *ms* after the minimum pressure of -1 *bar* was reached. Then, 2 *ms* after the minimum pressure of -1 *bar* was reached, the bubbles were predicted to have expanded to about 36 *mm* ($R \approx 18$ *mm*). The simulations predict that sizes of this order of magnitude should be visible since the negative pressure is sustained for comparable periods of time. The maximum bubble radii suggested by photographic records were about 2.5 *mm* (refer to section 6.12), an order of magnitude lower than the theoretical estimates.

Possible reasons for the discrepancies between the large predicted bubble sizes and those suggested by the photographic records are given in the following. Firstly, note the relatively slow frame rate of the camera used: Assuming that the bubble wall expands at the asymptotic rate $\dot{R}_{FINAL}$ equal to 8.26 $m.s^{-1}$, the diameter of the bubble under consideration will increase substantially, by about 16.5 *mm*, over 1 *ms*, the time between each photographic frame. This illustrates that the photographic records may significantly

underestimate the maximum bubble sizes by "missing" the corresponding instants in time. To capture the bubble growth such that the maximum observed sizes of bubbles are consistently recorded within a millimetre of the actual maximum values, a camera with a maximum frame rate in the order of tens of thousands of frames per second is needed. Simulations showed that bubble collapse involves even greater bubble wall velocities.

Secondly, it was thought that the rate of evaporation, which is finite, may have been too low to keep up with the expansion of the bubbles and consequently, that the velocities of the bubble walls had been limited to values below the rates predicted by the bubble dynamics analysis (which had not included such factors). It was thought that this may have explained why the radii of the experimentally observed bubbles, one or two milliseconds after the minimum pressure was reached, were smaller than the theoretically predicted values. From kinetic theory, it has been found [93] that the finite rate of evaporation $\dot{m}$ is:

$$\dot{m} = \frac{\alpha p_V}{\sqrt{2\pi RT}} = \alpha \rho_V \sqrt{\frac{RT}{2\pi}} = \rho_V V_D \tag{8.1}$$

where $\dot{m}$ is the mass of liquid that is evaporated or gas that is condensed per unit time, α is the accommodation coefficient of the liquid, V_D is the velocity associated with the rate of evaporation or condensation and p_V, ρ_V and T are the pressure, density and temperature of the vapour for which the ideal gas equation is assumed to apply. Assuming a value of one for the accommodation coefficient, the value of V_D in the present case is about 110 $m.s^{-1}$. Since this value is much greater than the maximum and final velocities of the bubble wall, it is concluded that the evaporation of the liquid occurs rapidly enough too keep up with the rate of expansion of the bubble.

Now, the validity of the Rayleigh-Plesset model is considered. The assumptions of the Rayleigh-Plesset equation (3.8) were listed in section 3.3.1. The assumptions that the bubbles were not affected by other bubbles, or solid particles or walls and that the bubbles remained spherical throughout are doubtful. The assumption that the liquid density is constant is justified, as liquid compressibility does not affect the bubble dynamics significantly. Its main effect is in the formation of shock waves at rebound after

collapse. While the effect of pressure on the surface tension is negligible, the temperature affects the liquid's surface tension significantly [10]. However, since thermal effects are neglected, the liquid viscosity may be considered constant. The assumption of negligible thermal effects during bubble growth was justified in section 3.3.1. However, at the final stage of bubble collapse, temperature effects are always significant due to the high compression of the non-condensed gas within the bubble. In addition, it should be noted that since bubble collapse usually becomes very rapid, there is insufficient time (collapse occurs in microseconds) for appreciable heat transfer to occur and the gas behaves adiabatically rather than isothermally i.e. to assume k =1.4, $k \neq 1$ [5]. This was assumed in most of the simulations.

Finally, it was assumed that the mass of gas (as opposed to the vapour of the liquid) within the bubble remained constant. This is implied by the equations (3.7), (3.9) and (3.10). The effect of non-condensable gases is to cushion the collapse of a bubble, thereby reducing the high pressures and temperatures that would occur at the final stage of collapse. The limited, finite rate of condensation of vapour is the same as the evaporation rate calculated above and thus, V_D = 110 $m.s^{-1}$. Since the condensation process occurs during bubble collapse, consider the figures in appendix R for the collapse of different bubbles subjected to pressure increases, as well as figure 7.10. In most cases, the radial velocity of the bubble wall reached negative values with magnitudes greater than 110 $m.s^{-1}$. In addition, in appendix M, a large bubble with a radius of about 2.5 *mm* was visible in frame 9 but practically invisible in frame 11. Assuming that the radius of the bubble is 0.5 *mm* in frame 11, the photographs suggest a bubble wall collapse velocity of at least 1000 $m.s^{-1}$. Thus, it is concluded that, during collapse, some bubbles collapse too quickly for the vapour within the bubble to condense. In these cases, the non-condensable vapour then acts more as though it was non-condensable gas and thus, the mass of gas effectively increases. A buildup of non-condensable gas near the bubble wall may form a barrier through which vapour must diffuse if it is to condense on the interface [5]. This may effectively slow the finite rate of condensation. In addition, if the effect of the increase in gas content (i.e. the additional cushioning of the collapsing bubble) were

included in the simulations, the results would have shown, presumably, more significantly damped oscillations.

Consider that photographic records showed that a few bubbles were visible well after the absolute pressure had increased to positive values. This is visible from the last frames of appendices M and N. In the present case, the relaxation shock wave postulated by Hassanein et al. [72] and discussed in section 3.1.1 may be expected to be weak due to the low magnitude of the negative pressure. It follows that the bubbles are not expected to persist for very long when the pressure increases i.e. the liquid is not discharged to a great extent from the bubble, which is thus expected to collapse during the positive pressure. The presence of bubbles after the pressure has increased may be attributable to non-condensable remaining in some of the bubbles [5], rather than relaxation shock waves.

There exists a fixed pressure ratio, that depends on the tube cross-section and the method of clamping, for any diaphragm or combination of diaphragms, which may be referred to as the natural bursting pressure ratio [48,172]. The diaphragm will rupture neatly and consistently if it is pricked and bursts when the pressure ratio is above this value [172]. Otherwise, messy flow and inconsistent rupture and hence shocks of different strengths, which are lower than is predicted by theory, for the same pressure ratio) result [172]. Theoretically, for the diaphragm pressure ratio of 7.93/0.027, i.e. approximately 293, the theory predicts a shock strength of about 9. Pressure traces from the transducer embedded in the tube wall of the driven section (transducer 1) showed that the shock wave was not fully developed. A shock generated using such a high pressure-ratio will only become fully formed after travelling a distance equivalent to 3 pipe diameters from the diaphragm station [48]. Since transducer 1 was 609 *mm*, or about 11 pipe diameters, from the diaphragm station, the shock is expected to be fully formed. The formation distance may be larger in the case of the Mach 3 shock tube due to the fact that the diaphragm was not completely removed: In each test, the diaphragm remained in one piece although the high pressure broke a hole through it. The remaining material probably disturbed the transient flow, thereby delaying the formation of the shock, even though the diaphragm was obviously at the natural burst pressure ratio. This is in contrast to findings [48] that the

closest agreement between the observed and theoretical shock strength occurs when the diaphragm shattered and left little material at the diaphragm station. This corresponded to when the diaphragm was near its natural bursting pressure ratio. This was not true in the case of the Mach 3 shock tube. The formation decrement may depend, not only on whether the diaphragm pressure ratio was above or below the natural bursting pressure ratio, but also on the brittle or plastic behaviour of the diaphragm material.

In section 7.1.2, the 'strong', downward-propagating shock that resulted from reflection of the first shock generated in the tube at the upper tube wall was considered. The strength of this shock, which impinges on the liquid column, was estimated as between 6 and 10. However, the pressure record for transducer 2, figure 6.1, shows that the shock strength was about 2. The fact that the initial shock pressure was lower than the value predicted theoretically is partly attributed to boundary layer effects. For the relatively strong air shock strengths involved, this is expected, with the theoretical value only reached behind the shock front, where the pressure increases [172].

Now consider how some of the factors in section 4.7 affect the Mach 3 shock tube. The rate of stressing caused by the Mach 3 shock tube is relatively low: The time taken for the pressure at transducer 3, at the base of the tube, to drop from 7.93 to –1 *bar* was approximately 1.33 *ms*. This value was consistently repeatable and varied within 0.04 *ms* of the mean. It follows that the stressing rate was approximately 6.7 $bar.ms^{-1}$. The conventional bullet-piston experiments listed in appendix H, table H.1 (excluding that of Williams and Williams who used a cattle stun gun to impact the piston) produced pulses with similar stress rates and times elapsed in decreasing the pressure to the cavitation threshold. These values were approximately 1 $bar.\mu s^{-1}$ [143] and 2.2 μs respectively. The other experiments listed in table H.1 involved higher stressing rates and lower times elapsed during the pressure drop. Where possible, these values are presented in the tables. In the tube-arrest experiments of Williams et al. [97], the stressing rate of the expansion wave was about 10 $bar.\mu s^{-1}$. Thus, the stressing rates of the expansion waves produced in the liquid in the Mach 3 shock tube were markedly lower than those of other experiments and partly accounts for the relatively low experimental tensile strength achieved: The

lowest magnitude of the maximum sustainable tension of untreated water, obtained from experiments involving tension pulses, listed in appendix H is 0.85 *MPa* or 8.5 *bar*, which is several times larger than the value found here.

Consider the measurement system used. The work by Marston and Unger [158], Williams and Williams [96] and Boteler and Sutherland [173] predicted similar, relatively high values for the tensile strength. The similarity between these experiments is that they did not use pressure transducers to measure negative pressures directly. Instead, Marston and Unger and Boteler and Sutherland estimated the tensions by recording the displacement and velocity of the membrane that acted as the free surface by interferometric means and relating the particle velocity to the shock strength and tension. Williams and Williams determined the tensile strength value by detecting cavitation by using transducers to record the time between arrival of the compression pulse from the piston and the secondary compression pulse emitted from bubbles at rebound and determining which parameters result in suppressed cavitational activity (i.e. no secondary pressure pulses) by extrapolation as detailed in [96]. In addition, these experimenters used distinctive methods of producing compression pulses that resulted in higher stress rates and contributed to their high tensile strength values. The method used in the present case, was to measure the pressures and tensions directly with PCB 113A21 transducers. The rise time of these transducer was less than 1 μs and natural frequency of these transducers were greater than 500 *kHz*. These performance measures, as well as the sampling rate of the transduction system equal or better those of transducers used by many other researchers in this field [156,123-127]. Williams et al. [124] showed the effect of slower transducers, which underestimate the magnitude of secondary pressure pulses (refer to section 4.7.4). The study validated the use of transducers such as the PCB 113A21 transducer. However, shock waves in water will have rise times of the order of nanoseconds and a short pulse length of only a few microseconds, which requires measurement systems with great temporal and spatial resolution [51,54]. A transducer or hydrophone with a smaller pressure sensing element may be installed for improved spatial resolution. Such micro-pressure hydrophones, which have very short rise times include the Müller-Platte-Gauge, as described in [42,51,54] and the KP-136 transducer

(*Ktech Corp., USA*) used by Williams and Williams [96], which have rise time of about 50 and 66 *ns* respectively and is ideal for the measurement of cavitation effects [42,96]. However, the liquid pulses generated in the Mach 3 and Mach 2 shock tubes are not discontinuous shocks and appear to have rise and fall times in the order of tenths of milliseconds for which the PCB transducers should be adequate.

Now, note that the photographic records showed very different cavitational behaviour occurring near the top of the liquid column than in the lower regions: Only a few bubbles were visible below the vaporising top layer of liquid (refer to figure 6.2), while many bubbles were visible throughout the lower regions (figures 6.3 and 6.4). In other words, the top layer of liquid shows intense cavitation, while the liquid directly below it appeared to experience very little cavitation. The explanation for these observations is firstly that the top layer of liquid had a lower, local tensile strength than the regions below it (due to its saturation with vapour nuclei), and cavitated intensely. Secondly, it is believed that the cavitation at the lower regions of the liquid column extinguished the expansion waves resulting from reflection of the transmitted expansion waves, at the base of the tube. This caused the pressure in the region just below the free surface to drop less than at the bottom of the liquid column and consequently resulted in the lower intensity of cavitation there. This could only be confirmed by installing a pressure transducer through the polycarbonate tube, just below the free surface.

One further factor should be mentioned with regards to cavitation. Within limitations of the optical method of detection used, the visible bubble radius R_V was chosen as 0.5 *mm* i.e. bubbles 1 *mm* in size could be discerned from photographs. Bubbles were assumed to be fully developed once they have reached this size. Kedrinskii [60] chose R_V equal to 0.1 *mm*.

8.2. The Mach 2 Shock Tube

The Mach 2 hydrodynamic shock tube demonstrated the use of conventional air shock tubes to produce liquid compression waves. However, the experiments did not produce cavitation by free surface reflection. The factors responsible for this failure to produce

visible cavitation are considered in this section. Firstly, consider the profiles of the compression pulses produced. It should be noted that the compression pulses recorded at the lowest transducer in the liquid section of the tube, transducer 2, resulted in peak, local static pressures of up to about 10 *bar*. Consider the durations of the pulses near the free surface. At transducer 4, the static pressures decreased to zero (i.e. absolute pressure dropped to atmospheric pressure) after several hundreds to thousands of microseconds. Consider the representative case of the typical pressure records of figure 6.5. The pressure record for transducer 4, which lies within the length of the window section, can now be understood: the tension pulse, from the free surface reaches the transducer in only 40 μs. Thus, since this is much smaller than the duration of the wave, the pulse reaches the transducer when the pressure there has not dropped much from the peak value.

Now, consider transducer 2. The wave diagram for a gas driver pressure of 12 *bar*, figure 7.12, shows that approximately 0.7 *ms* after the lower, submerged transducer experiences the initial, transmitted compression wave, expansion waves, transmitted from the gas section, reach it. Then, less than half a millisecond after the tail of this expansion fan passes the transducer, the first compression wave, of a family that results from free surface reflection of the expansion fan, passes. The drop and subsequent rise following the peak pressure, caused by the families of expansion and of compression waves is evident from the pressure records from transducer 2 on figure 6.5 (between the times marked 6 and 8 *ms*). Then, the pressure drops again due to the expansion wave that results from free surface reflection of the initial compression wave reaches the transducer. Now, an explanation for the apparent pressure rise that occurs at the time marked 10 *ms* is proposed. It is believed that the pressure rise is actually the remaining pressure left behind by the first compression wave. Figure 8.1 shows the recorded pressure variation at transducer 2 (dark line) with the proposed profile (light line) of the incident compression wave. It shows that expansion waves transmitted into the liquid after the compression wave and the wave resulting from free surface reflection of the relatively strong compression wave superimposed onto the pressure at transducer 2 (due to the first compression wave) taking into account the appropriate delay times. This could explain

the unexpected pressure variations there. The time intervals between the arrival different waves at the transducer correspond, adequately, with the wave diagram.

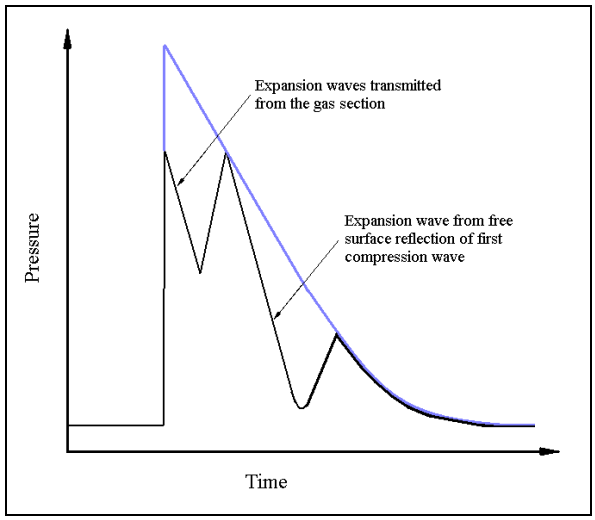


Figure 8.1. Suggested form of the pressure profile of the first compression wave transmitted into the liquid (transducer 2).

The considerations above explain why no absolute negative pressures are imposed on the liquid in the case of a 12 *bar* driver pressure. The lowest absolute pressure, which was recorded at transducer 4, 60 *mm* below the free surface, was an order of magnitude higher than the vapour pressure and no cavitation was observed through the windows.

As noted in section 6.2, the pressure records for an 8 *bar* driver pressure appeared different. The incident liquid compression wave appeared more difficult to characterise. Again, the pressure records showed that the liquid at transducers 2 and 3 sustained a negative static pressure of between –1 and –2 *bar* for a few milliseconds. These correspond to absolute negative pressures of between about –0.2 and –1.175. Then, at various times, the pressure rose abruptly to relatively high values. For most of the tests, two of these pressure pulses could be distinguished from the records of transducer 2 while one could usually be distinguished from those of transducer 3. It should be noted that these increases in pressure were recorded before the next compression wave transmitted from the gas section had arrived. The variability of the amplitude of the pressure rises suggests that cavitation occurred during the negative pressure phases at

these transducer: The collapse and rebound of many bubbles was though to have emitted shock waves. From the wave diagram, it was seen that the pressure rises that caused bubble collapse were due to:

1. The downward-travelling compression waves resulting from free surface reflection of the expansion fan and
2. The upward-travelling compression waves that result from reflection, at the gas-liquid interface at the base of the liquid column, of the expansion wave that results from free surface reflection of the first liquid compression wave.

However, since the liquid at these stations could not be observed since they were situated well below the windows, the cavitation could not be confirmed photographically. The fact the maximum tension value reached was close to the value of –1 *bar*, found in the Mach 3 shock tube and since the working fluid in both cases was settled tap water reinforce the belief that the negative pressures resulted in cavitation.

The wave diagram for an 8 *bar* driver pressure showed no major differences from the 12 *bar* driver case. The most significant difference was that, in the lower, gas section of the tube, the time between the arrival of the head of the expansion fan and the shock wave was less than in the 12 *bar* case. This is understandable since the lower diaphragm pressure ratio should affect the shock speed much more than the speed of the head of the expansion fan. Consider transducers 2 and 3: The drop in pressure from the positive value, after the peak is reached, to the negative pressure is attributed to the expansion wave from free surface reflection of the first liquid compression wave.

In the case of the 8 *bar* driver pressure, like that of the 12 *bar* driver pressure, no absolute negative pressures were imposed on the liquid at transducer 4. This was again attributed to the transducer being too close to the free surface and the tension pulse, resulting from free surface reflection, being superimposed on a positive pressure close to the peak value of the incident compression wave.

From all of the pressure records, it may be concluded that for a shorter pulse length or greater transducer depth, one could impose a maximum absolute negative pressure of

approximately –0.64 or –0.17 *bar* for a 12 or 8 *bar* driver pressure respectively. These maximum tensions are less than the tension that the Mach 3 shock tube is capable of imposing. One could theoretically subject the liquid to greater tensions if the first liquid compression pulses had not been attenuated during their propagation up the pipe, because a weakened compression wave would result in an equally weak expansion wave when reflected from the free surface. The attenuation was evident in all tests, regardless of the driver pressure.

Such attenuation of a compression wave travelling through a water-filled tube has been found to occur in other pulse reflection experiments involving water as the working fluid [95,98,116,174]. Overton and Trevena [116] found that the smaller the rise time of the pulse, the less attenuation occurs. This was attributed to the dissipative forces having less time to act for these higher stress rate. Earlier, they found that tension pulses also suffer attenuation when travelling through a liquid [95,116]. Couzens found that the pressure behind a pulse travelling in boiled, deionised water would decrease by about 10i% for every metre travelled. No other published work on the characteristics of shock attenuation in water was found. None of the experimenters described or analysed the cause of this attenuation.

It is evident, from appendix P (figures P.2-P.4), that the attenuation of the upward-travelling compression wave is greater from transducer 2 to 3 than from 3 to 4. Since these distances are equal, this indicates that either the attenuation of the pulse is a cumulative process or, alternatively, the discontinuous change in area, between transducers 3 and 4 contributed significantly to the attenuation.

It was shown that the change of area needed to incorporate the observation windows would not affect the liquid compression wave to the extent that pressure traces showed. The analysis showed that if the incident shock has strength of 6, it would be attenuated by about 8i% to strength of 5.54. The attenuation must be substantially less than 40i%. The apparent decay of the upward-travelling liquid compression wave could also not be explained by the effects of pipe wall elasticity: Simple calculations predicted that for a

shock with a peak pressure of 6 *bar*, the pressure would be attenuated to 5.08 *bar*. This corresponds to a decrease in shock strength of about 13i%. In addition, the application of Taylor's method predicted that no waves from the gas-liquid interface at the base of the liquid column would overtake and attenuate the shock.

Other factors that may contribute to attenuation of a moving shock are boundary layer and transverse wave effects. A boundary layer generates moving compression and expansion waves, which alter the properties in the region behind the shock, which becomes non-uniform, thereby decreasing the shock strength while the bulging of the diaphragm of the shock tube leads to the generation of a curved shock and, consequently, transverse waves [48]. The high slenderness ratio of the tube is expected to contribute to shock attenuation by increasing the effects of transverse wave reflections, the boundary layer and viscous dissipation [48,172]. The surface roughness and imperfections on the inside of the tube, which had not undergone any special surface finishing treatments, as well as the relatively high gas driver pressure leads to the growth of the boundary layer, which restricts the flow significantly, resulting in shock attenuation [172]. However, because of the high acoustic impedance of water, particle speeds behind the shock are low. This, as well as the near acoustic behaviour of waves in water, minimises the effect of the boundary layer.

It was thought that the liquid shock waves produced might have become unstable and split into two, weaker waves moving in the same or opposite direction as detailed in [10]. However, the equation of state of water is convex at all temperatures i.e. the value of the fundamental derivative G, a third derivative of the internal energy, is greater than zero. Secondly, its adiabatic constant k (= γ) is greater than Γ, the Grüneisen coefficient (a second derivative of energy). These conditions guarantee shock stability and indicated that shocks travelling in water will not become unstable and split up.

Over many tests, the incident gas shock strength varied quite widely. In addition, the initial pressure behind the gas shock was lower than that predicted by theory. This decrease in shock strength may be attributed to distance attenuation and formation

decrement described above [48,172]. To obtain more consistent shock strengths, the diaphragms must be more carefully selected as detailed in [172].

An important factor to consider, again, is the rate of stressing of the waves generated in the Mach 2 shock tube. Consider the pressure records for a 12 *bar* driver pressure, figures 6.5 and P.1. At transducer 2, the lowest submerged transducer, the rise time of the shock varied between approximately 60 and 90 μs. Near the free surface, the rise time of the shock varied between about 280 and 360 μs. For 8 *bar* driver pressures, the rise times of the compression wave at transducer 2 and 4 varied from 1.1-1.3 *ms* and from 0.325-0.415 *ms* respectively. Now, consider the effect of the transition layer in the case of the Mach 2 shock tube. A characteristic time of a transition layer of thickness z_o is the time taken by a pulse, propagating at the sound speed of the liquid c_l, to travel up and down the layer. It is equal to $2z_o/c_l$ [134]. If the characteristic time was very much smaller than the time constant of the incident wave, transition layer will not affect its reflection at the free surface. However, if the magnitudes of the characteristic time and incident wave time constant are comparable, the effect of the transition layer will be to lower the peak tension and spread out of the pulse [134]. The time constants of the compression pulses in the experiments of Sedgewick and Trevena, who found that the free surface reflected was not a mirror image of the incident compression wave, were in the order 10^{-4} *s* i.e. tenths of milliseconds [115,134]. Since these pulses were seriously distorted on reflection, Temperley and Trevena [134] inferred that the characteristic time delay introduced by such a free surface is of the same order. For 12 and 8 *bar* driver pressures, the time constants of the liquid compression waves near the free surface, generated in the Mach 2 shock tube, was thus an order of magnitude higher and of the same order of magnitude as the characteristic time respectively. Thus the transition layer is likely to have had an effect on the reflected tensions.

Again, since the waves involved were not discontinuous and had rise times in the order of tens and hundreds of microseconds, the transducers were judged to have adequately measured the pressures behind them. ~~Overlapping of tension pulses~~

9. Conclusions

Samples of water were forced to cavitate by generating tension in the liquid, using the Mach 3 hydrodynamic shock tube. Tensions of greater magnitude than about 6 or 7 *bar* could be imposed on the test liquid if the length of the driven section is increased. Bubble dynamics simulations showed reasonable, qualitative agreement: the bubbles generally grew during the negative pressure phase and exhibited oscillatory growth and collapse when the pressure increased to positive values, due to compression waves from the free surface and from the upper end of the tube. Pressure records showed secondary pressure pulsations, confirming the oscillatory nature of the collapse at each rise in pressure. More quantitative comparison of theory and experiments would require a high-speed camera with a higher frame rate.

Pulse reflection experiments were not successful in producing cavitation. The test facility was similar to bullet-piston equipment, except that the compression wave was generated by a conventional gas shock tube separated by a flexible sheet. Liquid compression waves with peak static pressures of up to about 10 *bar* were produced. However, no negative pressures or cavitation was observed through the optical section of the tube. Pressure records suggested that maximum negative pressures, similar to those obtained in the Mach 3 shock tube (~ -1 *bar*), and cavitation were generated for lower driver pressures. However, this could not be confirmed as these events occurred below the windows and were not visible. The fact that no absolute negative pressures or even pressures below the vapour pressure were experienced was attributed to the combination of two factors: the pulse duration and the position of the free surface with respect to the windows and the transducer near the free surface. The compression pulse length, which could not be predicted theoretically before design, was, in all tests, greater than 1000 μs. The free surface was not high enough above the transducer for the peak, reflected tension pulse to be superimposed on the lower pressure behind the incident compression wave. In addition, the transition layer should, in the case of the Mach 2 shock tube, have an effect in lowering the peak, reflected tension value.

10. Recommendations

10.1. Improvements of the Mach 3 Shock Tube Rig

Various means may be pursued for demonstrating more intense cavitation. One may seed the liquid with solid particles or free bubbles. As stated earlier, it would be possible to lengthen the driven section such that the arrival of the strong shock wave at the test section and subsequent collapse caused by it would be delayed. Also, the water can be heated to a temperature near the boiling point to further promote bubble growth [2].

To reduce the intensity of cavitation in the tube, the liquid and containers must be purified more. To reduce the amount of free gas entrained in the test liquid, the lower section of the tube should be modified, allowing the tube to be filled the through the bottom [54]. The rig could also be connected to an absorption system for absorbing any gas bubbles, while the dissolved gas content could be controlled by an air-content control system [2]. To generate large liquid tensions, heterogeneous nucleation must be avoided. For this purpose, special equipment is needed [81] while preliminary washing of experimental equipment is important [35]: The sample and its container must be elaborately and thoroughly cleaned as chemical cleaning agents in water may alter the microbubble size distribution, and thereby considerably affect cavitation in the liquid samples [1,35,86]. All surfaces would need to be ground down and a totally re-designed rig, with a test section designed to contain a smaller volume of liquid, to minimise impurities, would probably be needed.

Using a commercial gas cylinder, having a very low dew point, would minimise the effects of water condensation [48]. In light of the foregoing, it is obvious that a camera with a higher frame rate would be beneficial to the studies. In addition, a hydrophone could be installed into the tube to ensure that rapid changes are recorded accurately (note that the measurement of some shocks emitted at bubble collapse may be practically discontinuous and require a measurement system including a transducer with a faster response.

10.2. Improvements of the Mach 2 Shock Tube Rig

A material with lower inertia than insertion rubber may be used to act as the gas-liquid interface. One benefit of this may be in generating compression waves with shorter rise times (by accelerating the liquid more rapidly), thereby minimising the effect of the transition layer. Another effect might be in generating liquid compression pulses with shorter durations, resulting in cavitation within the length of the observation section of the tube. On the other hand, one may alter the tube length: The pressure records for a gas driver pressures of 8 *bar* showed negative absolute pressures and suggested that cavitation occurred at the lower part of the tube, at transducer 2. One could shorten the upper, liquid-filled section such that the transparent observation section is at this lower part of the tube. However, one would then have to ensure that unwanted overlapping of waves, near the base, does not occur. Alternatively the tube could be of modular structure such that is would be adjustable.

Shortening the liquid section of the tube would also result in less attenuation of compression pulses and thus, stronger tension waves. Alternatively, one could construct a transition section to make the change in cross-sectional area between the window section and the pipe more gradual. [93].

10.3. Further Studies

While Shock Wave Lithotripsy or SWL is commonly and effectively used to break kidney stones and for treating other uncomplicated, upper urinary tract calculi, it is currently ineffective in more complicated cases, such as that of urethral stones [27]. While cavitation plays a significant role in stone breakage in SWL, experiments have shown that cavitation is definitely linked with SWL-induced tissue damage [27]. For the development of SWL and improvement of lithotripsy procedures and techniques, the cavitation events must be controlled. Thus, further research on the parameters affecting and effects of cavitation as well as the precise mechanism of cavitation and stone breakage, which are not completely understood, would be worthwhile.

In particular, cavitation that results behind focussed sound waves using soft or pressure-release reflectors, as observed by [27,54], deserves further attention. It is particularly interesting as it may find application in medical procedures where conventional shock wave lithotripsy or SWL is ineffective. Müller first suggested the possible application of the "soft" focussing technique in manipulating human body tissue (which has a similar acoustic impedance to water) such as cancer cells, where focussed shocks are also ineffective [54]. He postulated that the combination of the tensile stresses and shocks from bubbles collapse may attack soft materials. The technique could also be used for more complicated cases of stone breakage, as mentioned above [27]. The effect of using non-rigid or "soft" reflectors is, effectively, to alter the pressure variation at the focus such that the negative pressure precedes the positive peak. The effects of soft reflectors are not yet completely understood and the studies of Müller and Bailey et al. are the only known experiments that involve them. As discussed in section 4.4, the experiments of Bailey et al. [27] showed that it may be safer than using conventional reflectors and improve SWL applications although it appears to be less effective in stone comminution (breakage) [27].

Such focussing experiments could easily be performed using the Mach 2 shock tube rig, which could be modified again to the focussing setup described and used by Karnovsky [42]. In his experiments using hard reflectors, absolute negative pressures and what appeared to be cavitation clouds were produced in water. As stated earlier, an advantage of focussing of waves is that one can produce true homogeneous nucleation away from solid boundaries.

Further studies may be worthwhile in the field of heterogeneous nucleation. Adequate techniques for resolving and characterising the size and nature of the total spectrum of nuclei have yet to be developed [80]. Experiments with this goal may involve the deliberate seeding of a test liquid with solid particles of known characteristics such as those of Arora et al. [34] and Marschall et al. [39]. Indeed, the characterisation of nuclei may be one of the least developed fields related to cavitation. Consensus has not been reached on the mechanism of stability of free gas nuclei. Until research yields a better

understanding of nuclei, exact predictions of the distribution and size of nuclei and improved heterogeneous nucleation models present in water samples cannot be made [7]. The Mach 3 or Mach 2 shock tube or modified versions of them could be employed for such studies.

11. References

1. Young, R. F. *Cavitation*. McGraw-Hill Book Company (U.K.) Limited, Maidenhead, Berkshire, U.K., 1989.
2. Knapp, R. T., Daily, J. W., Hammitt, F. G. *Cavitation*. McGraw-Hill Book Company, Inc., New York, U.S.A., 1970.
3. Giancoli, D.C. *Physics for Scientists and Engineers*: *Second Edition*. Prentice Hall, Englewood Cliffs, New Jersey, U.S.A., 1988.
4. Xiao, C., Heyes, M. E., Parker, M .E., Powles, J. G. *Cavitation in Liquids by Classical Nucleation Theory and Molecular Dynamics Simulations.* In: *Proceedings of the NATO Advanced Research Workshop on Liquids Under Negative Pressure*. Kluwer Academic Publishers, Dordrecht, The Netherlands, 2002. V.2.
5. Brennen, C. E. *Cavitation and Bubble Dynamics*. Oxford University Press, U.K. 1995. Also available at: http://caltechbook.library.caltech.edu/1/00/content.htm. (9)
6. Parmakian, J. *Waterhammer Analysis*. Prentice-Hall, New York, U.S.A., 1955. Longman's, Green, 1955.
7. Pearsall, I. S., *Cavitation*. Mills & Boon Limited, London, U.K., 1972.
8. Barrow, M. S., Bowen, W., Hilal, N., Al-Hussany, A., Williams, P. R., Williams, R. L. Wright, C. *A Study of Cavitation Phenomena Using an Atomic Force Microscope*. In: Proceedings of the NATO Advanced Research Workshop on Liquids Under Negative Pressure. Kluwer Academic Publishers, Dordrecht, The Netherlands, 2002. V3: 7
9. Suslick, K. S. *Sonochemistry*. Science, Vol. 247, 1990, p. 1439-1445.
10. Ben-Dor, G., Igra, O., Elperin, T. (Eds). *Handbook of Shock Waves, Volume 1, Theoretical, Experimental and Numerical Techniques*. Academic Press. San Diego, CA, U.S.A., 2001.
11. Putterman, S., Evans, P. G., Vazquez, G., Weninger, K. *Cavitation Science: Is There a Simple Theory of Sonoluminescence?* Nature, Vol. 409, 2001, p. 782 – 783.
12. Zhao, Z., Glod, S., Poulikakos, D. *Pressure and Power Generation during Explosive Vaporization on a Thin-Film Microheater*. International Journal of Heat and Mass Transfer, Vol. 43, 2000, p. 281-296.I THINK IT IS THIS REF. I LOST IT

13. Herman, B. A., Porter, J. M., Carey, R. F. *Study of an Acoustic Technique to detect Cavitation Produced by a Tilting Disc Valve*. Journal of Heart Valve Disease, Vol. 5, No. 1, 1996, p. 90-96.
14. Lin, H. Y., Biancucci, B., Deutsch, S., Fontaine, A., Tarbell, J. M. *Observation and Quantification of Gas Bubble Formation on a Mechanical Heart Valve*. Journal of Biomechanical Engineering, Vol. 122, 2000, p. 304-309.
15. Mason, T. J. *Sonochemistry: Theory, Applications and Uses of Ultrasound in Chemistry*, E. Horwood, Chichester, U.K., 1988.
16. Suslick, K. S., Didenko, Y., Fang, M. M., Hyeon, T., Kolbeck, K. J., McNamara, W. B. III, Mdleleni M. M., Wong, M. *Acoustic Cavitation and its Chemical Consequences.* Philosophical Transactions of the Royal Society A, Vol. 357, 1999, p. 335-353.
17. Mason, T. J. *Sonochemistry*, Oxford University Press, Oxford, U.K., 1999.
18. McLaughlin, M. C., Zisman, A. S. *The Acoustic Cleaning Handbook*. Alconox, Inc., N.Y., U.S.A., 2002.
19. Abramov, O. V., *High Intensity Ultrasonics: Theory and Industrial Applications***,** Gordon and Breach Science Publisher, London, U.K., 1999. 684 p
20. Brown, B. *High-Intensity Ultrasonics: Industrial Applications*. Iliffe Books, London, U.K., 1965.
21. Abramov, O. V. *Ultrasound in Liquid and Solid Metals*, CRC Press, LLc., Boca Raton, FL, U.S.A., 1995. 493 p
22. McCausland, L. J., Cains, P. W., Martin, P. D. *Use the Power of Sonocrystallization for Improved Properties*. Chemical Engineering Progress, Vol. 97, No. 7, 2001, p. 56-61.
23. Kalumuck, K. M., Chahine, G. L., Hsiao, C. T., Choi, J. K. *Remediation and Disinfection of Water Using Jet Generated Cavitation*. Proceedings of the Fifth International Symposium on Cavitation, Osaka, Japan, November 1-4, 2003, Cav03-OS-2-2-003.
24. Kakegawa, A., Kawamura, T. *An Experimental Study on Oxidation of Organic* Compounds by Cavitating Water-Jet. Proceedings of the Fifth International Symposium on Cavitation, Osaka, Japan, November 1-4, 2003, Cav03-OS-2-2-002.

25. Soyama, H., Macodiyo, D. *Improvement of Fatigue Strength on Stainless Steel by Cavitating Jets in Air*. Proceedings of the Fifth International Symposium on Cavitation, Osaka, Japan, November 1-4, 2003, Cav03-OS-2-3-002.
26. Juhasz, T., Kastis, G. A., Suarez, C., Bor, Z., Bron, W. E. *Time-resolved Observations of Shock Waves and Cavitation Bubbles Generated by Femtosecond Laser pulses in Corneal Tissue and Water*. Lasers in Surgery and Medicine, Vol 19, No. 1, 1996, p. 23-31. Wiley-Liss, Inc.
27. Bailey, M. R., Evan, A. P., Sapozhnikov, O. A., Cleveland, R. O., Colonius, T. *Cavitation in Shock Wave Lithotripsy*. Proceedings of the Fifth International Symposium on Cavitation, Osaka, Japan, November 1-4, 2003, Cav03-OS-2-1-006.
28. H. Shangguan, L. W. Casperson, A. Shearin, K. W. Gregory, and S. A. Prahl, *Photoacoustic Drug Delivery: The Effect of Laser Parameters on Spatial Distribution of Delivered Drug*, SPIE Proceedings of Laser-Tissue Interaction: VI, Jacques S. L. (Ed.), Proc. SPIE, Vol. 2391, 1995, p. 394-402.
29. Deng, C. X., Seiling, F., Pan, H., Cui, J. *Ultrasound-Induced Membrane Porosity*. Ultrasound in Medicine and Biology, Vol. 30, No. 4, 2004, p. 519-526.
30. Ohl, Claus-Dieter, Arora, M., Ikink, R., Delius, M., Wolfrum, B. *Drug Delivery Following Shock Wave Induced Cavitation*. Proceedings of the Fifth International Symposium on Cavitation, Osaka, Japan, November 1-4, 2003, Cav03-OS2-1-001.
31. Unger, E. C., Hersh, E., Vannan, M., McCreery, T. *Gene delivery using ultrasound contrast agents*. Echocardiography, Vol. 18, 2001, p. 355-361.
32. Tang, H., Wang, C. C. J., Blankschtein, D., Langer, R. *An Investigation of the Role of Cavitation in Low-Frequency Ultrasound-Mediated Transdermal Drug Transport.* Pharmaceutical Research, Vol. 19, No. 8, 2002, p. 1160 – 1169.
33. Allen, J. S., Yoshizawa, S., Kaneko, Y., Matsumoto, Y. *Development and Application of Contrast Agent* Models. Proceedings of the Fifth International Symposium on Cavitation, Osaka, Japan, November 1-4, 2003, Cav03-2-1-007.
34. Arora, M., Ohl, C., Mørch, K. A. *Cavitation Inception on Micro-Particles.* Proceedings of the Fifth International Symposium on Cavitation, Osaka, Japan, November 1-4, 2003, Cav03-OS-3-002.

35. Besov, A., Kedrinskii, V. K., De Vries, J., Kloosterman, M. *Cavitation Thresholds, Free Surface and Cavity Cluster Dynamics in Liquids at Shock Wave Reflection*. In: Proceedings of the NATO Advanced Research Workshop on Liquids Under Negative Pressure. Kluwer Academic Publishers, The Netherlands, 2002.(8)
36. Kedrinskii, V. K. *The Iordansky – Kogarko – van Wijngaarden Model: Shock and Rarefaction Wave Interactions in Bubbly Media*. Applied Scientific Research, Vol. 58, p. 115-130. In: Biesheuvel, A., van Heijst, G. J. F. (Eds), Fascination of Fluid Dynamics. Kluwer Academic Publishers, The Netherlands, 1998. (5)
37. Kedrinskii, V. K. *Rarefaction Waves and Bubbly Cavitation in Real Liquid*. Proceedings of the Fourth International Symposium on Cavitation, Pasadena, California, U.S.A., 20-23 June, 2001, Cav2001: session B4.001. (6)
38. Kedrinskii, V. K. *Relaxation Effects and Disintegration Problems of Cavitating Liquids at Pulse Loading*. In: Proceedings of the NATO Advanced Research Workshop on Liquids Under Negative Pressure. Kluwer Academic Publishers, Dordrecht, The Netherlands, 2002. (7)
39. Marschall, H. B., Mørch, K. A., Keller, A. P., Kjeldsen, M. *Cavitation Inception by Almost Spherical Solid Particles in Water,* Proceedings of the Fourth International Symposium on Cavitation, Pasadena, California, U.S.A., 20-23 June, 2001, Cav2001: session A1.002 1. Also in: Physics of. Fluids. Vol. 15, 2003, p. 494.
40. Caupin, F., Fourmond, V. *Ultrasonic Cavitation in Freon at Room Temperature*. In: Proceedings of the NATO Advanced Research Workshop on Liquids Under Negative Pressure. Kluwer Academic Publishers, The Netherlands, 2002. (V.8)
41. Autrey, T., Egereva, S., Foster, N. S., Fokin, A., Ovchinnikov, O. *Counting Particles by means of Optoacoustics: Potential Limits in Real Solutions*. Review of Scientific Instruments Volume 74, Number 1, January 2003.
42. Karnovsky, H. *Production of Free Surface Water Jets Using Focussed Underwater Shock Waves.* M.Sc. Thesis. University of the Witwatersrand, Johannesburg, 2000.
43. Kosing, O. *An Investigation of High Speed Metal Forming with Liquid Shock Waves*. Ph.D. Thesis. University of the Witwatersrand, Johannesburg, 1998.
44. Rudinger, G. *Wave Diagrams for Nonsteady Flows*. D. Van Nostrand Company, Inc., N.Y, U.S.A., 1955.

45. *Course Notes: MECN403, MECN426: Compressible Flow*. School of Mechanical Engineering, University of the Witwatersrand, Johannesburg.
46. Ben-Dor, G., Igra, O., Elperin, T. (Eds). *Handbook of Shock Waves, Volume 2, Shock Wave Interactions and Propagation*. Academic Press, San Diego, CA, U.S.A., 2001.
47. Anderson, J. D. *Fundamentals of Aerodynamics. Third Edition.* McGraw-Hill Higher Education, N.Y., U.S.A., 2001.
48. Skews, B. W., *The Construction and Calibration of a Gas Shock Tube.* M.Sc. Thesis. University of the Witwatersrand, Johannesburg, 1961.
49. Thompson, P. A. *Compressible-Fluid Dynamics***.** McGraw-Hill, New York, 1972.
50. Rao, S. R., *Mechanical Vibrations: 3rd Edition.* Addison-Wesley Publishing Company, Reading, Massachusetts, 1995.
51. Mortimer, B. J. P. *Liquid Wave Focussing and the Production of Pulsed Jets*. Ph.D. Thesis. University of the Witwatersrand, Johannesburg, 1997.
52. Moran, M. J., Shapiro, H. N. *Fundamentals of Engineering Thermodynamics. 3rd Edition.* John Wiley & Sons Ltd., Chichester, West Sussex, U.K., 1998.
53. Courant, R., and Friedrichs, K. O. *Supersonic Flow and Shock Waves.* Springer-Verlag, N.Y., U.S.A., 1976. Interscience Publishers, 1948.
54. Müller, M. *Experimental Investigations on Focusing of Weak Spherical Shock Waves in Water by Shallow ellipsoidal Reflectors.* Acustica, Vol. 64, 1987, p. 85-93.
55. Cole, R. H. *Underwater Explosions*. Dover Publications, Inc., N.Y., U.S.A., 1965.
56. Glass, I. I., Sislian, J. P. *Nonstationary Flows and Shock Waves*. Clarendon Press, Oxford, U.K., 1994. (The Oxford engineering science series - 39).
57. Yomita, Y., Tsubota, M., An-anaka, N. *Energy Evaluation of Shock Wave Emission and Bubble Generation by Laser Focusing in Liquid Nitrogen.* Proceedings of the Fourth International Symposium on Cavitation, Pasadena, California, U.S.A., 20-23 June, 2001, Cav2001: session A2.006.
58. Henderson, L. F. *On the Refraction of Shock Waves.* Journal of Fluid Mechanics, Vol.198, 1989, p. 365-386. Great Britain.
59. Trevena, D. H. *Cavitation and Generation of Tension in Liquids*. Journal of Physics D: Applied Physics, Vol. 17, 1984, p. 2139-64.

60. Kedrinskii, V. *Surface Effects from an Underwater Explosion (Review)*. Translated from Zhurnal Prikladnoi Mekhaniki i Tekhnicheskoi Fiziki, No. 29, July-August 1978, p. 66-78.(2) (No.??????, MAKE UP: 29, EXTRAPOLATED MONTHLY FROM (1))
61. Kedrinskii, V. K. *Dynamics of the Cavitation Zone During an Underwater Explosion Near a Free Surface*. Translated from Zhurnal Prikladnoi Mekhaniki i Tekhnicheskoi Fiziki, No. 5, September-October 1975, p. 68-78. (1)
65. Faizullin, M., Skripov, V. P. *The Thermophysical Properties of Liquids on the Melting Line at Negative Pressures*. In: Proceedings of the NATO Advanced Research Workshop on Liquids Under Negative Pressure. Kluwer Academic Publishers, The Netherlands, 2002. (II.2)
66. Balibar, S., Caupin, F. *Metastable Liquids*. Journal of Physics: Condensed Matter Vol. 15, 2003, p. 875–882.
67. Házi, G., Imre, A. *Negative Pressure Tail of a Reflected Pressure Pulse: A Lattice-Boltzmann Study*. In: Proceedings of the NATO Research Workshop on Liquids Under Negative Pressure. Kluwer Academic Publishers, The Netherlands, 2002. (V.7)
68. Imre, A. R. *Liquid-Liquid Phase Equilibria in Binary Mixtures Under Negative Pressure*. In: Proceedings of the NATO Advanced Research Workshop on Liquids Under Negative Pressure. Kluwer Academic Publishers, The Netherlands, 2002. *II.3.
69. Martinás, K. Imre, A. *Classical Thermodynamics of States with Negative Absolute Pressure*. In: Proceedings of the NATO Research Workshop on Liquids Under Negative Pressure. Kluwer Academic Publishers, The Netherlands, 2002. *I.3
70. Akulichev, V. A. *Acoustic Cavitation Thresholds of Ocean Water*. In: Proceedings of the NATO Advanced Research Workshop on Liquids Under Negative Pressure. Kluwer Academic Publishers, The Netherlands, 2002. *V.1
71. Hassanein, A., Konkashbaev, I. *Modelling and Simulation of Fragmentation of Suddenly Heated Liquid Metal Jets*. Argonne National Laboratory Report ANL-ET/01-13, June 2001.
72. Hassanein, A., Konkashbaev, I., Norem, J. *Thermoelastic Response of Suddenly Heated Liquid Targets in High-Power Colliders*. Proceedings of the 2001 Particle Accelerator Conference, Chicago, Argonne National Laboratory, Argonne, IL, USA

73. Williams, P. R., Williams, P. M., Brown, S. W. J., Temperley, H. N. V. *On the Tensile Strength of Water Under Pulsed Dynamic Stressing*. Proceedings of the Royal Society of London A, 1999, Vol. 455, p. 3311-3323. DUPLICATE! Williams, Williams, Brown, Temperley. 1999.
74. Sedgewick, S. A., Trevena, D. H. *An Estimate of the Ultimate Tensile Strength of Water*. Journal of Physics D: Applied Physics, Vol. 9, 1976, p. L203-205. Letter to the Editor
75. Temperley, H. N. V. *The Behaviour of Water Under Hydrostatic Tension: III*. Proceedings of the Physical Society, Vol. 59, No. 2, 1947, p. 199-208. 1 March
76. Temperley, H. N. V., Trevena, D. H. *Metastability of Phase Transitions and the Tensile Strength of Liquids*. Proceedings of the Royal Society of London, Series A, Mathematical and Physical Sciences, Vol. 357, No. 1690, Nov. 4, 1977, p. 395-402.
77. Winterton, R. H. S. *Nucleation of Boiling and Cavitation*. Journal of Physics D: Applied Physics, Vol. 10, 1977, p. 2041-2056.
78. Joseph, D. D. *Cavitation and the State of Stress in a Flowing Liquid*. Cav2001 Fourth International Symposium on Cavitation, Pasadena, California, U.S.A., 20-23 June, 2001 (http://www.aem.umn.edu/people/faculty/joseph/papers/cavupdate.pdf).
79. Eldridge, J. E., Fye, P. M., Spitzer, R. W. *Photography of Underwater Explosions I.* OSRD, Vol. 6246, 1946.
80. Kedrinskii, V. *Liquid Fracture at Explosive Loading*. In: Brun, R., Dumitrescu, L. (Eds). *Shock Waves @ Marseille III*. Springer-Verlag, Berlin, Heidelberg, 1995. (4)
81. Zheng, Q., Green, J., Kieffer, J., Poole, P., Shao, J., Wolf, G., Angell, C. *Limiting Tensions for Liquids and Glasses from Laboratory and MD Studies*. In: Proceedings of the NATO Research Workshop on Liquids Under Negative Pressure. Kluwer Academic Publishers, The Netherlands, 2002. I.4.
82. Fetter, A. L. *Vortices and Ions in Helium.* In: Benneman, K. H., Ketterson, J. B. (Eds.). *The Physics of Liquid and Solid Helium*. Wiley, N.Y., 1976, p. 207-305.
83. Weyl, W. A., Marboe, E. C. *Some Mechano-Chemical Properties of Water*. O.N.R. Report., November, 1948.
84. Epstein, P. S., Plesset, M. S. *On the Stability of Gas Bubbles in Liquid-Gas Solutions*. Journal of Chemistry and Physics, Vol. 18, 1950, p. 1505-1509.

85. Harvey, E. N., Barnes, D. K., McElroy, W. D., Whiteley, A. H., Pease, D. C., Cooper, K. W. *Bubble Formation in Animals: I, Physical Factors*. Journal of Cellular and Comparative Physiology., Vol. 24, No. 1, August 1944, p. 1-22. Harvey et al (Stabilization model)
86. Fox, F. E. and Herzfeld, K. F. *Gas Bubbles with Organic Skin as Cavitation Nuclei*. Journal of the Acoustical Society of America., Vol. 26, No. 6, 1954, p. 984-989. Nov
87. Chesterman, W. D. *The Dynamics of Small Transient Cavities*. Proceedings of the Physical Society B, Vol. 65, No. 11, November 1952, p. 846–858.
88. Maris, H. J., Konstantinov, D. *Nucleation of Bubbles on Electrons in Liquid Helium.* In: Proceedings of the NATO Advanced Research Workshop on Liquids Under Negative Pressure. Kluwer Academic Publishers, The Netherlands, 2002. (There's another ref in Junk) **IV-4**
89. Rayleigh, Lord (Strutt, J. W.). *On the Pressure Developed in a Liquid during the Collapse of a Spherical Cavity*. Philosophical Magazine, Vol. 34, 1917, p. 94-98.
90. Plesset, M. S. *The Dynamics of Cavitation Bubbles*. ASME Journal of Applied Mechanics, Vol. 16, 1949, p. 228-231.
91. Plesset, M. S., Prosperetti, A. *Bubble Dynamics and Cavitation*. Annual Review Fluid Mechanics, Vol. 9, 1977, p. 145-185.
92. Kedrinskii, V. K. *Peculiarities of Bubble Spectrum Behaviour in Cavitation Zone and its Effect on Wave Field Parameters*. Proceedings of the International Symposium on Ultrasonics: Ultrasonic-85, London, 1985, p. 225-230. (0)
93. Fujikawa, S., Akamatsu, T. *Observation of Cavitation Bubble Collapse Produced in a Water Shock Tube*. Bulletin of the Japanese Society of Mechanical Engineers, Vol. 21, 1978, p. 223-230. WRONG REFERENCE, COULDN'T FIND IT.
94. Fujikawa, S., Akamatsu, T. *Effects of the Non-equilibrium Condensation of Vapour on the Pressure Wave Produced by the Collapse of a Bubble in a Liquid*. Journal of Fluid Mechanics, Vol. 97, 1980, p. 481-512.
95. Overton, G. D. N., Trevena, D. H. *Cavitation Phenomena and the Occurrence of Pressure-tension Cycles Under Dynamic Stressing*. Journal of Physics D: Applied Physics, Vol. 14, 1981, p. 241-50.
96. Williams, P. R., Williams, R. L. *Measurements of the Cavitation Threshold of Liquids Under Dynamic Stressing by Pulses of Tension*. In: Liquids Under Negative Pressure. Also in: Williams, P. R., Williams, R. L. *Cavitation of Liquids Under*

Dynamic Stressing by Pulses of Tension. J Phys. D: Appl. Phys., Vol. 35, 2002, p. 2222-30. Also in: Williams, P. R., Williams, R. L. *Cavitation and the Tensile Strength of Liquids under Dynamic Stressing*. Molecular Physics, October 2004, Vol. 102, No. 19–20, p. 2091–2102. (V.6)

97. Berthelot, M. *Sur Quelques Phenomenes de Dilatation Force des Liquids*. Annales de chimie et de physique, Vol. 30, 1850, p. 232–237.
98. Sedgewick, S. A., Trevena, D. H. *Breaking Tensions of Dilute Polyacrylamide Solutions*. Journal of Physics D: Applied Physics, Vol. 11, 1978.
99. Temperley, H. N. V., Chambers, L. G. *The Behaviour of Water under Hydrostatic Tension: I*. Proceedings of the Physical Society, Vol. 58, No. 4, 1946, p. 420-436. 1 July
100. Temperley, H. N. V. *The Behaviour of Water under Hydrostatic Tension: II*. Proceedings of the Physical Society, Vol. 58, No. 4, 1946, p. 436-443. 1 July
101. Richards, B. E., Trevena, D. H. *The Measurement of Positive and Negative Pressures in a Liquid contained in a Berthelot Tube*. Journal of Physics D: Applied Physics, Vol. 9, No. 11, 1976, p. L123-126.
102. Evans, A. *Evidence for Bulk Nucleation in the Berthelot Tube at Ground Level*. Journal of Physics D: Applied Physics, Vol. 17, 1984, p. L97-100.
103. Overton, G. D. N., Trevena, D. H. *Cavitation Experiments with Water in a Steel Berthelot Tube*. Journal of Physics D: Applied Physics, Vol. 13, No. 7 (14 July 1980), p. 1309-1314
104. Briggs, L. J. *Limiting Negative Pressure of Water*, Journal of Applied Physics, Vol. 21, 1950, p. 721-722. *OR Limiting Negative Pressure*
105. Davies, R. M., Trevena, D. H., Rees, N. J. M., Lewis, G. M. *The Tensile Strength of Liquids Under Dynamic Stressing*. Proceedings of the 1955 National Physical Laboratory Symposium on Cavitation in Hydrodynamics, 1956, Paper 5, p. 20.
106. Kedrinskii, V. K. *Explosion Hydrodynamics: Experiment and Models*. In: Meier, G. E. A., Thompson, P. A. (Eds.) *Adiabatic Waves in Liquid-Vapor Systems*. IUTAM Symposium Göttingen, Germany, 1989, Springer-Verlag, Berlin, 1990. (3)
107. Temperley, H. N. V., Trevena, D. H. *Metastable Effects Associated with the Reflection of a Pressure Pulse at the Free Surface of Water*. Journal of Physics D: Applied Physics, Vol. 12., 1979.

108. Wilson, D. A., Hoyt, J. W., McKune, J. W. *Measurement of Tensile Strength of Liquid by Explosion Technique*. Nature, Vol. 253, 1975, p. 723-5. Wilson et al '75

109. Richards, B. E., Trevena, D. H., Edwards, D. H. *Cavitation Experiments using a Water Shock Tube*. Journal of Physics D: Applied Physics, Vol. 13, No. 7, 1980, p. 1315-1323. 14 July

110. Wentzell, R. A., Scott, H. D., Chapman, R. P. *Cavitation Due to Shock Pulses Reflected from the Sea Surface.* The Journal of the Acoustical Society of America. Vol. 36, No. 3, Part 2, 1969. (From free surface reflection)

111. Couzens, D. C. F., Trevena, D. H. *Critical Tension in a Liquid Under Dynamic Conditions of Stressing*. Nature, 1969, London. Vol. 222, p. 473-4. [C&T'69]

112. Couzens, D. C. F., Trevena, D. H. *Tensile Failure of Liquids under Dynamic Stressing*. Journal of Physics D: Applied Physics, Vol. 7, 1974, p. 2277-87. [C&T'74]

113. Bull, T. H. *The Tensile Strength of Liquids Under Dynamic Loading*, Philosophical Magazine, Vol. 8, 1956, p. 153-165. FROM APPENDIX (TENSIONS) 20:

114. Carlson, G. A., Levine, H. S. *Dynamic Tensile Strength of Glycerol*. Journal of Applied Physics, Vol. 46, 1975, p. 1594-1601.

115. Sedgewick, S., Trevena, D. H. *Limiting Negative Pressure of Water under Dynamic Stressing*. Journal of Physics D: Applied Physics, Vol. 9, 1976, p. 1983-1990.

116. Overton, G. D. N., Trevena, D. H. *Some Factors which Influence the Observed Dynamic Breaking Tensions of a Liquid*. Journal of Physics D: Applied Physics, Vol. 15, 1982, p. L3-6. Letter to the Editor,

117. Carlson, G. A., Henry, K. W. *Technique for Studying Dynamic Tensile Failure in Liquids: Application to Glycerol*. Journal of Applied Physics, Vol. 44, 1973, p. 2201-2206.

118. Carlson, G. A. *Dynamic Tensile Strength of Mercury*. Journal of Applied Physics Vol. 46, 1975, p. 4069.

119. Davydov, M. N., Kedrinskii, V. K. *Two-phase Models of Formation of Cavitating Spalls in a Liquid*. Journal of Applied Mechanics and Technical Physics, Vol. 44, No. 5, 2003, p. 660-666. [Davydov-Kedrinskii (PMTF)]

120. Davydov, M. N., Kedrinskii, V. K. *Mathematical Simulation of Bubbly Clusters and Spall Formation in a Liquid at Dynamic Loading*. Proceedings of the Fifth

International Symposium on Cavitation, Osaka, Japan, November, 1-4, 2003, Cav-03-GS-4-003.

121. Kedrinskii, V., Besov, B., Davydov, M., Makarov, A., Stebnovsky, S. *Shock Tube Simulation and Direct Observation of Fragmentation in Viscous Liquid at Dynamic and Quasi-Static Loading*. Proceedings of the Fifth International Symposium on Cavitation, Osaka, Japan, November 1-4, 2003, Cav-03-GS-4-004.
122. Overton, G. D. N., Williams, P. R., Trevena, D. H. *The Influence of Cavitation History and Entrained Gas on Liquid Tensile Strength*. Journal of Physics D: Applied Physics, Vol. 17, 1984, p. 979-87.
123. Williams, P. R., Williams, P. M. *Pressure-Tension Cycles Induced by Dynamic Stressing and Cavitation in Liquids*. Journal of Physics D: Applied Physics, Vol. 29 1996, p. 1904-1909.
124. Williams, P. R., Williams, P. M., Brown, S. W. J. *Pressure Waves Arising from the Oscillation of Cavitation Bubbles under Dynamic Stressing*. Journal of Physics D: Applied Physics, Vol. 30, 1997, p. 1197-1206.
125. Williams, P. R., Williams, P. M., Brown, S. W. J. *An Instrument for Studying Cavitation Phenomena in Liquids Subjected to Tension Generated ab initio and by Free-Surface Reflection of Compressional Waves*. Measurement Science and Technology. Vol. 9, 1998, p. 976-982.
126. Williams, P. R., Williams, P. M., Brown. *Cavitation Phenomena in Water Involving the Reflection of Ultrasound Pulses from a Free Surface, or from Flexible Membranes*. Physics in Medicine and Biology, Vol. 43, 1998, p. 3101-3111.
127. Williams, P. R., Williams, P. M., Brown, S. W. J., Temperley, H. N. V. *On the Tensile Strength of Water under Pulsed Dynamic Stressing*. Proceedings of the Royal Society of London A, 1999, Vol. 455, p. 3311-3323.
128. Williams, P. R., Overton, G. D. N., Jones, W. M., Trevena, D. H. Proceedings of the Forum on Cavitation and Polyphase Flow, N. Y., ASME, Paper 2, 1982.
129. Lackmé, C. (1978) Proceedings of the Colloquium, Ispra, 1977 (Luxembourg: Commission of the European Communities)
130. Hansson, I., Kedrinskii, V. K., Mørch, K. A. *On the Dynamics of Cavity Clusters*. Journal of Physics D: Applied Physics, Vol. 15, 1982, p. 1725-1734.

131. Mader, H. M., Zhang, Y., Phillips, J. C., Sparks, R. S. J., Sturtevant, B. Stolper, E. *Experimental Simulations of Explosive Degassing of Magma.* Nature, Vol. 372, 1994, p. 85-88.

132. Alidibirov, M., Dingwell, D. B. *An Experimental Facility for the Investigation of Magma Fragmentation by Rapid Decompression.* Bulletin of Volcanology. Vol. 58, 1996, p. 411-416.

133. Sturtevant, B., Glicken, H., Hill, L., Anilkumar, A. V. *Explosive Volcanism in Japan and the United States: Gaining an Understanding by Shock Tube Experiments*. Proceedings of the 18th International Symposium on Shock Waves. In: "Shock Waves", p. 129–40, K. Takayama (Ed.), 1992, Springer-Verlag, N.Y.

134. Temperley, H. N. V., Trevena, D. H. *Why is the Tensile Strength of Water Measured Dynamically less than that Measured Statically?* Journal of Physics D: Applied Physics, Vol. 20, 1987, p. 1080-1.

135. Chavanne, X., Balibar, S., Caupin, F. *Acoustic Nucleation of solid helium 4 on a clean Glass Plate*. Journal of Low Temperature Physics, Vol. 125, 2001, p. 155-64.

136. Balibar, S. Caupin, F. *The Limits of Metastability of Liquid Helium*. In: Proceedings of the NATO Advanced Research Workshop on Liquids Under Negative Pressure. Kluwer Academic Publishers, Dordrecht, The Netherlands, 2002. (IV.1)

137. Harvey, E. N., Whiteley, A. H., McElroy, W. D., Pease, D. C., Barnes, D.K. *Bubble Formation in Animals: II, Gas Nuclei and their Distribution in Blood and Tissues*. Journal of Cellular and Comparative Physiology, Vol. 24, No. 1, 1944, p. 23-24.

138. Harvey, E. N., Barnes, D. K., McElroy, W. D., Whiteley, A. H., Pease, D. C., Cooper, K. W. *Removal of Gas Nuclei from Liquids and Surfaces*. Journal of the American Chemical Socity, 1945, Vol. 67, p. 156.

139. Harvey, E. N., McElroy, W. D., Whiteley. *On Caviy Formation in Water*. Journal of Applied Physics, Vol. 18, No. 2, 1947, p. 162-72.

140. Knapp, R. T. *Cavitation and Nuclei*. Transactions of the ASME, Vol. 80, 1958, p. 1315-1324.

141. Briggs, L. J. *Maximum Superheating of Water as a Measure of Negative Pressure*. Journal of Applied Physics, Vol. 26, 1955, p. 1001-1003.

142. Kenrick, F. B., Gilbert, G. S., Wismer, K. L. *The Superheating of Liquids*. J. Phys. Chem., 1924, Vol. 28, p. 1297-1307.

143. Trevena, D. H. *Time Effects in Cavitation Experiments*. Journal of Physics D: Applied Physics, Vol. 15, 1982, p. L111-4.

144. Iyengar, K. S., Richardson, E. G. *Measurements on the Air-Nuclei in Natural Water which give rise to Cavitation*. British Journal of Applied Physics, Vol. 9, 1958, p. 154-158.

145. Hayward, A. T. J. *Measuring the extensibility of liquids*. Nature, Vol. 202, 1964, p. 481-482.

146. Hayward, A. T. J. *The Role of Stabilized Gas Nuclei in Hydrodynamic Cavitation Inception*. Journal of Physics D: Applied Physics, Vol. 3, 1970, p. 574-9.

147. Jones, W. M., Overton, G. D. N., Trevena, D. H. Journal of Physics D: Applied Physics, Vol. 14, 1981, p. 1283-91. [FROM O&E&T-'82]

148. Overton, G. D. N., Edwards, M. J. Trevena, D. H. *Dissolved gas content and the static breaking tension of water*. Journal of Physics D: Applied Physics, Vol. 15, 1982, p. L129-31.

149. Ohde, Y., Tanzawa, Y. *Dependance on Kinds of Impurity Gases in Metals of Negative Pressures in Water/Metal Berthelot Tube Systems*. In: Proceedings of the NATO Advanced Research Workshop on Liquids Under Negative Pressure. Kluwer Academic Publishers, The Netherlands, 2002.(8[VI.1]

150. Gavrilov, R. L. *Power Ultrasonic Fields*, Moscow, Nauka, 1970.

151. Hammitt, F. G., Koller, A., Ahmed, O. S. M., Pyun, J. J., Yilmaz, E. *Cavitation Threshold and Superheat in Various Fluids*. In: Proceedings of the Conference on Cavitation, Edinburg, 3-5 September, 1974, c. 185, London, N.~Y.: Mech. Eng. Publ. Ltd., p. 341-354.

152. Besov, A., Kendrinskii, V. *Dynamics of Bubbly Clusters and Free Surface at Shock Wave Reflection*. Proceedings of the International Symposium On Bubble Dynamics and Interface Phenomena, Birmingham, U.K., 1994, p. 93-103.

153. Kedrinskii, V. K. 1993 *Nonlinear Problems of Cavity Liquid Fracture at Explosive Loading (review)*. Journal of Applied Mechanics and Technical Physics, Vol. 3, p. 74-91. FROM [(4)]

154. Keller, A. P. *Investigations Concerning Scale Effects of the Inception of Cavitation*. Proceedings of the Institute of Mechanical Engineers, Conference on Cavitation, 1974, p. 109-117.

155. Temperley, H. N. V., Trevena, D. H. *Metastability of phase transitions and the tensile strength of liquids*. Proceedings of the Royal Society of London A., Vol. 357, 1977, p. 395-402.

156. Williams, P. R., Williams, R. L. *On Anomalously Low Values of the Tensile Strength of Water*. Proceedings of the Royal Society, London A, Vol. 456, 2000, p. 1321-1332.

157. Als-Nielsen, J. *The Liquid-Vapour Interface*. Z. Phys. B., Vol. 61, 1985, p. 411-414.

158. Marston, P. L., Unger, B. T. *Rapid Cavitation Induced by the Reflection of Shock Waves.* In: Shock Waves in Condensed Matter, New York, Plenum, 1986, p. 401–5.

160. Bayer Corporation, Plastics Division. *Makrolon ® 3103, 3105, 3107, and 3158 Polycarbonate Resins*, 2002. Available from www.BayerPlastics.com.

161. Juvinall, R. C., Marshek, K. M. *Fundamentals of Machine Component Design, 3rd Edition*. John Wiley & Sons, Inc., 1999, New York

162. PCB Piezotronics, Pressure and Force Sensors Division. *Pressure Catalog: Piezoelectric Sensors for Dynamic Pressure Measurements.* Available from www.pcb.com.

163. PCB Piezotronics, Pressure and Force Sensors Division. *Pressure Sensor General Operation Manual: Models M113A21, A22, A23, A24, A26.* PCB Piezotronics, Inc. Depew, New York. 1998.

164. Dupont, P., Okamura T. *Cavitating Flow Calculations in Industry*. International Journal of Rotating Machinery, Vol. 9, No. 3, 2003, p. 163–170. **(CFD)**

165. Greatrix, D. R., Gottlieb, J. J. *An Analytical and Numerical Study of a Shock Wave Interaction with an Area Change*. U.T.I.A.S. Report No. 268, November 1982.

166. Igra, O., Wang, L., Falcovitz, J. *Non-Stationary Compressible Flow in Ducts with Varying Cross-Sections.* Proceedings of the Institution of Mechanical Engineers, Vol. 212, Part G, p 225-243.

167. Taylor, G. I. *The Pressure and Impulse of Submarine Exposion Waves on Plates. The Scientific Papers of G. I Taylor, Vol. 3*. Cambridge University Press, Cambridge, U.K, 1963.

168. Streeter, V. L. *Fluid Mechanics. 4th Edition.* McGraw-Hill, Inc. New York, U.S.A., 1966.

169. Streeter, V. L. *Hydraulic Transients.* McGraw-Hill, Inc. New York, USA. 1967.

170. Green, N. W., Mesler, R. B. Proceedings of the ASME Conference in Detroit, Vol. 1-8, 1970, New York.

171. Kosky, P. G., Henwood, G. A. British Journal of Applied Physics, Vol. 2, 1969, p. 630.

172. Doyle, G. K. E. *Shock Wave Interactions with Porous Beds*. M.Sc. Thesis, University of the Witwatersrand, Johannesburg, 1999.

173. Boteler, J. M., Sutherland, G. T. *Tensile Failure of Water due to Shock Wave Interactions*. Journal of Applied Physics Vol. 96, No. 11, 2004. 1 December

174. Couzens, D. C. F. 1970, *PhD Thesis*, University of Wales, Aberystwyth.

175. Crum, L. A., Fowlkes, J. B. *Acoustic Cavitation Generated by Microsecond Pulses of Ultrasound*. Nature, Vol. 319, 1986, p. 52-54.

176. Henderson, S. J., Speedy, R. J. *A Berthelot-Bourdon Tube Method for Studying Water under Tension*. Journal of Physics E: Scientific Instrumentation, Vol. 13, 1980, p. 778-782.

177. Vincent, R. S. *Examination of the Berthelot Tube Method of Measuring Tension in Liquids*. Proceedings of the Physical Society of London, Vol. 55, 1943, p. 376.

178. Dixon, H. H. *Note on the Tensile Strength of Water*. Scientific Proceedings of the Royal Dublin Society, Vol. 12, 1909, p. 60-65.

179. Meyer, J. *Zur Kenntnis des Negativen Druckes in Flüssigkeiten*. Abhandl. Deut. Bunsen Ges., Band III, No. 1: der ganzen Reihe No. 6, 1911.

180. Rees, E. P., Trevena, D. H. *Cavitation Thresholds in Liquids under Static Conditions*. ASME Forum on Cavitation, p. 12, 1966.

181. Strube, H. W., Lauterborn, W. *Investigation by the Centrifuge Method of Cavitation Nuclei at the Interface Between Glass and Water*. Z. Angew. Phys., Vol. 29, p. 349-357.

182. Reynolds, O. *On the Internal Cohesion of Liquids and the Suspension of a Column of Mercury to a height of More than Double that of the Barometer*. Mem. Manchester Lit. Phil. Society, Vol. 7, 3d ser., p. 1-19, 1882.

183. Knapp, R. T. *Cavitation and Nuclei*. Transactions of the ASME, Vol. 80, 1958, p. 1315-1324.

184. Zheng, Q., Durben, D. J., Wolf, G. H., Angell, C. A. *Liquids at Large Negative Pressure: Water at the Homogeneous Nucleation Limit*. Science, Vol. 254, 1991, p. 829-832.

185. Roedder, E. *Metastable Superheated Ice in Liquid Water Inclusions Under High Negative Pressures*. Science, Vol. 155, 1967, p. 1413-1417.

186. Henderson, S. J., Speedy, R. J. *Temperature of Maximum Density of Water at Negative Pressure*. Journal of Physics and Chemistry, Vol. 91, p. 3062-3068.

187. Greenspan, M., Tschiegg, C. E. *Radiation-Induced Acoustic Cavitation; Apparatus and Some Results*. Journal of Research of the National Bureau of Standards, Section C, Vol. 71, 1967, p. 299-312.

188. Galloway, W. J. *An Experimental Study of Acoustically Induced Cavitation in Liquids*. Journal of the Acoustical Society of America, Vol. 26, p. 849-857.

189. Willard, G. W. *Ultrasonically Induced Cavitation in Water: A Step-by-Step. Process* Journal of the Acoustical Society of America, Vol. 25, 1953, p. 669-686.

190. Briggs, L. J. *The Limiting Negative Pressure of Mercury in Pyrex glass*. Journal of Applied Physics, Vol. 24, p. 488-9.

191. Carlson, G. A. *Dynamic Tensile Strength of Mercury*. Journal of Applied Physics, Vol. 46, 1975, 4069–4070.

192. Besov, A. S., Bichenkov, E. I., Kedrinskii, V. K., Palchikov, E. I. *Investigation of Initial Stage of Cavitation by Diffraction Optic Method*. In: Pichal, M. *Proceedings of the IUTAM International Symposium on Optical Methods in Dynamics of Fluids and Solids.* Pichal, M. (Ed.), Springer-Verlag, Berlin, Heidelberg, 1984, p. 129-135.

193. *Franc, J. P. Partial Cavity Instabilities and Re-Entrant Jet*. Proceedings of the Fourth International Symposium on Cavitation, Pasadena, California, U.S.A., 20-23 June, 2001, Cav2001: lecture 002. (6)

194. Fluent, Inc. *FLUENT 6.1.22 User Guide*. Section 22.5.3.

195. CD-adapco. *STAR-CD V3.15A Methodology Manual*.

196. Maître, T., Pellone, C. *Numerical Modelling of Unsteady Partial Cavities Behind a Backard Facing Step*. Fourth International Symposium on Cavitation, June 20-23, 2001, Pasadena, California, U.S.A., Cav2001: sessionB2.002.

197. Fleck, N. A., Deschpande, V. S. *The Resistance of Clamped Sandwich Beams to Shock Loading*. Transactions of the ASME, Vol. 71, May 2004, p. 386-401.

198. Ridley, J. N. *Further Engineering Mathematics (Algebra and Multivariable Calculus),* 1999.

199. Blevin. *Formulas for Natural Frequency and Mode Shape*. Van Nostrand Reinhold, N.Y., 1981. (Chapter 11 Plates)

200. Wong, W. O. *Vibration–mode Shape Visualization with a Time Average TV Holography System.* International Journal of Engineering Education. Vol. 14, No. 4, p. 241-247, 1998.

201. Lamb, H. *The Dynamical Theory of Sound.* Arnold, London, 1910.

202. Airey, J. R., *The Vibrations of Circular Plates and their Relation to Bessel Functions.* Vibration Beams, Plates and Shells. Dowden, Hutchinson & Ross, Inc. Pennsylvania, 1976. Also in: Proceedings of the Physical Society of London, Vol. 23, 1911, p 225-232. by the institute of physics, London.

203. Harris, C. M., Crede, C. E**.** *Shock And Vibration Handbook*. Mcgraw-Hill, New York, 1961.

Appendix A

Entropic Relations for Arbitrary Gas States

The relations between pressure, density and sound speed in ideal gases will now be derived. Multiplying equation (2.19) by $1/c_p(\gamma-1)$ and defining the non-dimensional form of the specific entropy s as $S = s/c_p(\gamma-1)$,

$$S_2 - S_1 = \ln(T_2 / T_1)^{\frac{1}{\gamma-1}} - \ln(p_2 / p_1)^{\frac{1}{\gamma}}$$

$$S_2 - S_1 = \ln\left((T_2 / T_1)^{\frac{1}{\gamma-1}} (p_2 / p_1)^{-\frac{1}{\gamma}}\right) \tag{A.1}$$

$$-\gamma(S_2 - S_1) = \ln\left((T_2 / T_1)^{\frac{-\gamma}{\gamma-1}} (p_2 / p_1)\right) \tag{A.2}$$

This may be rearranged to give:

$$e^{-\gamma(S_2-S_1)} = (T_2 / T_1)^{\frac{-\gamma}{\gamma-1}} (p_2 / p_1)$$

Thus,

$$\frac{p_2}{p_1} = \left(\frac{T_1}{T_2}\right)^{\frac{\gamma}{\gamma-1}} e^{-\gamma(S_2-S_1)} = \left(\frac{\gamma R}{a_1^2}\frac{a_2^2}{\gamma R}\right)^{\frac{\gamma}{\gamma-1}} e^{-\gamma(S_2-S_1)} = \left(\frac{a_2^2}{a_1^2}\right)^{\frac{\gamma}{\gamma-1}} e^{-\gamma(S_2-S_1)}$$

$$\frac{p_2}{p_1} = \left(\frac{a_2}{a_1}\right)^{\frac{2\gamma}{\gamma-1}} e^{-\gamma(S_2-S_1)} \tag{A.3}$$

Similarly, using the ideal gas equation (2.17) and the sound speed equation (2.22),

$$\frac{\rho_2}{\rho_1} = \left(\frac{a_2}{a_1}\right)^{\frac{2}{\gamma-1}} e^{-\gamma(S_2-S_1)} \tag{A.3}$$

Appendix B

Common Relations Across a Liquid Shock Wave

Here, expressions for the ratios of the Mach number, pressure, density, sound speed and particle velocity behind a liquid shock wave to those properties ahead of the shock, are derived. These ratios are the most commonly tabulated parameters in shock tables. A similar derivation, for air, is given in [45].

The conservation of mass equation is

$$\rho_1 u_1 = \rho_2 u_2 \tag{2.6b}$$

$$\rho_1 M_1 a_1 = \rho_2 M_2 a_2$$

Using the sound speed equation (2.41),

$$\rho_1 M_1 \sqrt{np'_1}\rho_1^{-1/2} = \rho_2 M_2 \sqrt{np'_2}\rho_2^{-1/2}$$

$$\sqrt{p'_1} M_1 \rho_1^{1/2} = \sqrt{p'_2} M_2 \rho_2^{1/2}$$

Using Tait's equation,

$$\sqrt{p'_1} M_1 \sqrt{\rho_1} = \sqrt{p'_2} M_2 \sqrt{\rho_1} (p'_2 / p'_1)^{1/2n}$$

$$\sqrt{p'_1} M_1 = \sqrt{p'_2} M_2 (p'_2 / p'_1)^{1/2n}$$

$$\frac{M_1}{M_2} = \left(\frac{p'_2}{p'_1}\right)^{1/2} \left(\frac{p'_2}{p'_1}\right)^{1/2n}$$

Thus,

$$\frac{M_1}{M_2} = \left(\frac{p'_2}{p'_1}\right)^{\frac{n+1}{2n}} \tag{B.1}$$

Conservation of Momentum:

$$p_1 + \rho_1 u_1^2 = p_2 + \rho_2 u_2^2 \tag{2.7b}$$

$$p_1 + \rho_1 M_1^2 np'_1 \rho_1^{-1} = p_2 + \rho_2 M_2^2 np'_2 \rho_2^{-1}$$

$$p_1 + B + M_1^2 np'_1 = p_2 + B + M_2^2 np'_2$$

$$p_1'(1 + nM_1^2) = p_2'(1 + nM_2^2)$$

$$\frac{p_2'}{p_1'} = \frac{1 + nM_1^2}{1 + nM_2^2} \tag{B.2}$$

Combining equations (B.1) and (B.2), The upstream and downstream Mach numbers may be related by:

$$\frac{M_1^2}{M_2^2} = \left(\frac{1 + nM_1^2}{1 + nM_2^2}\right)^{\frac{n+1}{n}} \tag{B.3}$$

This equation has two roots:

$$M_1 = M_2 \qquad \text{which corresponds to a Mach wave} \tag{B.4}$$

$$M_2 = M_1\left(\frac{1 + nM_1^2}{1 + nM_2^2}\right)^{\frac{n+1}{2n}} \qquad \text{which corresponds to a shock wave.} \tag{B.5}$$

Equation was used to draw up shock tables for normal shock waves in liquids. Generally, the particle speed ahead of the shock wave is assumed to be zero. Thus, $M_1=M_S$. It follows that the shock table will include all values where $M_1 \geq 0$ ($M_1<0$ corresponds to rarefaction shocks) and $M_1 \geq M_2$.

The density ratio across the shock wave, also included in shock tables can be calculated directly from the pressure ratio across the shock and Tait's equation:

$$\frac{\rho'}{\rho} = \left(\frac{p'}{p}\right)^{1/n} \tag{B.6}$$

The sound speed ratio across the shock is determined as follows: From equation (2.41):

$$\frac{a_2}{a_1} = \frac{\sqrt{np_2'\rho_2^{-1}}}{\sqrt{np_1'\rho_1^{-1}}} = \frac{\sqrt{p_2'\rho_1}}{\sqrt{p_1'\rho_2}}$$

Using Tait's equation (2.37),

$$\frac{a_2}{a_1} = \sqrt{\frac{p_2'}{p_1'}}\sqrt{\left(\frac{p_1'}{p_2'}\right)^{1/n}}$$

Thus,

$$\frac{a_2}{a_1} = \left(\frac{p_2'}{p_1'}\right)^{\frac{n-1}{2n}} \tag{B.7}$$

or

$$\frac{a_2}{a_1} = \left(\frac{\rho_2}{\rho_1}\right)^{\frac{n-1}{2}} \tag{B.8}$$

These equations are analogous to the isentropic relations (2.26) and (2.27) and, like Tait's equation, is valid for liquids at pressures up to 2500 *MPa*.

From the equation of continuity, the particle velocity ratio across a shock wave is:

$$\frac{u_2}{u_1} = \frac{\rho_1}{\rho_2} \tag{B.9}$$

Appendix C

Wave Diagram Considerations

C.1. Non-dimensional Forms of the State Variables

Wave diagram procedures are greatly facilitated by the use of non-dimensional quantities. The following non-dimensional forms of the speed of sound, particle velocity and specific entropy are defined as [44]:

$$\hat{A} = \frac{a}{a_0} \tag{C.1}$$

$$\hat{U} = \frac{u}{a_0} \tag{C.2}$$

$$S = \frac{s}{C_P(\gamma - 1)} \quad (\text{where } S_0 = s_0 = 0) \tag{C.3}$$

C.2. Method of Characteristics

From the fundamental differential equations (conservation mass and momentum equations), the following characteristic relations, derived by Rudinger [44], allow systematic solution of nonsteady-flow problems.

$$\frac{\delta_+ P}{\delta\tau} = -\hat{A}\hat{U}\frac{\partial \ln A}{\partial \xi} - \hat{A}\frac{\partial \ln A}{\partial \tau} + \hat{A}\frac{\delta_+ S}{\delta\tau} + (\gamma - 1)\hat{A}\frac{DS}{D\tau} + \Im - \Psi\hat{A}^{\frac{\gamma-3}{\gamma-1}}e^{\gamma S} \tag{C.4}$$

$$\frac{\delta_- Q}{\delta\tau} = -\hat{A}\hat{U}\frac{\partial \ln A}{\partial \xi} - \hat{A}\frac{\partial \ln A}{\partial \tau} + \hat{A}\frac{\delta_- S}{\delta\tau} + (\gamma - 1)\hat{A}\frac{DS}{D\tau} - \Im - \Psi\hat{A}^{\frac{\gamma-3}{\gamma-1}}e^{\gamma S} \tag{C.5}$$

where $\Im$ is the non-dimensional form of f (the sum of body and dissipative forces per unit mass) $\Im = fL_0 / a_0^2$ and Ψ is the non-dimensional form of ψ (the mass flow removed per unit length) $\Psi = L_0 a_0 \psi / \gamma p_0 \hat{A}$.

It is evident from these equations that changes in the parameters (P and Q, S) may be calculated by eliminating negligible terms and multiplying both sides of the equations by the differential time $\delta\tau$.

The fundamental differential equations used to derive the characteristic relation do not apply across discontinuities such as shock waves, which effectively separate a wave diagram into two parts. Each part must be treated separately and appropriately matched along the shock boundary and for the shock tube case the regions on either side of the shock may be treated as isentropic. The terms involving entropy in equations (C.4) and (C.5) may then be equated to zero. For the isentropic regions on either side of the shock,

$$\frac{\delta_{+}P}{\delta\tau} = -\hat{A}\hat{U}\frac{\partial \ln A}{\partial \xi} - \hat{A}\frac{\partial \ln A}{\partial \tau} + \Im - \Psi\hat{A}^{\frac{\gamma-3}{\gamma-1}} \tag{C.6}$$

$$\frac{\delta_{-}Q}{\delta\tau} = -\hat{A}\hat{U}\frac{\partial \ln A}{\partial \xi} - \hat{A}\frac{\partial \ln A}{\partial \tau} + -\Im - \Psi\hat{A}^{\frac{\gamma-3}{\gamma-1}} \tag{C.7}$$

These expressions may be further simplified since, in most applications, the mass flow removed is usually insignificant and since, in gases, the gravitational body force may be neglected, as shown by Rudinger [44]. Neglecting these terms yields the following equations, which show that cross-sectional area variations are the only remaining factor influencing the values of *P* and *Q*.

$$\frac{\delta_{+}P}{\delta\tau} = -\hat{A}\hat{U}\frac{\partial \ln A}{\partial \xi} - \hat{A}\frac{\partial \ln A}{\partial \tau} \tag{C.8}$$

$$\frac{\delta_{-}Q}{\delta\tau} = -\hat{A}\hat{U}\frac{\partial \ln A}{\partial \xi} - \hat{A}\frac{\partial \ln A}{\partial \tau} \tag{C.9}$$

The first terms of these equations are only used when the cross-section of the duct is not uniform while the second terms are only used when the tube area is variable with time.

C.3. Other Useful Quantities for Wave Diagram Construction

In this section, the parameters that are particularly useful in tthe construction of wave diagrams (when tabulated in shock tables), namely $\Delta P/\hat{A}$, $\Delta Q/\hat{A}$, $\Delta|\hat{U}|/\hat{A}$ and ΔS, are expressed in terms of more well-known and commonly tabulated terms. From the definition of the characteristic quantity *P*,

$$\frac{\Delta P}{\hat{A}} = \frac{1}{\hat{A}}\left(\frac{2}{\gamma - 1}\hat{A}' + U'\right) - \frac{1}{\hat{A}}\left(\frac{2}{\gamma - 1}\hat{A}' + U'\right)$$

$$= \frac{1}{\hat{A}}\left[\frac{2}{\gamma - 1}\left(\hat{A}' - \hat{A}\right) + \left(U' - U\right)\right]$$

$$= \frac{2}{\gamma - 1}\left(\frac{\hat{A}'}{\hat{A}} - 1\right) + \frac{U' - U}{\hat{A}} = \frac{2}{\gamma - 1}\left(\frac{\hat{A}'}{\hat{A}} - 1\right) + \frac{U' - U}{U}\frac{U}{\hat{A}}$$

$$= \frac{2}{\gamma - 1}\left(\frac{\hat{A}'}{\hat{A}} - 1\right) + \left(\frac{U'}{U} - 1\right)\frac{U}{\hat{A}} \tag{C.10}$$

The quantities $\hat{A}$, $\hat{A}'$ and M_S are always positive, but U' and U may be positive (for *Q*-shocks) or negative (for *P*-shocks). Thus,

For a *P*-shock: $$\frac{\Delta P}{\hat{A}} = \frac{2}{\gamma - 1}\left(\frac{\hat{A}'}{\hat{A}} - 1\right) + \left(1 - \frac{\hat{U}'}{\hat{U}}\right)M_S \tag{C.11}$$

For a *Q*-shock: $$\frac{\Delta P}{\hat{A}} = \frac{2}{\gamma - 1}\left(\frac{\hat{A}'}{\hat{A}} - 1\right) - \left(1 - \frac{\hat{U}'}{\hat{U}}\right)M_S \tag{C.12}$$

Similarly, from the definition of the characteristic quantity *Q*,

For a *P*-shock: $$\frac{\Delta Q}{\hat{A}} = \frac{2}{\gamma - 1}\left(\frac{\hat{A}'}{\hat{A}} - 1\right) - \left(1 - \frac{\hat{U}'}{\hat{U}}\right)M_S \tag{C.13}$$

For a *Q*-shock: $$\frac{\Delta Q}{\hat{A}} = \frac{2}{\gamma - 1}\left(\frac{\hat{A}'}{\hat{A}} - 1\right) + \left(1 - \frac{\hat{U}'}{\hat{U}}\right)M_S \tag{C.14}$$

The parameter $\Delta\left|\hat{U}\right| / A$ may be calculated from as follows:

$$\frac{\Delta|U|}{\hat{A}} = \left|\frac{U'}{\hat{A}'}\frac{\hat{A}'}{\hat{A}} - \frac{U}{\hat{A}}\right| = \left|M_2\frac{\hat{A}'}{\hat{A}} - 1\right| = \left|M_2\frac{a'}{a} - 1\right| \tag{C.15}$$

The equations above apply for shock waves in any medium. For gases, which are treated as non-isentropic, the non-dimensional entropy changes may be expressed in terms of the shock Mach number as follows: Using the ideal gas equation, equation (A.1) becomes:

$$S_2 - S_1 = \frac{1}{\gamma(\gamma - 1)}\ln\left((T_2 / T_1)^{\gamma}(p_2 / p_1)^{-\gamma+1}\right)$$

and using the Rankine-Hugoniot relation (2.11) and equation (2.10) gives [10,44]:

$$S_2 - S_1 = \frac{1}{\gamma(\gamma - 1)}\ln\left[\left(\frac{1 + \frac{1}{2}(\gamma - 1)M_S^2}{\frac{1}{2}(\gamma + 1)M_S^2}\right)^{\gamma}\left(\frac{2\gamma}{\gamma + 1}M_S^2 - \frac{\gamma - 1}{\gamma + 1}\right)\right] \tag{C.16}$$

Appendix D

One-Dimensional Interaction Problems

The collision of a shock or rarefaction wave with a wall or contact surface is discussed in section 2.8.1. The other types of one-dimensional wave interactions are discussed here.

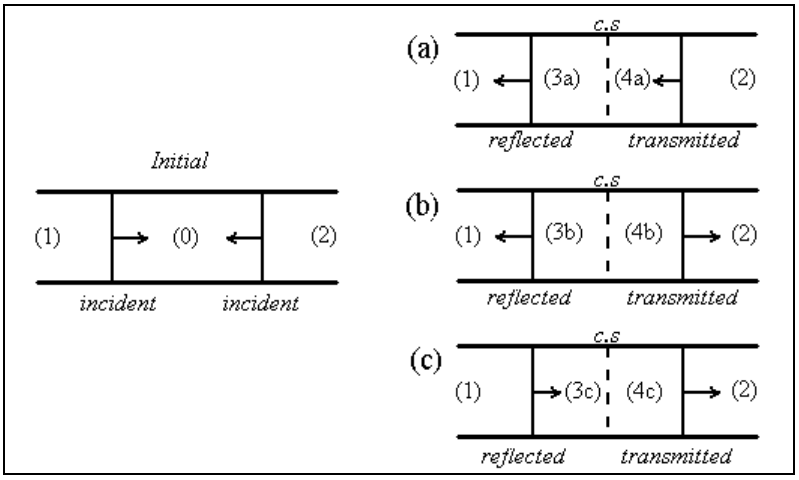


Figure D.1. Collision of waves: Initial and final Conditions

Collision problems involve two waves propagating towards each other through a state (denoted by *0*), as illustrated in figure D.1. The state *0* and the states behind each wave (states *1* and *2*) are usually known. The unknown state *3* then prescribes the strengths of both waves (waves *c* and *d*) resulting from the collision. The loci of all states that may be connected through a shock or rarefaction to the states *1* and *2* may be plotted on a (*p,u*) diagram. The state *3* formed after the collision must lie on both curves and is found at their intersection. However, only one of the final states is physically possible.

- For two shock or rarefaction waves colliding head on, only the state (b), with both of the resulting waves being shock or rarefaction waves respectively, is possible [46]. Generally, weak shocks are always weakened by the collision [44].
- If the initial wave, travelling from left to right, is a shock and the other initial wave is a rarefaction wave, only the state (b) is possible (with the shock travelling

left to right and the rarefaction wave travelling from right to left). The result will be a decrease or increase of pressure, depending on the strength of the waves [44].

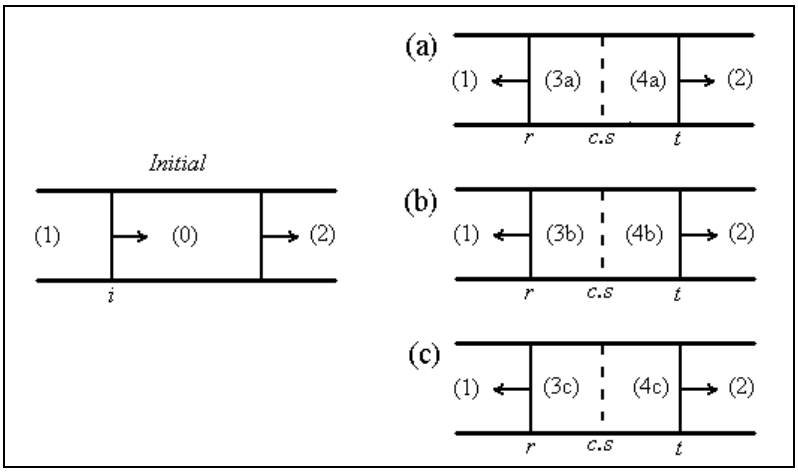


Figure D.2.Overtaking of one wave by another: Initial and final Conditions

Overtaking problems, as illustrated, generally, in figure D.2, involve either a shock overtaking a shock or rarefaction wave, or a rarefaction wave overtaking a shock.

- For a shock overtaking another shock, the transmitted wave is always a shock, while the reflected wave can be a shock, rarefaction or Mach wave [46].
- When a rarefaction wave overtakes a shock, the shock strength is attenuated (it may attenuate the shock to a Mach wave, resulting in a transmitted rarefaction wave). The reflected waves may be compression, Mach or expansion waves [46].
- When a shock overtakes a rarefaction wave, the resulting wave pattern depends on the strength of the shock. The reflected wave may be a shock, rarefaction or Mach wave. The transmitted wave will be a rarefaction wave, for weak overtaking shocks, and a shock, for stronger overtaking waves [46].

When shock waves of different strength collide or when one shock overtakes another, the entropy rise of the fluid depends on which of the shocks is crossed first. As a result, the particle path through the intersection point, where the interaction occurs, becomes a contact surface separating regions of different entropy as illustrated in figures D.1 and D.2. In a liquid medium, since entropy changes may usually be neglected, one may disregard this contact surface.

Appendix E

Collision and Reflection of Waves from a Rigid wall

E.1. Acoustic Waves

The present discussion is strictly limited to reflection at infinitely rigid walls. In the case of acoustic waves, the reflection from an infinite rigid body results in a pressure change at the surface, which is twice the incident pressure [55]. Denoting the pressures behind the incident, reflected and transmitted waves as $p_{i,} p_r$ and p_t respectively,

$$p_t = p_r = 2p_i \tag{E.1}$$

E.2. One-dimensional Wall Reflection of Finite Waves in Air

The difference between the acoustic condition (E.1) and the real reflection of finite waves in gases may be very large. When a shock propagating in air is reflected at a rigid wall, the pressure ratio across the reflected shock p_r/p_i may be expressed in terms of the incident shock wave Mach number M_i and the specific heat ratio behind the incident shock as follows γ_i:

$$\frac{p_r}{p_i} = \frac{-2(\gamma_i - 1) + M_i^2(3\gamma_i - 1)}{2 + M_i^2(\gamma_i - 1)} \tag{E.2}$$

E.3. One-dimensional Wall Reflection of Finite Waves In Water

Since shock waves in water are regarded as weak, reflection of these waves obeys rules close to those of acoustic theory [54]. Even for relatively large pressures, the departures from acoustic “pressure doubling” are not very large [55]. In the special case of reflection of a plane shock from a rigid wall when the boundary is normal to the incident wave, Cole [55] derived the following expression for the ratio of reflected to incident pressures using the equations of conservation of mass and momentum for the incident and reflected waves,

$$\frac{p_r - p_0}{p_i - p_0} = 1 + \frac{\rho_r}{\rho_0} \frac{(\rho_i / \rho_0) - 1}{(\rho_r / \rho_0) - 1} \tag{E.3}$$

where the subscript 0 implies properties ahead of the incident shock. Also, using Tait's relation (2.37) for compression for the incident, reflected and transmitted waves,

$$\frac{p_r - p_0}{p_i - p_0} = \frac{(\rho_r / \rho_0)^n - 1}{(\rho_i / \rho_0)^n - 1} \tag{E.4}$$

Equations (E.3) and (E.4) may be solved simultaneously for the pressure and density in terms of the specified values of the parameters behind the incident wave. The pressure ratio on the left hand side of equations (E.3) and (E.4) is always greater than 2 and approaches this value for weak shocks.

Appendix F

Wave Interaction with Discontinuous Change in Cross-Section

Two methods, used to solve problems involving propagation of a shock wave through a discontinuous change in cross-section, are discussed in the following sections. First, the "wave diagram" or "quasi-steady" method, described in [44,46,165,166], is considered. Then, the "waterhammer" method, described in [6], is discussed briefly. For the similar problem of propagation of an expansion or isentropic wave through a discontinuous change in cross section, the analysis of Parmakian or a simplified adaptation of the quasi-steady method, as shown in [44,165] may be applied.

F.1. The Quasi-Steady Method

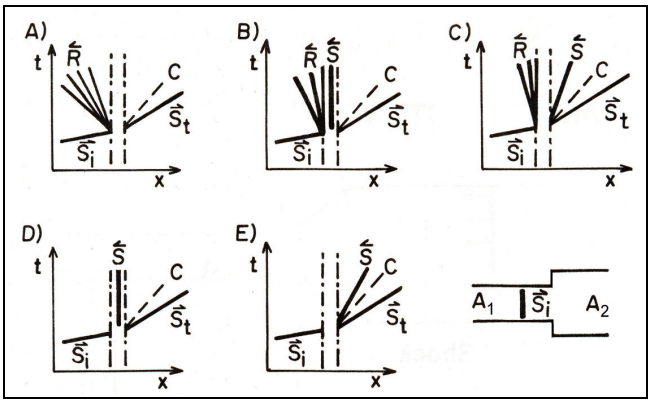


Figure F.1. Possible steady flow wave patterns for the passage of a shock wave through a small area enlargement [165].

When a shock wave passes through a discontinuous change in cross section, it causes unsteady and generally two-dimensional, local flow disturbances at the discontinuity. These transients include transmitted disturbances, which overtake and change the transmitted shock and reflected disturbances, which may form a shock or rarefaction wave moving upstream [46]. The actual flow pattern may, after a certain period has elapsed and once all significant, unsteady disturbances and interactions have subsided,

reach an asymptotic steady flow pattern as shown by Greatrix and Gottlieb [165]. Quasi-steady analysis yields an approximate solution, obtained by neglecting all two-dimensional and unsteady wave phenomena [165,166].

In the most general case, in the case of the passage of a shock wave (S_i) through an area enlargement, 5 unique (quasi-steady flow at late times) wave patterns are possible [165,166]. For discontinuous cross-sectional area changes in gas flows, it is generally not possible to determine which one occurs [46]. In all cases, a shock (S_t) is transmitted.

F.2. The Analysis of Parmakian

When incident waves are weak, a simpler method than that described by Rudinger may be applied to the problem of a shock wave passing through a change in cross-section. Parmakian [6] detailed a simple method, which allow the pressure heads of the incident and transmitted wave to be related by simple functions of the area and sound speed on either side of the change in cross section. This method is valid, in the case under consideration in chapter 7, due to the near acoustic behaviour of waves in water.

When a wave is incident at a change in cross-sectional area, the pressure heads of the incident and transmitted wave are related by:

$$H_2 = sH_1 \tag{F.1}$$

while the heads of the incident and reflected waves are related by:

$$f_1 = rH_1 \tag{F.2}$$

The transmission coefficient s and the reflection coefficient r are defined as:

$$s = \frac{2A_1 / a_1}{A_1 / a_1 + A_2 / a_2} \tag{F.3}$$

$$r = \frac{A_1 / a_1 - A_2 / a_2}{A_1 / a_1 + A_2 / a_2} \tag{F.4}$$

and may related to one another by $s - r = 1$, which follows from the compatibility condition that the pressure behind the reflected and transmitted waves must be equal ($H_2 - f_1 = H_1$). A wave reflection occurs at every change in pipe area.

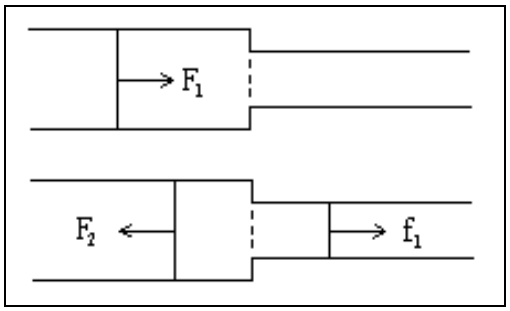


Figure F.2. Incident (F_1), reflected (F_2) and transmitted (f_1) waves in the interaction of a wave with an area enlargement discontinuity [6].

Appendix G

Physical and Thermodynamic Properties of Substances

In this section, the physical and thermodynamic properties of various substances relevant to the experimental facilities, namely water, air, helium, polycarbonate and insertion rubber, are discussed. It is implied that these values are assumed throughout this thesis.

G.1. Properties of Liquid Water

For any cavitation experiment, the knowledge of the liquid properties is of major importance [1]. Water, the most universal of all liquids, is of principal importance in nature, chemical and technological applications and the number of devices utilising it as the working fluid greatly exceed all others [2]. Water is commonly involved in cavitation studies and is also the most common liquid used in shock wave research [51]. While its transparency allows direct visual and photographic detection of cavitation, water does not transmit light waves perfectly. Attenuation of light intensity occurs mainly due to impurity content [2,55].

Table G.1. Properties of liquid water.

Property	**Magnitude**	**Units**	**Comments**
Molecular Weight M	18.02	$kg./kmol$	[52]
Density ρ	1000	$kg.m^{-3}$	At 4°C and 1 atm [10,52]. Within 2% of exact value in the temperature range 0-50°C.
Sound Speed a	1482	$m.s^{-1}$	Calculated.
Bulk Modulus K	2.1963×10^{9}	Pa	Accurate for pressures below one megapascal [10].
Isentropic Compressibility β_S ≈ Isothermal Compressibility at low pressures/temperatures	4.5531×10^{-10}	Pa^{-1}	Accurate for pressures below one megapascal [10].

Table G.1. Properties of liquid water: Continued.

Property	Magnitude	Units	Comments
Surface Tension S	7.28×10^{-2}	$N.m^{-1}$	At 20°C and 1*atm*. [Efunda] This quantity varies significantly with temperature but not pressure [10].
Kinematic Viscosity ν	0.010	cm^2/s	At 20°C and 1 *atm* [10].
	1×10^{-6}	M^2/s	
Adiabatic Exponent γ	7.415	--	Obtained empirically [10].
Characteristic Property A_W	296.3×10^{6}	Pa	Obtained empirically [10].
Acoustic Impedance Z	1.482×10^{6}	kg/m^2s	At 20°C, and 1 *atm*.
Vapour Pressure p_V	2339	Pa	At 20°C [52].
	0.02339	bar	
Boiling Point T_{sat}	100	$°C$	At 1 *atm* [3].
Specific Latent Heat of Vaporisation	2260	kJ/kg	At boiling point of: 100°C at 1 *atm*.
Specific Heat c	4.179	$kJ/kg.K$	At 27°C, and 1 *atm.* Within 0.9% of exact value from 0-100°C [52].
Gruneisen Coefficient Γ	0.1	--	[10] Table 2.1
Fundamental Derivative G	3.60	--	At 30°C, and 1 *atm* [10].T.3

G.2. Properties of Air

Table G.2. Properties of air (equivalent).

Property	Magnitude	SI Units	Comments
Gas constant R	287	$J/kg.K$	[45,52]
Density ρ	1.205	$kg.m^{-3}$	[52]
Molecular weight M	28.97	$kg.kmol^{-1}$	[52]
Sound speed a	343.6	$m.s^{-1}$	[47]
Isentropic Compressibility β_S	3.1872×10^{-4}	Pa^{-1}	[55]
Specific Heat c_p	1.005	$kJ/kg.K$	at 300K (air) [52].
Specific Heat c_v	0.718	$kJ/kg.K$	at 300K (air) [52].

Table G.2. Properties of air (equivalent): Continued.

Property	**Magnitude**	**SI Units**	**Comments**
Specific Heat Ratio γ	1.4	--	At 300 *K* [52].
Acoustic Impedance *Z*	430	kg/m^2s	At 15°C, and 1 *atm*.
Dynamic Viscosity μ	1.71×10^{-5}	*kg/m.s*	[56] $N.s.m^{-2}$
Kinematic Viscosity *v*	1.419×10^{-5}	m^2/s	

G.3. Properties of Helium

Table G.3. Properties of helium gas.

Property	**Magnitude**	**SI Units**	**Comments**
Gas Constant *R*	2077	*J/kg.K*	[45,52]
Density ρ	0.179×10^{-3}	kg/m^3	
Molecular weight *M*	4.003	$kg.kmol^{-1}$	[52]
Sound Speed *a*	1007	$m.s^{-1}$	
Isentropic Compressibility β_S	?	Pa^{-1}	
Specific Heat Ratio γ	1.667	--	[56]
Acoustic Impedance Z	0.1799	kg/m^2s	At 20°C, and 1 *atm*.
Dynamic Viscosity μ	1.9×10^{-5}	*kg/m.s*	--
Kinematic Viscosity *v*	0.1064	m^2/s	--

G.4. Properties of Polycarbonate, Grade: Makrolite 3103.

Polycarbonate tubes are resistant to liquids: When submerged in water, at room temperature, the absorption is only 0.12 % after 24 hours and only 0.30 % after equilibrium is reached. Polycarbonate is not be damaged by frequent, intermittent contact with hot water [160]. Polycarbonate is about 250 times stronger than glass, has good impact strength and is easily machinable. The properties given in table G.4 are for Makrolite 3103, which is a general-purpose grade of polcarbonate.

Table G.4. Properties of Polycarbonate (Grade: Makrolite 3103).

Property	**Magnitude**	**Units**	**Comments**
Density ρ	~1200, (1150-1570)	$kg.m^{-3}$	[160]
Tensile Yield Strength	65	*MPa*	[160]
Tensile Ultimate Strength	70	*MPa*	[160]
Compressive Yield Strength	76	*MPa*	[160]
Optical Refractive Index	1.587	--	[160]
Modulus of Elasticity	~2.2	*GPa*	[160]
Coefficient of Thermal Expansion	3.9×10^{-5}	K^{-1}	[160]

G.5. Properties of Insertion Rubber

Insertion rubber was used to support the liquid column in the Mach 3 shock tube. Since the properties if rubber vary widely, only a few quantities are given here definitively.

Table G.5. Properties of insertion rubber.

Property	**Magnitude**	**Units**	**Comments**
Density ρ	1440	$kg.m^{-3}$	From correspondance with manufacturers.
Tensile Strength	3.60	*MPa*	
Poisson's Ratio	~0.49	--	

Appendix H

Summary of Experimental Cavitation Thresholds Values

In this section, various cavitation threshold values are presented. They are classified as pulse reflection, tube-arrest, Berthelot tube, centrifugal method, superheating, inclusion, ultrasonic and other experiments. In most of these studies, the data is associated with visible cavities [80]. All tension waves are for water except the last section, which lists a few values for mercury.

Table H.1. Tensile strength values recorded from pulse reflection experiments.

	Magnitude of Peak Tension Recorded (*MPa*)	**Comments (Liquid Quality/ Compression Pulse Parameters)**	**Source of Compression Pulses**
Marston and Unger [158] *	-10- to –11	Degassed and distilled water. Compressive pulse duration 1.7μs and amplitude ~10 *MPa*.	"Impactor" plate impacted on buffer in contact with a liquid. (Flexible Mylar membrane).
Boteler and Sutherland [173]	-8.7±0.2	Triple-distilled, triple filtered (removed particles larger than 0.2- μm), de-ionised, and degassed water. Baker-analysed, high purity, low conductivity, with measured pH of 7. Initial liquid compression pulse duration: 2.07±0.15 μs.	"Impactor" plate impacted on buffer in contact with liquid. (Flexible 5 μm-thick aluminised Mylar membrane). Experiments performed initially at 24 °C. Cell configuration. Particle velocity measurements at the water-air free surface.
Williams and Williams [96]	-8.5 to -9.5	Degassed, deionised, filtered water. Compressive pulse rise time between 50 and 100 μs.	B-P (cattle stun gun). Tensions recorded by a transducer with a rise time of ~ 66 *ns*.
Williams and Williams [96]	-9.1 to -10.1	Degassed, deionised, filtered water. Compressive pulse rise time between 50 and 100 μs.	B-P (cattle stun gun). Tensions determined partly by detecting bubble activity as detailed in [96].

Table H.1. Tensile strength values recorded from pulse reflection experiments: Continued

	Magnitude of Peak Tension Recorded (*MPa*)	**Comments (Liquid Quality/ Compression Pulse Parameters)**	**Source of Compression Pulses**
Besov et al. [35]	2.7	Distilled water. Compression pulse peak pressure = 2.9 *MPa*. Stressing rate ≈ 19.2 $bar.\mu s^{-1}$.	Electromagnetic acoustic emitter.
Brown [60]	-2.0- to 3.7	Aged tap water.	B-P (Bullet-piston).
Bull [113] *	-1.6 to -1.5	Untreated (tap) water. Stressing rate ≈ 1 $atm.\mu s^{-1}$ [143].	B-P and underwater explosions.
Couzens and Trevena [111]	-1.5	Degassed (boiled), deionised water.	B-P.
	-0.85	Ordinary untreated tap water.	
Couzens and Trevena [112]	-1.0	Deionised water.	B-P.
Sedgewick and Trevena [115]	0.9	Ordinary tap water.	B-P.
	-1.0	Deionised water.	B-P.
	-1.15	Boiled tap water.	B-P.
	-1.45	Boiled deionised water.	B-P.
Davies et al. [105][14]* K	-1.0	Degassed and distilled water.	B-P. In some experiments, a light piston acted as a free surface, while in others, the pulse was reflected at a true free surface.
Wilson [108] *	–1.5	Deionised and degassed (evacuated).	Underwater explosion from detonation of 0.1 *g* explosive charge.
	–0.85	Settled, untreated (tap) water.	
Crum and Fowlkes [175]	-1.2	Distilled water.	Pulses of ultrasound.
Richards et al. [109]*	-1.2	Deionised water.	Shock tube. Explosion in air resulted in shock in liquid. (flexible Mylar membrane for free surface). B-P

The experiments listed in table H.1 involved free surface reflection, as opposed to reflection at a low impedance medium, unless otherwise specified.

Table H.2. Tensile strength values recorded from tube-arrest experiments.

	Magnitude of Tension Recorded (*MPa*)	**Comments (Liquid Quality/ Stressing rate)**	**Method**
Williams et al. [124]	62.5 *MPa*	Degassed, deionised , filtered water. Stress rate 10 $bar.\mu s^{-1}$.	Mean value.
Overton, Williams and Trevena [122]	2.00 *atm*	Sea-water (degassed)	Ater repeated testing at a frequency of 1 per minute.
	1.87 *atm*	Deionised water (degassed)	
	1.76 *atm*	Fresh tap water (degassed)	
	0.94 *atm*	Deionised water (saturated)	
	0.86 *atm*	Fresh tap water (saturated)	
	0.82 *atm*	Sea-water (saturated)	

Table H.3. Tensile strength values recorded from Berthelot tube experiments.

	Magnitude of Tension Recorded (*MPa*)	**Comments (Liquid Quality)**	**Method**
Henderson & Speedy [176]	-16	Distilled water	Glass Berthelot tubes.
Vincent [177] [55]	-15.7	Degassed water	Glass Berthelot tube.
Dixon [178] [15]	-5 to –15	Degassed water	Glass Berthelot tube.
Berthelot [97] [4]	-5	Degassed water	Glass Berthelot tube.
Jones et al. [147]	-4.7	Degassed, distilled water	Steel Berthelot tube.
Jones et al. [147]	-3.5	Distilled water	Steel Berthelot tube.
Meyer [179] [38]	-3.4	Degassed water	Glass Berthelot tube.
Rees and Trevena [180] [43	-1.3	Degassed water	Steel Berthelot tube.
Sedgewick & Trevena [98]	Minimum: -1.38 Maximum: -2.81 Mean value: -2.23 ± 0.09	Deionised water	26 repeated tests. The first 5 showed no cavitation.

Differences between cavitation thresholds in table H.3 are partly attributed to cleaning and degassing procedures, tube materials (it appears that steel tubes, in general, have more nucleation sites) and assumptions made in calculating tensions [2].

Table H.4. Tensile strength values recorded from centrifugal stressing experiments.

	Magnitude of Tension Recorded (*MPa*)	**Comments (Liquid Quality)**	**Method**
Briggs [104]	-28.1 at 10ºC -26.3 at 20ºC -22.0 at 50ºC	Degassed water	Centrifugally induced tension was applied to a water column.
Strube and Lauterborn [181] *	-17.5	Degassed water	
Reynolds [182] (K: [44])	-0.48	Tap water	
Temperley and Chambers [99] (K: [51])	-0.22 to –0.565	Tap water	

The following cavitation threshold values, shown in table H.5, were inferred from the boiling points of samples of water. All of these experiments involved pre-pressurisation or small liquid volumes to allow significant effective tensions to be sustained.

Table H.5. Tensile strength values recorded from superheating experiments.

	Magnitude of Tension Recorded (*MPa*)	**Comments**	**Method**
Kendrick et al. [142]	270ºC (-5.5 *MPa*)	Tension sustained for 5 seconds.	Thin-walled capillary tube, open to atmosphere.
Harvey et al. [137]	202-206ºC (-1.6-1.8)	Initially pressurised water. Determined effective tensile strength from boiling points.	After pressurising samples at 100 *MPa* for 15-30 minutes.
Knapp [2,183]	-0.25 to -2.6	Pressurised tap water, in Pyrex tubes. Liquid volume: ~300 cm^3.	Determined effective tensile strength from boiling points.

Table H.5. Tensile strength values recorded from superheating experiments: Continued.

	Magnitude of Tension Recorded (*Mpa*)	**Comments**	**Method**
Briggs [141]	264-267ºC (-4.9 to -5.2 *MPa*)	Sustained for a few seconds before boiling explosively. Initially pressurised, distilled, boiled water. Liquid volume: ~0.005 cm^3.	Thin-walled capillary tube. Bore Diameter less than 0.5 *mm*, open to atmosphere.
Skripov [81] [I.4: 17]	300ºC (~ - 8.6 *MPa*)	Water in inclusions in crystals.	Pulsed heating.
Zheng et al. [81]	307ºC (~ - 9.5 *MPa*)	Water in inclusions in crystals.	Determined by isochoric cleaning.

Table H.6. Tensile strength values recorded from inclusion experiments.

	Magnitude of Tension Recorded (*MPa*)	**Comments**	**Method**
Zheng et al. [184]	80-130	Water.	In inclusions within Quartz crystals.
Roedder [185]	-80	Water.	In inclusions within Quartz crystals. Extrapolations of melting point vs. pressure line. [185]
Henderson and Speedy [186] [VI.1]	At least –22	Measured density and temperature of water at this tension.	In small-volume capillaries using the Berthelot method.

Refer to [81] for further discussions these, and other related experiments and the methods used in inclusion studies. Even greater tensions are possible in solutions.

The experiments summarised in table H.7 involve ultrasonic cavitation. The values illustrate great differences (order of magnitude discrepancies) in cavitation threshold values, even for water samples of comparable purity.

Table H.7. Tensile strength values recorded from ultrasonic experiments.

	Magnitude of Tension Recorded (*MPa*)	**Comments (Liquid Quality)**	**Method**
Greenspan & Tschiegg [187]	-16 to –21	'Suitably clean' water	Cavitation was induced ultrasonically.
Galloway [188]	-20	Degassed water	
Willard [189,107]	-2	Degassed water	
Willard [189,107]	-0.1	'Gassy' water	

Table H.8. Tensile strength values recorded from other experiments.

	Magnitude of Tension Recorded (*MPa*)	**Comments**	**Method**
Müller [54]	-7 to -9		Wave Focussing.
Knapp [183]	-0.351	Hydrodynamic cavitation	Venturi tube.
Harvey et al. [139]	No value was determined	Pressurised water	Rapid withdrawal of a submerged rod.

Table H.9. Values of the tensile strength of Mercury.

	Magnitude of Tension Recorded (*MPa*)	**Comments**	**Method**
Briggs, L. J. [190]	42.5	In a Pyrex glass container	Static method.
Williams et al. [125]	300	Stressing rate: 1 $bar.\mu s^{-1}$	Tube arrest method. Pulsed dynamic stressing:
Carlson, G. A. [191]	1900	Stressing rate: 106 $bar.\mu s^{-1}$	Dynamic method: Pulse reflection. Pulsed stressing by a pulsed electron beam generator.

Appendix I

The Initial State of Samples of Liquid Water

In this section, experimental data obtained by various researchers, with regards to the initial impurity content in samples of water, is summarised. The summary is intended to give a good idea of the size of cavitation nuclei. The main parameters are the radii R_o of bubbles containing undissolved gas and uncondensed vapour, the bubble number density N_o (the number of bubble nuclei per unit volume) and the volume concentration of the vapour/gas phase k_o.

Table I.1. Summary of experimentally obtained values of the range of bubble radii R_o.

Source	Radii R_o (μm)	Comments	Method
Hammit et al. [151]	3-6	Settled water.	Acoustic and other diagnostic methods.
Gavrilov [150]	0.5	Water which has been left standing.	Acoustic and other diagnostic methods.
	50	Relatively fresh water.	
Besov et al. [192]	1.3-1.7 (average 1.5)	Distilled (once) water.	Light scattering method and shock tube method. Detailed in [35,38].
Kedrinskii [80,153]	4 (maximum in spectrum)	Fresh distilled water.	Detailed in [153].
	0.85 (maximum in spectrum)	Settled distilled water.	Detailed in [153].

Table I.2. Summary of experimentally obtained values of bubble number density N_o.

Source	Density N_o (cm^{-3})	Comments	Method
Hammit et al. [151]	1-100 *bubbles.cm*$^{-3}$	Settled water.	Acoustic and other diagnostic methods.
Gavrilov [150]	~1 *bubbles.cm*$^{-3}$	Settled water.	Acoustic and other diagnostic methods.
Besov et al. [’94,’84]	Microheterogeneities: 10^5-10^6 Microbubbles 10^3-10^4	Distilled (once) water	Light scattering method and shock tube method. Detailed in [35,38].

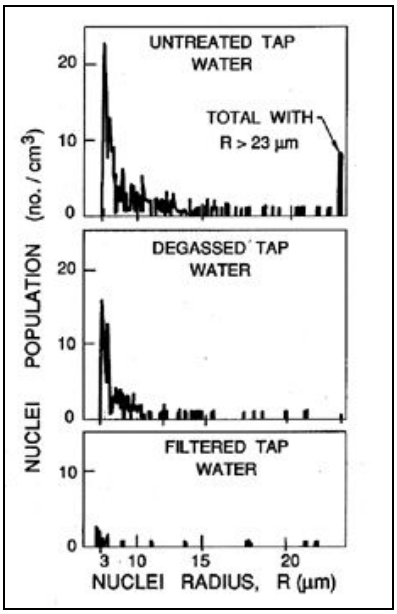


Figure I.1. Histograms of nuclei number densities N_o in untreated, degassed and filtered tap water [5,154].

The data of Keller, shown in figure I.1, is in order of magnitude agreement with the data for non-distilled water shown in tables I.1 and I.2.

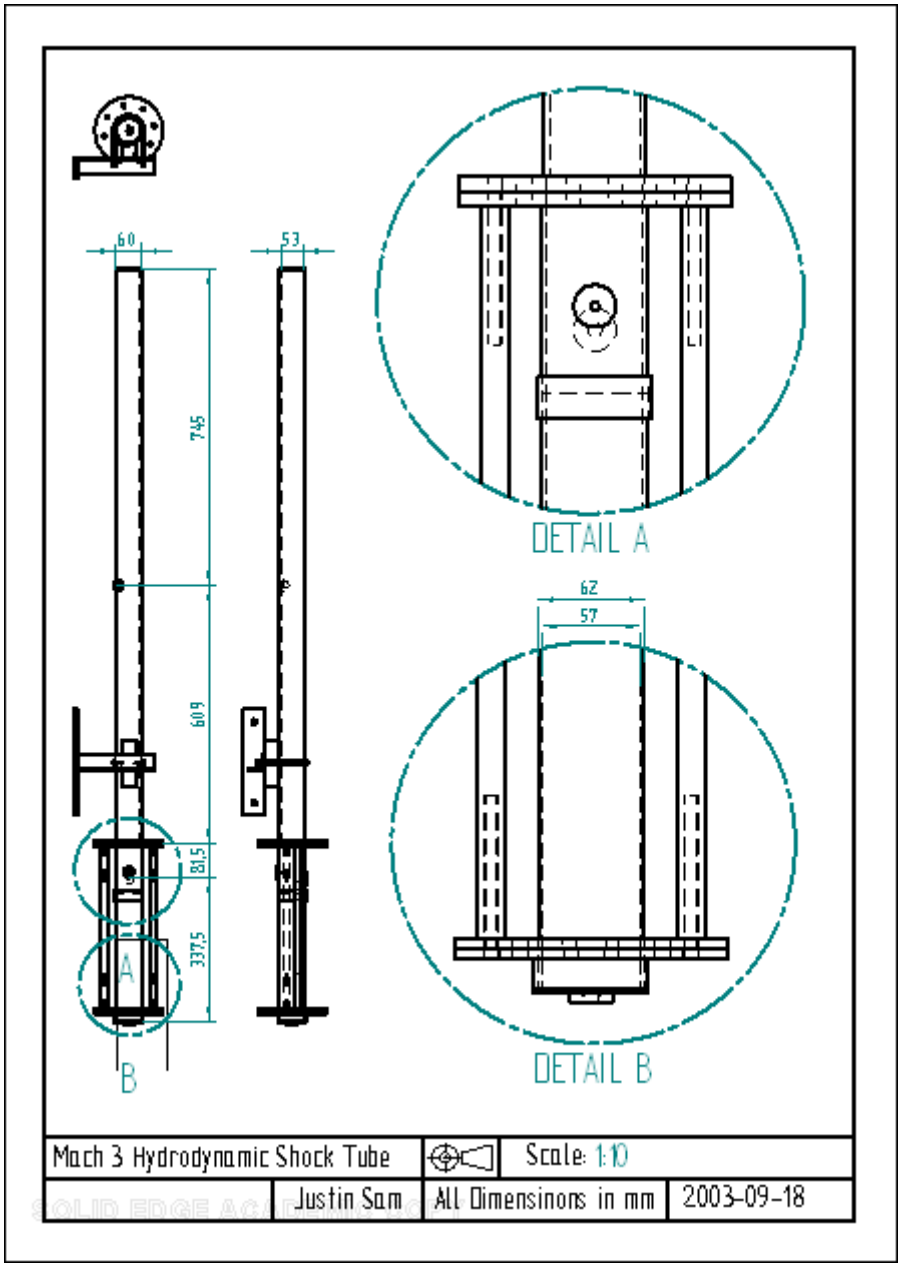
Most data is for gas nuclei only [38], although the data of Besov et al. [152] accounted for both microheterogeneities (including solid particles) and undissolved gas bubbles i.e. 10^5-10^6 microheterogeneities of submicron size and 10^3-10^4 undissolved gas bubbles, with radii of about 1.5 μm are present in a cubic centimetre of distilled water.

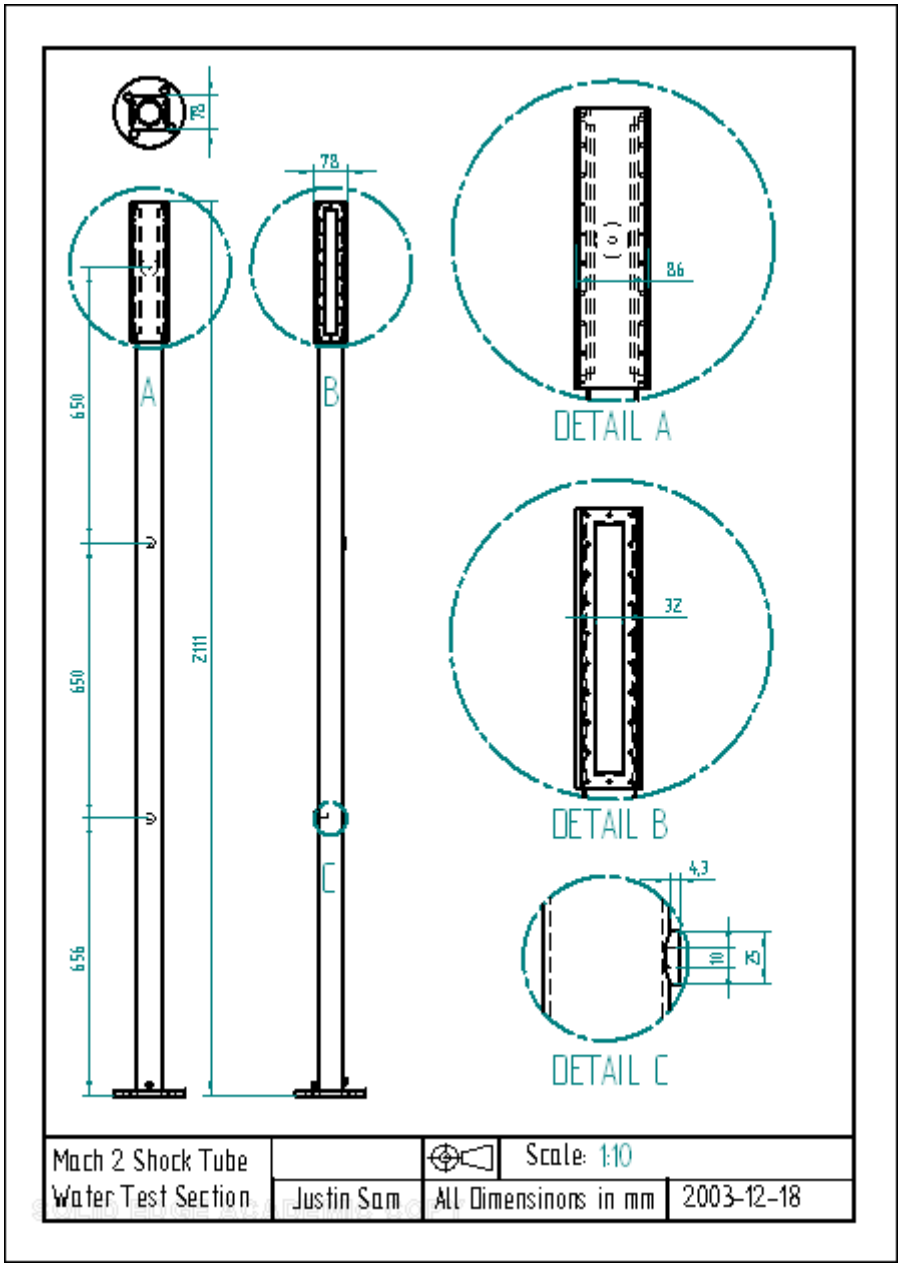
Kedrinskii [80] estimated the total density of microheterogeneities, present in fresh distilled water, from the experimental spectrum data of Hammit et al., as 1.5×10^5 per cubic centimetre.

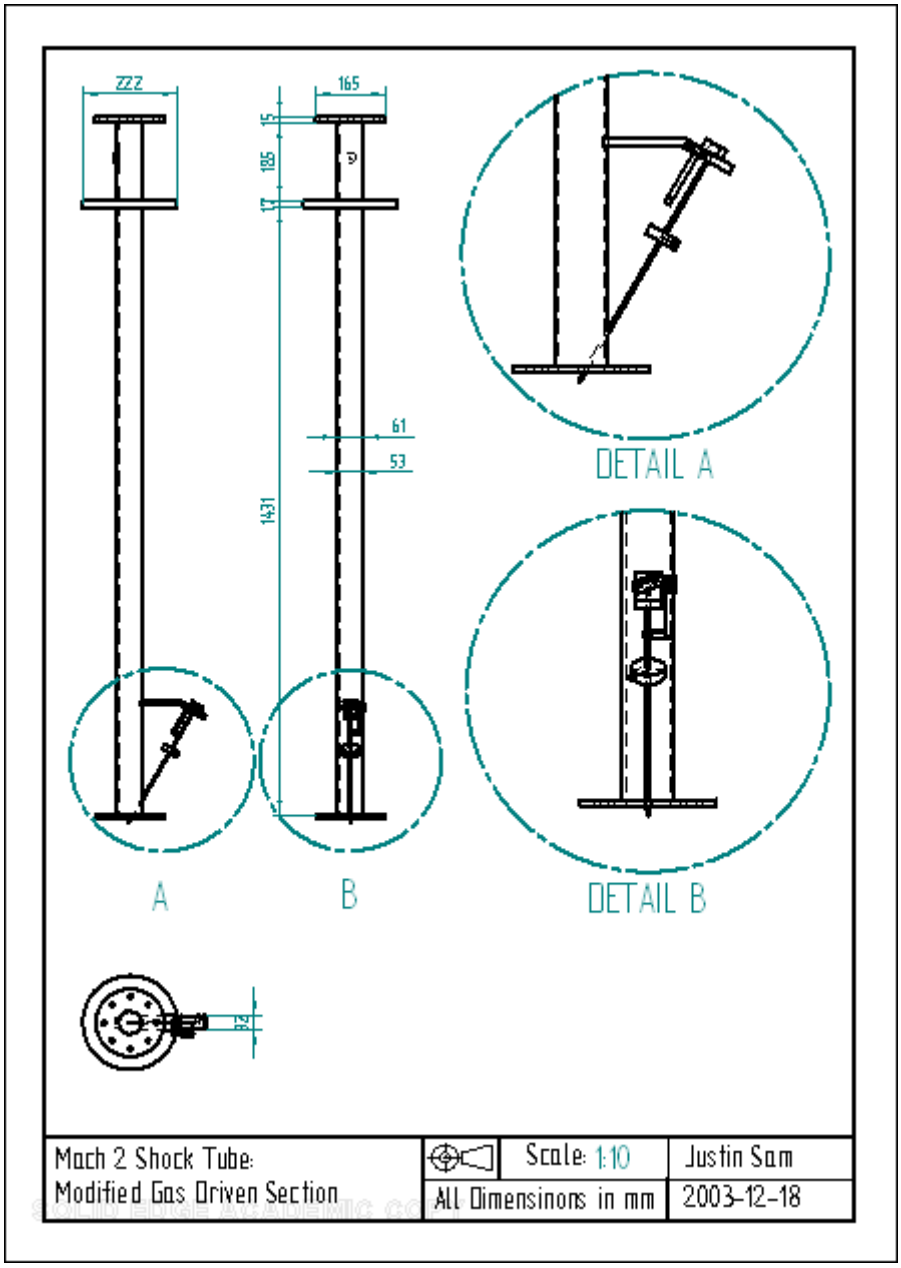
Gavrilov [150] found that the initial concentration k_o, in settled water, ranges from 10^{-8}-10^{-12} while, according to Kedrinskii [60], k_o ranges from 10^{-9} to 10^{-8} for relatively fresh water and from 10^{-12} to 10^{-10} for water which has been left standing.

Appendix J

Assembly Drawings of the Mach 3 and Mach 2 Hydrodynamic Shock Tubes


60
53
745
609
81,5
337,5
A
B
DETAIL A
62
57
DETAIL B
Mach 3 Hydrodynamic Shock Tube
Scale: 1:10
Justin Sam
All Dimensions in mm
2003-09-18


78
78
A
B
C
650
650
656
2111
86
DETAIL A
32
DETAIL B
4,3
10
25
DETAIL C
Mach 2 Shock Tube
Water Test Section
Justin Sam
Scale: 1:10
All Dimensions in mm
2003-12-18


222
165
15
185
17
9
61
53
1431
DETAIL A
DETAIL B
A
B
82
Mach 2 Shock Tube:
Modified Gas Driven Section
Scale: 1:10
All Dimensions in mm
Justin Sam
2003-12-18

Appendix K

Transducer Specifications and Gauge Factors

K.1. Transducers Specifications

The PCB 113A21 transducers are of the ICP® (Integrated Circuit Piezoelectric) type i.e. a voltage mode-type sensor featuring built-in microelectronic amplifiers, which convert the high-impedance charge into a low-impedance voltage output [162,163]. ICP® sensors are generally not affected by moisture [163].

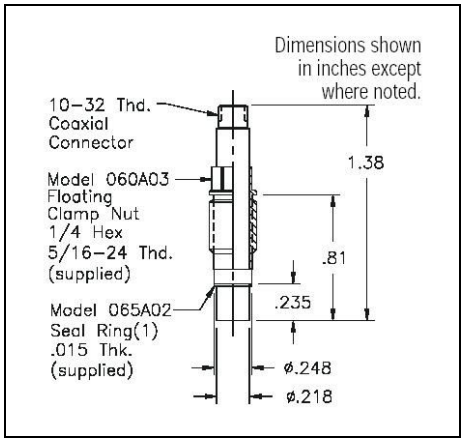


Figure K. 1. Drawing of the PCB transducer, model 113A21 [163].

Table K. 1. PCB 113A21 Pressure Transducer Performance [162,163].

Performance	**SI units**
Measurement Range: (for ± 5*V* output)	1379 *kPa*
Measurement Range: (for ± 10*V* output)	2760 *kPa*
Approximate Sensitivity:	(±15%) 25 $mV.psi^{-1}$ (3.6 $mV.kPa^{-1}$)
Low Frequency Response:	(-5%) 0.5 *Hz*
Resonant Frequency:	≥ 500 *kHz*
Electrical Connector:	10-32 Coaxial Jack
Resolution	0.021 *kPa*
Maximum Pressure	6900 *kPa*
Rise time	≤ 1 μs
Linearity	<1% Full Scale.

K.2. Transducer Gauge Factors

Five transducers were used throughout the experiments using both shock tubes. Here, their gauge factors, calculated from calibration certificates provided by PCB Piezotronics, Inc., are given,

Transducer # 10624:

Sensitivity = 23.63 $mV\ psi^{-1}$ = 3.427 $mV\ kPa^{-1}$

Gauge factor = 0.29179 $kPa\ mV^{-1}$

Transducer # 10620:

Sensitivity = 26.34 $mV\ psi^{-1}$ = 3.820 $mV\ kPa^{-1}$

Gauge factor = 0.26177 $kPa\ mV^{-1}$

Transducer # 9515:

Sensitivity = 28.98 $mV\ psi^{-1}$ = 4.203 $mV\ kPa^{-1}$

Gauge factor = 0.23792 $kPa\ mV^{-1}$

Transducer # 7345:

Sensitivity = 28.53 $mV\ psi^{-1}$ = 4.138 $mV\ kPa^{-1}$

Gauge factor = 0.24168 $kPa\ mV^{-1}$

Transducer # 7938:

Sensitivity = 26.30 $mV\ psi^{-1}$ = 3.814 $mV\ kPa^{-1}$

Gauge factor = 0.26218 $kPa\ mV^{-1}$.

Appendix L

Mach 3 Shock Tube: Additional Pressure Records

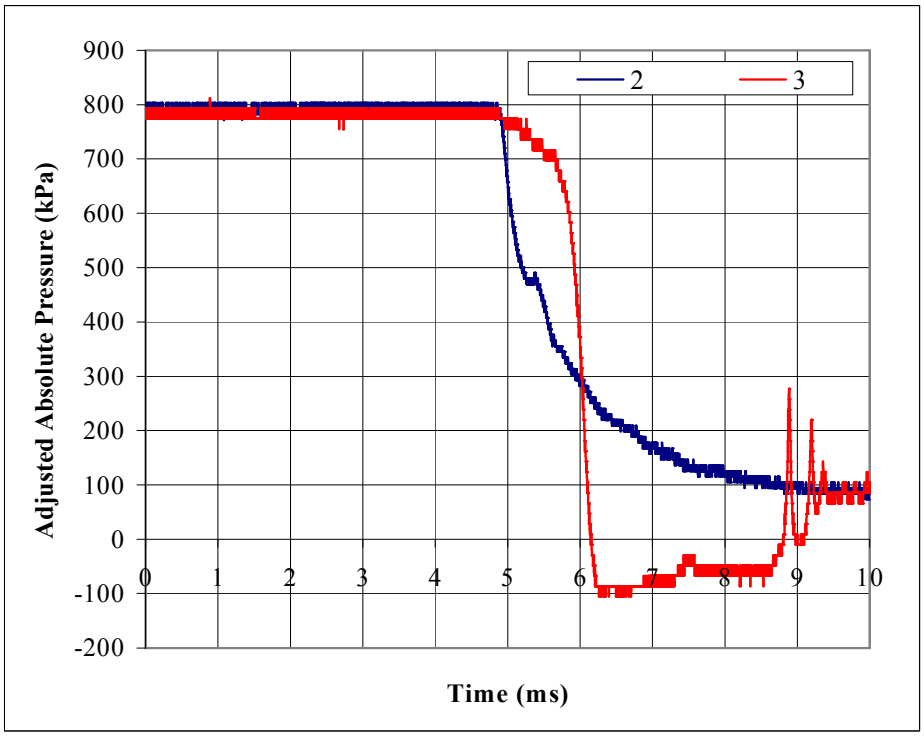


Figure L.1. Pressure trace from test using the Mach 3 shock tube. Sampling rate 1 *MHz*, 10000 data points.

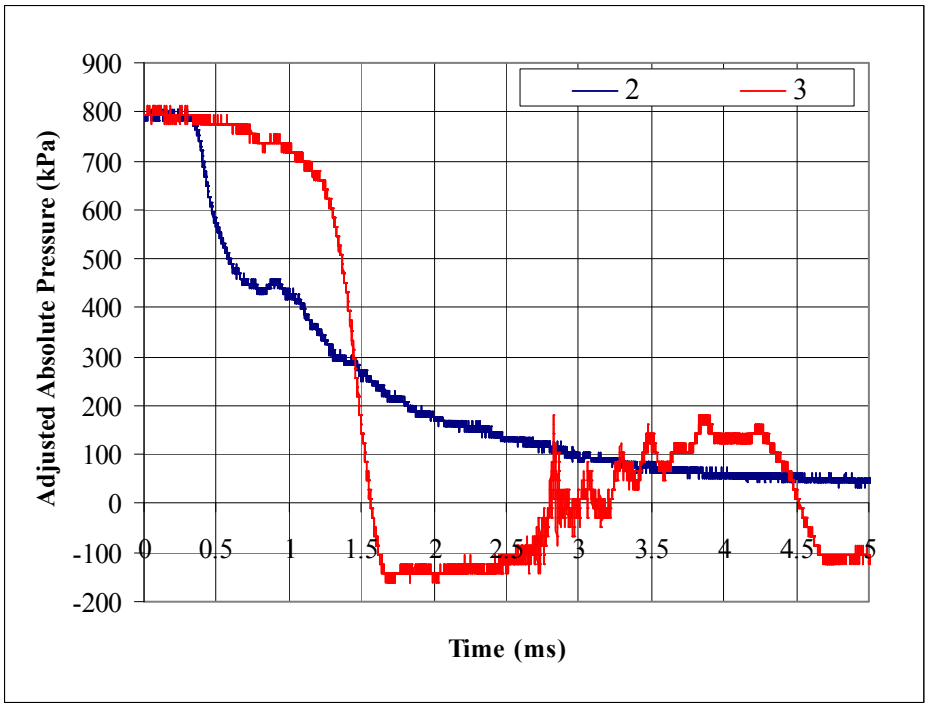
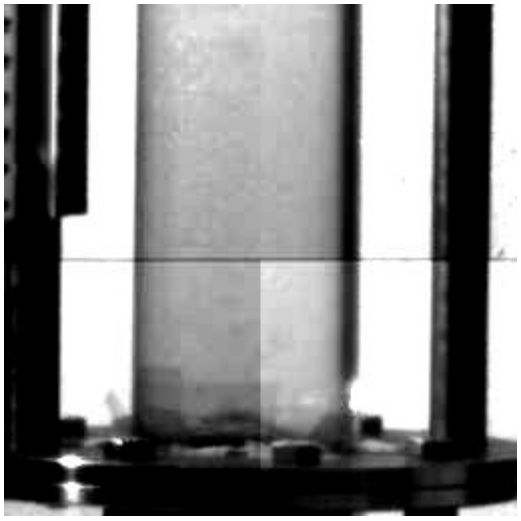
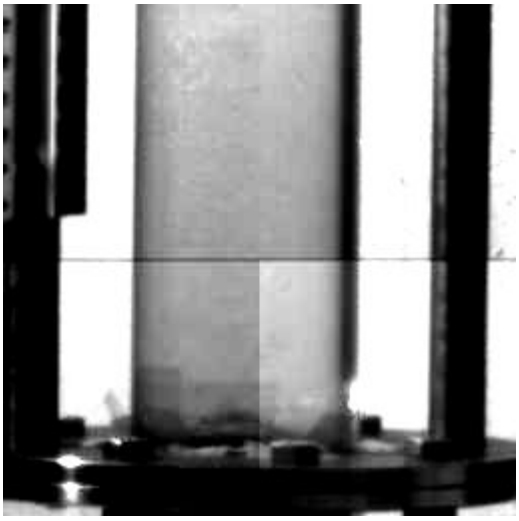


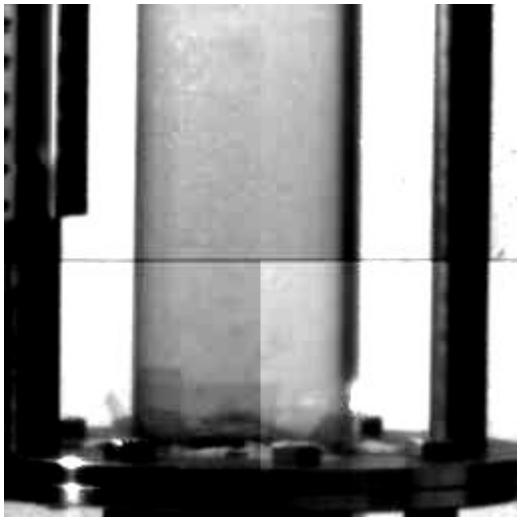
Figure L.2. Pressure trace from test using the Mach 3 shock tube. Sampling rate 2 *MHz*, 10000 data points.

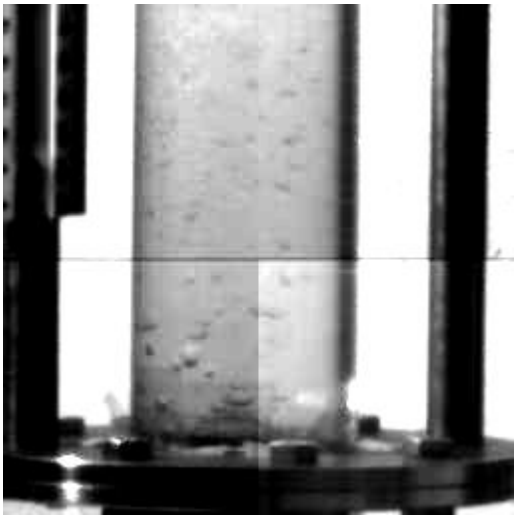
Appendix M

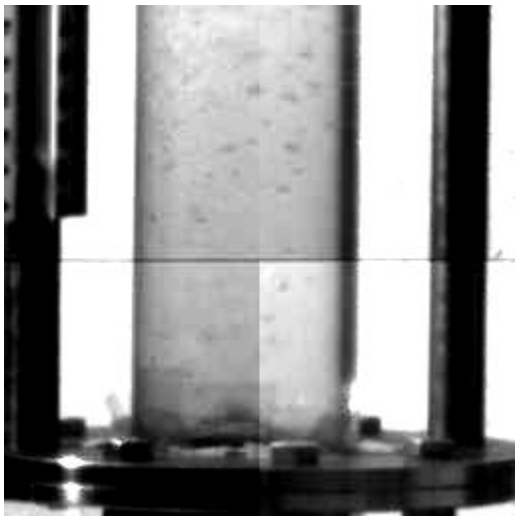
Mach 3 Shock Tube: Photographic Records of the Lower Section of the Tube

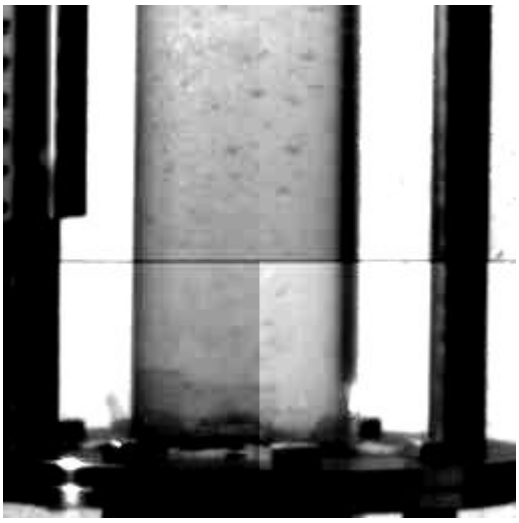

01

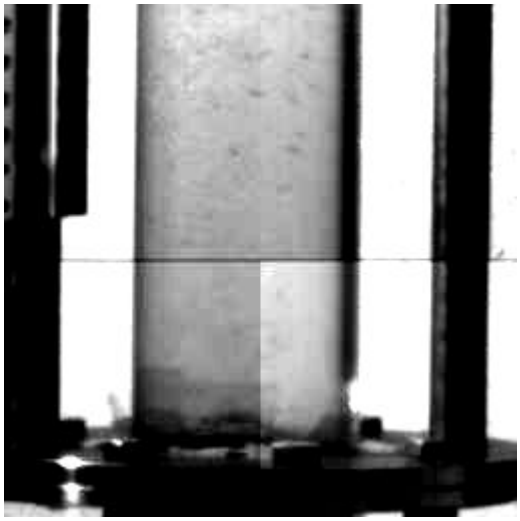

02


03

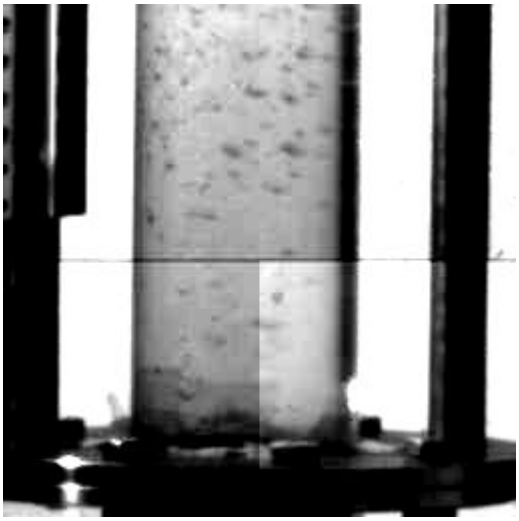

04


05

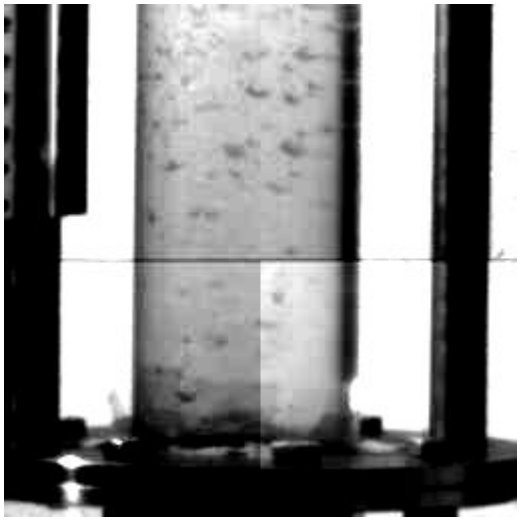

06



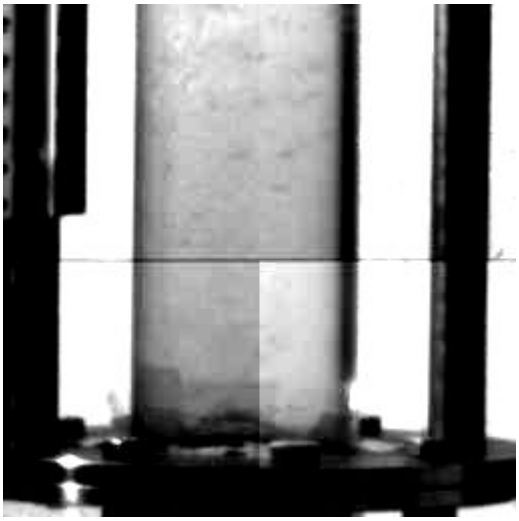
07



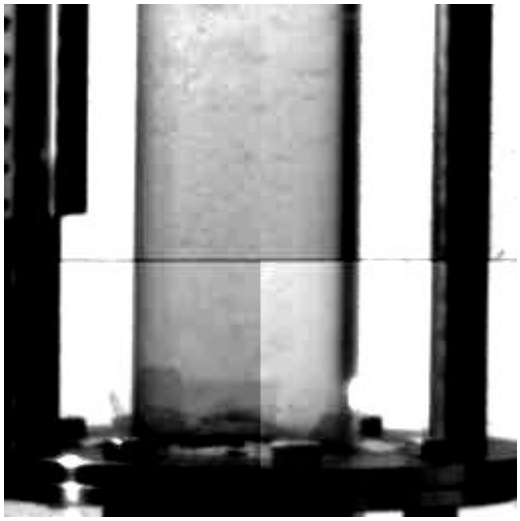
08



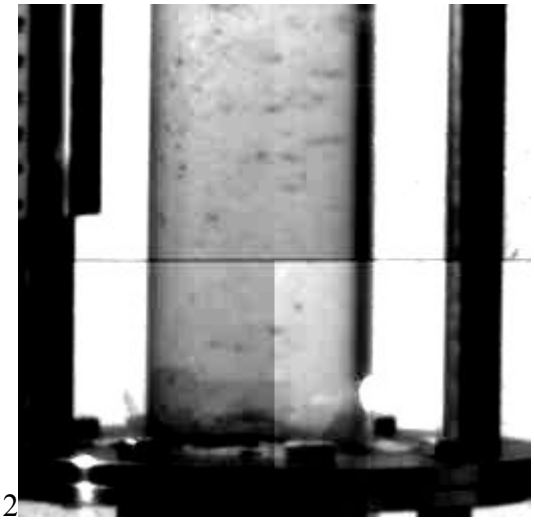
09



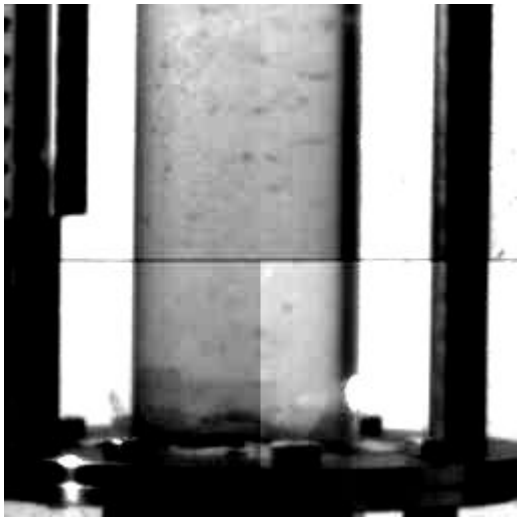
10

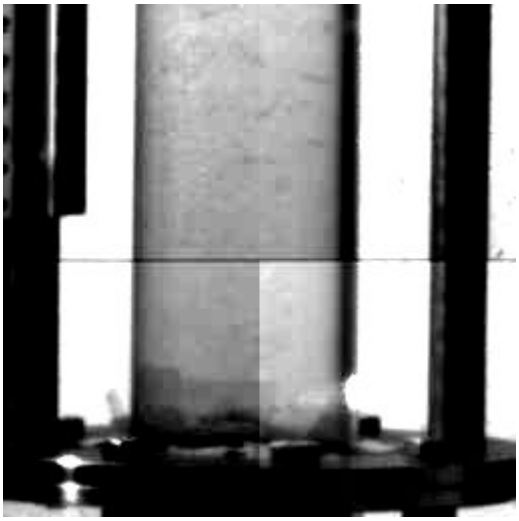


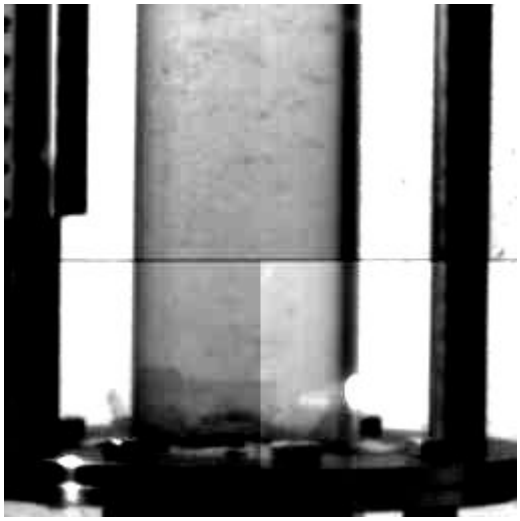
11

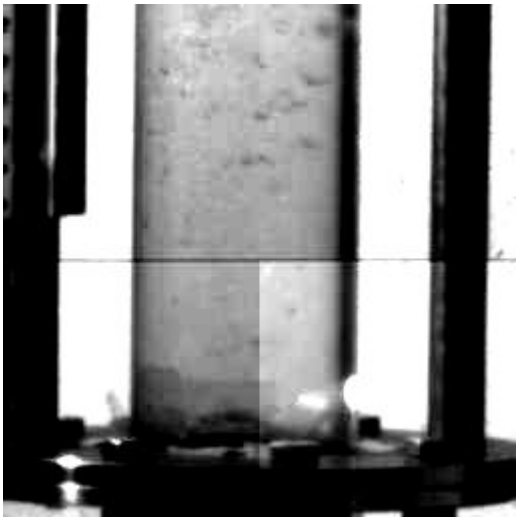


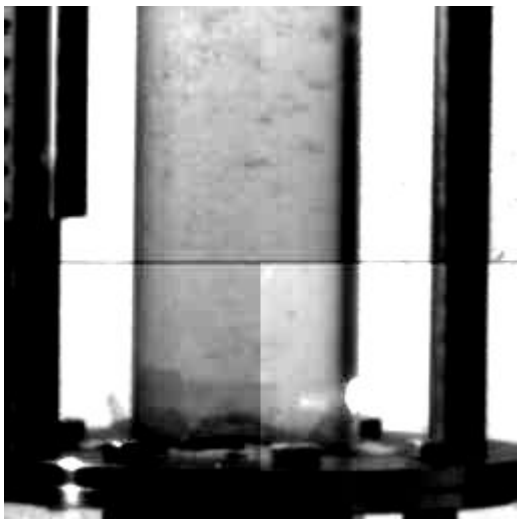
12

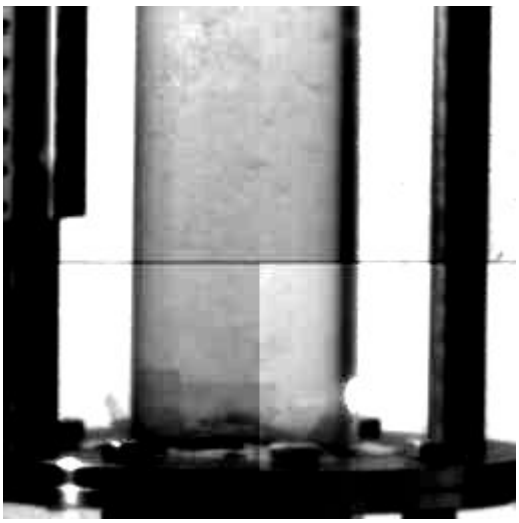
13 

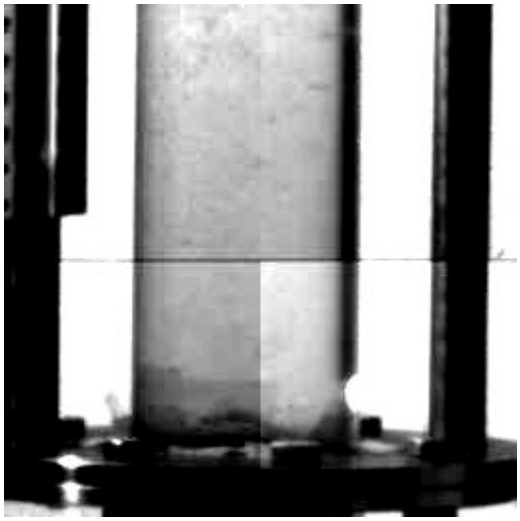
14 

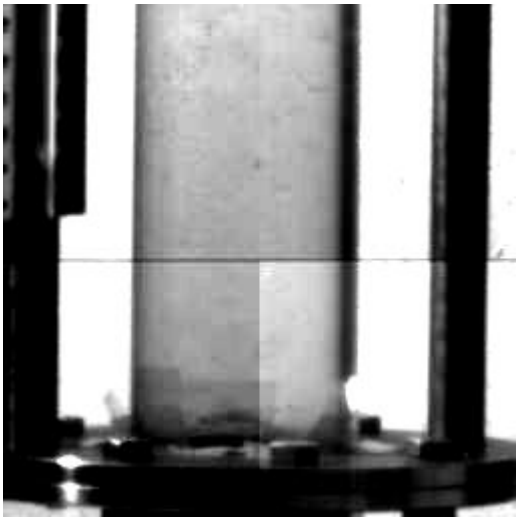
15 

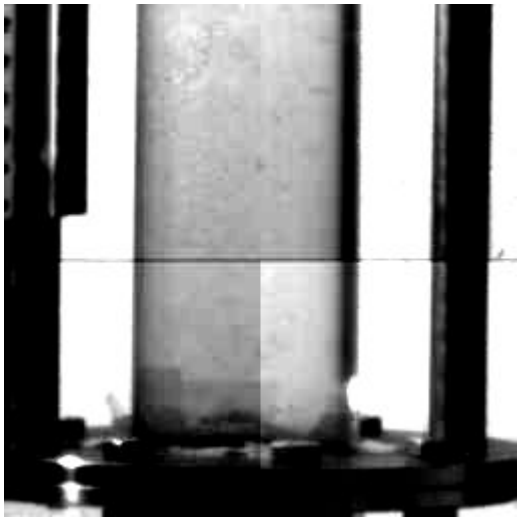
16 

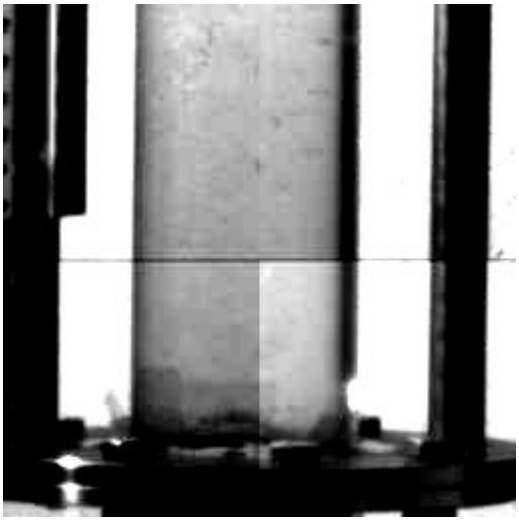
17 

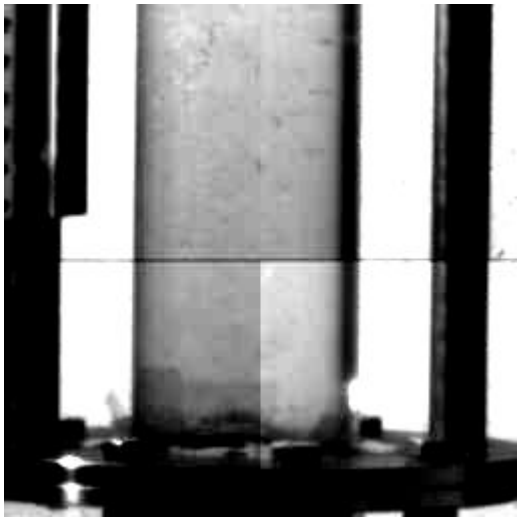
18 

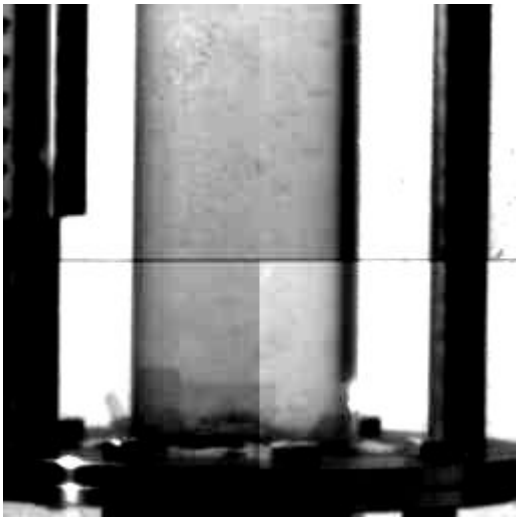

19


20


21

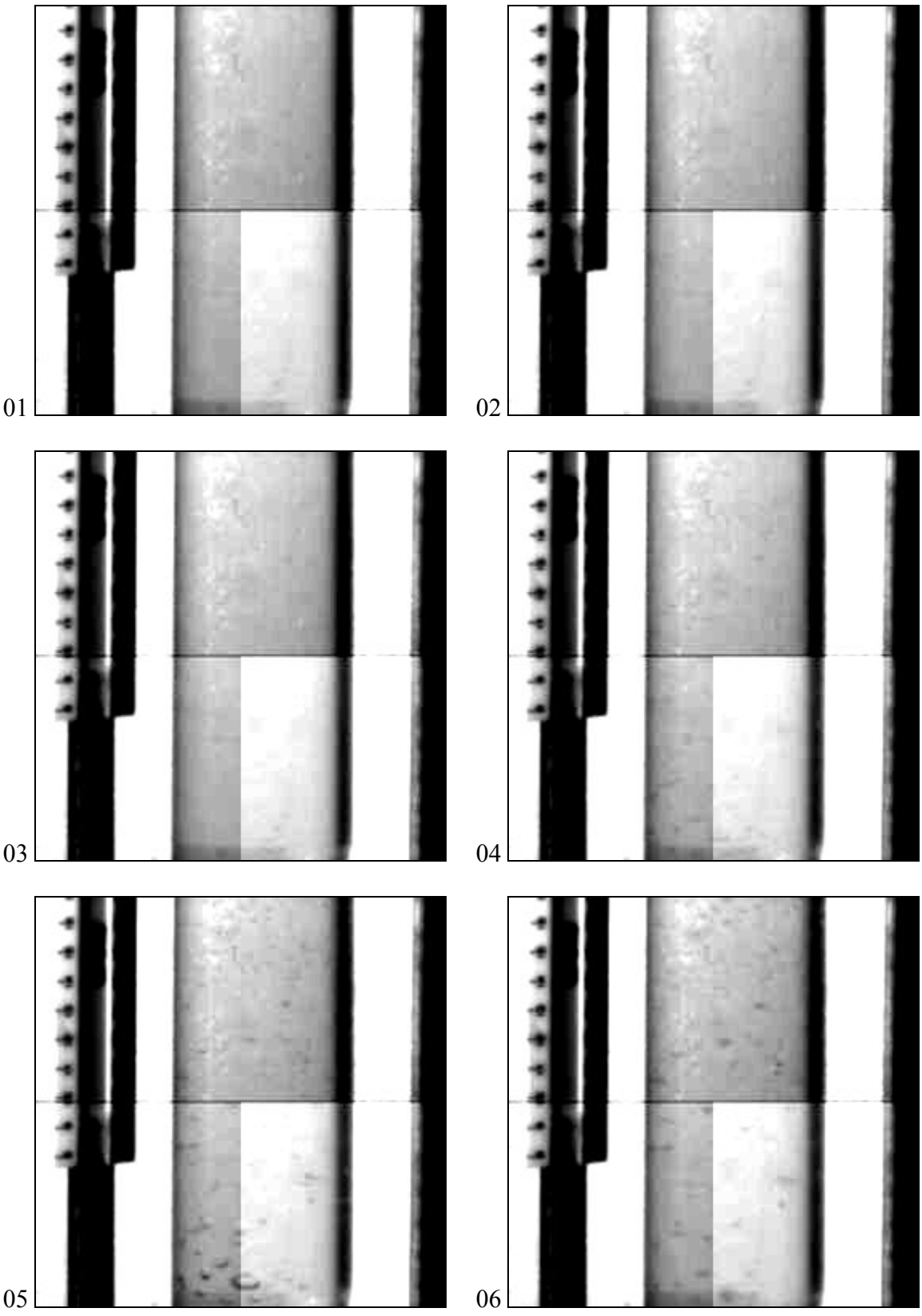

22

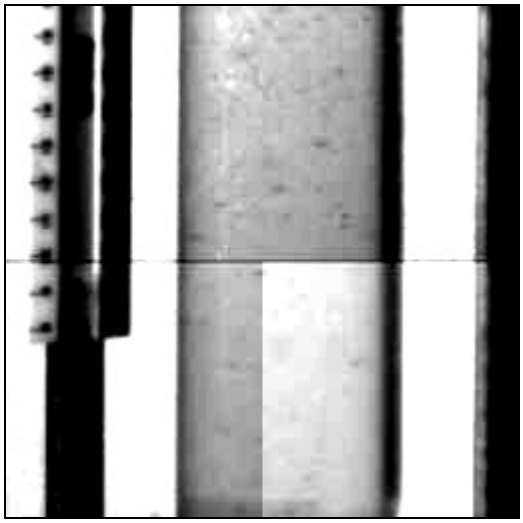

23

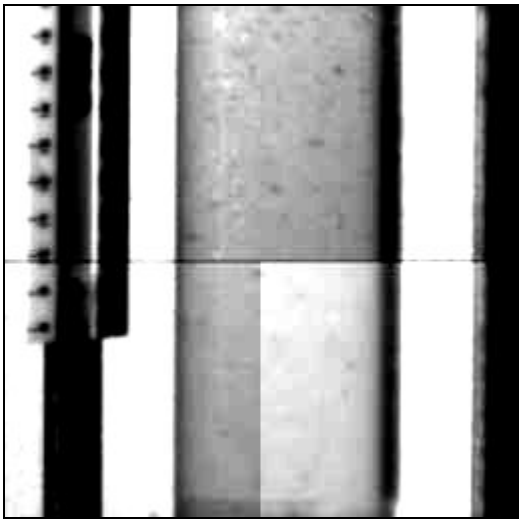

24

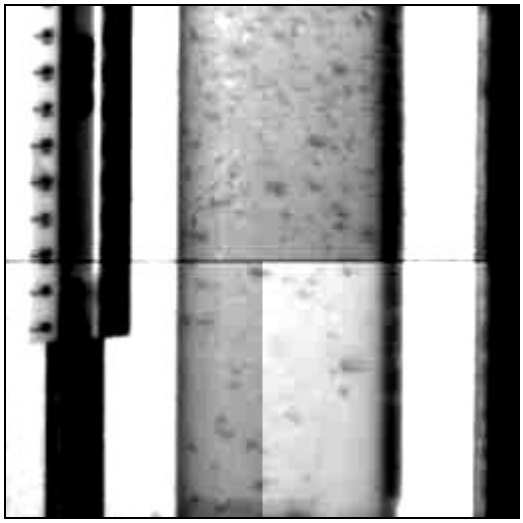
Appendix N

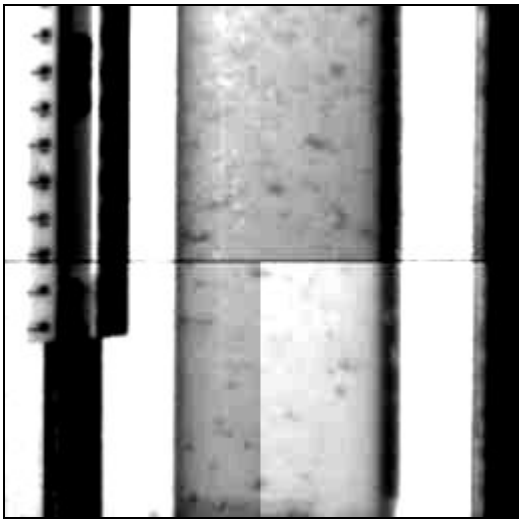
Mach 3 Shock Tube: Photographic Records of the Middle Section of the Tube

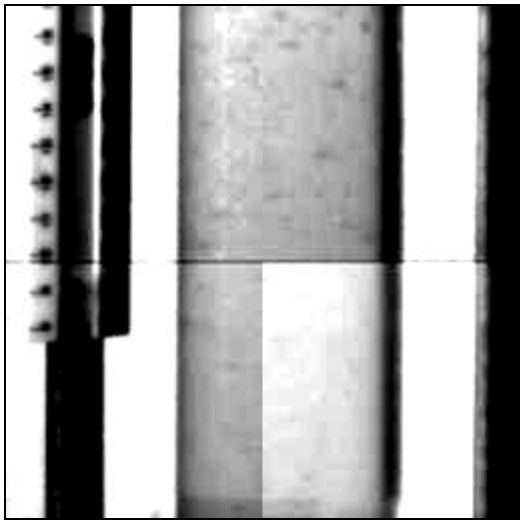

01
02
03
04
05
06

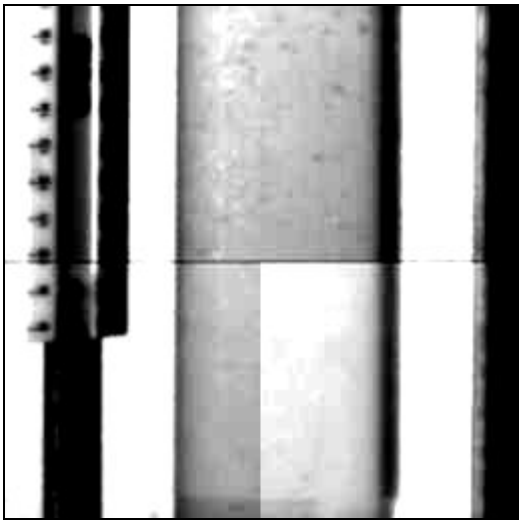
07 

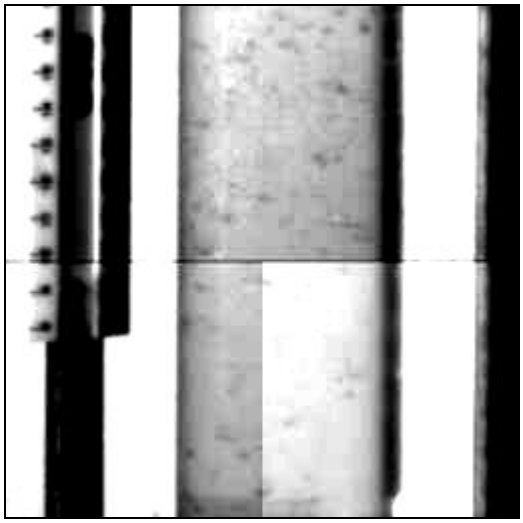
08 

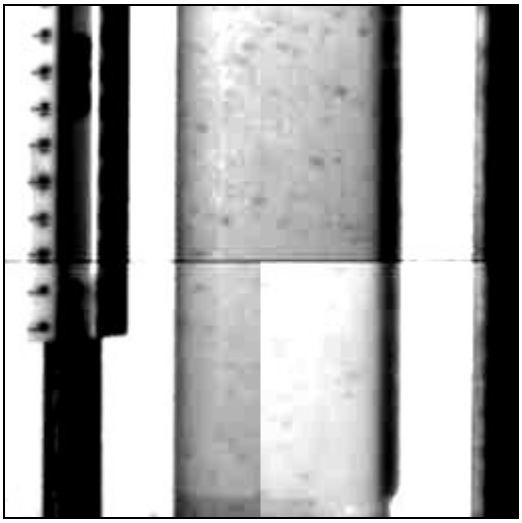
09 

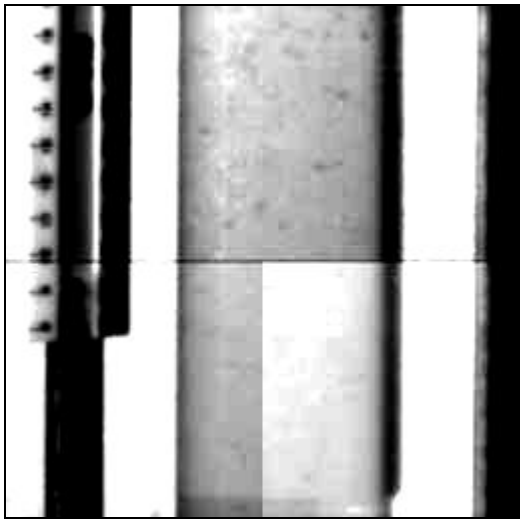
10 

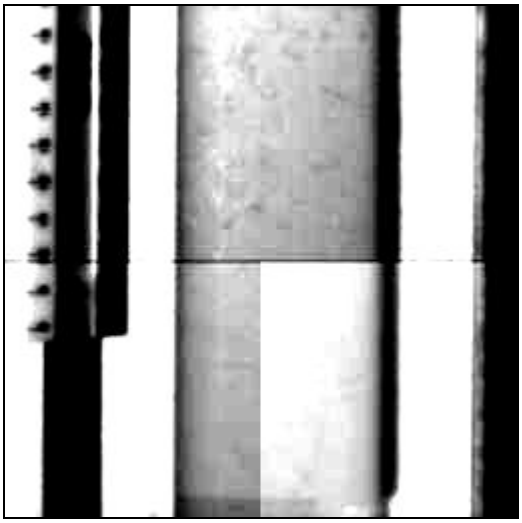
11 

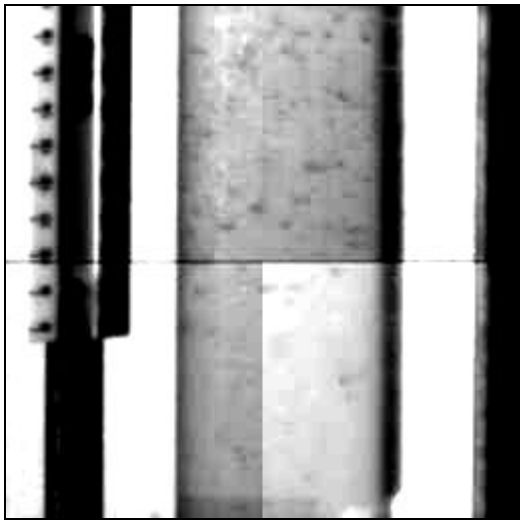
12 

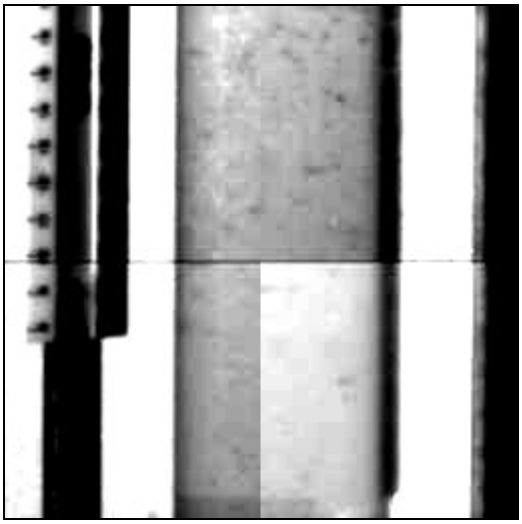
13 

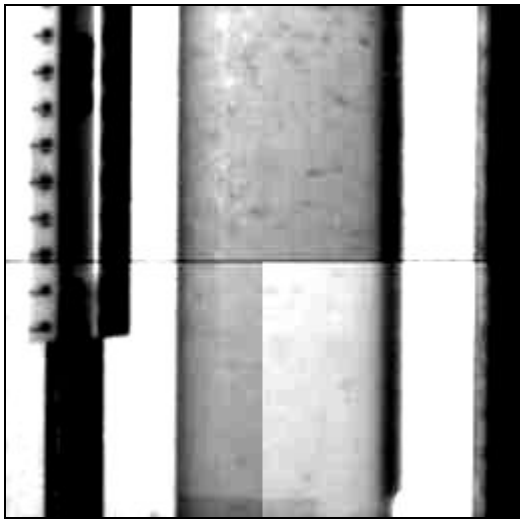
14 

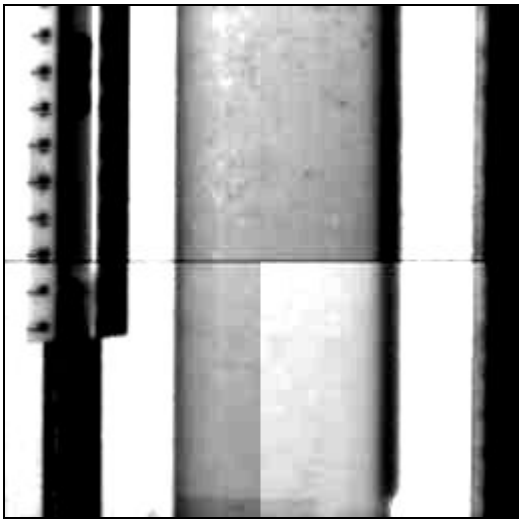
15 

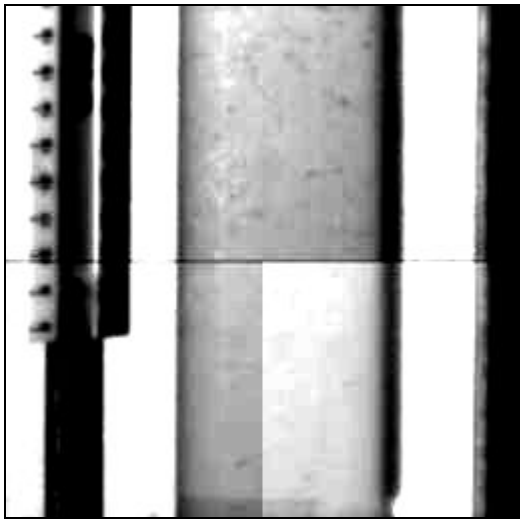
16 

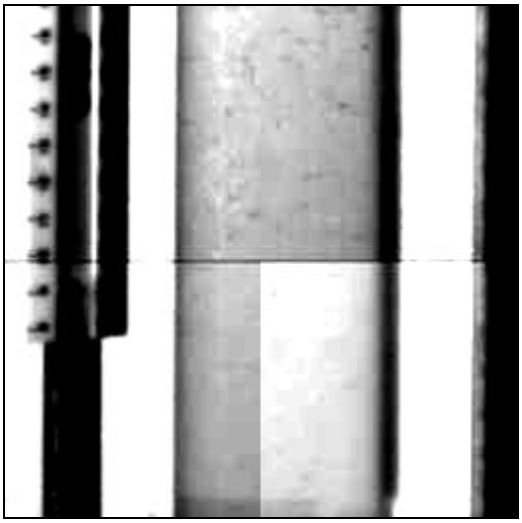
17 

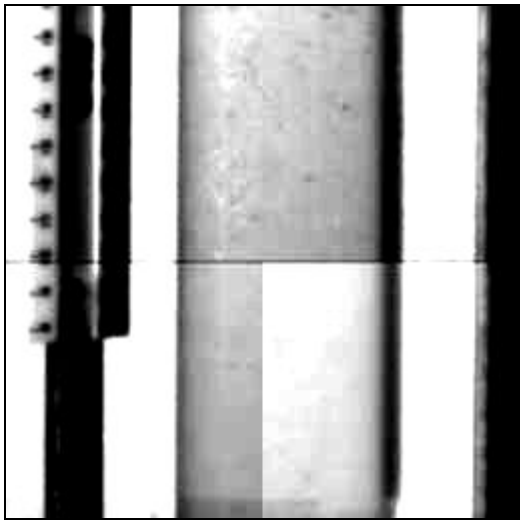
18 

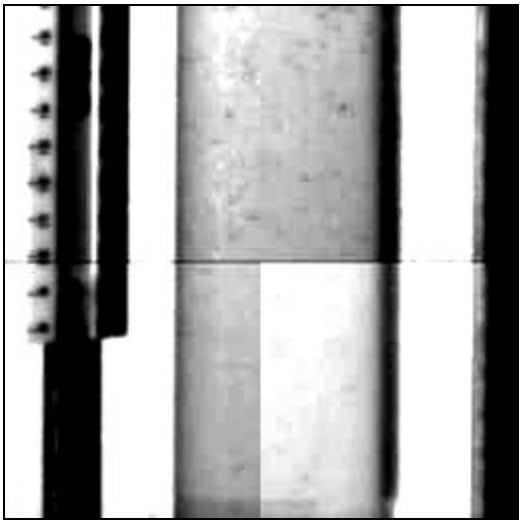
19 

20 

21 

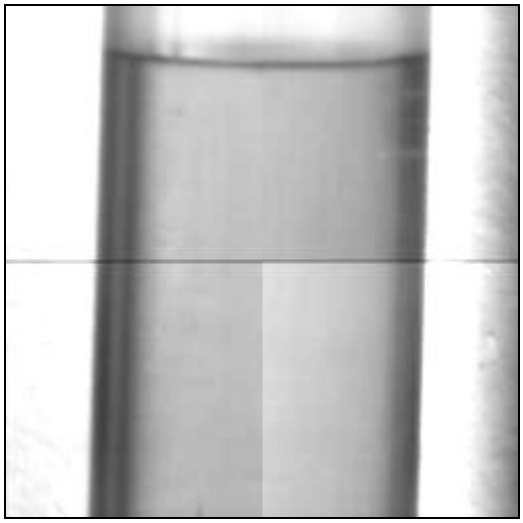
22 

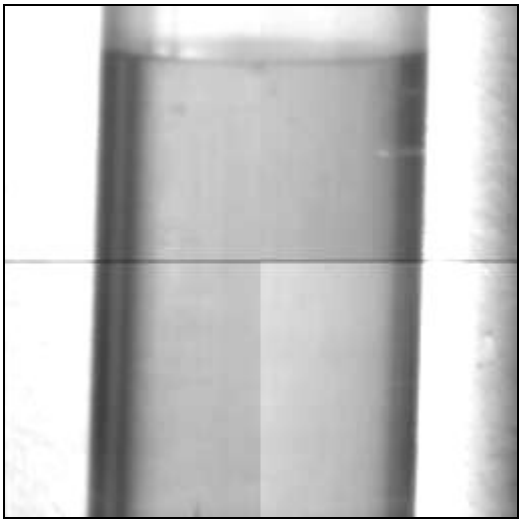
23 

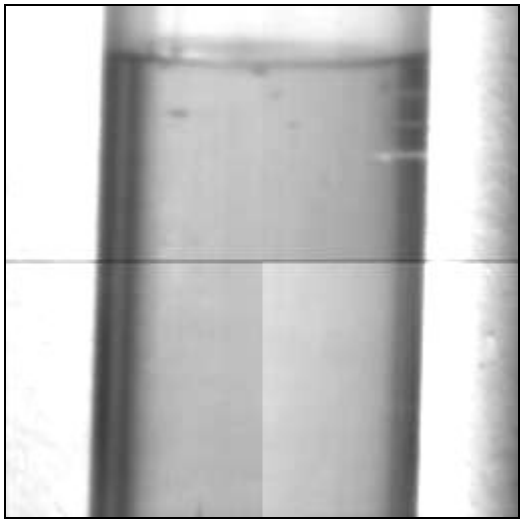
24 

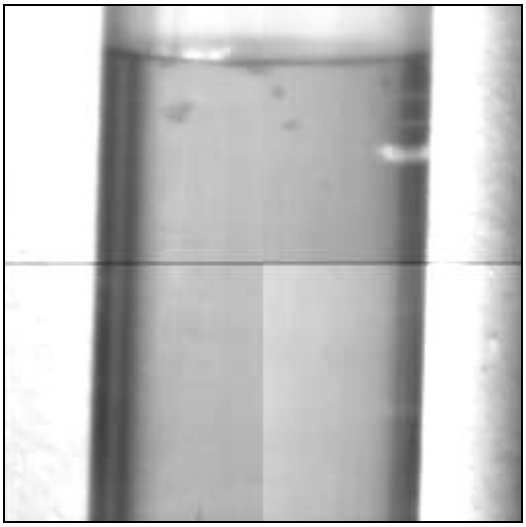
Appendix O

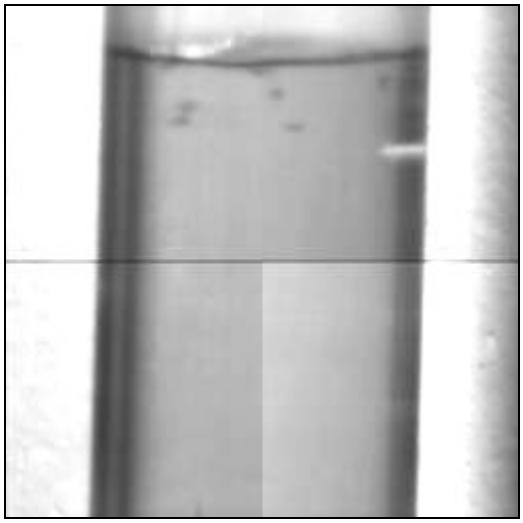
Mach 3 Shock Tube: Photographic Records of the Free Surface of the Liquid Column

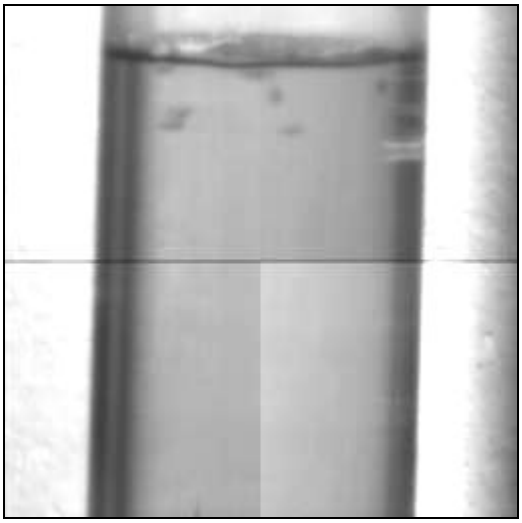
01 

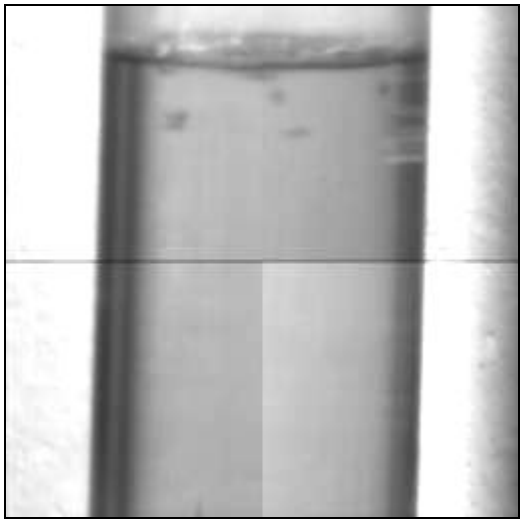
02 

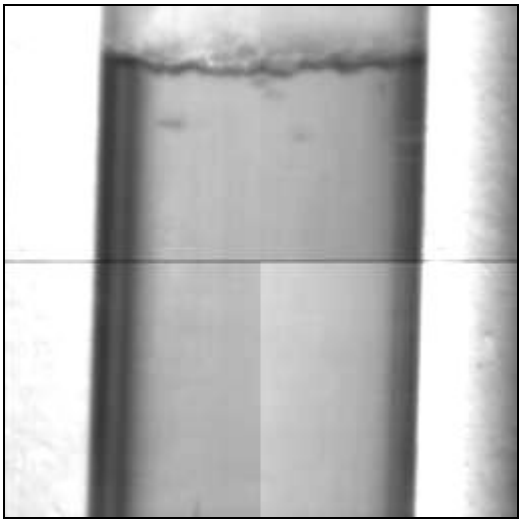
03 

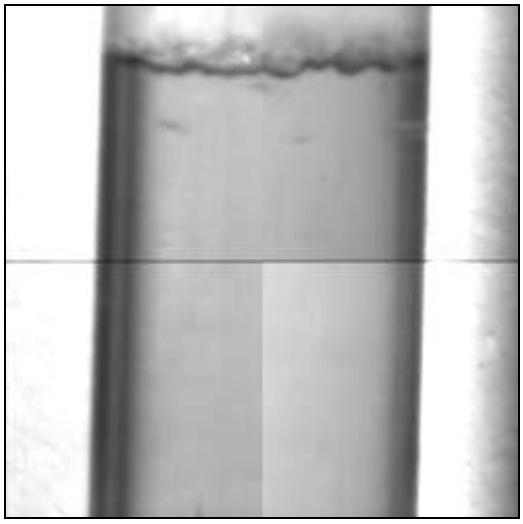
04 

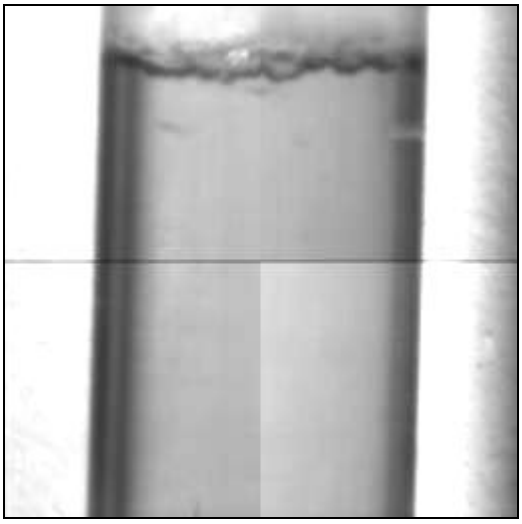
05 

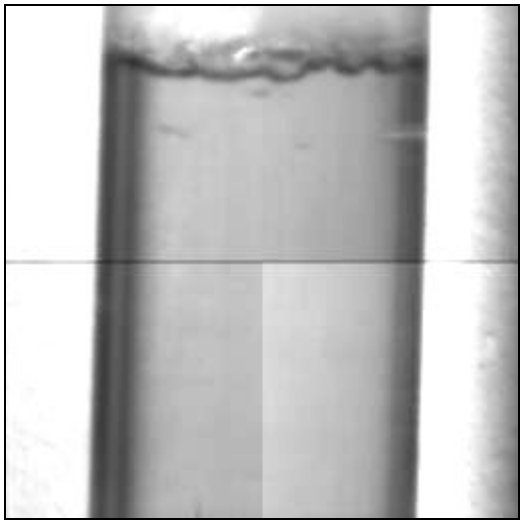
06 

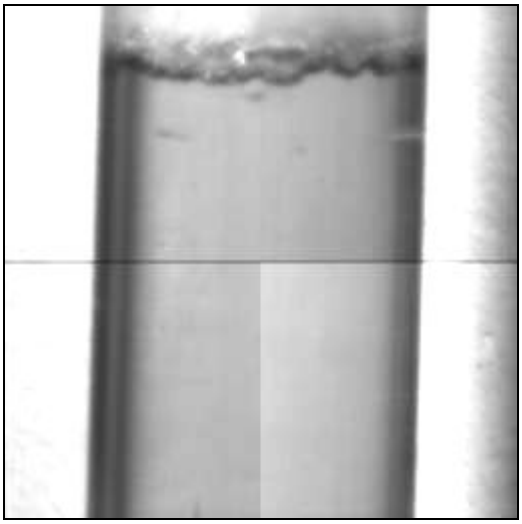
07 

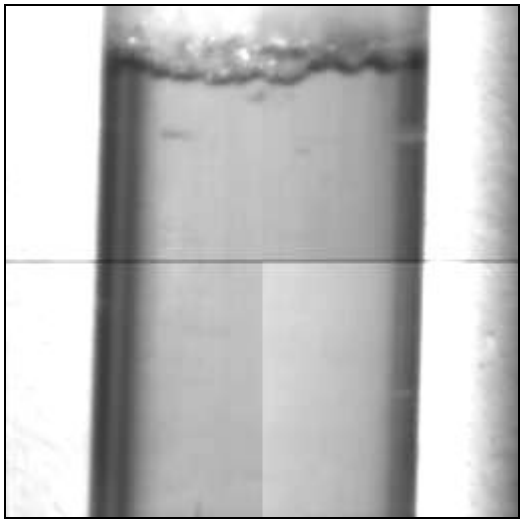
08 

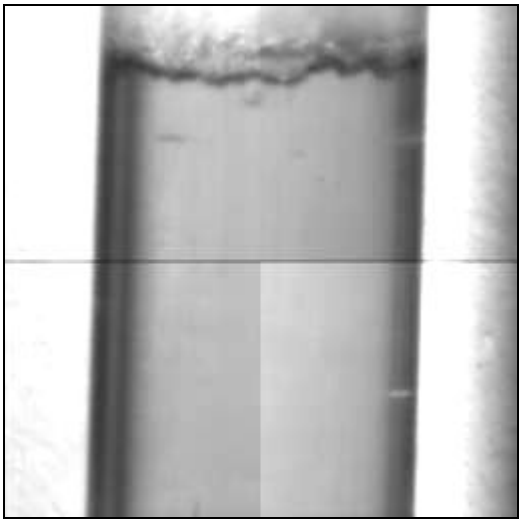
09 

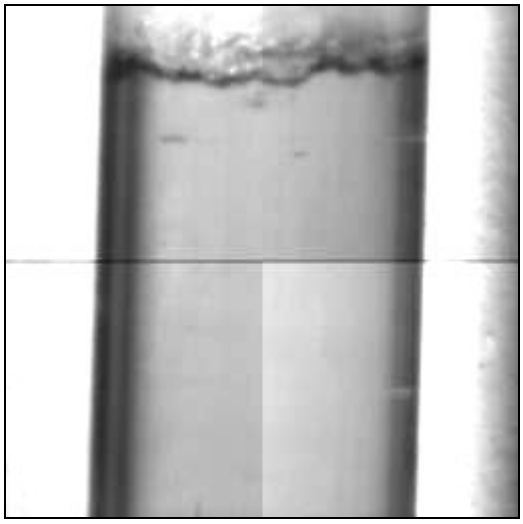
10 

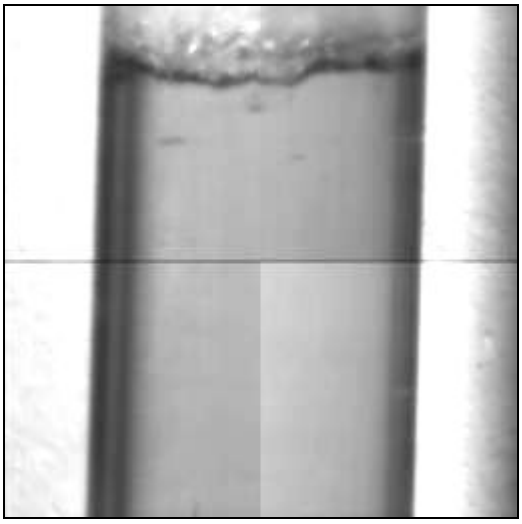
11 

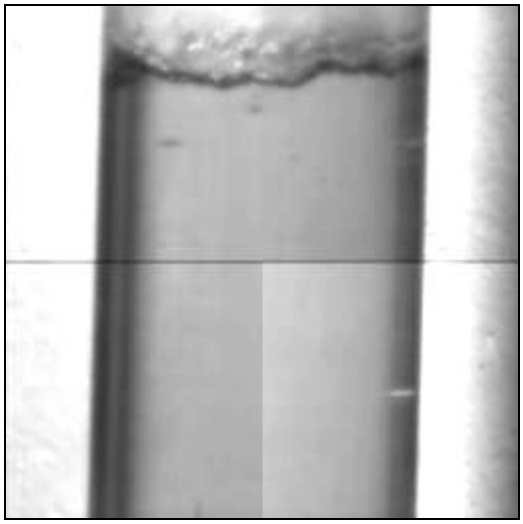
12 

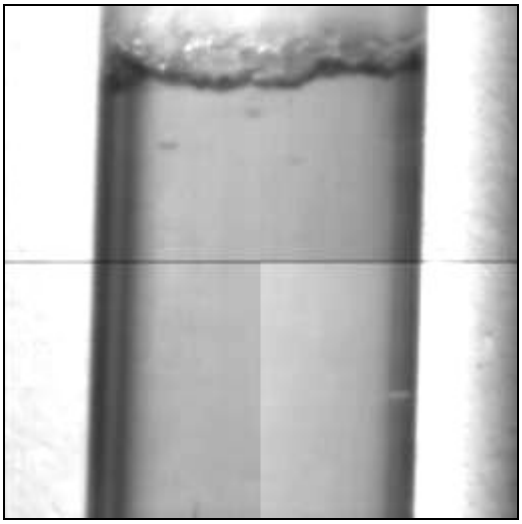
13 

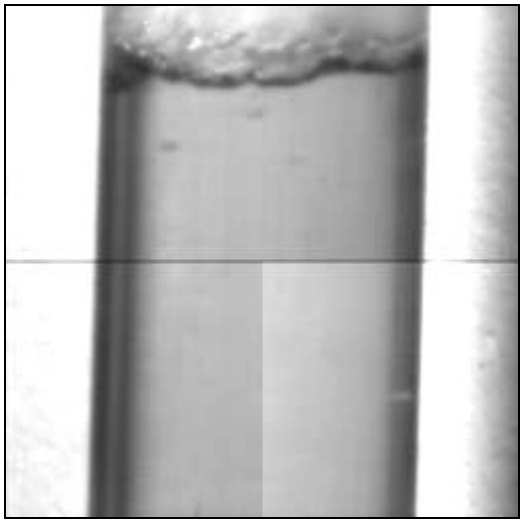
14 

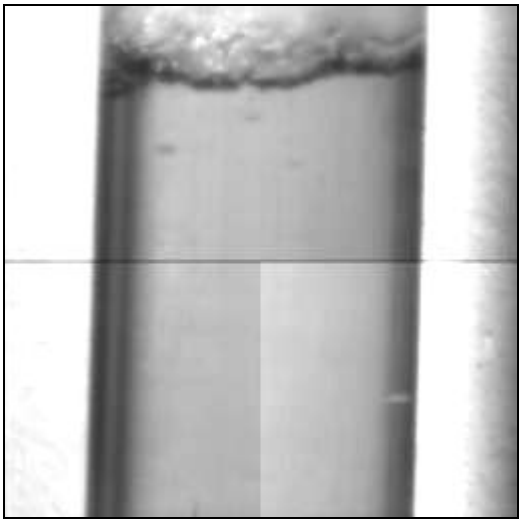
15 

16 

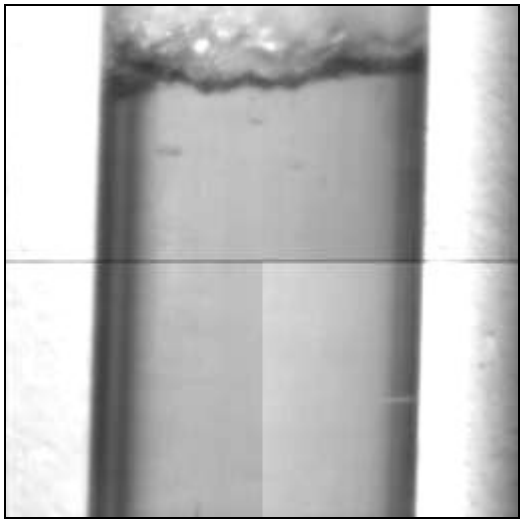
17 

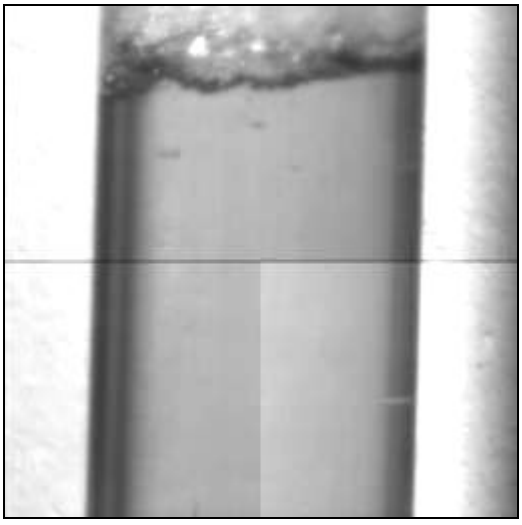
18 

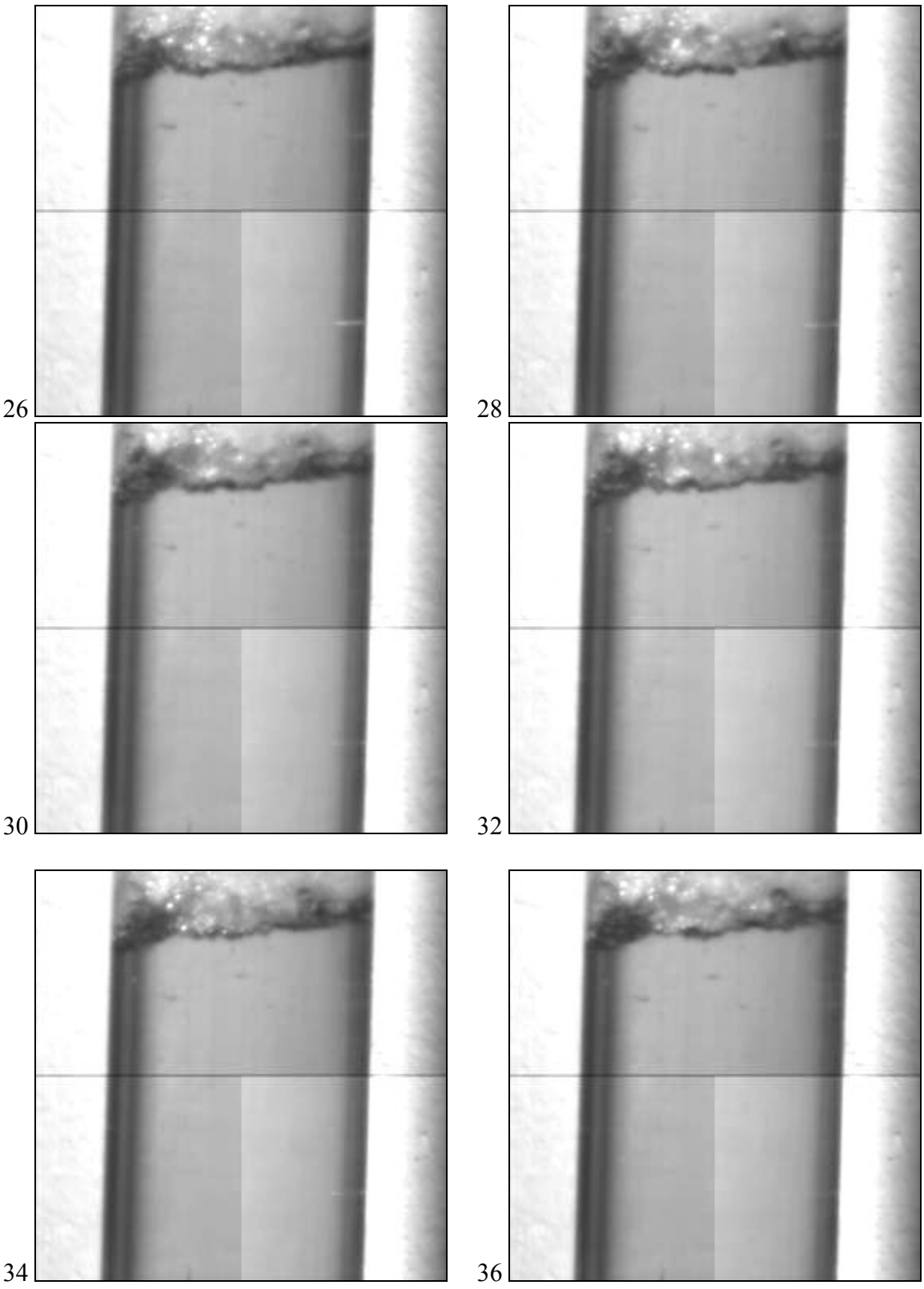
19 

20 

Note that in the following, pictures are separated by two-millisecond intervals for brevity.

22 

24 


26
28
30
32
34
36

Appendix P

Mach 2 Shock Tube: Additional Pressure Records

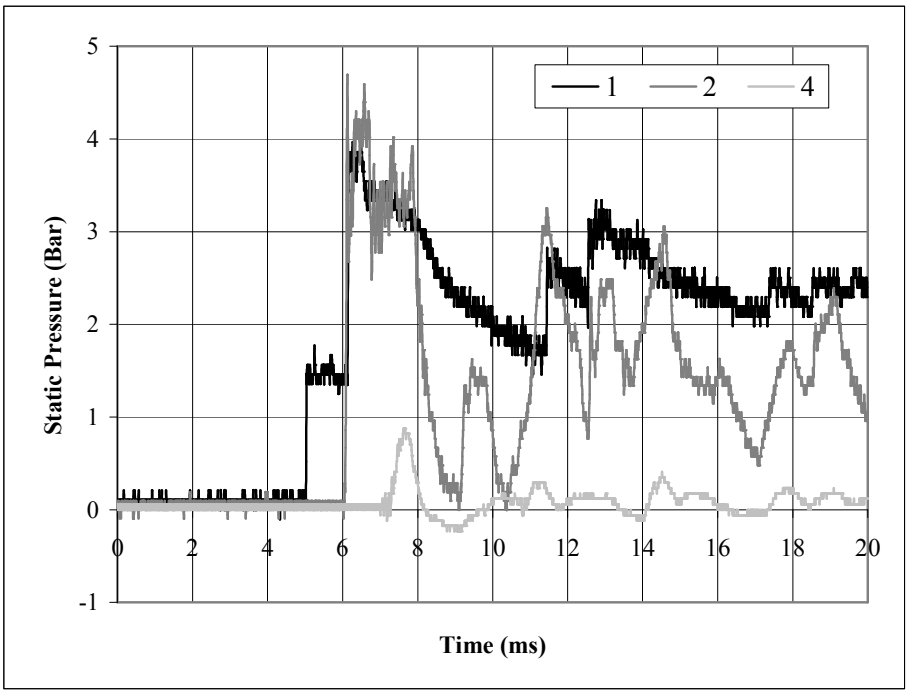


Figure P.1. Driver section filled with helium at 12 *bar*; Sample Rate 200 *kS/s*; Trigger level +0.1 *V*, source CH-1 (transducer 1), position –4, delay 0.

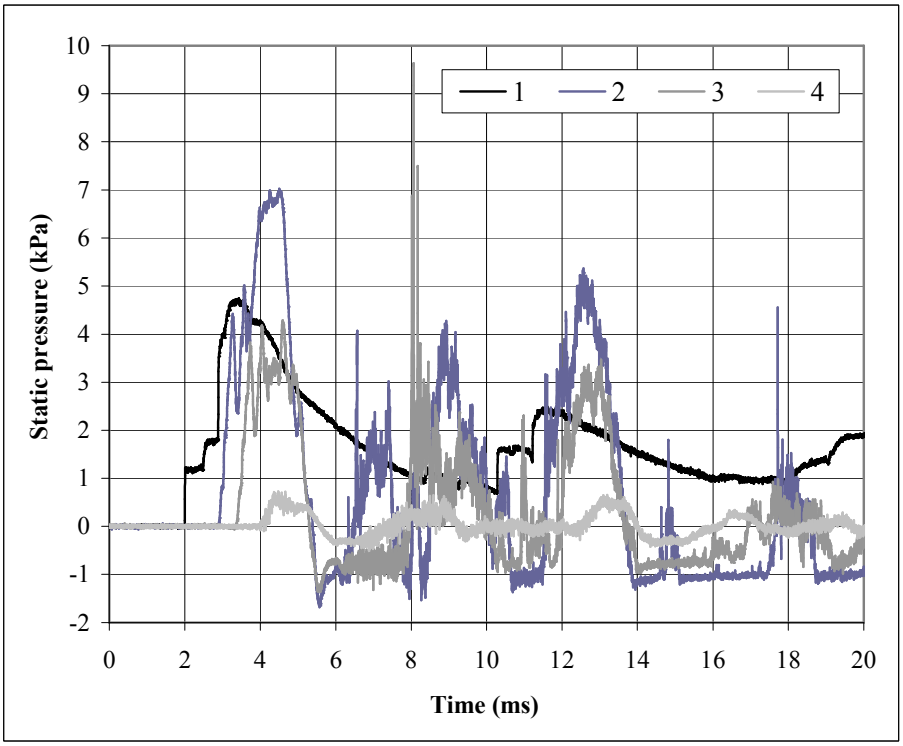


Figure P.2. Driver section filled with helium at 8 *bar*; Sample Rate 500 *kS/s*; Trigger level +0.1 *V*, source CH-1 (transducer 1), position 10%, delay 0.

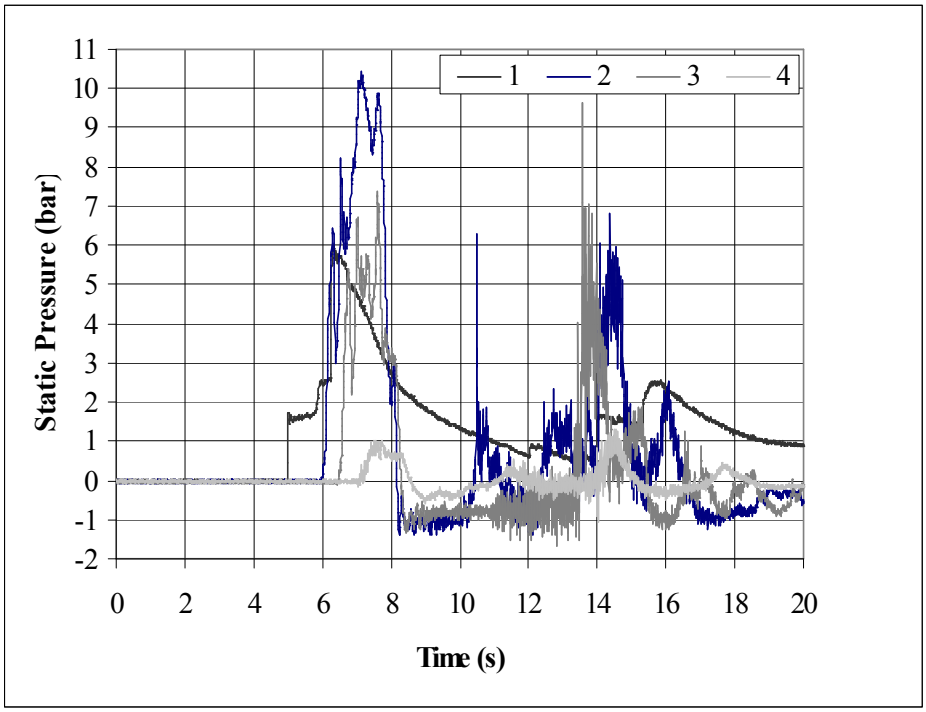


Figure P.3. Driver section filled with helium at 8 *bar*; Sample Rate 200 *kS/s*; Trigger level +0.1 *V*, source CH-1 (transducer 1), position 10%, delay 0.

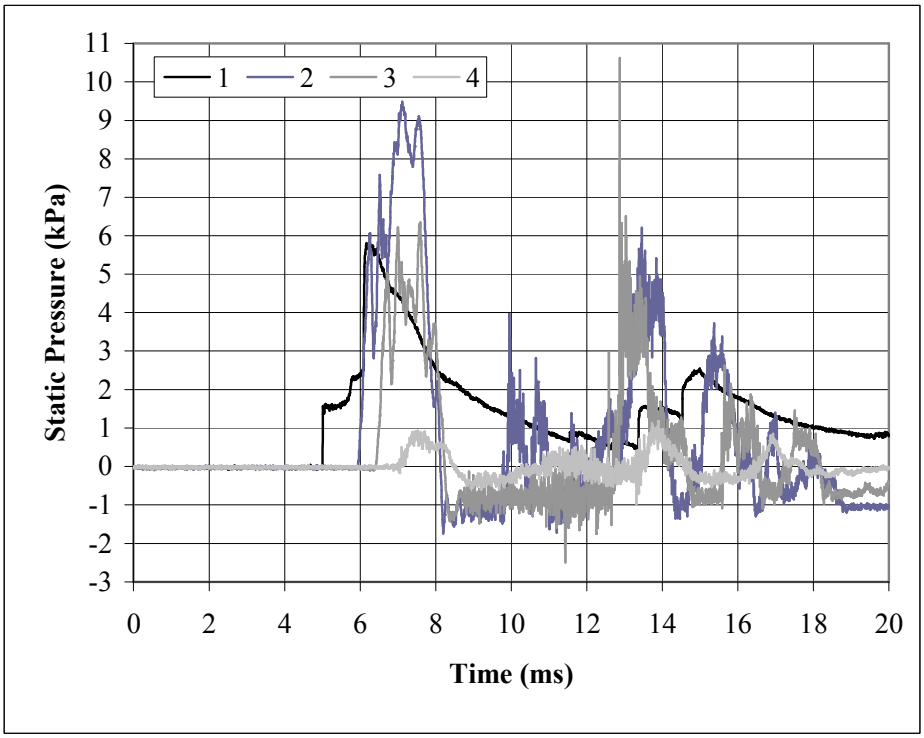


Figure P.4. Driver section filled with helium at 8 *bar*; Sample Rate 200 *kS/s*; Trigger level +0.1 *V*, source CH-1 (transducer 1), position 10%, delay 0.

Appendix Q

Details of the States of the Wave Diagrams of the Mach 3 and Mach 2 Shock Tubes

Table Q.1. Values of the parameters in the regions of the wave diagram of the Mach 3 shock tube.

	Pressure (*bar*)	T (*K*)	Density (kg/m^3)	u (*m/s*)	a (*m/s*)	p/p₀ (p_o=0.027 *bar*)	*s* (*kJ/kg K*)	P	Q	U	A	U+A	U-A	Gradients	
														P-wave	Q-wave
A	0.027	293.0	0.032	0	343.661	1.000	7.912	5.000	5.00	0	1.000	1.000	-1.000	344	-344
B	7.930	293.0	9.391	0	343.661	293.704	6.275	5.000	5.00	0	1.000	1.000	-1.000	344	-344
C	0.231	684.9	0.117	-681.743	519.004	8.556	8.171	5.567	9.53	-1.984	1.510	-0.474	-3.494	-163	-1201
D	0.231	106.8	0.752	-681.743	207.566	8.556	6.275	1.036	5.00	-1.984	0.604	-1.380	-2.588	-474	-889
E	1.071	1114.2	0.334	0	652.508	39.667	8.276	9.493	9.49	0.000	1.899	1.899	-1.899	653	-653
F	1.872	1281.9	0.507	-286.492	697.054	69.333	8.281	9.308	10.98	-0.834	2.028	1.195	-2.862	411	-984
G	1.872	245.7	2.644	-286.492	314.801	69.333	6.513	3.746	5.41	-0.834	0.916	0.082	-1.750	28	-601
H	0.329	118.1	0.968	-627.993	218.313	12.185	6.275	1.349	5.00	-1.827	0.635	-1.192	-2.463	-410	-846
I	0.469	130.7	1.246	-571.459	229.617	17.370	6.275	1.678	5.00	-1.663	0.668	-0.995	-2.331	-342	-801
J	0.668	144.6	1.603	-511.998	241.505	24.741	6.275	2.024	5.00	-1.490	0.703	-0.787	-2.193	-270	-754
K	0.951	159.9	2.064	-449.458	254.008	35.222	6.275	2.388	5.00	-1.308	0.739	-0.569	-2.047	-195	-703
L	1.355	176.9	2.657	-383.680	267.157	50.185	6.275	2.770	5.00	-1.116	0.777	-0.339	-1.894	-117	-651
M	1.929	195.7	3.420	-314.495	280.984	71.444	6.275	3.173	5.00	-0.915	0.818	-0.098	-1.733	-34	-595
N	2.746	216.5	4.402	-241.726	295.520	101.704	6.275	3.596	5.00	-0.703	0.860	0.157	-1.563	54	-537
O	3.911	239.5	5.667	-165.188	310.796	144.852	6.275	4.041	5.00	-0.481	0.904	0.424	-1.385	146	-476
P	5.569	264.9	7.295	-84.682	326.836	206.259	6.275	4.509	5.00	-0.246	0.951	0.705	-1.197	242	-412

Table Q.1. Values of the parameters in the regions of the wave diagram of the Mach 3 shock tube: Continued.

	Pressure (*bar*)	p'/p₀' (p_o = 7.5 *bar*)	p/p₀	u (*m/s*)	a (*m/s*)	p/p₀ (p_o = 0.027 *bar*)	Density (kg/m^3)	P	Q	U	A	U+A	U-A	Gradients	
														P-wave	Q-wave
W_1	7.930	1.0000	1.0000	0.000	1482.000	293.70	1000.00	0.31177	0.31177	0.00000	1.00000	1.000	-1.000	1482	-1482
W_2	3.852	0.9986	0.4858	-0.274	1481.120	142.67	999.815	0.31140	0.31177	-0.00018	0.99941	0.999	-1.000	1481	-1481
W_3	-0.645	0.9973	-0.0813	0.000	1480.241	-23.888	999.630	0.31140	0.31140	0.00000	0.99881	0.999	-0.999	1480	-1480

W_4, W_5, W_6 and W_7 could not be calculated using the conventional wave diagram method.

Table Q.1. Values of the parameters in the regions of the wave diagram of the Mach 3 shock tube: Continued.

	Pressure (*bar*)	T (*K*)	p/p₀ (p_o = 7.5 *bar*)	u (*m/s*)	a (*m/s*)	p/p₀ (p_o = 0.027 *bar*)	*s* (*kJ/kg.K*)	P	Q	U	A	U+A	U-A	Gradients	
														P-wave	Q-wave
X	3.852	239.1	0.486	-0.274	309.954	142.667	6.275	4.50880	4.51039	-0.001	0.902	0.901	-0.903	310	-310
V	2.652	215.0	0.334	-80.627	293.884	98.226	6.275	4.04117	4.51039	-0.235	0.855	0.621	-1.090	213	-375
U	1.824	193.2	0.230	-157.086	278.592	67.574	6.275	3.59620	4.51039	-0.457	0.811	0.354	-1.268	122	-436
T	1.254	173.5	0.158	-229.811	264.047	46.427	6.275	3.17297	4.51039	-0.669	0.768	0.100	-1.437	34	-494
S	0.860	155.8	0.108	-298.971	250.215	31.856	6.275	2.77048	4.51039	-0.870	0.728	-0.142	-1.598	-49	-549
R	0.589	139.9	0.074	-364.732	237.063	21.829	6.275	2.38777	4.51039	-1.061	0.690	-0.371	-1.751	-128	-602
Q	0.403	125.5	0.051	-427.260	224.557	14.938	6.275	2.02388	4.51039	-1.243	0.653	-0.590	-1.897	-203	-652

Table Q.2. Values of the parameters in the regions of the wave diagram of the Mach 2 shock tube.

	Pressure (*bar*)	T (*K*)	*γ or n*	Density (kg/m^3)	u (*m/s*)	a (*m/s*)	p/p₀ (p_o = 0.83 *bar*)	*s* (*kJ/kg.K*)	P	Q	U	A	U+A	U-A	Gradients	
															P-wave	Q-wave
A	0.830	293	1.400	0.983	0	1007.169	1.0000	6.925	14.66	14.66	0	2.931	2.931	-2.931	1007.2	-1007.2
B	12.000	293	1.667	1.972	0	343.661	14.4578	26.265	2.999	2.999	0	1.000	1.000	-1.000	343.66	-343.66
C	4.717	544	1.400	2.978	517.707	467.516	5.68313	7.068	8.306	5.294	1.506	1.360	2.866	0.146	984.93	50.175
D	4.717	202	1.667	1.126	517.707	835.635	5.68313	26.265	8.798	5.786	1.506	2.432	3.938	-0.926	1353.3	-318.23
E	1.495	127	1.667	0.565	0	664.031	1.8012	26.265	5.793	5.793	0	1.932	1.932	-1.932	663.95	-663.95
F	17.893	840	1.349	7.423	0	570.173	21.5578	7.137	9.507	9.507	0	1.659	1.659	-1.659	570.13	-570.13
G	0.83	293	7.415	1000	0	1482.000	1.0000	--	0.312	0.312	0	1.000	1.000	-1.000	1482.0	-1482.0
H	0.83	293	7.415	1000	0	1482.000	1.0000	--	0.312	0.312	0	1.000	1.000	-1.000	1482.0	-1482.0

The parameters in region *I* could not be predicted theoretically as the characteristics of transmission of waves through the gas-liquid interface and the attenuation of the liquid pulses were not known. The pressure throughout region *I* is non-uniform.

Appendix R

Results of Simulations of Bubble Response to an Applied Pressure

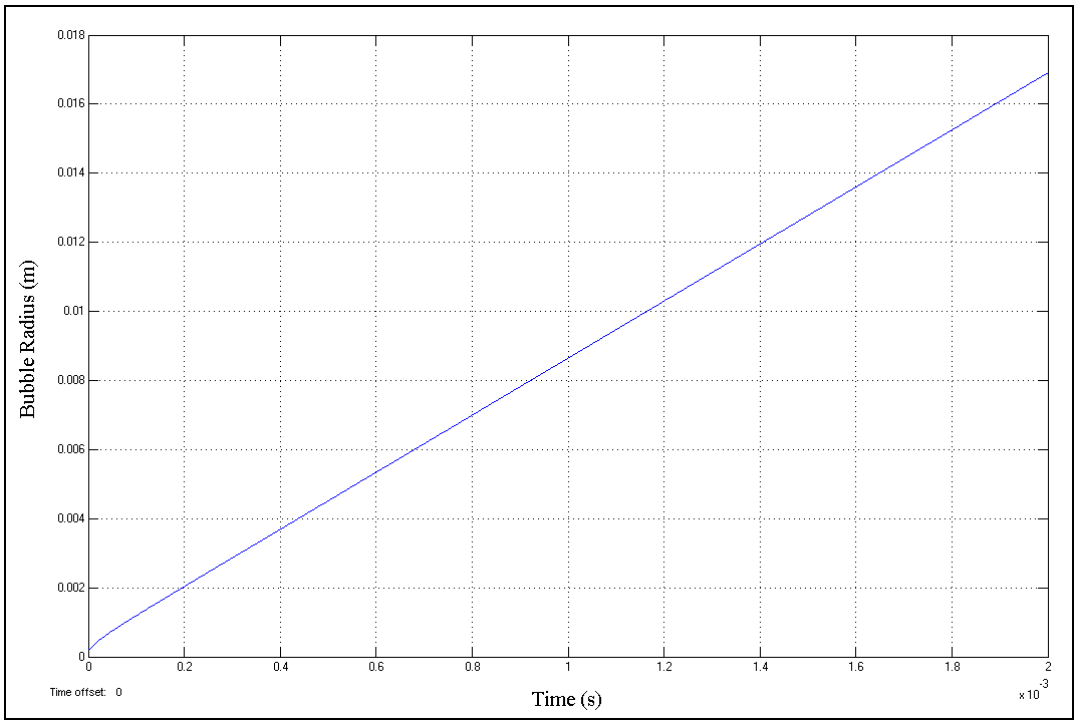


Figure R.1. Variation of bubble radius with time for growth of bubble (R_o 0.2 *mm*) subjected to step-function pressure drop from 7.93 to –1 *bar* at time zero.

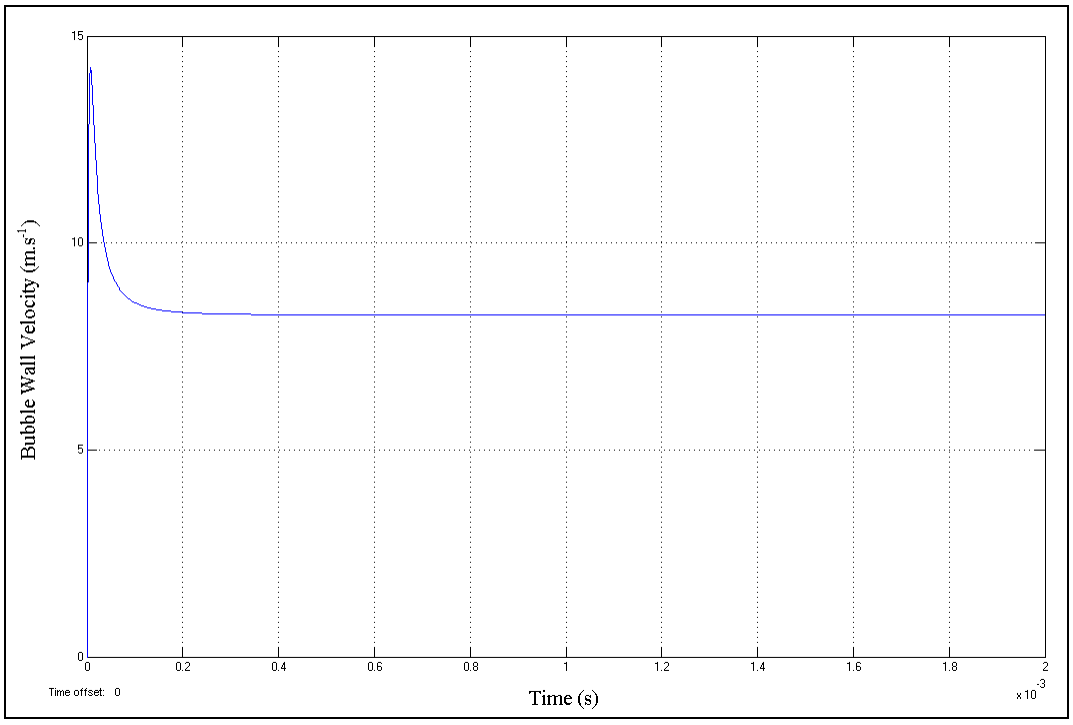


Figure R.2. Variation of bubble wall velocity with time for growth of bubble (R_o 0.2 *mm*) subjected to step-function pressure drop from 7.93 to –1 *bar* at time zero.

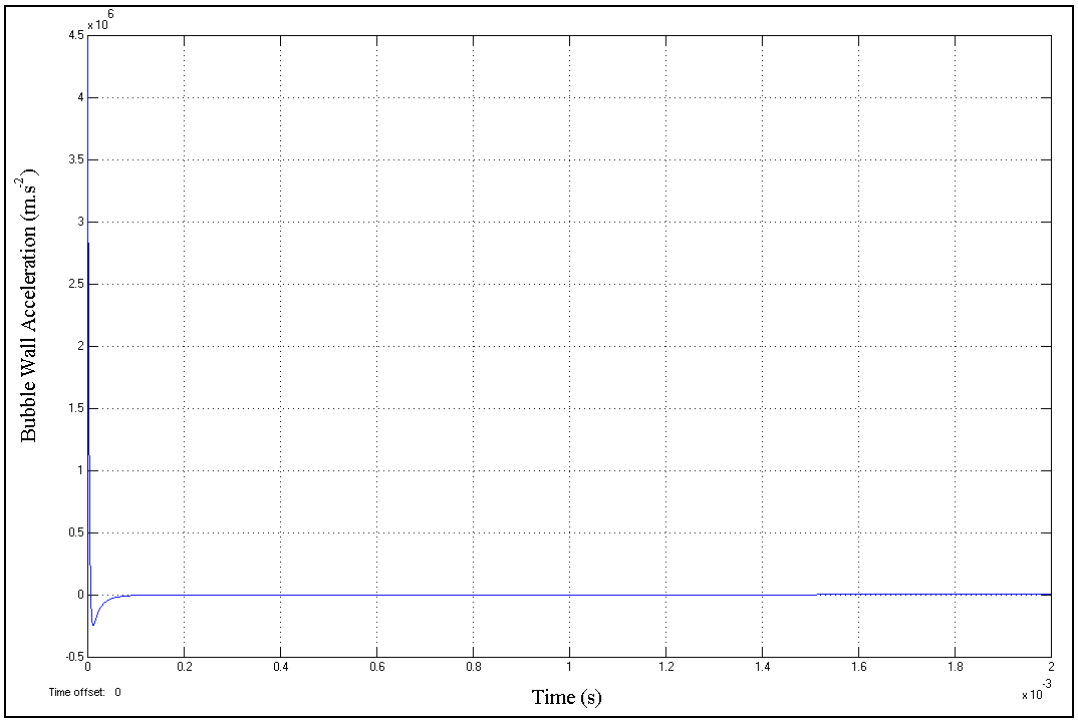


Figure R.3. Variation of bubble wall acceleration with time for growth of bubble (R_o 0.2 *mm*) subjected to step-function pressure drop from 7.93 to –1 *bar* at time zero.

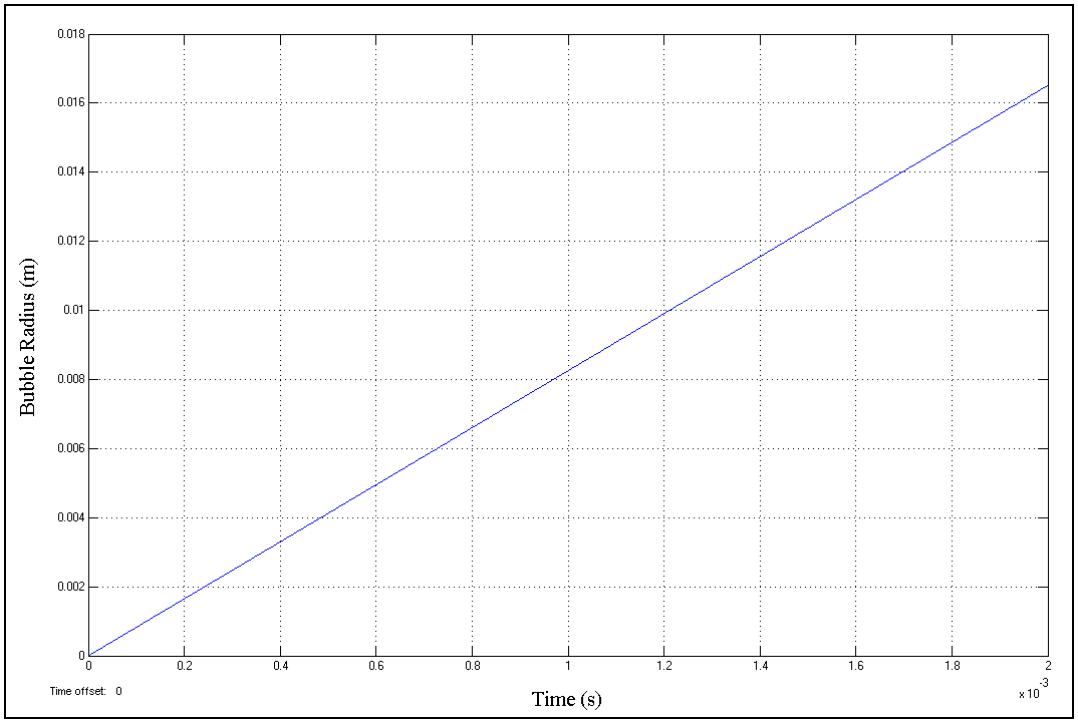


Figure R.4. Variation of bubble radius with time for growth of bubble (R_o 1 μm) subjected to step-function pressure drop from 7.93 to –1 *bar* at time zero.

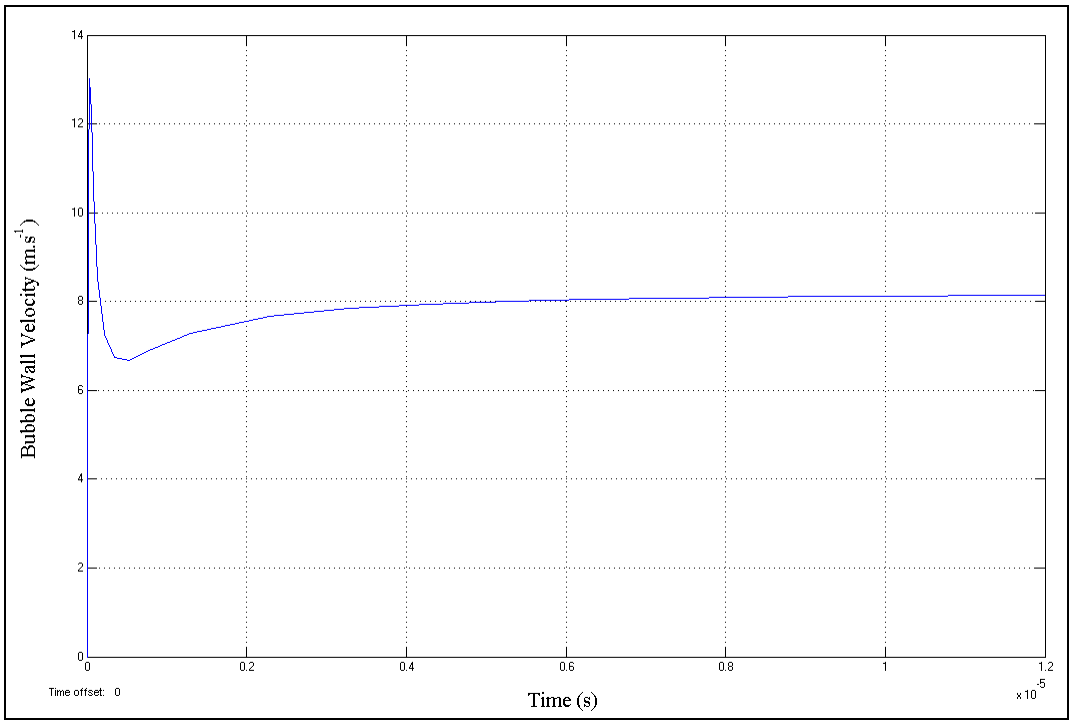


Figure R.5. Variation of bubble wall velocity with time for growth of bubble (R_o 1 μm) subjected to step-function pressure drop from 7.93 to –1 *bar* at time zero.

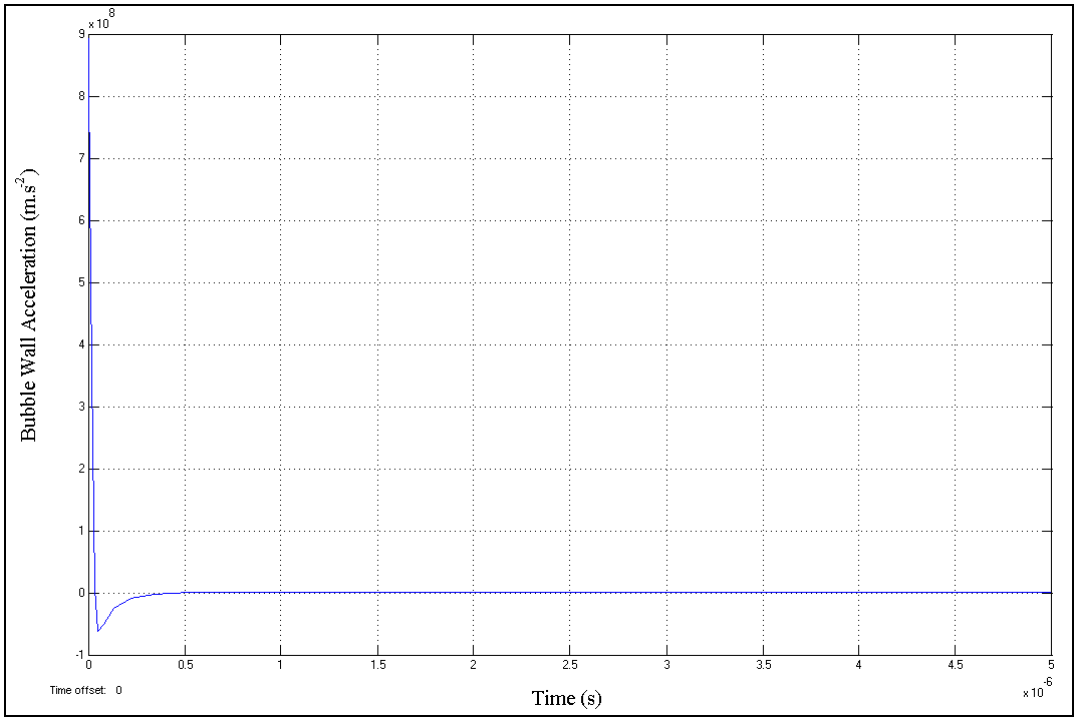


Figure R.6. Variation of bubble wall acceleration with time for growth of bubble (R_o 1 μm) subjected to step-function pressure drop from 7.93 to –1 *bar* at time zero.

Table R.1. Results of Simulations using Simulink - Adiabatic Case (R_V taken as 1 *mm*).

Initial Bubble Radius R_o *(m)*	$V_o/(R_o^3/R_V^3)$	**Time Taken in Attaining Visible size T_V** *(ms)*	**Radius R after 1 *ms*** *(mm)*	**Radius R after 2 *ms*** *(mm)*	$\dot{R}_{MAX}$ $(m.s^{-1})$	**Time of Attaining $\dot{R}_{MAX}$** *(ms)*	$\dot{R}_{Final}$ $(m.s^{-1})$
1.0E-03	1.00E+00	0.0000	10.100	18.4	14.2467	3.69E-02	8.2710
9.0E-04	7.29E-01	0.0152	9.965	18.2	14.2462	3.38E-02	8.2681
8.0E-04	5.12E-01	0.0221	9.780	18.1	14.2466	2.97E-02	8.2657
7.0E-04	3.43E-01	0.0282	9.594	17.9	14.2454	2.56E-02	8.2637
6.0E-04	2.16E-01	0.0344	9.406	17.7	14.2455	2.25E-02	8.2622
5.0E-04	1.25E-01	0.0416	9.217	17.5	14.2454	1.84E-02	8.2610
4.0E-04	6.40E-02	0.0505	9.027	17.3	14.2402	1.54E-02	8.2604
3.0E-04	2.70E-02	0.0624	8.835	17.1	14.2432	1.13E-02	8.2597
2.0E-04	8.00E-03	0.0782	8.642	16.9	14.2264	7.88E-03	8.2594
1.0E-04	1.00E-03	0.0984	8.449	16.7	14.2097	3.44E-03	8.2593
5.0E-05	1.25E-04	0.1097	8.351	16.6	14.2092	1.81E-03	8.2593
1.0E-05	1.00E-06	0.1193	8.272	16.5	14.1046	3.58E-04	8.2592
1.0E-06	1.00E-09	0.1218	8.251	16.5	13.0102	3.23E-05	8.2592
5.0E-07	1.25E-10	0.1223	8.247	16.5	11.9553	1.51E-05	8.2592

Table R.2. Results of Simulations using Simulink - Isothermal Case (R_V taken as 1 *mm*).

Initial Bubble Radius R_o *(m)*	$V_o/(R_o^3/R_V^3)$	**Time Taken in Attaining Visible size T_V** *(ms)*	**Radius R after 1 *ms*** *(mm)*	**Radius R after 2 *ms*** *(mm)*	$\dot{R}_{MAX}$ $(m.s^{-1})$	**Time of Attaining $\dot{R}_{MAX}$** *(ms)*	$\dot{R}_{Final}$ $(m.s^{-1})$
1.0E-03	1.00E+00	0.0000	10.600	19.0	15.4453	4.09E-05	8.2998
9.0E-04	7.29E-01	0.0151	10.400	18.7	15.4451	3.68E-05	8.2910
8.0E-04	5.12E-01	0.0217	10.200	18.5	15.4450	3.27E-05	8.2833
7.0E-04	3.43E-01	0.0272	9.959	18.3	15.4470	2.86E-05	8.2767
6.0E-04	2.16E-01	0.0326	9.726	18.0	15.4445	2.45E-05	8.2712
5.0E-04	1.25E-01	0.0386	9.490	17.8	15.4441	2.04E-05	8.2668
4.0E-04	6.40E-02	0.0460	9.250	17.5	15.4435	1.64E-05	8.2635
3.0E-04	2.70E-02	0.0561	9.005	17.3	15.4425	1.23E-05	8.2613
2.0E-04	8.00E-03	0.0709	8.758	17.0	15.4357	7.88E-06	8.2600
1.0E-04	1.00E-03	0.0926	8.508	16.8	15.4002	4.44E-06	8.2594
5.0E-05	1.25E-04	0.1064	8.381	16.6	15.4339	2.04E-06	8.2593
1.0E-05	1.00E-06	0.1185	8.278	16.5	15.2845	4.57E-07	8.2592
1.0E-06	1.00E-09	0.1217	8.252	16.5	14.1669	4.53E-08	8.2592
5.0E-07	1.25E-10	0.1221	8.249	16.5	13.2302	1.93E-08	8.2592

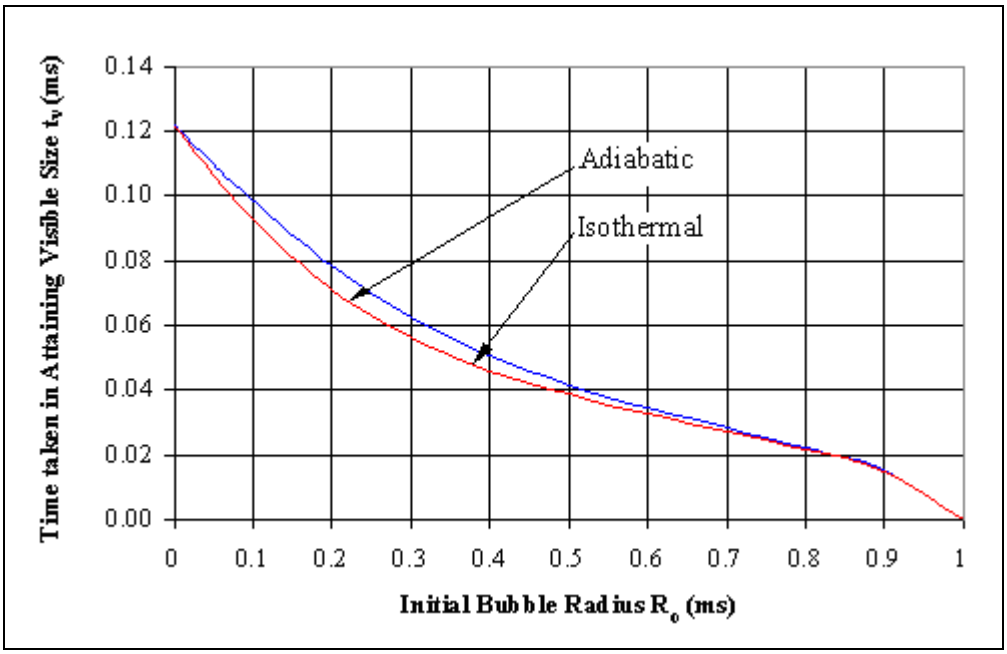


Figure R.7. Time taken (t_V) for bubbles, of different initial radii (R_o), to expand to visible size (R_V) in adiabatic and isothermal growth cases (R_V was taken as 1 *mm*).

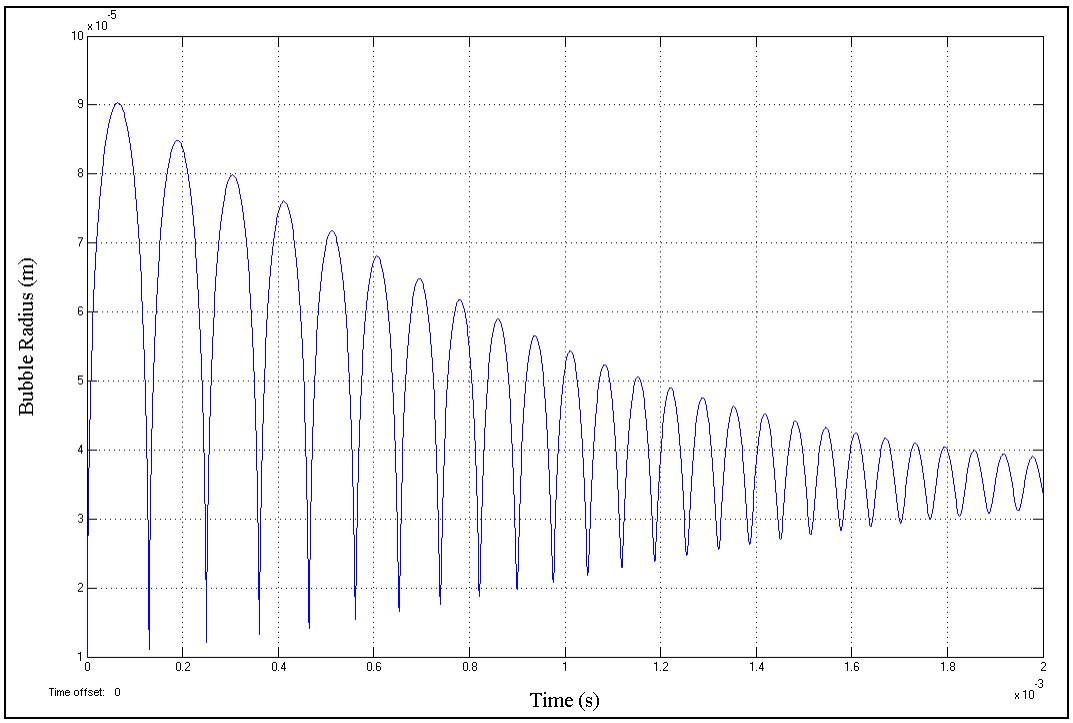


Figure R.8. Variation of bubble radius with time for growth of bubble (R_o 10 μm) subjected to step-function pressure drop from 7.93 *bar* to 2339 *Pa* at time zero.

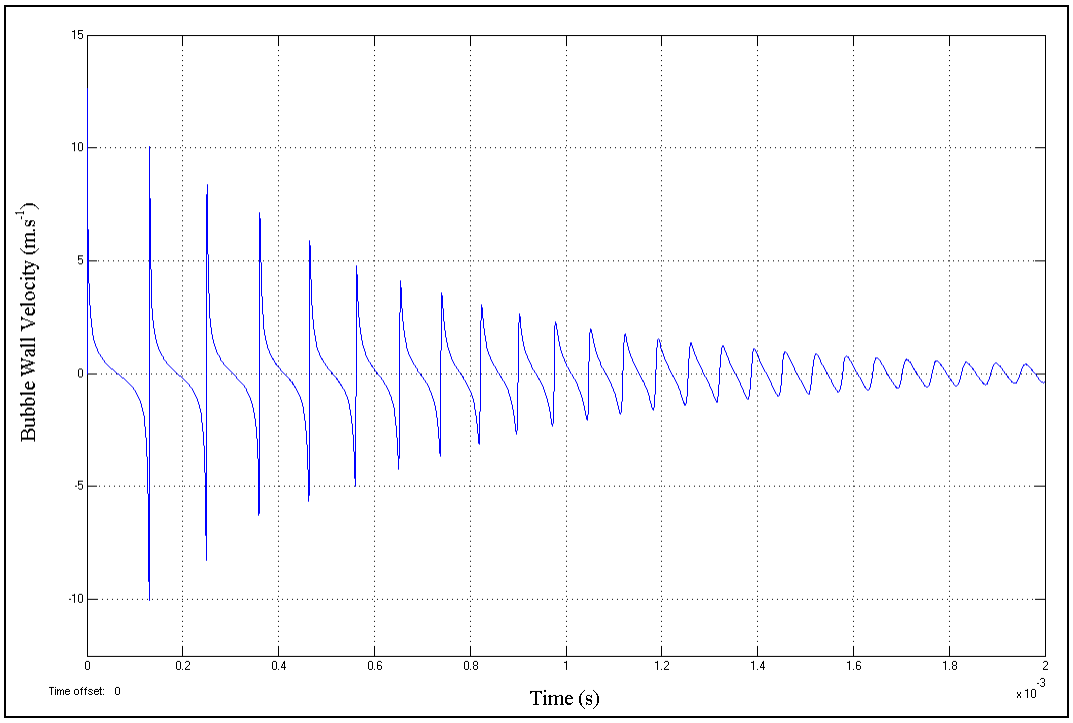


Figure R.9. Variation of bubble wall velocity with time for growth of bubble (R_o 10 μm) subjected to step-function pressure drop from 7.93 *bar* to 2339 *Pa* at time zero.

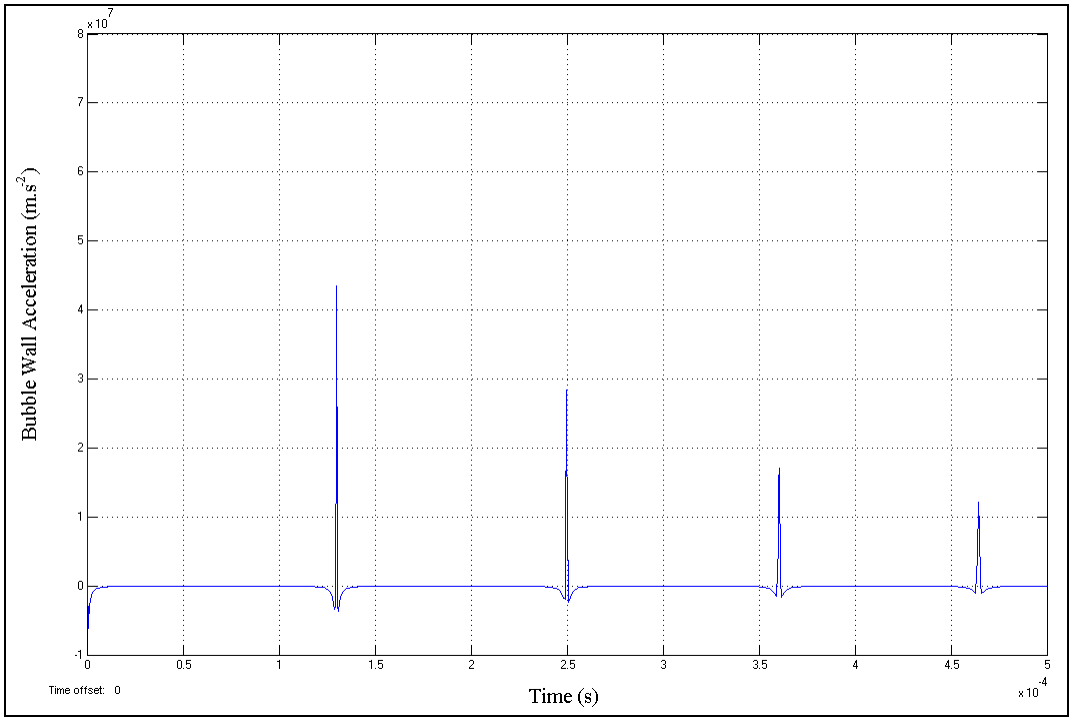


Figure R.10. Variation of bubble wall acceleration with time for growth of bubble (R_o 10 μm) subjected to step-function pressure drop from 7.93 *bar* to 2339 *Pa* at time zero.

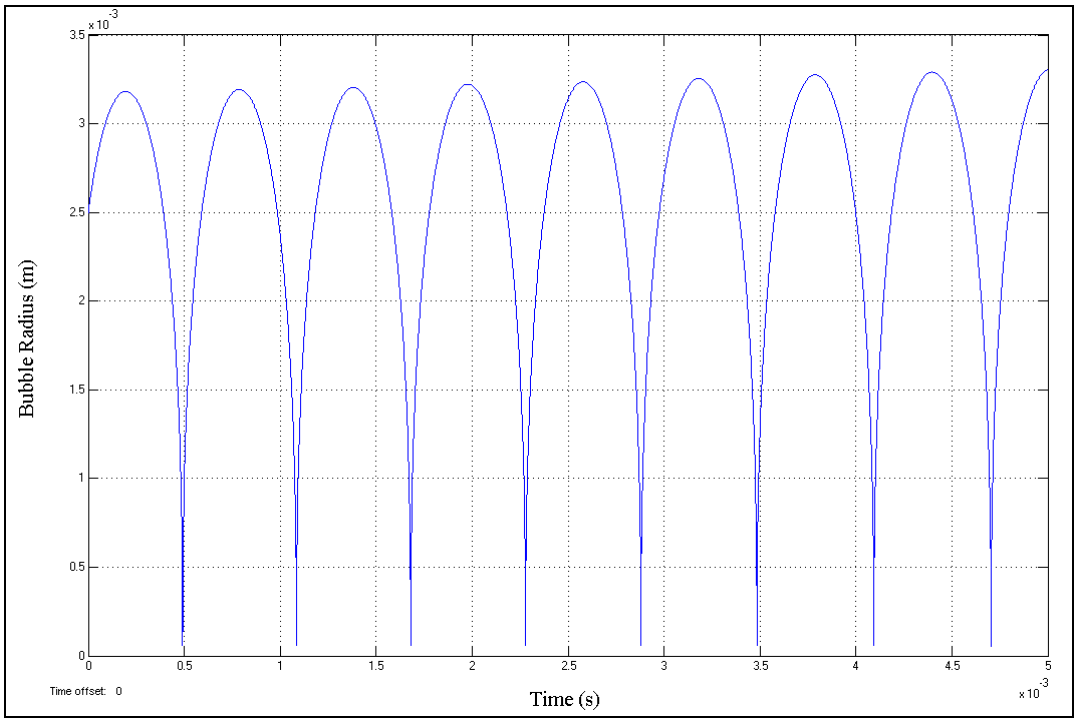


Figure R.11. Variation of radius with time for collapse of a bubble (R_o 0.5 *mm*) subjected to step-function pressure rise from -1 to 1 *bar* at time zero. $R(0)$=2.5 *mm*, $\dot{R}(0)$=8.3 $m.s^{-1}$

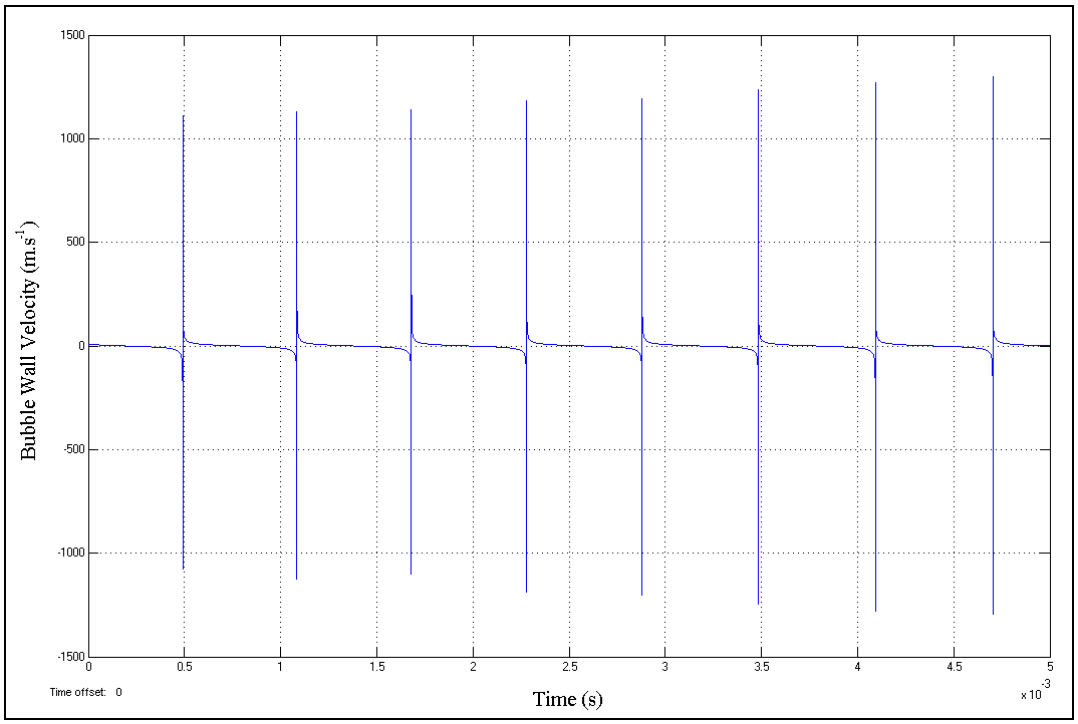


Figure R.12. Variation of bubble wall velocity with time for collapse of bubble (R_o 0.5 *mm*) subjected to pressure rise from -1 to 1 *bar* at t = 0. $R(0)$=2.5 *mm*, $\dot{R}(0)$=8.3 $m.s^{-1}$

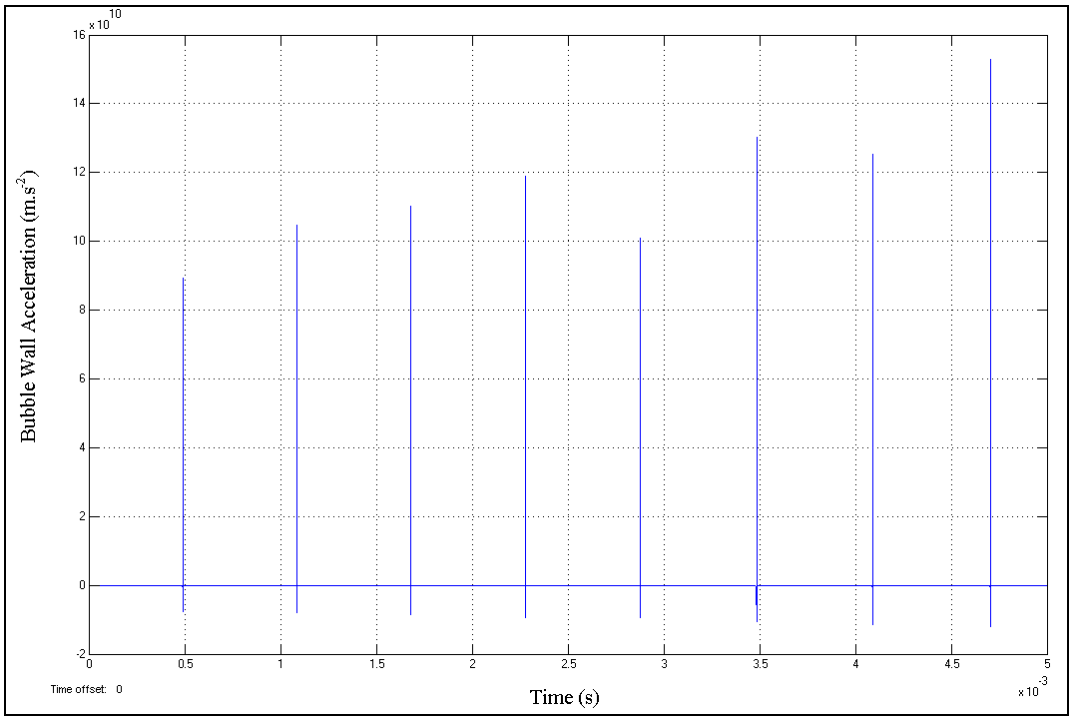


Figure R.13. Variation of bubble wall acceleration with time for growth of bubble (R_o 0.5*mm*) subjected to pressure rise from -1 to 1 *bar* at t = 0. $R(0)$=2.5 *mm*, $\dot{R}(0)$=8.3 $m.s^{-1}$

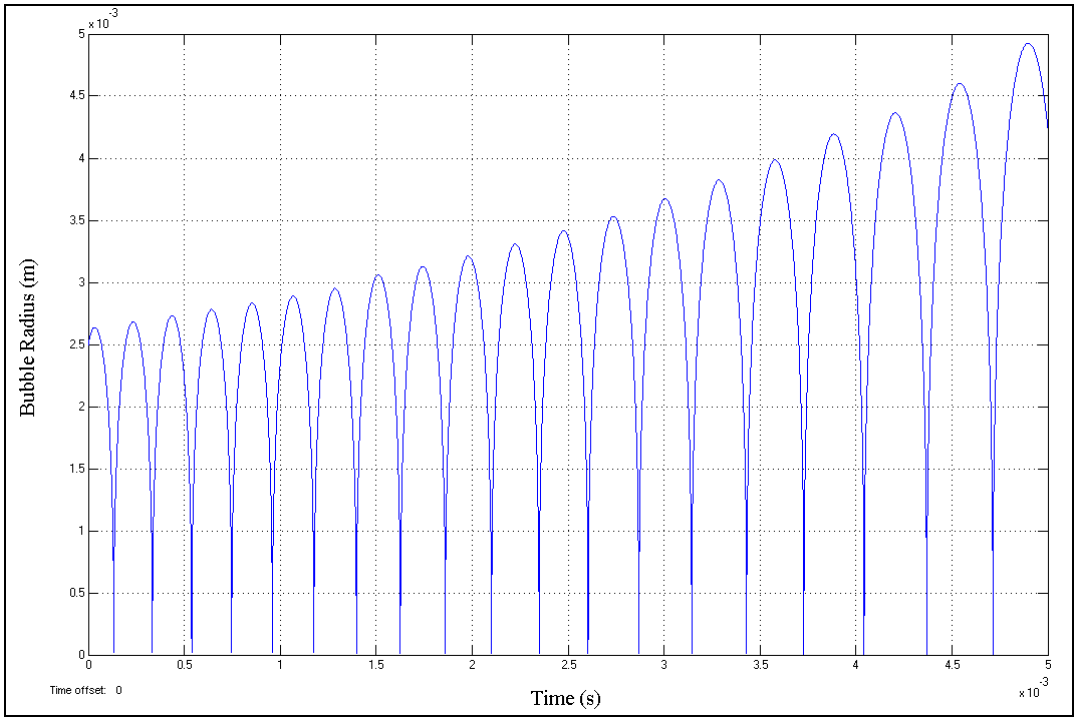


Figure R.14. Variation of radius with time for collapse of a bubble (R_o 0.5 *mm*) subjected to step-function pressure rise from -1 to 6 *bar* at time zero. $R(0)$=2.5 *mm*, $\dot{R}(0)$=8.3 $m.s^{-1}$

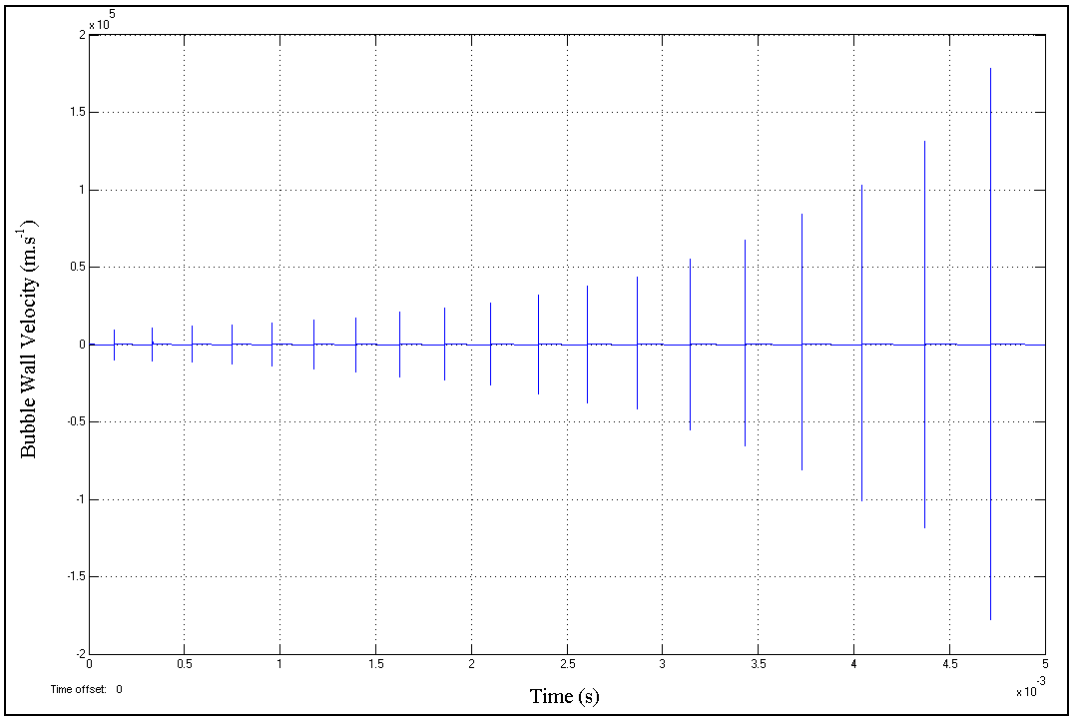


Figure R.15. Variation of bubble wall velocity with time for collapse of bubble (R_o 0.5 *mm*) subjected to pressure rise from -1 to 6 *bar* at t = 0. $R(0)$=2.5 *mm*, $\dot{R}(0)$=8.3 $m.s^{-1}$

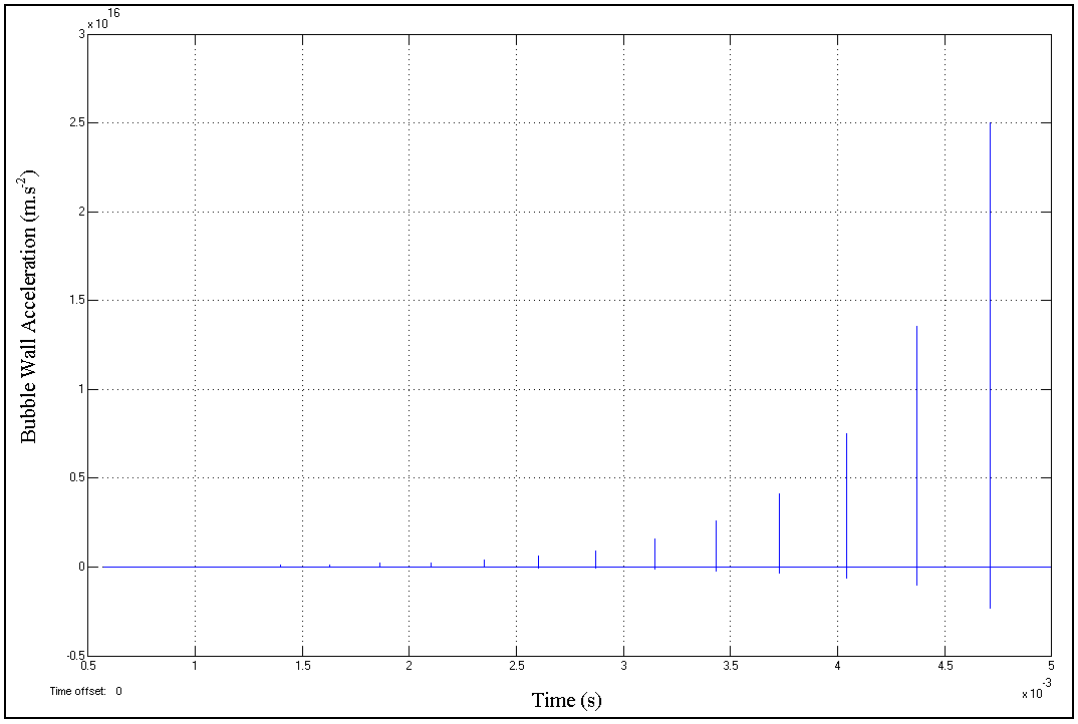


Figure R.16. Variation of bubble wall acceleration with time for collapse of bubble (R_o 0.5*mm*) subjected to pressure rise from -1 to 6 *bar* at t = 0. $R(0)$=2.5 *mm*, $\dot{R}(0)$=8.3 $m.s^{-1}$

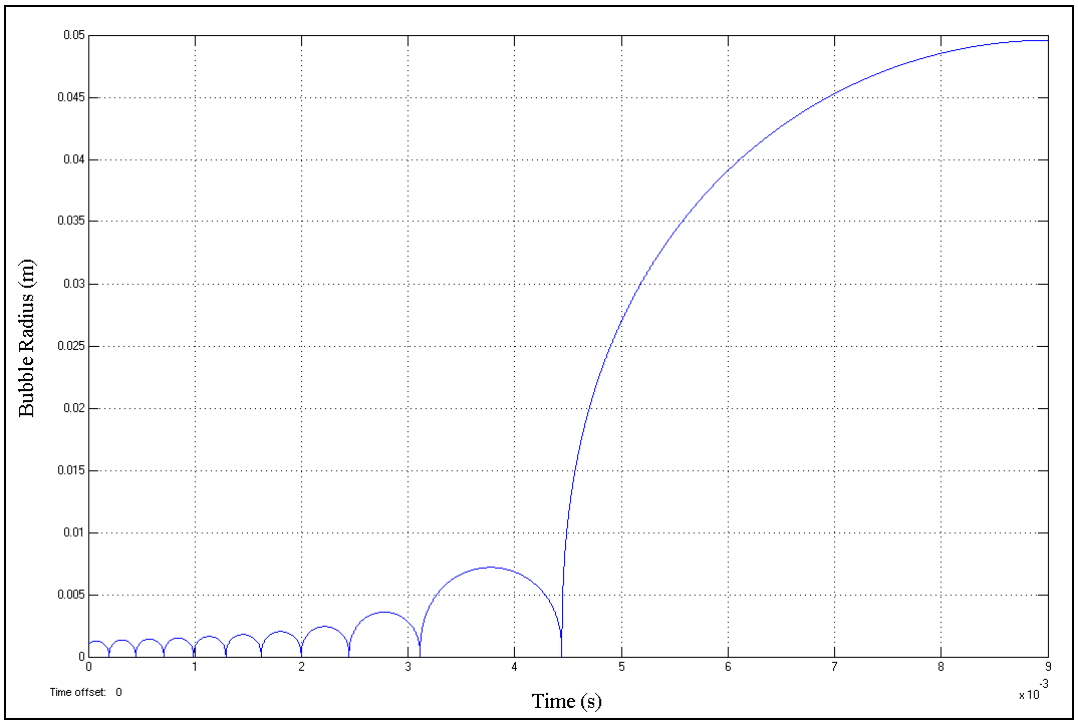


Figure R.17. Variation of radius with time for collapse of a bubble (R_o 0.1 *mm*) subjected to pressure rise from -1 to 1 *bar* at time zero. $R(0)$ = 1 *mm*, $\dot{R}(0)$ = 8.3 $m.s^{-1}$.

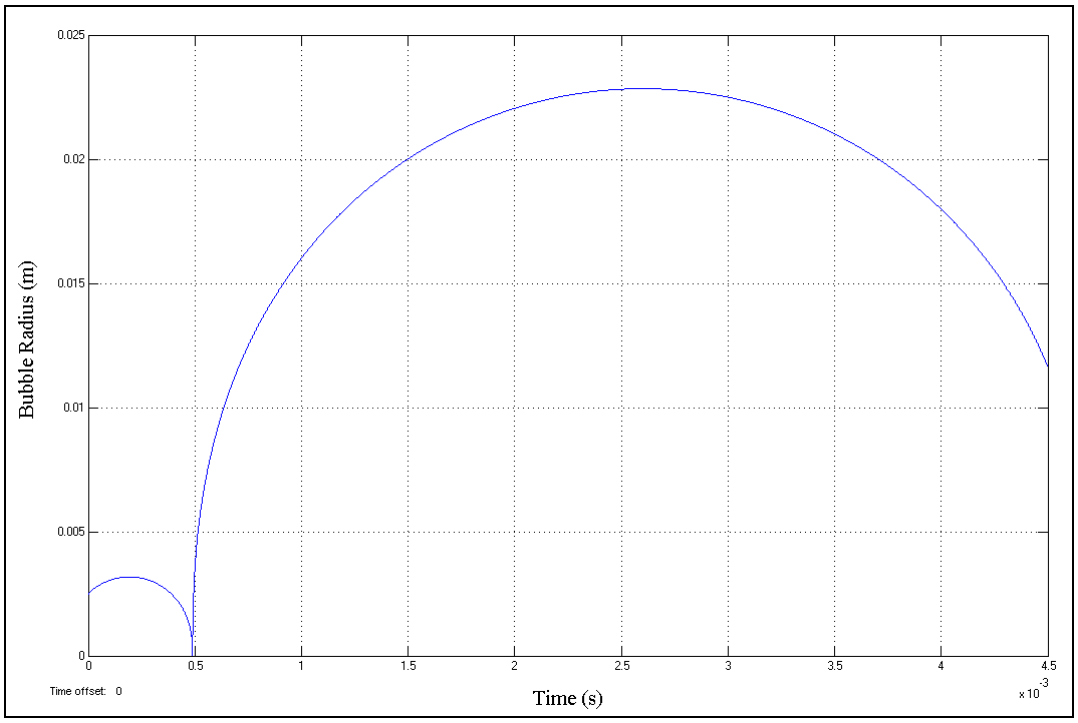


Figure R.18. Variation of radius with time for collapse of a bubble (R_o 0.05 *mm*) subjected to pressure rise from -1 to 1 *bar* at t=0. $R(0)$=2.5 *mm*, $\dot{R}(0)$=8.3 $m.s^{-1}$.

Appendix S

Cavitation Models Employed by Available CFD Codes

Numerical techniques used for modelling two-phase flows may be distinguished as either interface tracking or continuum methods. In the continuum method, the two phases are considered to be the same fluid. The interface is not distinct and the density of a cell reflects its liquid and vapour content. In the newer interface tracking method, each phase is treated separately resulting in more equations to be solved and increased computational demand. In this method, interfaces may be tracked using several techniques, which may be classified according to physical and mathematical approaches as either capturing (also known as self-adjusting or moving grid or Lagrangian approach) methods, tracking (also known as fixed or static grid or Eulerian approach) methods or combined methods. The Euler-Lagrange (the primary and secondary phases are treated by Eulerian and Lagrangian approaches respectively) approach is an example of a combined method. Tracking methods, also known as Euler-Euler methods (since both phases are treated in an Eulerian way), may be further distinguished as surface and volume tracking [193].

The volume-of-fluid (VOF) method is a widely adopted type of volume tracking method and is built-in in commercial codes including the three packages available to the author during this study, namely STAR-CD, FLUENT and CFX (Two-phase problems are mathematically treated as singular, not-interpenetrating fluids separated by a moving, discontinuous surface across which mass transfer may occur. In STAR-CD and CFX, cavitation is studied using an extension of the two-phase VOF algorithm, while the cavitation model in FLUENT is incompatible with the VOF model and is used with the mixture model, another Euler-Euler method. The cavitation models of both STAR-CD and Fluent include modified versions of the Rayleigh-Plesset differential equation [193, 194,195]. In both the mixture model in FLUENT and the VOF model in STAR-CD, a volume fraction equation is solved for each secondary phase [194,196].

In STAR-CD, the free surface and cavitation modelling methodology is, presently, only applicable if the densities of all fluids is constant [195], as confirmed by consultations with a STAR-CD agent. The mixture model in FLUENT allows three fluids, a liquid, its vapour and a fixed fraction of non-condensable gases, to be included in a simulation. However, while the secondary phase (vapour and gas) may be compressible, the primary phase (the liquid) must be incompressible [194]. This eliminates the possibility of simulating cavitation effects and shock or expansion waves simultaneously. In conclusion, the available CFD software is unable to simulate cavitation induced by acoustic waves propagating into the liquid.

Appendix T

Analysis of a Finite, Non-Rigid Plate Subject to a Square Wave

T.1. Equations of Motion of the Plate

Taylor [167] considered the behaviour of a finite, non-rigid plate. This theory has been applied in different cases in [55] and [197] for waves in air and water. Taylor made certain assumptions, which are inapplicable to the relevant case, the Mach 2 shock tube. The relevant equations and basic outline concerning the present circumstances will now be derived. Firstly, for a square wave, the incident wave pressure may be expressed as:

$$p_i = p_0 \tag{T.1}$$

Consequently, the reflected wave will be of the form,

$$p_r = p_o \Phi(t + x/a) \tag{T.2}$$

where ($x = 0$) corresponds to the front face of the plate. Thus, the net pressure due to the incident and reflected waves, at the plate surface, is:

$$p = p_i + p_r \tag{T.3}$$

and since only the pressure at the surface ($x = 0$) is required, $\Phi(t + x/c) = \Phi(t) = \Phi$ and

$$\frac{p}{p_0} = 1 + \Phi \tag{T.4}$$

From the definition of wave impedance, the particle velocity behind a wave may be expressed as $u = \rho.a$. Thus, the particle velocities behind the incident and reflected waves may be expressed as:

$$u_i = \frac{p_i}{\rho_i a_i} \tag{T.5}$$

$$u_r = -\frac{p_r}{\rho_r a_r} \tag{T.6}$$

The equation of continuity at the plate requires that the velocity of the solid surface be equal to that of the fluid adjacent to it. Since the incident and reflected waves contribute to this velocity,

$$\dot{\zeta} = u_i + (-u_r) = \frac{p_0}{\rho_i a_i} - \frac{p_0 \Phi}{\rho_r a_r}$$

$$\frac{\dot{\zeta}}{p_0} = \frac{1}{\rho_i a_i} - \frac{\Phi}{\rho_r a_r} \tag{T.7}$$

Differentiating equation (T.7) with respect to *t* yields an expression for the acceleration:

$$\frac{\ddot{\zeta}}{p_0} = -\frac{\dot{\Phi}}{\rho_r a_r} \tag{T.8}$$

Integrating equation (T.7) with respect to *t* yields an expression for the displacement:

$$\frac{\zeta}{p_0} + c = \frac{t}{\rho_i a_i} - \frac{\int \Phi dt}{\rho_r a_r} \tag{T.9}$$

The inertia of the plate, the pressure and the external constraints determine the motion of the plate. The effect of the clamping constraint, which must be to restrict the motion is taken into account by assuming that it is equivalent to a spring of stiffness *k*, which in combination with the inertia of the plate (mass per unit area *m*) will determine the natural frequency ω_n of the system i.e. the constraints cause the plate to oscillate freely with a period *T* equal to $2\pi / \omega_n$. The equation of motion of the system is then:

$$F = M\ddot{\zeta} + k\zeta$$

$$pA = mA\ddot{\zeta} + k\zeta$$

$$\frac{p}{m} = \ddot{\zeta} + \frac{k}{mA}\zeta$$

$$\frac{p}{m} = \ddot{\zeta} + \omega_n^2 \zeta \tag{T.10}$$

Substituting the expressions for acceleration (T.8) and displacement (T.9) into the equation of motion (T.10) and using equation (T.4) yields

$$\frac{p_0(1+\Phi)}{m} = -p_0 \frac{\dot{\Phi}}{\rho_r a_r} + \omega_n^2 \left(\frac{t}{\rho_i c_i} - \frac{\int \Phi dt}{\rho_r a_r} - c \right) p_0 \tag{T.11}$$

Differentiating with respect to *t*, and substituting $Z_i = \rho_i a_i$ and $Z_r = \rho_r a_r$,

$$\frac{p_0 \dot{\Phi}}{m} = -p_0 \frac{\ddot{\Phi}}{Z_r} + \omega_n^2 \left(\frac{1}{Z_i} - \frac{\Phi}{Z_r} \right) p_0$$

$$\ddot{\Phi}\,\frac{p_0}{Z_r} + \dot{\Phi}\,\frac{p_0}{m} + \Phi\omega_n^2\,\frac{p_0}{Z_r} = \omega_n^2\,\frac{1}{Z_i}\,p_0 \tag{T.12}$$

Multiplying throughout by Z_r / p_0

$$\ddot{\Phi} + \dot{\Phi}\,\frac{Z_r}{m} + \Phi\omega_n^2 = \omega_n^2\,\frac{Z_r}{Z_i} \tag{T.13}$$

Thus, the solution of the original equation of motion, in effect, requires solution of Φ only. In *D-operator* notation, equation (T.13) is [198]:

$$\left(D^2 + D\,\frac{Z_r}{m} + \omega_n^2\right)\Phi = \omega_n^2\,\frac{Z_r}{Z_i} \text{ or}$$

$$\frac{1}{P(D)}\,\Phi = \omega_n^2\,\frac{Z_r}{Z_i} \tag{T.14}$$

This differential equation has the solution:

$$\Phi = \Phi_0 + \Phi_1 \tag{T.15}$$

where Φ_o is the complementary function and Φ_1 is the particular solution. Firstly, the complementary function may be expressed as:

$$\Phi_0 = Ae^{S_1 t} + Be^{S_2 t} \tag{T.16}$$

where s_1 and s_2 are the roots of the quadratic equation:

$$s^2 + s\,\frac{Z_r}{m} + \omega_n^2 = 0 \tag{T.17}$$

Thus,

$$s_1, s_2 = \frac{-(Z_r / m) \pm \sqrt{(Z_r / m)^2 - 4\omega_n^2}}{2} \tag{T.18}$$

In section T.3, the natural frequency of the plate is calculated. Since the plate under consideration (the gas-liquid interface in the Mach 2 shock tube) had a small radius and was relatively stiff, the natual frequency turned out to be high. It followed that in this present case, $4\omega_n^2 > (Z_r / m)^2$ and thus, the roots, s_1 and s_2, were complex:

$$s_1 = -(Z_r / 2m) + \omega_n i \text{ and } s_2 = -(Z_r / 2m) - \omega_n i \tag{T.19}$$

Although this will yield the general solution, its form is unsatisfactory as the solution contains complex roots. Since, the displacement and pressure, and thus Φ as well, must be real, equation (T.16) is rewritten in real form:

$$\Phi_0 = Ae^{\left(-\frac{Z_r}{2m}+\omega_n i\right)t} + Be^{\left(-\frac{Z_r}{2m}-\omega_n i\right)t}$$

$$\Phi_0 = e^{-\frac{Z_r}{2m}t}\left(Ae^{(+\omega_n i)t} + Be^{(-\omega_n i)t}\right) \qquad \text{(T.20)}$$

and since $e^{i\theta} = cos\theta + isin\,\theta$,

$$\Phi_0 = e^{-\frac{Z_r}{2m}t}\left(P\cos\omega_n t + Q\sin\omega_n t\right) \qquad \text{(T.21)}$$

where P and Q are arbitrary constants.

Now, from equation (T.14), the particular solution is:

$$\Phi_1 = \frac{1}{D^2 + D\dfrac{Z_r}{m} + \omega_n^2}\,\omega_n^2\,\frac{Z_r}{Z_i} \qquad \text{(T.22)}$$

This may be written as

$$\Phi_1 = \frac{1}{\omega_n^2\left(1 + \left(D^2/\omega_n^2\right) + \left(DZ_r/m\right)\right)}\,\omega_n^2\,\frac{Z_r}{Z_i}, \qquad \text{(T.23)}$$

which may be expanded, using the binomial series, to

$$\Phi_1 \cong \left[1 - \left(\frac{Z_r}{m\omega_n^2}D + \frac{1}{\omega_n^2}D^2\right) + \text{higher order terms}\right]\frac{Z_r}{Z_i} \qquad \text{(T.24)}$$

Ignoring higher order terms and since Z_r / Z_i is a constant,

$$\Phi_1 \cong \frac{Z_r}{Z_i} \qquad \text{(T.25)}$$

Thus, the solution of the differential equation (T.14) is, from (T.21) and (T.25):

$$\Phi \cong e^{-\frac{Z_r}{2m}t}\left(P\cos\omega_n t + Q\sin\omega_n t\right) + \frac{Z_r}{Z_i} \qquad \text{(T.26)}$$

Thus, the derivative of equation (T.26) with respect to t is expressed in equation (T.27):

$$\dot{\Phi} \cong -\frac{Z_r}{2m}e^{-\frac{Z_r}{2m}t}\left(P\cos\omega_n t + Q\sin\omega_n t\right) + e^{-\frac{Z_r}{2m}t}\left(-P\omega_n\sin\omega_n t + Q\omega_n\cos\omega_n t\right)$$

While the integral of equation (T.26) is:

$$\int \Phi \; dt \cong \int e^{-\frac{Z_r}{2m}t} P \cos\omega_n t \; dt + \int e^{-\frac{Z_r}{2m}t} Q \sin\omega_n t \; dt + \frac{Z_r}{Z_i} t \qquad \text{(T.28)}$$

T.2. Boundary Conditions

Three boundary conditions are needed to solve for the constants in equations (T.26), (T.27) and (T.28). Consider the boundary condition $t = 0$, $\dot{\zeta} = 0$ i.e. the plate is initially at rest. Substitution into equation (T.7) yields

$$\frac{(0)}{p_0} = \frac{1}{Z_i} - \frac{\Phi}{Z_r} \text{ (at } t = 0\text{) and}$$

$$\Phi = Z_r \; / \; Z_i \text{ (at } t = 0\text{)} \qquad \text{(T.29)}$$

Hence, equation (T.28) becomes

$$\frac{Z_r}{Z_i} \cong e^{(0)}\left(P(1) + Q(0)\right) + \frac{Z_r}{Z_i} \text{ (at } t = 0\text{).}$$

The result is that

$$P = 0 \qquad \text{(T.30)}$$

The second boundary condition is that the initial acceleration of the plate is equal to the force on it, divided by its mass i.e. at $t = 0$, $\ddot{\zeta} = FM = p/m$. So, equation (T.8) becomes:

$$\frac{(p \; / \; m)}{p_0} = -\frac{\dot{\Phi}}{Z_r} \text{ (at } t = 0\text{)} \qquad \text{(T.31)}$$

And by equation (T.4),

$$\frac{p_0(1 + \Phi)}{p_0 m} = -\frac{\dot{\Phi}}{Z_r} \text{ (at } t = 0\text{) or}$$

$$(1 + \Phi)\frac{Z_r}{m} + \dot{\Phi} = 0 \text{ (at } t = 0\text{)} \qquad \text{(T.32)}$$

Now, at $t = 0$, equations (T.26) and (T.27) become

$$\Phi \cong e^{(0)}\left(P(1) + Q(0)\right) + \frac{Z_r}{Z_i} \text{ (at } t = 0\text{) and} \qquad \text{(T.33)}$$

$$\dot{\Phi} \cong -\frac{Z_r}{2m} e^{(0)}\left(P(1) + 0\right) + e^{(0)}\left((0) + Q\omega_n(1)\right) \text{ (at } t = 0\text{)} \tag{T.34}$$

respectively. Substituting (T.33) and (T.34) into equation (T.32),

$$(1 + P + \frac{Z_r}{Z_i})\frac{Z_r}{m} - \frac{Z_r}{2m} P + Q\omega_n = 0 \text{ (at } t = 0\text{)} \tag{T.35}$$

And since it was found that $P = 0$ (T.30), the result is that

$$(1 + \frac{Z_r}{Z_i})\frac{Z_r}{m} + Q\omega_n = 0 \text{ or}$$

$$Q = -\frac{1}{\omega_n}\left(\frac{Z_r}{m} + \frac{Z_r^2}{Z_i m}\right) \tag{T.36}$$

Before considering the third (displacement) boundary condition, note that it was also found that:

$$\int e^{-\frac{Z_r}{2m}t} \sin\omega_n t\, dt = -\frac{2m}{Z_r} e^{-\frac{Z_r}{2m}t} \cos\omega_n t \frac{\left((2m\omega_n / Z_r) + 1\right)}{1 + \left(2m\omega_n / Z_r\right)^2} \tag{T.37}$$

and thus, at $t = 0$,

$$\int e^{-\frac{Z_r}{2m}t} \sin\omega_n t\, dt = -\frac{2m}{Z_r} \frac{\left((2m\omega_n / Z_r) + 1\right)}{1 + \left(2m\omega_n / Z_r\right)^2} \text{ (at } t = 0\text{)} \tag{T.38}$$

The third boundary condition is $\zeta = 0$ at $t = 0$. Thus equation (T.9) becomes, using the result (T.30) that $P = 0$,

$$\frac{(0)}{p_0} + c = \frac{(0)}{Z_i} - \frac{\int \Phi dt}{Z_r} \text{ (at } t = 0\text{) or}$$

$$\int \Phi\, dt = -Z_r c \text{ at } t = 0 \text{ (at } t = 0\text{)} \tag{T.39}$$

Thus equation (T.28) becomes

$$-Z_r c = (0) + \int e^{-\frac{Z_r}{2m}t} Q \sin\omega_n t\, dt + (0) \text{ (at } t = 0\text{)} \tag{T.40}$$

Substituting equations (T.36) and (T.38) into equation (T.40):

$$c = -\frac{1}{\omega_n} \frac{2Z_i + 2Z_r}{Z_i Z_r} \frac{\left((2m\omega_n / Z_r) + 1\right)}{1 + \left(2m\omega_n / Z_r\right)^2} \tag{T.41}$$

Having calculated the constants P, Q and c from the boundary conditions of velocity, acceleration and displacement, the displacement of the plate and the pressure a the front surface may be determined from equations (T.9), (T.28), (T.30), (T.36) and (T.41).

An important point should be noted: since air, through which the incident shock in the Mach 2 shock tube propagates, cannot sustain a tension, the pressure on the plate may become zero and cease. The distance it moves before being brought to rest will then depend only on the nature of the external supports. The equation of motion would then be the free vibration equation [50,167]:

$$m\ddot{\zeta} + k\zeta = 0 \tag{T.42}$$

the solution of which may be expressed as

$$\zeta(t) = A\cos(\omega_n t - \vartheta) \tag{T.43}$$

where $A^2 = \zeta^2 + \dot{\zeta}^2/\omega_n^2$ [50,167]

T.3. The Fundamental Natural Frequency of the Plate

The natural frequency is the lowest inherent rate of vibration and is assumed when a system is vibrating freely. Each natural frequency is associated with a natural mode of vibration i.e. a characteristic of a system undergoing vibration, representing the pattern of nodes (where some characteristic of the system has zero amplitude) and antinodes. The fundamental frequency and mode are the lowest natural frequency and corresponding mode respectively, of a system [199]. A plate is a continuous system with an infinite number of degrees of freedom and natural modes and frequencies but vibrates with significant amplitude at only a limited number of frequencies (often only the one that is excited dictates the plane of motion) [200]. For the fundamental mode of a clamped plate the only nodal points are the fixed or supported points. The natural frequencies of vibration of a circular plate, clamped along its edge may be calculated by [199-201].

$$\omega_{n(ij)} = \frac{\lambda_{ij}^2}{r^2}\sqrt{\frac{Et^3}{12m(1-\nu^2)}} = \frac{\lambda_{ij}^2}{r^2}\sqrt{\frac{D}{\rho t}} \tag{T.44}$$

$$f_{ij} = \frac{\lambda_{ij}^2}{2\pi r^2}\sqrt{\frac{Et^3}{12m(1-\nu^2)}} \qquad \text{(T.45)}$$

where m is the mass per unit area of the plate and t, r, ν and ρ are the thickness, radius and Poisson's ratio and density of the plate respectively. D is the flexural rigidity $D.=.E.t^3/12.m.(1-\nu^2)$. λ_{ij} is the dimensionless eigenvalue, which is a function of i and j [199], the number of nodal diameters of the specified mode and the number of nodal circles or rings (excluding the boundary) of the specified mode (in the mode shape), excluding those enforced by boundary conditions. Specification of i and j, determines a specific natural frequency and associated mode shape.

The plate had a mass per unit area M was approximately 5.8 $kg.m^2$. The portion of the rubber interface that was exposed to the flow had a diameter of 61 mm, making the exposed area equal to 0.0292 m^2. Consequently, the mass of the 4 mm thick rubber that was exposed to the flow and free to move was approximately 17 g. Poisson's ratio the rubber was taken as 0.49 (limited, by definition, to less than 0.5). The value of the eigenvalue for the first, lowest mode of vibration was taken as 10.2158, in accord with values of [200-203]. Young's modulus for the rubber was assumed to be 4 MPa. The flexural rigidity is then

$$D = 0.0284\ N.m^2$$

The value of the natural frequency is

$$\omega_n = 782.513\ rad.s^{-1} \text{ or}$$

$$f_n = 124.541\ s^{-1}$$

In the present case, the plate is supported against vibration by the column of liquid above it, which raises the natural frequency of the plate. The foundation modulus, E_f, is defined as the ratio of the pressure applied per unit area of foundation to the deformation that pressure produces [199].

$$E_f = \frac{k_f}{\Delta^2} \qquad \text{(T.46)}$$

Since the plate movement was shown to produce a compression wave with a short rise time in the water, the column of water may as well not be free at the top surface and the foundation modulus may be substituted by the bulk modulus of water:

$$Ef = B = 2.1963\times10^{9}\ Pa$$

Then, equation (T.46) yields:

$$\frac{E_f}{4\pi^2 M} = 9.59188\times10^{6}\ s^{-2}$$

The natural frequency of a uniform thin plate on elastic foundations may be found by modifying the expression for the frequency in the absence of the foundation by [199]:

$$f_{ij} = \left(f_{ij}^2 \Big|_{\substack{without\\foundation}} + \frac{E_f}{4\pi^2 M} \right)^{\frac{1}{2}} \qquad \text{(T.47)}$$

From equation (T.13), the effective natural frequency of vibration of the interface in the first mode was found to be:

$$\omega_n = 19475.2\ rad.s^{-1} \text{ or}$$

$$f_n = 3099.58\ s^{-1}$$